Fully Coupled Elasto-plastic Computational Framework for Fluid Pressurised Crack Evolution in Porous Media

Alex Hardcastle

Thesis submitted to The University of Nottingham for the degree of Doctor of Philosophy
October 2020

Contents

List of Figures **iv**

List of Tables **xi**

1 Introduction **1**

2 Literature review **5**

2.1 Hydrofracture 5
2.2 Fracture mechanics 17
2.3 Existing fracture models and current gaps in existing methods 20
2.3.1 Continuum damage model 20
2.3.2 Extended finite element models 24
2.3.3 Cohesive model 27
2.3.4 Discrete element modelling 28
2.4 Rock properties 29
2.5 Plasticity 31
2.5.1 Plasticity in fracture 33
2.5.2 The process zone 34
2.6 Energy 37
2.7 Finite strain 40
2.8 Summary 42

3 Fracture prediction using the energy minimisation Technique **44**

3.1 Damage model 51
3.1.1 Finite deformation 51
3.2 Fracture methodology 54
3.2.1 Fracture algorithm 55
3.3 Constitutive Equations 58
3.4 Simple fracture and the effect of orientation on crack path verification 61

3.5 Summary 78

4 Fully coupled fracture and pore pressure model 80

4.1 Dual porosity coupling framework 81

4.1.1 Spatial discretisation 90

4.2 Re-visiting minimisation 95

4.2.1 Hydrofracture algorithm 97

4.2.2 Time discretisation 100

4.2.3 Fracture permeability 100

4.2.4 Matlab implementation 101

4.3 Summary 101

5 Hydrofracture verifications 102

5.1 Consolidation verification 102

5.2 Hydrofracture verification 110

5.2.1 Stress contour verification 117

5.2.2 Undamaged fracture opening vs theoretical result . . . 128

5.3 Continuous fracture flow example 131

5.3.1 Continuous flow undamaged 131

5.3.2 Continuous flow damaged 143

5.3.3 Fluid lag behaviour 146

5.4 Non-uniform pressure field crack prediction 150

5.5 Summary 166

6 An Introduction to Plasticity 167

6.1 Finite deformation procedure 167

6.2 Algorithm applicability 169

6.2.1 Plastic flow update 170

6.3 Constitutive Equations 172

6.3.1 Elastic component 173

6.3.2 Plasticity component 173

6.3.3 Plastic energy dissipation 176

6.4 Finite deformation plasticity verification 180

6.5 Summary 188

7 Analysis **189**
7.1 Minimisation algorithm analysis for fracture 189
7.2 Hydrofracture algorithm analysis 194
7.3 Plastic algorithm analysis 198

8 Conclusion **201**
8.1 Further work 203

9 References **204**

Appendix A: Newton-Raphson Solver **223**

Appendix B: Chapter 3 results **226**

Appendix C: Chapter 5 results **231**

List of Figures

1 Typical fracking set up in industry [120] 6
2 Hydrofracture tip [21] 8
3 Micro-tomography extraction of two sand packs (a) and (b) to conversion to equivalent pore network models (c) and (b) [138] 12
4 Contour Damage map example of dual porosity model [95] . . 14
5 Pressure in well-bore overtime modelled using dual porosity model [95] 15
6 Dual porosity model principles 16
7 Classical Griffith crack 18
8 Different crack modes for various load cases [76] 20
9 Branched crack predicted via minimisation damage model [16] 23
10 Enrichment function across domain, representing fracture [109] 25
11 Interaction-integral example 2D, [113] 27
12 Cohesive energy graph [118] 28
13 Discrete element modelling of process zone (Red-fracture zone, Blue-plastic zone) [140] 29
14 Stress-strain curves for various confining pressures on rock [63] 30
15 Stress-strain curves for rock in tensile failure [12] 31
16 Mohr-Coulomb yield Criterion [143] 32
17 Different crack zones in energy distribution for a typical fracture [140]: showing the fracture zone and plastic zone . . . 35
18 Process zone of progressing (left to right) fracture captured with X ray with accompanying force (N) vs time (s) plot on sample [141] 36
19 General Stress-Strain graph from Figure 14: classes 1-3 of rock deformation sectioned off from left to right 38
20 Particle rearrangement associated with the various classes of rock loading 38
21 Finite strain principle [15] 41

22 Energy plot of 1D bar under tension over time (Red line- Fracture energy threshold, Blue line- Stored energy 48
23 Energy field example showing regions of increasing energy intensity near crack tips 49
24 Convex free energy function of Neo-Hookean constitutive model 50
25 Translation of square element 53
26 Translation and rotation of square element 53
27 Schematic for fracture methodology verification 61
28 Experimental (gray) and traced experimental (white) fracture initiations for various angled slit results from reference paper [74] 63
29 Numerical fracture initiations for various angled slit results from reference paper [74] 64
30 Stress strain plot for intact and 30 degree slit over time 65
31 Stress strain plot for 60 and 90 degree slit over time 66
32 Experimental fully developed fractures for various angled slit results from reference paper [74] 67
33 Damage plots; proposed numerical solution (left) and reference numerical solution (right) for intact specimen [74] 68
34 Damage plots; proposed numerical solution (left) and reference numerical solution (right) for intact specimen [74] 69
35 Deformation plots; proposed numerical solution (left) and reference numerical solution (right) for 45 degree slit at initiation [74] 70
36 Damage plots; proposed numerical solution (left) and reference traced experimental solution (right) for fracture initiation of 45 degree slit [74] 71
37 Deformation plots; proposed numerical solution (left) and reference numerical solution (right) for 0 degree slit at initiation [74] 72

38 Damage plots; proposed numerical solution (left) and reference traced experimental solution (right) for fracture initiation of 0 degree slit [74] 73
39 Corrected crack path for 0 degree fracture initiation (Proposed numerical result) 75
40 Damage plots; proposed numerical solution (left) and reference experimental solution (right) for full fracture of 60 degree slit [74] 76
41 Deformation plots; proposed numerical solution (left) and reference numerical solution (right) for 60 degree slit at initiation [74] 76
42 Energy plot over time consisting of fracture (surface energy) and stored energy (bulk) for 60 degree notch 77
43 Deformation gradient plot before fracture initiation 78
44 Example of fluid lag 97
45 Schematic for one dimensional consolidation test 104
46 Graph showing the applied load during one dimensional consolidation test 105
47 One dimensional graph showing pore pressure at various height intervals through the sample over time during the consolidation process 107
48 Pore pressure distributions through the one dimensional sample at various times 108
49 Consolidation snapshot with pressure and flow distributions . 109
50 Schematic for pressured penny crack test 110
51 Crack opening over time [106] 112
52 Pressure development with time at crack tip 114
53 Fluid pressure distribution across A-A at 50s and 80s with fluid compressibility enabled 115
54 Fluid pressure distribution across A-A, B-B and C-C at 50s and 80s with fluid compressibility disabled 116
55 Validation case: Hydrofracture fluid schematic 121

56 Crack opening over time with constant pressure; analytical solution (blue) vs proposed solution (Orange) 122
57 Crack length over time with constant pressure-theoretical solution (blue) vs proposed solution (Orange) 123
58 Effective Stress y-y homogeneous numerical hydrofracture result 125
59 Effective pressure y-y homogeneous numerical hydrofracture result 126
60 Fluid pressure distribution result from proposed solution . . . 127
61 Fluid pressure distribution result from reference solution . . . 128
62 Crack opening over time with rising pressure Theoretical solution (blue) vs proposed solution (Orange) 129
63 Hydrofracture fluid schematic 132
64 Deformation profile through section A-A at various time steps reference solution (Dashed lines) vs proposed solution (solid lines) 135
65 Pressure profiles along segment D-D reference (Dashed lines) vs proposed solution (Solid lines) 140
66 D-D pressure profile across fracture, analytical (Blue) vs proposed (orange) 141
67 Tip deformation over time reference solution vs proposed solution 142
68 Pressure variation over time inside of fracture (Reference solution [146]) 143
69 Pressure variation over time inside of fracture (Proposed solution) 144
70 Accumulative damaged over time during hydrofracture progress (Proposed solution) 145
71 Cumulative damage (Bonds broken) over time during hydrofracture progress (Reference solution [146]) 145
72 Fracture propagation over time during hydrofracture propagation showing symmetry 146
73 Fluid lag behaviour captured in hydrofracture experiment [22]. 147

74 Non-uniform pressure schematic (left) and experimental set up (right) 150
75 Test 1, Experimental fracture path [136] 153
76 Test 1, Numerical Hydrofracture at time=0s showing from left to right; fluid pressure distribution, X deformation and damage distribution 154
77 Test 1, Numerical Hydrofracture at time=25s showing from left to right; fluid pressure distribution, X deformation and damage distribution 155
78 Test 1, Numerical hydrofracture at time=35s showing from left to right; fluid pressure distribution, X deformation and damage distribution 156
79 Test 1, Fluid pressure in hole one over time 158
80 Test 5, Experimental fracture path [136] 160
81 Test 5, Numerical Hydrofracture at time=0s showing from left to right; fluid pressure distribution, X deformation and damage distribution 161
82 Test 5, Numerical Hydrofracture at time=25s showing from left to right; fluid pressure distribution, X deformation and damage distribution 162
83 Test 5 Numerical Hydrofracture at time=35s showing from left to right; Fluid pressure distribution, X deformation and damage distribution 163
84 Test 5 fluid pressure in hole one over time (Test 5) 164
85 Example of updating spatial coordinates with plastic considerations 176
86 Energy usage in a constitutive model 177
87 Upper bound solution by Prandtl for bearing capacity 180
88 Pad verification model layout 182
89 Load displacement graph for a loaded foundation comparing; Abaqus output (yellow) and proposed solution (blue) 183
90 Elastic deformation from proposed solution (left) and Abaqus solution (right) 184

91 Elastic deformation from proposed solution (left) and Abaqus solution (right) 185
92 Plastic deformation from proposed solution (left) and Abaqus solution (right) 186
93 Plastic deformation from proposed solution (left) and Abaqus solution (right) 187
94 Plastic yield plots from proposed solution (left) and Abaqus solution (right) 188
95 Deformation and Damage plots; proposed numerical solution (left) and reference numerical solution (right) for 15 degree slit at initiation [74] 226
96 Deformation and Damage plots; proposed numerical solution (left) and reference numerical solution (right) for 30 degree slit at initiation [74] 227
97 Deformation and Damage plots; proposed numerical solution (left) and reference numerical solution (right) for 75 degree slit at initiation [74] 228
98 Energy plot over time consisting of fracture (surface energy) and stored energy (bulk) over time (s) for 75 degree notch . . 229
99 Deformation and Damage plots; proposed numerical solution (left) and reference numerical solution (right) for 90 degree slit at initiation [74] 230
100 Test 2, Experimental fracture path [136] 231
101 Test 2, Numerical Hydrofracture at time=0s showing from left to right; fluid pressure distribution, X deformation and damage distribution 232
102 Test 2, Numerical Hydrofracture at time=25s showing from left to right; fluid pressure distribution, X deformation and damage distribution 232
103 Test 2, Numerical Hydrofracture at time=35s showing from left to right; fluid pressure distribution, X deformation and damage distribution 233
104 Test 2, fluid pressure in hole one over time 233

105 Test 3, Experimental fracture path [136] 234
106 Test 3, Numerical Hydrofracture at time=35s showing from left to right; fluid pressure distribution, X deformation and damage distribution 234
107 Test 3, Numerical Hydrofracture at time=25s showing from left to right; fluid pressure distribution, X deformation and damage distribution 235
108 Test 3, Numerical Hydrofracture at time=35s showing from left to right; fluid pressure distribution, X deformation and damage distribution 235
109 Test 3, fluid pressure in hole one over time 236
110 Test 4, Experimental fracture path [136] 236
111 Test 4, Numerical Hydrofracture at time=0s showing from left to right; fluid pressure distribution, X deformation and damage distribution 237
112 Test 4, Numerical Hydrofracture at time=25s showing from left to right; fluid pressure distribution, X deformation and damage distribution 237
113 Test 4, Numerical Hydrofracture at time=35s showing from left to right; fluid pressure distribution, X deformation and damage distribution 238
114 Test 4, fluid pressure in hole one over time (Test 4) 238

List of Tables

2 Material properties for single slit experiment 62
3 Material properties in consolidation test 103
4 Material properties in single slit hydrofracture 111
5 Material properties in second hydrofracture verification 120
6 Material properties for large scale penny crack hydrofracture . 133
7 Experimental setups 151
8 Material properties 152
9 Internal energies 181
10 Material properties for numerical pad experiment 182

List of Algorithms

1 Fracture procedure 56
2 Hydro-fracture procedure 98
3 Hydro flow procedure 106
4 Fracture procedure with plasticity 179

PUBLISHED INTERNATIONAL JOURNAL PAPERS (with peer-review)

Hardcastle, A., Mousavi Nezhad, M., Rezania, M., Tizani, W. and Ranjith, P.G. (2019). A fully coupled computational framework for fluid pressurised crack evolution in porous media. Journal of Porous Media, 22(8): 939-956.

Nomenclature

Symbol	Description	Unit
	Latin Symbols	
a	Crack half length	m
a_n	numerical constant	ND
a_0	Initial crack half length	m
C_u	Cohesion	N/mm^2
c	Compressibility	mm^2/N
c_f	Fluid compressibility	mm^2/N
c_s	Grain compressibility	mm^2/N
c_v	Compressibility	mm^2/N
c_d	Damaged compressibility	mm^2/N
dE	Bulk energy component	J/m^2
h	Hardening function	ND
f	Arbitrary function	ND
f_y	Yield function	ND
g_p	Plastic potential function	ND
g	Fitting function in minimisation process	ND
h	Fracture opening	m
h_s	softening function	m
i	Media notation i=1 (Porous), 1=2 (fractured) ND	
j	Iterator	ND
k_i	Permeability of respective region	m/s
k_f	Permeability of fractured region	m/s
l	Length	m
m_v	Check	ND
n_i	Force normal	N
n	Iterator	ND
n	Iteration of algorithm when used as subscript	ND
p_f	arbitrary fluid pressure	N/mm^2
$\dot{p}_i$	Approximated pressure	N/mm^2
p_i	Scalar pressure	N/mm^2
p_i^{n+1}	Iterated scalar pressure	N/mm^2

q_c	Flow scalar	m^3/s
q	Arbitrary flow rate	m^3/s
q_{frac}	Fracture velocity	m/s
r	distance from fracture	mm
s	Surface area of internal faults	mm^2
s_o	Initial surface area of internal faults	mm^2
t	Time	s
t_c	Critical Time	s
t_{full}	Runtime of simulation	s
u^i	Velocity in media i	m/s
$v(k)$	Arbitrary function	ND
$v(k)$	Arbitrary function	ND
v_α	fluid velocity in fracture	ND
v_s	fluid velocity in fracture	ND
v_D	fluid into fracture	ND
x	Coordinates	m
x_c	Distance along crack	m
y	Coordinates	m
$y(t)$	Arbitrary function of time	ND
y_t	Arbitrary function evaluated at time t	ND
z	Height in sample t	m
	Capital Latin Symbols	
A	Area of void space	mm^2
A	Initial area of void space	mm^2
C	Empirical constant	ND
D	Damage	ND
D_0	Initial damage	ND
E	Young's Modulus	N/mm^2
E_i	Internal energy	J/m^2
E_1	Exponential integral	ND
E_e	Internal elastic energy	J/m^2
E_p	Internal plastic energy	J/m^2

K_{bulk}	Bulk Modulus	N/mm^2
KE	Kinetic energy	J
KE_d	Kinetic energy of damaged elements	J
G	Energy release rate	$J/m^2/s$
H	Pore-elastic expansion coefficient	ND
H_d	Height of drainage channel for consolidation purposes	m
H^{N-1}	Hausdorff measure	ND
I_1	First strain invariant	ND
II_2	Second strain invariant	ND
III_3	Third strain invariant	ND
J	Volume change	ND
M_v	check	ND
Q	Fluid flow into fracture	mm^3/s
R_0	Fracture energy term	J/m^2
T_s	Loading time	s
T_v	Consolidating time	s
V_α	Volume of solids	m^3
V_{total}	Total volume	m^3
W	Work	J/m^2
W_p	Plastic Work	J/m^2
Y	Empirical constant	ND
	Greek Symbols	
α	Domain differentiator	ND
α_i	Coupling coefficient	ND
α_p	P-Wave modulus	kg/m
α_{ii}	Fluid compressibility term	ND
α_{12}, α_{21}	Relative fluid compressibility term	mm^2/N
α_{id}	Damaged coupling coefficient	ND
α_{iid}	Damaged fluid compressibility term	ND
$\alpha_{12d}, \alpha_{21d}$	Damaged relative fluid compressibility term	Pa/s
β	Interpolation constant	ND
ϵ	General strain	ND

ϵ_e	Elastic strain	ND
ϵ_p	Plastic strain	ND
$\dot{\epsilon}$	Rate of strain	ND
μ_f	Dynamic viscosity	N/mm^2
μ_i	Arbitrary constant	N/mm^2
μ	Shear modulus	N/mm^2
Δ_p	Pressure change	N/mm^2
Δ_t	time increment	s
Δ_y	Change in arbitrary solution	ND
Γ	Domain boundary	ND
σ	Stress	N/mm^2
σ_0	Initial stress	N/mm^2
σ_m	Mean stress	N/mm^2
σ_1, σ_3	Principal stresses	N/mm^2
σ_d	Damaged stress	N/mm^2
σ_p	Plastic stress	N/mm^2
σ_c	Critical stress	N/mm^2
σ_f	Yield stress	N/mm^2
σ_h	Horizontal stress	N/mm^2
σ_v	Vertical stress	N/mm^2
γ	Leak-off coefficient	ND
γ_p	consistency parameter	ND
Γ	Boundary containing integral	ND
π	pi	ND
λ	Lamé's constant	N/mm^2
λ_n	numerical constant	ND
Ω	Domain	ND
Ψ	Free energy function	ND
ψ_0	Energy required for cohesion breakage	J
ψ	Angle of dilation	ND
ϕ_i	Porosity of respective region	ND
ϕ_f	Porosity of fractured region	ND
ϕ_m	Porosity of porous region	ND

ϕ	Angle of friction	ND
ρ_f	Fluid density	kg/m^3
ν	Poisson ratio	ND
τ	Shear stress	N/mm^2
$d\tau$	Shear energy component	J
	Matrix letters	
$\mathbf{b}$	Left Cauchy Green strain tensor	ND
$\boldsymbol{B_1}$	Shape function derivative	ND
$\boldsymbol{B_2}$	Shape function derivative	ND
$\boldsymbol{B_3}$	Shape function derivative	ND
$\boldsymbol{C_{ijkl}}$	Compliance tensor	N/mm^2
$\boldsymbol{C}$	Cauchy stress matrix	N/mm^2
$\boldsymbol{C_c}$	Coupling matrix	ND
$\boldsymbol{D}$	Damage prescribed to every element	ND
$\boldsymbol{E}$	Work conjugate	ND
$\boldsymbol{F_m}$	Force matrix	N/mm^2
$\boldsymbol{F}_{exterior}$	General external Force matrix	N/mm^2
$\boldsymbol{F}_{interior}$	General interior Force matrix	N/mm^2
$\boldsymbol{F}_{res}$	Residual force	ND
$\boldsymbol{F}^b$	Body forces	N/mm^2
$\boldsymbol{F}$	Deformation gradient	ND
$\boldsymbol{F_p}$	Plastic Deformation gradient	ND
$\boldsymbol{F_e}$	Elastic Deformation gradient	ND
$\boldsymbol{g}$	Gravity	m/s^2
$\dot{\boldsymbol{F}}_{\boldsymbol{m}}$	Rate of Force matrix	N/s
$\boldsymbol{H_i}$	Continuum permeability matrix	m^{-1}
$\boldsymbol{I}$	Identity matrix	ND
$\boldsymbol{I_c}$	Trace of strain matrix	N/mm^2
$\boldsymbol{K_i}$	Permeability matrix	N/mm^2
$\boldsymbol{K}$	General global stiffness matrix	N/mm^2
$\boldsymbol{K_1}$	Fracture toughness for mode one crack	J/mm^2
$\boldsymbol{K_{Fratt}}$	Fracture energy	J

$\boldsymbol{L}$	Flow potential matrix	N/mm^2
$\boldsymbol{M}$	Mass matrix	ND
$\boldsymbol{\nabla'}$	Differential operator	ND
$\boldsymbol{n}$	surface normal	ND
$\boldsymbol{N}$	General Shape functions	ND
$\boldsymbol{N_i}$	Shape functions	ND
$\Delta\boldsymbol{p}$	Pressure change	N/mm^2
$\boldsymbol{Q_i}$	Boundary flow matrix	m^3/s
$\tilde{\boldsymbol{p}}_{\boldsymbol{i}}$	Trial pressure matrix for receptive region	N/mm^2
$\boldsymbol{R_f}$	Internal reaction forces	N/mm^2
$\boldsymbol{R}$	Rotation matrix	ND
$\boldsymbol{R_e}$	Elastic Rotation matrix	ND
$\boldsymbol{R_p}$	Plastic Rotation matrix	ND
$\boldsymbol{T}$	Stress	N/mm^2
$\boldsymbol{S}$	Piola-Kirchoff stress matrix	N/mm^2
$\boldsymbol{v}_r^\alpha$	relative velocity in fluid	m/s
$\boldsymbol{v}_s$	relative velocity in solid media i	m/s
$\boldsymbol{W}$	Work done	J
$\boldsymbol{W_p}$	Plastic work	J
$\tilde{\boldsymbol{u}}$	Trial deformation matrix	ND
$\boldsymbol{U}$	General stretch matrix	ND
$\boldsymbol{U_e}$	Elastic Stretch matrix	ND
$\boldsymbol{U_p}$	Plastic Stretch matrix	ND
$\boldsymbol{X}$	Spatial Coordinates	m
$\boldsymbol{\delta}$	Kronecker matrix	ND
$\boldsymbol{\sigma}$	Stress matrix	ND
	Other	
ℓ	Aperture size	m
ℓ_0	Initial aperture size	m
$\dot{\mathrm{M}}_{in}$	Mass in	Kg/s

Note: ND = Non-Dimensional

Abstract

A dual porosity damage model is developed with the intention for the efficient solving of complex hydrofracture problems. The model is developed by utilising two pre-existing methodologies and adapting them for the purpose of solving hydrofracture problems. The damage model uses a Neo-Hookean finite deformation elastic constitutive model to calculate internally stored elastic energy. The constitutive model is derived from the three strain invariants so that with volume change, mechanical behaviour maintains consistency, a property that will be discussed in the literature, important to the development of both fracture and hydrofracture framework.

The energy required for material breakage is derived from the material property: fracture strength. The two energy values are calculated over the considered model domain and are used with the energy minimisation technique to find the global minimum energy that contains the sum of the two aforementioned energy types. While calculating the domain configuration which has the lowest energy sum, fracture behaviour can be deduced from the required energy releases from the system to achieve the global energy minimum.

This fracture methodology is combined with a dual porosity methodology that is derived by considering the fluid interface between interconnected porous and fractured domains. Mass balance and effective stress concepts have been utilised to derive partial differential equations which model fluid flow through these two domains in an interconnected manner. This aspect of the model is used to model the fluid transfers that occur in hydrofractures.

The set of equations that govern the coupled porous flow are solved using the finite element method. The Galerkin method of the spatial discretisation is applied and solved using a Eularian scheme to iterate the solution of the governing linearised equations utilising the Newton Raphson approach.

The plastic behaviour of rock like materials has been described utilising Mohr Coulomb plastic model through the application of the Hencky strain conversion to apply the infinitesimal framework to the hydrofracture framework.

A continuum damage model (CDM) method relying on the energy minimisation theory has been applied in a finite deformation context.

The variable minimised within the considered domain is mechanical energy, in doing so fracture behaviour can be captured through the energy exchanges required to maintain a global minimum.

Several methodologies from geomechanics and fracture mechanics have been considered to create a model that can simulate post fracture behaviour in terms of strength and fluid flow. Combining two pre-existing concepts one for fracture problem and another for fluid flow modelling, a simple practical computational framework for hydrofracture is produced. The developed minimisation methodology is proven suitable for modelling complex fracture behaviour, by comparing numerical outputs against experimental and numerical fracture paths. The minimisation approach produced is computationally inexpensive, flexible and simple to implement within existing framework.

Section 5.2 and 5.2.1 also showed how leakage from fractures to the surrounding porous system dictate pressure changes within the continuum and the resultant mechanical changes further proving that leakage is an important consideration mechanically as well as environmentally. Section: 5.1 also showed that the developed methodology can capture geotechnical behaviour. All whilst maintaining fracture/ hydrofracture capability and suitability. The dual porosity coupling can be used to capture the flow properties of hydro fractures. The use of which has the potential to reduce the number of required variables.

In Section 5.2 and 5.2.1 the issue of two dimensional consolidation in closely confined thin horizontal fractures that inhibit hydrofracture progress are classified. The considered thin fractures or "penny cracks" within a large domain are shown in section: 5.3, further verifying this behaviour trend.

Acknowledgements

I want to mention my appreciation to Associate Professor Dr Tizani, whom which has been a great supervisor providing excellent words of guidance, particularly during the writeup stage of this thesis.

Thanks to Dr Rezania for securing funding for three years.

I would also like to thank Assistant Professor Dr Tao for guidance and for allowing me to experience the wonders of lecturing in the finite element module and even a little Guide work in London for the little school from China.

Special thanks to Dr Mohaddeseh Mousavi Nezhad for the guidance on the numerical, publication side of things and general guidance on thesis writing near the end of my study, fitting in around my new job.

Special thanks for the majority of Office C01: Matthew, Carlos, Zack, Aziz, Andre and the rest who have always been of great support, providing plenty of laughs during the past three years.

I am extremely grateful to my now wife Bella who has provided endless support both emotionally and even technically as an occasional rubber duck for my research at times. I would also take this opportunity to thank my mother who has helped support me though my entire life, without here I never have got the help I needed. Without which I may have never qualified for a degree of any calibre.

I would also like to extend my thanks to Sophie, Grandad, Juliet, Elsbeth and Nana for always being available for a friendly chat and words of encouragement. A special thanks to Nich for his guidance that aided in the acquisition of my new job at Groundline engineering.

1 Introduction

Cracks occur constantly in nature, yet they are not fully understood in respect to their behaviour [24], furthermore their interaction with fluid is less understood especially within many required applications.

Fracking, pressurising cracks with fluid is often used to improve the permeability of rock like materials and aids in the application of shale gas extraction [124]. This research aims to create practical models which can deal with versatile rock and stress conditions while requiring minimal material constants and therefore minimal laboratory work.

Hydrofracture models are needed for improved resource mining such as in the extraction of shale gas for better control of the mining process. Shale gas extraction used to be deemed uneconomical but with the introduction of more efficient fracking techniques and other resources becoming less cost effective, previously untapped natural gas resources have become relatively more viable [124]. Shale gas extraction is constantly increasing in popularity, profit margins increasing due to the supply from traditional methods decreasing [70]. Therefore, companies have become more interested recently in cheaply evaluating whether a fracking venture is worth it, this requires overall better prediction models that are computationally cheap [6], simple to use and require minimal laboratory work for finding input variables.

Shale gas is naturally stored in porous rocks due to the formation process, better gas yields typically come from rocks with higher porosity, with an impermeable layer above to stop the gas from leaking and escaping [88]. Containing shale rock may have low porosity and poor interconnection [94] between its pores hence pumping gas directly does not produce high yields of shale gas. To solve this issue fracking is used to break apart pores within the rock, improving pore connectivity and permeability.

The fracking process starts with a hole drilled into the ground to the depth where shale gas is present or where extraction is most convenient [126]. Holes

drilled in the 1990 - 2000's consisted heavily of vertical drilling methods instead of the far more efficient method of horizontal drilling. The reason for the new prevalence in horizontal drilling is due to the ease it brings to the hydrofracture procedure; in vertical drilling the fluid must overcome vertical effective stresses as opposed to the naturally lower horizontal pressures created during horizontal drilling [36].

A two way pump is inserted, building high pressure to break apart the pore structure, increasing permeability. Once the hydrofractured zone grows and pressure can no longer build sufficiently for further hydrofracture the pump is reversed and shale gas is extracted through the additional newly created and previously existing pore channels, the gas sometimes being displaced by water or carbon dioxide [79].

During hydrofracture additives are usually used to accommodate the process using proppants helping to hold fractures open [33]. These additives typically are adsorbed by the rock, these additives can however potentially leak if an error is made during the fracking process.

Leakage to local aquifers is a recurring problem in fracking, difficult to remedy if any contaminate should leak. The best removal methods being; plugging, extraction pumps, complete excavation and foam pumping, costly and time consuming and interfering with ground conditions making further shale gas extraction more difficult [158]. Fluid leakage tarnishes the reputation of fracking, leading to further difficulties in the planning process for even unrelated fracking plans. This shows the importance of prediction tools to extract correctly on the first attempt in shale gas extraction. Tools which can predict how each stage of hydrofracture occur while still being usable by engineers practically [134].

The three main challenges in modelling hydrofracture in geomaterials are, describing: how fluid pressures change within the continuum, how the fracture progresses and how said progress further influences the domain's behaviour post fracking. Integrating mathematical models which describe these

three processes into a single model is essential to predict hydraulic fracturing and is a challenging task requiring complex solutions that are difficult to apply practically in practice.

An aim of this study is to compare several modelling methods and apply one with constitutive modelling and cracking criteria to model the effects of hydraulic crack propagation, supporting the theories and concepts used with critically analysed literature.

Parts of other constitutive models will be combined together to model the variations in the yield surface and pore pressure.

The interaction of these properties will be analysed in rocks and the behaviour will be studied to build a robust, capable model.

Limitations of the created model will be quantified and tested against other existing model's numerical/analytical hydrofracture experiments and some practical hydrofracture experiments.

The aim is to produce a highly capable simple hydrofracture model with low computational demand so that it may be possible to scale up the model to represent large fracking operations in the future.

The derived model will verified for relevant geotechnical and fracture behaviour through various verifications under various conditions against reference numerical and experimental tests, found in the literature.

Fluid pressure evolution is completely different within a fracture compared to porous flow because of the large change in pore inter-connectivity and fluid pressure, a standard permeability model can be used to describe the effect of having different permeability for each media but in doing so behaviour is assumed constant and any exchange between both mediums would be neglected [95]. A double permeability model is most suitable for this reason,

not only is it generally more capable but it has greater potential to treat each flow scenario differently as should be the case. The double permeability model considers two domains within the whole continuum, a porous and a fractured medium [58].

This thesis documents the theory used in the double permeability concept followed by the fracture propagation modelling used for this thesis.

The second chapter introduces the relevant literature on current methods used to model hydrofractures and the associated phenomena. The third chapter introduces the key theory for fracture prediction using the energy minimisation approach, this is accompanied by a verification example on experimental data that analyse slit orientation effects fracture propagation in a rectangular sample. The fourth chapter introduces the utilised porous flow coupling to the previously introduced fracture methodology. The fifth chapter uses the newly developed hydrofracture methodology to analyses hydrofracture examples from the literature to test each aspect of the model in terms of fracture and fluid behaviour prediction capabilities. The sixth chapter develops the methodology to account for the effects of plasticity, going on to revaluating the two more complex verifications examples from the third and fifth chapters. The final chapters are the conclusions and references and future proposals for the discussed and developed methodology.

2 Literature review

This chapter begins with a comparison of current hydrofracture models under development available in the literature; their strengths and weaknesses summarised. The latter part of this chapter introduces key concepts used throughout the study of hydrofracture and, in particular, the developed model created during this study, the associated novelty of modelling the effects of a growing fracture network and the resulting effect on flow through a fractured media.

2.1 Hydrofracture

With the increasing rise in costs of energy, shale gas extraction through fracking is becoming economically viable [126]. The increase in fracking activity has been controversial with the potential for pollution, land degradation and subsidence due to fracking still not fully understood [44].

The process of fracking starts when natural gas is first prospected, then the setup for a large drill pad is built. The drill pad is often accommodated with proppant storage facilitates, pumps, monitoring stations and drill [124]. The drill digs a narrow hole that can vary in depth, typically depending on the depth of the shale rock. Once shale rock strata layer is reached, the drill is turned horizontally, parallel to the layer of shale. Drilling horizontally through the shale allows ease of access to the layer of rock in terms of fracking as shown in Figure 1.

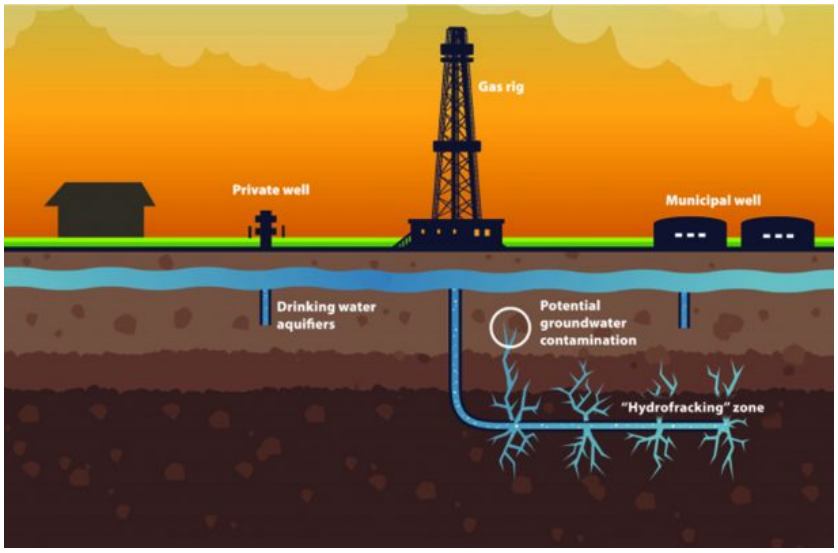

Figure 1: Typical fracking set up in industry [120]

The drilled hole is lined with an impermeable steel tube to reduce groundwater pollution risks and any undesired fluid leakage. At this point a fracking fluid with a mixture of soluble and insoluble additions are pumped at high pressures, up to 62 MPa in some cases. Fracking fluid builds pressure and eventually creating multiple fractures but more importantly additional flow options for both the injected fluid and shale gas [124]. Several pumping stages may occur before the injected fluid is pumped back out, the cyclic application of pumping liquid allows fractures to close at the end of one cycle partially. Pressure can then be built up more readily elsewhere in the strata to create further fracturing maximising shale gas extraction [156].

As fluid is pumped in, it becomes progressively more difficult to build fluid pressure as fracking persists to create new fractures as there is a higher surface to maintain the pressure over i.e. more energy is required [8].

Once fracking is complete, natural gas is extracted by displacing the natural gas with water, then carbon dioxide, usually succeeding in yielding up to 80 % of the natural gas. Additives used in the initial pumping fluid help to keep fractures open, lubricate the fracture surface aiding natural gas ex-

traction [42].

Fractures and pores have different properties regarding their reaction to fluid pressure; pore pressure exclusively pushes/sucks internally from the pores, swelling or dilating the soil. Pore pressure exerts a net pressure throughout a considered continuum. Internal fracture pressure pushes against fracture walls assuming low permeability; opening the fracture and increasing stress concentrations at the crack tips.

The hydrofracture process puts surrounding rock under high stress conditions; causing cracks and large movements within the continuum [73]. These changes affect how fluid flows through the continuum due to internal flow routes changes and large fluid pressure variations. The changes in flow routes are an important attribute to capture when modelling hydrofracture.

Rock strata at great depths are constantly under high confining stress, this confinement acts to close all voids and fractures; either pre-existing or newly created [19]. A resistance to fracture closure during the process itself is the fluid pressure (assuming the crack is sufficiently long to negate material strength at tips), and how much traction that fluid has on the boundary layer [43]. For example, a closed 2 dimensional thin fracture "penny crack" with incompressible fluid and impermeable boundaries remain open whereas a similar penny crack with permeable boundaries will leak all of its fluid and pressure into the surrounding medium, closing. Therefore, the threshold ground pressure must be surpassed by the fluid pressure to allow crack propagation. This threshold pressure is dependent on the surrounding ground pressure, here shown as σ_0, in Figure 2.

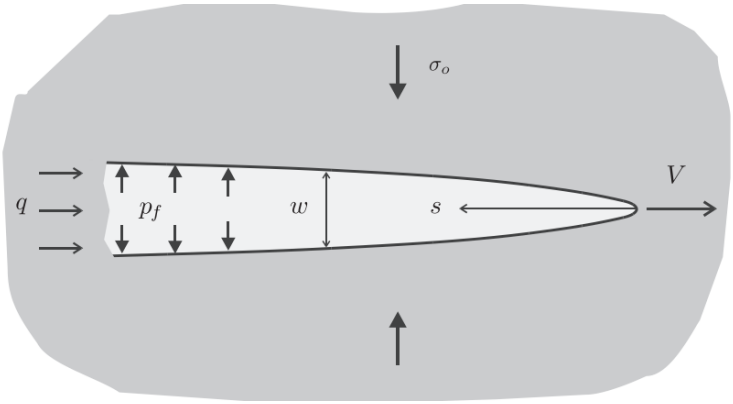

Figure 2: Hydrofracture tip [21]

Figure 2 shows a simplified hydrofracture under ground where an inflow of fluid, q is building pressure p_f. The fluid pressure is maintaining the crack's opening, opposing the vertical/surrounding ground stress σ_0. Figure 2 shows that the fluid pressure, p_f must exceed the vertical earth pressure, σ_0 at a minimum to induce tension at the fracture tip, otherwise the total force acts to shorten the crack [21].

Permeability has been found to increase in dilative cases opening up cracks, creating greater crack inter-connectivity, leading to an increase in permeability overall. These effects start to decrease after some time, [69] giving rise to a logarithmic trend, due to other internal effects such as viscosity and pore wall friction taking over, i.e. more cracks mean more surface area and drag.

Modelling the permeability of fractured pore systems is difficult in practice due to the large variation of scenarios the fluid systems can undergo, be it different flow paths or large open voids of stationary fluid [55]. The complexity of the calculating the permeability of fractured media has in the past couple decades met with equally complex solutions.

Biot's flow has been applied in several cases to the hydrofracture problem with varying degrees of success. However due to the assumption that flow in a Biot system is far greater than deformation rate of the containing

continuum modelling flow in a crack becomes an issue due to the high local strains involved in crack tip deformation. Furthermore, in the formulation of the theory, other assumptions include linear elasticity [13]. Cracks require non-linear elastic models to remain accurate during the large strains produced during fracture propagation which will be commented on in the finite deformation section in this thesis.

Use of Navier-stokes is problematic due to solver issues, the constantly changing boundary conditions due to crack propagation, increasing solving process complexity, especially in 3D simulations [80]. For this reason, there is little literature on the practical use of Navier-stokes in hydrofracture modelling [91]. In most cases, Navier-stokes equations have been used for the simulation of a simplified channel flow down a single crack [62] and [53] . No multi fracture applications have been sourced in the literature review using the Navier-Stokes equations.

Research has found agreement with the idea of crack density and it's relation to permeability/flow. This can be used to arrive to a reasonable solution with some merits of validation [97]. [73] has suggested how the pressure evolves in relation to the permeability. They have suggested that in order to model micro cracks reasonably well the aperture must be considered to change according to low pressure volume strain and shear sliding.

Poiseuille's law has been applied to simplify theoretical models predicting permeability change with fracture propagation [137]. More simplistic models have been created that are empirical and prove effective, however they again need unique parameters that are not naturally procured during triaxial tests and have no theoretical basis of which to rely on.

Flow speed through a porous medium is dictated heavily by the medium's permeability, this behaviour is captured by Darcy flow assuming laminar flow, typically described as shown in equation 1.

$$q = \frac{k}{\mu_f} \Delta p \tag{1}$$

where q is fluid flow rate, k is permeability, μ_f is the dynamic viscosity ($8.9.10^{-4} m^2/s$ for water) and Δp is the pressure difference.

Research on high pressure flow in porous media has found that flow prediction from Darcy's laws are less accurate as fluid gains momentum and becomes more energy dense, because Darcy equations do not contain any momentum terms assuming laminar flow [14]. Once higher energy flows are considered Biot's flow or Navier-Stokes equations become more practical in theory for accuracy due to their consideration of turbulent flow.

Darcy flow on its own assumes a homogeneous continuous flow, as demonstrated previously. This is not strictly true in the case of hydrofracture [125]. Intertwining fractures complicate the evaluation of permeability and more sophisticated approaches are required, such as the pore network modelling method which account for varying flow paths.

Permeability depends on, several factors including but not limited to: chemical composition, charge, pore wall roughness [19], pore volume fraction, pore interconnectivity and pore size distribution; the latter proven vital to describe fluid flow using pore network modelling.

Pore network modelling has shown that the inter-connectivity of pores heavily influences the permeability [145]. When a fracture occurs locally, the permeability will naturally increase due to extra connections created.

The creation of pore networks are typically created using ultrasonic imaging techniques with many slices of a small rock/soil sample or any other imaging techniques allowing for the 3D pore network to be captured [139]. The many slices are then input into a rendering program to identify pore spaces and material grains, this 3D model can then be used to simulate permeability at the correct confining pressures which are difficult to recreate in a laboratory specimen. In pore network models, pores are modelled as

fluid storing nodes and connected by throats as channels for the pores/nodes to transfer fluid, simplifying the modelling process, an example is shown in Figure 3c, 3d showcasing a pore network interpreted from 3D imaged rock samples seen in 3.

Higher permeability is also attributed to either a coordination value, in that the pores are well connected and/or high void fraction so that fluid flow can occur more freely inside a porous medium. In application, this adds additional complexity to models and the required amount of laboratory work, reducing practicality but does improve accuracy of predictions in terms of fluid flow prediction [139]. Pore network modelling gives an insight to the effect of fractures on permeability that laboratory experiments cannot. This is due to both the confining pressure being difficult to model, the other reason is due to sample deterioration caused by sample extraction and the cost associated with laboratory testing. When a sample of rock is removed at 500m the sudden change or reduction in confining pressure creates micro fractures in the rock changing the permeability of the sample, however at a microscopic scale some areas of the sample can be considered un-fractured.

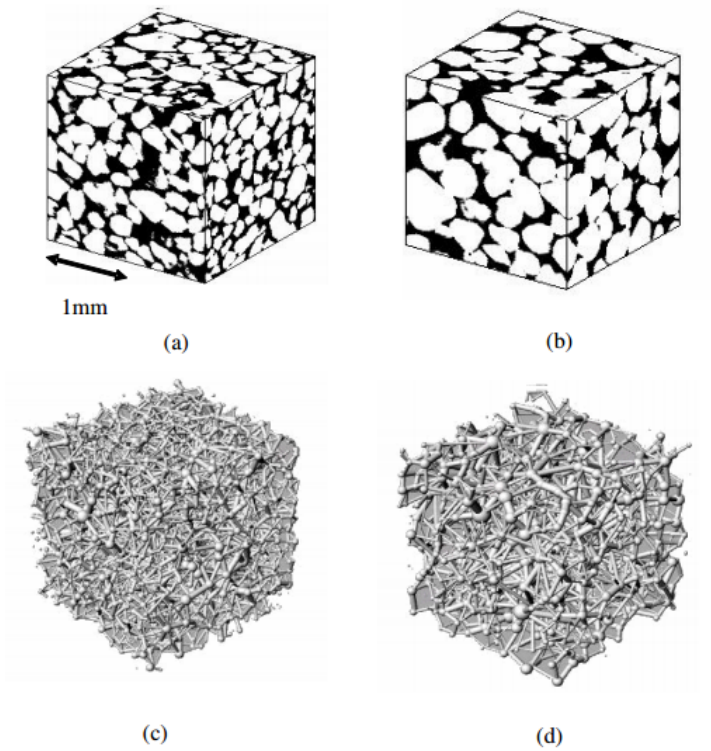

Figure 3: Micro-tomography extraction of two sand packs (a) and (b) to conversion to equivalent pore network models (c) and (b) [138]

Figure 3 shows several stages of pore network modelling in the following stages, sub figures a) and b) show an initial micro-tomography extraction of two sand packs. Sub figures (b) and (c) demonstrate equivalent networks of both sand packs.

Connectivity and porosity can be used alone to empirically estimate permeability. However, in the case of a crack where sensitive local changes are needed to be recorded, full pore network simulations of samples loaded in different scenarios are required. The connectivity of fractures or void space is a big impact factor on material permeability at both the micro and macro scales as previously mentioned [3]. Therefore, computational models used in the prediction must be able to count for multiple fractures with varying degrees of interaction, in order to calculate hydrofracture behaviour. It has also been shown experimentally that with longer cracks, pressure variations

are unpredictable due to accumulative errors [128], pore networking models can predict the pressure variation to some accuracy, however after sufficient crack length the number of input variables required substantially increases.

Pore networks can further be enhanced to account for additional criteria such as throat shape [145] and roughness [75]. Roughness can have such an effect that dry throats have a vastly different hydraulic conductivity to their wet counterpart [131]. Furthermore, pore systems with larger specific areas (total area of pores and throats) will experience more fluid adsorption. At higher confining pressures pores and throat channels decrease, decreasing flow capabilities of a porous medium.

In order to simulate permeability accurately, these must all be considered, which requires many experimental tests such as macro-pore scanning. Furthermore, the computational efforts required by pore network modelling are impractically large; often the permeability is analysed for a small sample and scaled up in a multi-scale model approach.

Pore network modelling is computationally demanding because every individual throat, connection and void space [55] is modelled by an equivalent pipe in a discrete manner. Demands are too high to allow practical modelling of large pore networks or to allow the coupling of other behaviour types such as fractures [3].

Dual porosity modelling considers fluid channels not as individual pipes, but instead as a set of overlapping partial differential equations [26] [95]. The dual porosity model thus separates the hydrofracture problem into a pore flow and fracture flow problem. The models currently developed have a different permeability, pressure head and porosity associated with each zone citeref204, [95].

Solving two coupled partial differential equations increases the method's efficiency [72] over that of the equivalent pore network model approach [3]. To achieve this, the dual porosity approach requires that the fractures are represented and discretised with sufficient fidelity [72]. Dual porosity models

have been shown to even replicate the expansion and contraction of flow channels in fracture networks with the corresponding change in permeability [34].

Jianjun Ma uses the dual porosity approach to replicate hydrofracture phenomena, specifically within the context of wellbores [95]. This specific application of the dual porosity model overlays two networks: porous and fractured, in doing this the influence of fractures are homogenised and the directionality of hydrofractures is lost.

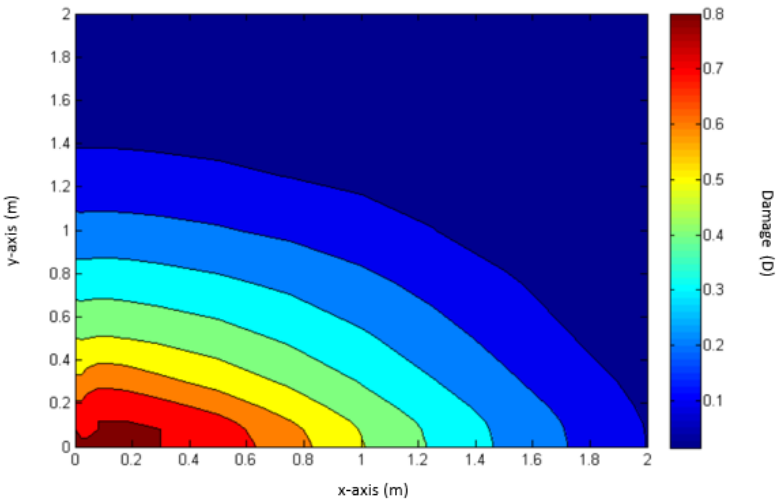

Figure 4: Contour Damage map example of dual porosity model [95]

Figure 4 plots damage incurred by a pressured borehole, Figure 5 shows building pressure over time as this hydrofractures develop within the model.

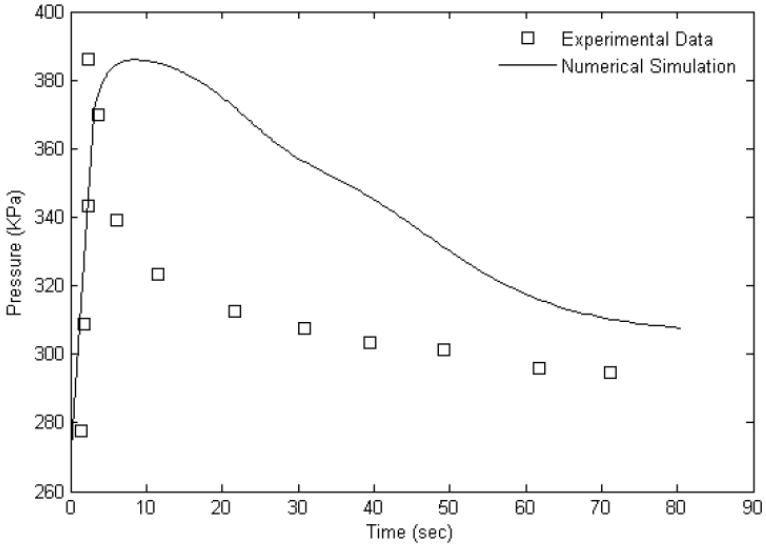

Figure 5: Pressure in well-bore overtime modelled using dual porosity model [95]

Figure 5 compares pressure profiles against Papanastasiou's numerical experiments [115], achieving a more brittle response. This is due to the difference in approach, Ma uses a continuum approach where fluid pressures are spread over considered damaged elements whereas Papanastasiou uses lubrication theory, as a result fluid pressure is more concentrated leading to more concentrated loading and a more brittle response. Figures 4 and 5 show that the key principles of hydrofractures are modelled reasonably by the dual porosity approach. The pressure is built within the well-bore until fracture propagation begins, from this point on, the fluid pressure is lost to newly created fractures.

Furthermore, as fractures propagate, rebuilding pressure becomes more difficult due to the increasing pore pressure of which the fracture pressure is leaking into.

The dual porosity methodology demonstrated in Figures 4 and 5 assumes that fracture and porous flow coexist within the same space, similar to the example presented in Figure 6.

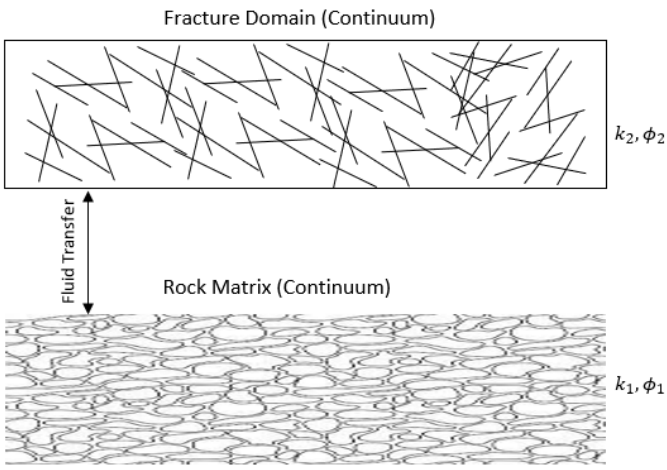

Figure 6: Dual porosity model principles

Figure 6 shows a typical dual porosity setup, consisting of two components, a fractured and porous zone which interact via internal flow and leakage.

Where k_2 and ϕ_2 are the permeability and porosity for the fractured domain, k_1 and ϕ_1 are the permeability for the porous domain. The fluid transfer shown in Figure 6 describes flow between the two zone types utilised in the dual porosity methodology.

It is clear that hydrofracture models should account for both fracture and porous flow separately as shown in Figure 6. What is not clear is the interaction between the two, to capture the exchange of fluid, a leakage parameter is considered to couple the fluid flow in two media

The leakage parameter acts to equalise the pressure between both mediums, once achieved the fluid driving aspect of the fracture fluid vanishes. The same can be said when there is excess pressure in the porous medium effectively closing the fractures [106]. The leakage parameter also dictates the rate of pressure build up in a crack, if fluid flows out of a fracture quicker than intake, the considered fracture will not be able to build up pressure for fluid driven fracture propagation.

The dual porosity model has also been shown to be effective [71], [95] in practical uses due to associated low computational costs.

The leakage parameter in the work of [95] describes the leakage parameter acting constant across the whole domain, where a porous and fracture pressure coexist constantly throughout the continuum. In other work it is seen applied bridging two permeable mediums together. This allows the pressure difference to contribute to fracture propagation as a step change in the pressure gradient can be more easily achieved.

The dual porosity's ability to model the permeability of fractured porous systems is apparent as seen in countless examples of literature: [48] [49] [58] and [123].

However, the dual porosity model cannot predict the growth of fractures and/or hydrofracture growth alone [49] A fracture methodology, specifically one that can be integrated into the dual porosity model is required. Theoretically; if the growth of fracture can be represented accurately and the associated fracture and porous zones are updated with hydro-fracture growth then the evolving permeability could be potentially captured.

2.2 Fracture mechanics

Fracture mechanics is a topic in mechanical science that alludes the use of simple theoretical basis and modelling. Accurate models are difficult for the simple fact that each created crack heavily influences the onset of other cracks [164].

Griffith crack criterion The first real breakthrough in fracture mechanics came shortly after the realisation that the fracture strength for intermolecular glass bonds was far higher than regular sized glass samples [52]. This led to Griffith formulating a new relationship dependent on surface energy, explaining why fracture strength is not wholly dependent on molecular strength, but on sample size and geometry [67]. This led to the discovery

of the minimal energy concept, founded with a classical example of fracture mechanics; the slit in a thin plate under plane stress conditions shown in Figure 7.

This classic example stems from one of Griffith's conclusions, "The breaking load of a thin plate of glass having in it a sufficiently long straight crack normal to the applied stress, is inversely proportional to the square root of the length of the crack", here shown in equation 2 [52] under the assumption of an infinite continuum containing the crack. Equation 2 is demonstrated in Figure 7.

$$K_{\mathrm{I}} = \sigma\sqrt{\pi a} \tag{2}$$

This relationship was later extrapolated and became the first of many intensification factor equations. Solutions would become more versatile yet more complicated. A unit thickness is assumed in 2D.

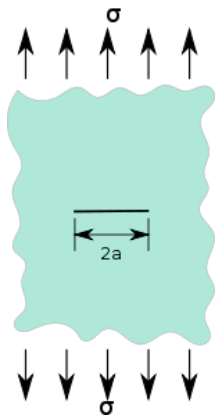

Figure 7: Classical Griffith crack

where a is the crack half-length and K_{I} is the stress intensity value and σ is stress as shown in Figure 7. The stress intensity value can be related to the strain rate in plane mechanics.

When the critical value is exceeded the energy dissipation rate is used to determine how the strain fields are altered. The strain rate G is shown in equation 3 for a simple crack in plane stress conditions [121].

$$G = \frac{K_1^2}{E} \tag{3}$$

where G is the strain energy release rate, E is the Young's Modulus and K_1 can be interchanged with fracture toughness and represents whether a certain material will resist fracture.

The reader may have noticed that there are several problems with this solution for fracture. First, this solution is not a boundary value problem and while it can be applied to bounded problems, as the aperture approaches the edge, solutions become less accurate.

Second the crack path is predefined, this is impossible to know ahead of time even with simple geometric brittle materials and the resulting crack paths can be difficult to predict.

The rate of a crack's growth found by Griffith can be more generally defined in terms of energy and crack area as shown in equation 4 [77].

$$G = \frac{dW}{dA} \tag{4}$$

where dW is the work done per unit area on material and dA is the area in the crack front.

According to equations 3 and 4, when there is sufficient energy concentrated in a small enough area that exceeds the material's excepted strain growth rate, a fracture will grow or initiate.

Crack initiation

When crack initiation is considered the usual way to describe the crack is through three failure modes, here demonstrated in Figure 8.

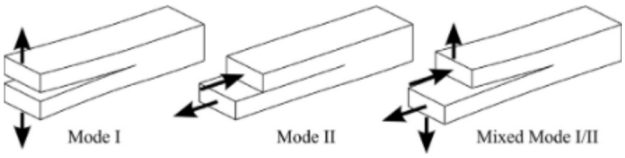

Figure 8: Different crack modes for various load cases [76]

Figure 8 shows the various mode of fracture possible: Mode 1 is a tension crack, mode 2 is through shear and mode 3 through torsional effects [77].

Less work has been done on branching cracks [98] but they should be considered in certain cases to resolve omni-directional force cases, such as a highly pressurised nozzle in a hole exerting load in all directions.

Crack branching occurs when the splitting of a fracture is required to maintain equilibrium of force direction. This becomes more likely as higher energies are considered as there is typically more fracture to resolve. Multiple cracks provide several energy paths complicating many fracture prediction methodologies.

Branching is why standard equilibrium methods are unsuitable as the method makes it difficult to differentiate between creating one long crack or two short cracks.

2.3 Existing fracture models and current gaps in existing methods

The following section will compare existing fracture models developed for hydrofracture. Each section will showcase the relative strengths, weaknesses and existing challenges of each methodology type.

2.3.1 Continuum damage model

The continuum damage model (CDM) method uses a damage variable to model fractures. A damage variable is used to model material degradation, often associated with the occurrence of micro voids/fractures that reduces both the remaining strength and stiffness. The damage variable can be linked

to other phenomena such as permeability or conductivity with the correct modelling approaches if required.

Damage is not truly quantifiable in that no experiment can be used to measure damage directly, instead decrease in stiffness is commonly used as a supplementary measure. Typically, a damage variable varies from one to zero; one representing fully intact and zero fully deteriorated.

When the damage variable is zero it is typical to assume some residual strength or that the considered damage element ceases in that the considered element no longer has any impact on the simulation. These considerations prevent numerical problems that could arise with unrealistically low material stiffness [95].

The damage variable is controlled by a damage law that can be influenced by energy, stress or strain concentrations [64]. Different damage laws are required for varying materials, rock/glass/brittle materials lose all strength shortly after failure, however asphalt/rubber/ductile materials have a less dramatic decrease in stiffness, both requiring different damage laws. These are often derived from theory or experiments that test the decrease in stiffness under various failure mode/processes.

A damage model requires two key components; a damage evolution law as mentioned prior. The second key component is a set of equations that impact material degradation. The change in stiffness can be described by a step change or a curve fitted to pre-existing experimental data. Damage is considered to occur when a user defined damage criterion is surpassed. There are two methods used favourably in the literature; energy or stress based. An energy based methodology can be based on thermodynamic principles to ensure conservation of energy in terms of elastically stored energy and energy released via the breakage of material bonds [66]. The method attempts to calculate how much internal energy a material can sustain. This can be calculated by the area under a stress-strain graph of the considered material, requiring prior testing. A damage criterion can also be defined similarly to a yield surface in terms of principal stresses [64] [27] [163].

With damage calculated, the influence of the new damage must be found. This stage of the calculation is usually heavy on the use of empirical equations

to assess changes in material stiffness. Empirical equations can be modified to assimilate whichever mathematical trend is best suited to the considered material, such as step changes for brittle and logarithmic or power laws for more ductile materials [38].

Mechanical degradation is usually a result of micro-cracks within the continuum too small to consider individually with reasonable computational effort, therefore a broader approach is needed [3]. If each micro crack was considered and included within calculations, the computational time would become unfeasible for large scale simulations [84].

Francfort and Marigo [16] formulated several theoretical equations to predict mechanical energy stored which in turn can be used to predict a development towards fracture. The theoretical basis with an experimentally calculated fracture energy term aids the description of a damage evolution law that can both describe crack initiation and propagation [45].

The methodology allows multi cracks to be predicted; in this case due to two forces pulling in separate directions as shown in Figure 9.

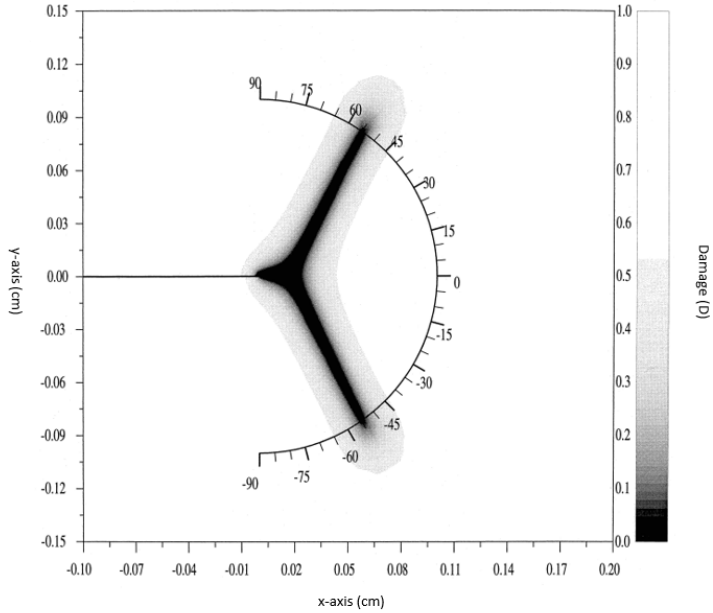

Figure 9: Branched crack predicted via minimisation damage model [16]

Figure 9 shows a continuum damage model where the fractured region is modelled by the 0 damage value [16]. The model captures the influence of large local deformations influencing regions outside of modelled fracture, see gray area surrounding the fracture in figure. This phenomena; process zone, is later discussed in further detail in this thesis.

Continuous damage mechanics assumes that the area of resisting material represented here by s, is acting to the carry load, F_m. The available resisting area, s is reduced by micro cracks thus stress also increases when micro cracks occur [85] this is represented in equations 5 - 7.

$$\frac{F_m}{s} = \frac{\sigma_0}{1 - D} \tag{5}$$

Hence the damage variable can be described by the reduction of resisting material.

$$D = \frac{s - s_1}{s} \tag{6}$$

thus

$$\sigma_d = \frac{\sigma_0}{1 - D} \tag{7}$$

where F_m is the load, s is the internal resisting area, s_1 the initial internal resisting area, σ_0 is true stress, D is damage and σ_d is stress accounting for damage effects.

2.3.2 Extended finite element models

The extended finite element method (Xfem) was developed in 1999 by Ted Belytschk and colleagues [18]. The method's main advantage is lack of re-meshing required, reducing computational efforts. The main drawback is that tying the method to constitutive models often pose both mathematical solver and coding difficulties due to the nonlinearity introduced [18]. The difficulty arising from the step function used to discern both sides of a fracture, separating behaviour to the correct nodes.

The method works by splitting a continuous domain usually denoted Ω into two sub-domains denoted Ω^- and Ω^+ on either side of a fracture. The fracture or discontinuity is defined geometrically by Γ. When the displacement is considered constant across the discontinuity but however if there is a change in stress then it is considered as a weak discontinuity [77]. If the discontinuity is defined by two geometric lines and the displacement varies between the two lines, where the discontinuity is considered strong.

Enrichment is used to modify the behaviour of elements with varying circumstances affecting the global or local systems [106] where required by adding extra degrees of freedom to model fluid flow or heat transfer problems.

The discontinuity is usually modelled with the aid of the Heaviside function but other functions describing step changes such as the Dirac delta function can be used [107]. When implemented it prevents elements from being able

to transmit forces in the direction perpendicular to the direction of the crack through the elements when required.

Solving the imposed nonlinear constitutive models are a significant drawback in the Xfem methodology, as the computational cost to solve the complex systems of equations is vast.

Complexity and computational demand further increase with extra fractures or adding behaviours captured such as heat transfer or flow. Ensuring material behaviour remains consistent in and around a crack is challenging, to ensure stability and convergence with all possible crack scenarios, it is easy to see why the methodology is difficult to implement efficiently.

When a crack is created in Xfem, both crack tips (or a single tip if edge crack) start to intensify the stresses locally due to sudden changes in structure. Stress intensification is modelled as asymptotic towards the crack tip [165]. This increase in stress is assumed up to the crack tip, the implemented asymptotic behaviour can exaggerate stress in certain cases [132]. Each of the stress intensification factors (SIF) considers different crack propagation combinations of tensile, shear and compression.

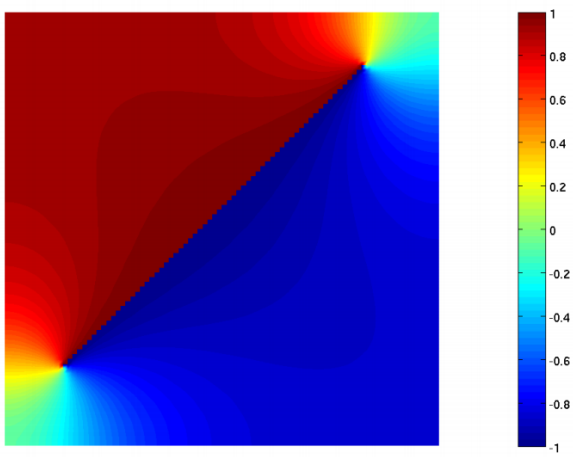

Figure 10: Enrichment function across domain, representing fracture [109]

Figure 10 shows an enrichment function used to help a model differentiate the two sides of a fracture, using a scalar operator ranging from -1 to 1 so

pressure fields, stiffness matrices, etc can account for fractures and their behaviour.

An example of when a local enrichment is needed would be a crack as two discrete elements can no longer transmit forces and thus model behaviour must be modified [78].

Enrichment is a large component of X-fem [109] particularly along with other modelling methods, an enrichment field considered could be sourced from the Laplace equation, allowing the Heaviside functions to interact cohesively within an element as shown by Duarte and Kim [78].

Interaction integrals are used to calculate the total energy available to a fracture. Interaction integrals are another means to use energy in fracture mechanics, used frequently and can be accurate, but only look at one crack per interaction integral. Multiple interaction integrals are needed for branching cracks, increasing computational demands. Branch fractures complicate the interaction-integrals because their interaction must also be accounted for [25].

While calculating the interaction integrals, Rice's formula is a favourite among extended finite element researchers [154], also known as the J-integral, shown in equation 8 and Figure 11.

$$G = \int_{\Gamma} W_i - n_i \boldsymbol{\sigma}_{ij} \boldsymbol{F} \tag{8}$$

where Γ is the crack boundary, W_i strain energy density, n_i is the normal of the considered stress in relation to the crack, where the deformation's distribution relates strain energy to the deformation gradient and stress throughout the considered element and eventually the entire domain. $\boldsymbol{\sigma}_i$ is the Cauchy stress and $\boldsymbol{F}$ is the deformation gradient describing how deformation occurs relative to affixed nodes within a certain element, as shown in Figure 11.

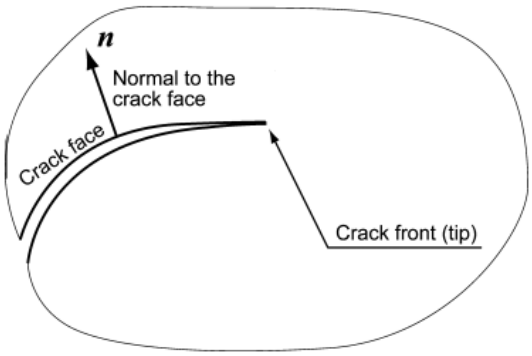

Figure 11: Interaction-integral example 2D, [113]

Figure 11 shows typical considerations when applying the interaction-integral methodology,

The formula is applicable to 2D and 3D examples the only difference is that describing the integral in a 3D manner is both more complicated and naturally more computationally demanding [113].

3D does improve the accuracy of predictions as the scenario is more realistic [30] but in a lot of cases it is simply better to focus on constitutive model development, the enrichment or some other section of the modelling process for more efficient allocation of resources when aspiring for accuracy [157].

Plastic energy accumulated can be stored in the interaction-integral [154] by manipulating the strain energy accordingly.

Studies have been done on cracking in plastic situations and have shown that the interaction-integral is not only path dependent but when the sample becomes small, the crack becomes heavily dependent on sample geometry [140]. That is that the boundary conditions play a more important role on a crack's path. The same paper mentions that the crack geometry will always be dependent on the whole domain in some way regardless of size.

2.3.3 Cohesive model

Cohesive models are dictated by specific strain dependent strength behaviour along element boundaries, showcasing typically a hardening regime

followed by softening, similar to the function shown in Figure 12. Damage associate excess strains with a decrease in cohesion [96].

More realistic crack models have been achieved by making the traction forces dependent on a potential function [118].

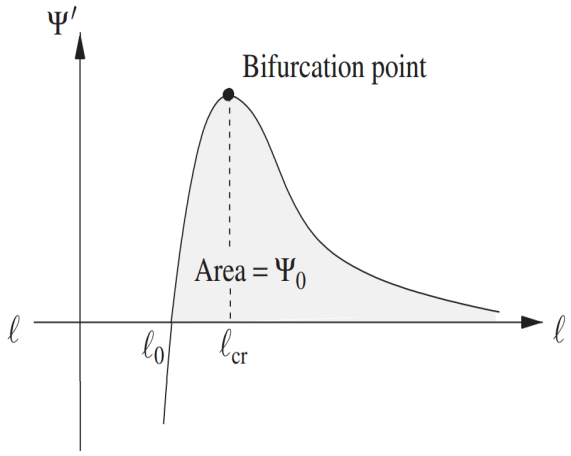

Figure 12: Cohesive energy graph [118]

where ℓ is aperture size, ℓ_0 is the initial aperture size, ψ is energy and ψ_0 is energy required to split.

Figure 12 shows a potential function used to model the process zone for each fracture. As the fracture lengthens as shown on the x axis the resistance varies, peaking at point of fracture.

2.3.4 Discrete element modelling

By considering individual particles or bonds in a solid it becomes possible to account for unseen behaviour traits in fracture mechanics, provided the initial set up is correct. Discrete element modelling has high accuracy yet large computational costs. This method can uncover macroscopic behaviours that other fracture frameworks cannot pickup on such as how strain rate can depend on stochastic characteristics of used particles [161].

This technique has shown that the size of the plastic zone, is fully dependent on particle size as shown in Figure 13 [140].

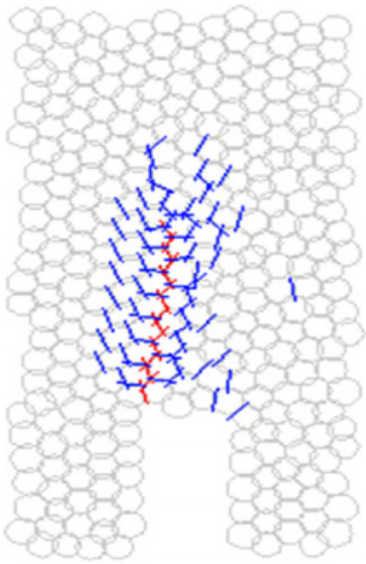

Figure 13: Discrete element modelling of process zone (Red-fracture zone, Blue-plastic zone) [140]

Figure 13 shows a discrete element model of a fracture, the red shows material breakage and the blue shows plastic deformation due to the large local deformations that occur during fracture propagation.

In the work presented by [140], metal materials where particles are considerably smaller than soil particles and the bonds are relatively small and hence found that the process zones are considerably smaller as a result.

2.4 Rock properties

Rocks have many unique mechanical properties which make them difficult to model realistically; properties that vary significantly with the stress state and condition of the rock [50].

Rock formations take millions of years to form, in the years of formations the rock's stress state can vary significantly, causing the creation of rock fabrics and internal faults [28]. The rock fabrics can be formed due to a temperature change, atmospheric change or change in deposit type/process. Rock fabric contributes to anisotropic behaviour in the rock as each layer

can have varying strength or stiffness and cause stress to distribute unevenly with loading [28]. Rock faults dictate the strength and pore flow, as there is a region of reduced stiffness and excess void space. The impact that rock faults have on material properties is dependent on the rock fault's orientation, roughness and face pressure [11].

In mining engineering, the effect of confining pressure has to be taken into account as rock material behaviour is heavily dictated by confining pressure as shown in Figure 13 [63] [12]. Fracking operations occur at similar depths; therefore, it is important that numerical models developed can account for the difference in behaviour exhibited by rock at great depths.

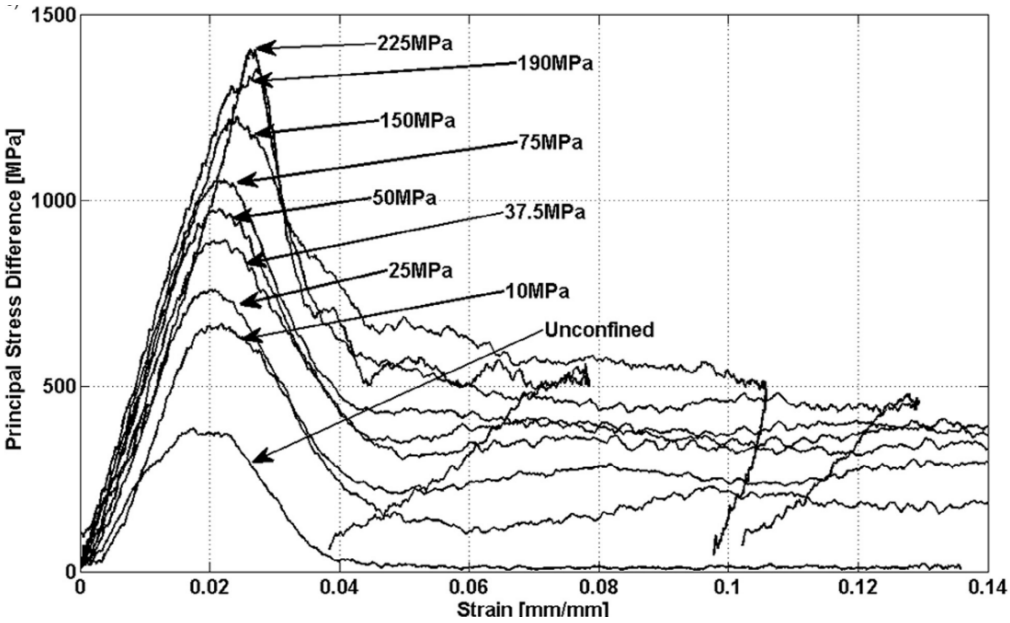

Figure 14: Stress-strain curves for various confining pressures on rock [63]

Figure 13 shows stress scenarios that are only relevant for shear fractures. During hydrofracture tensile failure of rock is typical. As discussed previously, in order for this to occur compressive confinement and cohesive strength must be overcome [152]. Hydrofractures take the path of least resistance pushing cracks open, perpendicular to major stress of compression in rock strata, propagating in the principal stress direction.

Tensile fractures, of which are the primary failure mode incurred during hydrofracture are often brittle and energetic, as shown in figure 15 [12].

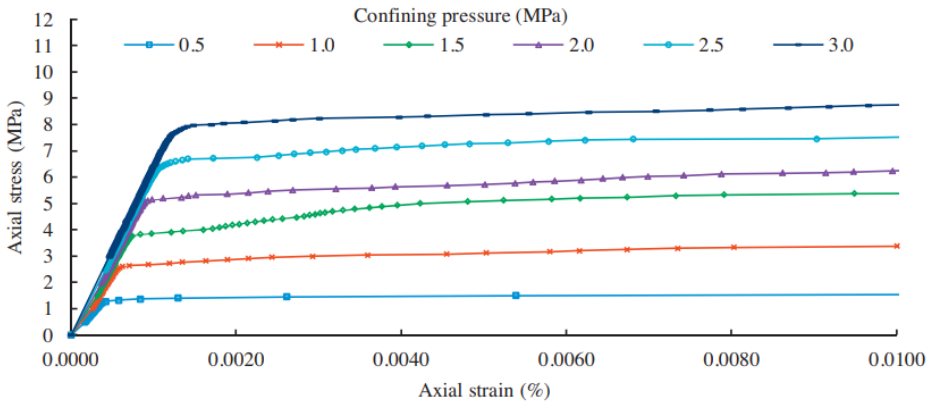

Figure 15: Stress-strain curves for rock in tensile failure [12]

Loss of tensile strength is important to account for post fracture as the change in structure can have large ramifications on future hydrofractures [12].

2.5 Plasticity

Plasticity is defined as non-linear irrecoverable deformation, irrecoverable in the fact that if unstressed the original position is lost [155]. Plasticity does not occur until a material is stressed past the yield point [95]. At the point of yield, particles slide over each other, into a different rearrangement, whether the newer particle arrangement is stronger depends on both the nature of the material and loading. In geomechanics soil/ rock can temporarily stiffen due to dilatancy.

Dilatancy [83], is caused when particles cannot move through each other as they must be raised so that particles may slide over others as shown later in Figure 20.

Additional movement of the particles requires additional energy as the extra internal movements come with greater energy requirements. The effect of dilatancy is more evident in geomaterials under confining stress, the confined stress must be overcome in order for particles to move [152].

The effect of this temporary increase in resistance is only in effect when particles are moving from their initial orientation. Once movement becomes steady the only resistance becomes purely frictional. The increase in resistance due to strains is often associated with the term strain-hardening or hardening regime, whereas the loss of cohesion and normalisation of particle sliding is denoted as strain-softening or hardening regime [92]. For this reason, plasticity behaviour is a specialist subject and has countless papers published in its study.

Plasticity behaviour is typically described using a yield surface, flow rule and consistency equation. The yield surface is plotted in true stress space; that it can be represented in terms of principal stresses. Yield surfaces are usually mathematically described as geometrical surfaces. The inside of the yield surface is known as the elastic region and the boundary or outside the plastic region [96]. When the boundary is reached a yield is declared and the corresponding plastic strain is calculated from the later discussed flow rule. Yield surfaces are dependent on stress in such a way that an increase in confining stress delays the onset of yield as shown in Figure 16.

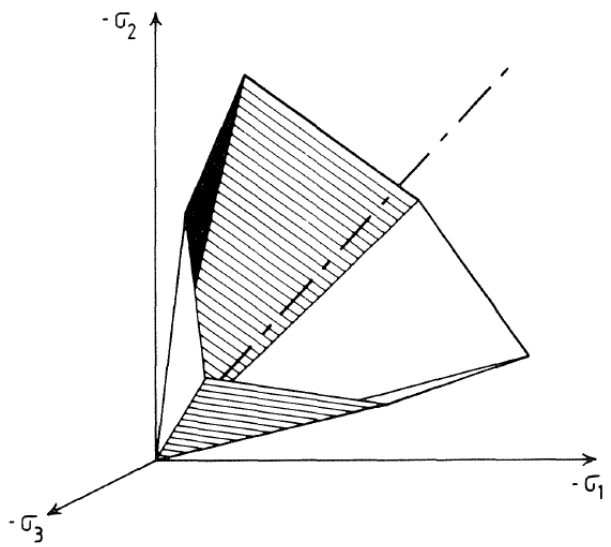

Figure 16: Mohr-Coulomb yield Criterion [143]

Figure 16 shows the Mohr-Coulomb yield criterion, here defined by the

three principle stresses.

This models the resistance of particle sliding phenomenon mentioned prior, which is modelled by a proposed flow function developed and described later in chapter 6.

Flow functions are termed associated or non-associated, the term describes the relation between the yield function and the flow function [96]. The derivative of the flow rule with regards to stress describes plastic deformation, change in stiffness and plastic strain, the consistency equation is fundamentally the same for all sets of plasticity equations, based on the Drucker-Prager's postulate.

The flow rule and consistency equation contribute to modelling hardening and softening behaviour of different materials [59]. Different rocks and soils have differing particle arrangements and characteristics, and thus far there is no general description for all hardening/softening regimes hence diligence is required when selecting constitutive plasticity equations for a model.

2.5.1 Plasticity in fracture

Plasticity is a material property that absorbs excess energy [54]. Therefore, it comes as no surprise that ductile materials are more fracture resistant and unpredictable in regards to fracture growth.

However as discussed above, hydrofractures cause rocks to fail through mostly mode 1 fractures: tensile failure. As such prescribed equations used to model plasticity must account for tensile fracture [117]. Due to the simpler interaction of bonds during tensile failure so too are the required governing equations [89].

At a crack tip, large deformations form due to crack propagation, the large local deformations in a ductile material cause early onset of plasticity and changing the conditions that the crack front must travel through. Strain hardening increases the amount of energy required for further fracture [116].

Large deformation capable models are hence important in predicting fracture behaviour as the loss of stiffness in the region leads to dramatic structure changes [144]. As the number of significant fractures required for modelling grows, so too does the need for models that can interpret the resulting stress redistribution.

2.5.2 The process zone

When a fracture propagates, significant mechanical movement occurs around the tip, in effect expanding the surrounding region, this region is often denoted as the process zone [56]. The process zone acts to help the mechanical energy to dissipate in the region; a process zone often occurs as an initial means to absorb energy, [135]. When as is often the case the process zone cannot dissipate enough energy, a fracture occurs to alleviate the energy build up as described by equation 4 [41]. There are several factors that effect the size and shape of the process zone including; energy contained within the crack to be dissipated, sample size in relation to crack size [140], [46], material stiffness [57] and to some extent the grain size of the material. In cracking, the zone around a crack tip has three theoretically defined sections, these vary in how much energy they consume through various amounts of plasticity as shown in Figure 17. The fracture process zone is dictated by material breakage in the region close to the fracture tip, the plastic zone where the deformation is significant enough to create plastic deformation and the total zone in the rest of the continuum [140]. The shape of the process zone is typically balloon shaped if not impaired by sample size [149] as shown in Figure 17.

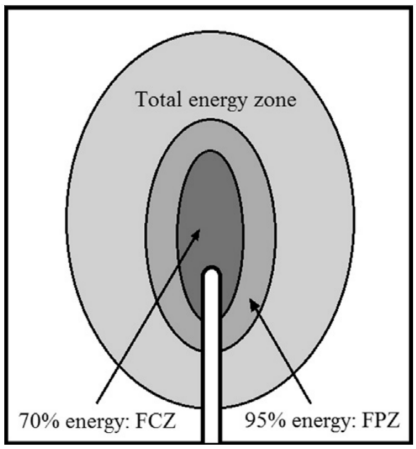

Figure 17: Different crack zones in energy distribution for a typical fracture [140]: showing the fracture zone and plastic zone

Figure 17 shows the typical energy used up in the crack zone is usually higher nearer the centre of the crack tip, as the majority of the energy is dissipated through high local plastic strains and internal damage [129]. The development of the process zone with the crack disrupts a materials homogeneity by leaving varying amounts of damage/plasticity in the cracks' wake [31], therefore it is imperative to capture these changes to predict post fracture behaviour [135].

Numerical models capture the effect of the process zone by utilising the cohesive zone model; in a typical finite element model when a fracture occurs, the surrounding zone is enriched with cohesive element with the material strength akin to that described by Figure 12, a temporary sharp increase in stiffness followed by a steady decrease in stiffness and strength [57] [46].

The increase in stiffness allows the process zone to better dissipate energy across a wider area, this explains why higher stiffness materials exhibit larger process zones, although higher stiffness materials generally have greater fracture toughness values [148]. Furthermore, with the restriction of sample size it is clear how energy dissipated in the process zone becomes impeded with smaller samples [51].

The process zone is difficult to visualise and/or capture in experimental situations during fracture propagation. [141] Leona Vavroa et al performed a three point bending test on a cylindrical specimen 29mm diameter by 120mm next to an X-ray source. Using radiography, both the fracture path and process zone, are captured as observed in Figure 18 [141].

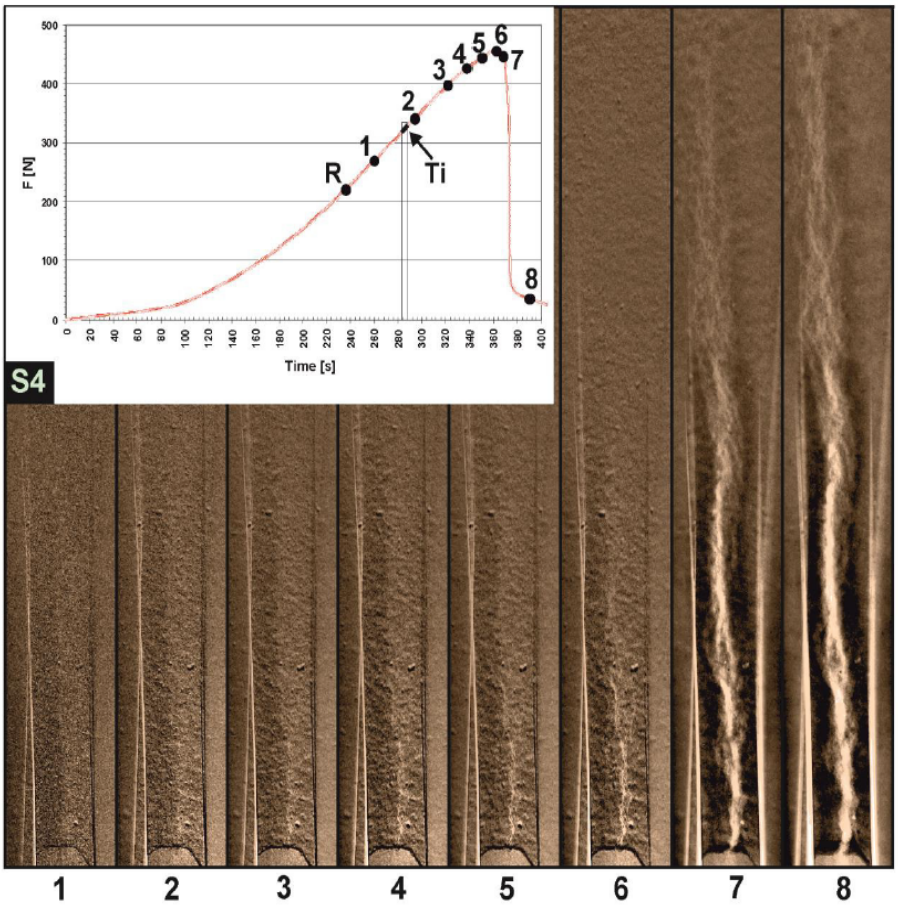

Figure 18: Process zone of progressing (left to right) fracture captured with X ray with accompanying force (N) vs time (s) plot on sample [141]

Figure 18 shows eight time stamps taken with accompanying X-ray snapshots from left to right of a fracture propagating. As the fracture propagates, material either side of the fracture compresses, increasing in density. This increase in density is captured by X-ray, hence the process zone can be captured in real time as the fracture propagates. The fracture is not as distinct

as one would imagine. Figure 18 shows a more spread out crack with many paths. The time of fracture initiation is shortly before the second snapshot is taken. The darker regions in snapshots seven and eight show an increase in material density around the crack, this is what is meant by the process zone. [141] further illustrated that the process zone is restricted by sample size, here compressing at the outer boundaries.

Large deformations are expected near crack tips. In classical plasticity this becomes an issue as they are based on the principles of infinitesimal strain. [68] found that during indentation modelling, these assumptions led to inaccurate results, infinitesimal strain based models are unable to maintain accurate results at high strains. [99] showed that with the application of deformation gradients within constitutive models, the distribution of stresses increased and had a significant effect on the both the process zone and resulting fracture behaviour.

2.6 Energy

Griffith successfully associated energy concentration with crack propagation. Hence it comes as no surprise that energy is heavily involved in many fracture frameworks, energy conservation is key during formulating these frameworks.

Understanding how a certain material can absorb energy internally is critical in the determination of fracture models. Rocks have several stages to their strength through loading, highlighted in a typical stress-strain plot of rock shown in Figure 19. The various stages each impact how well a rock sample can absorb energy.

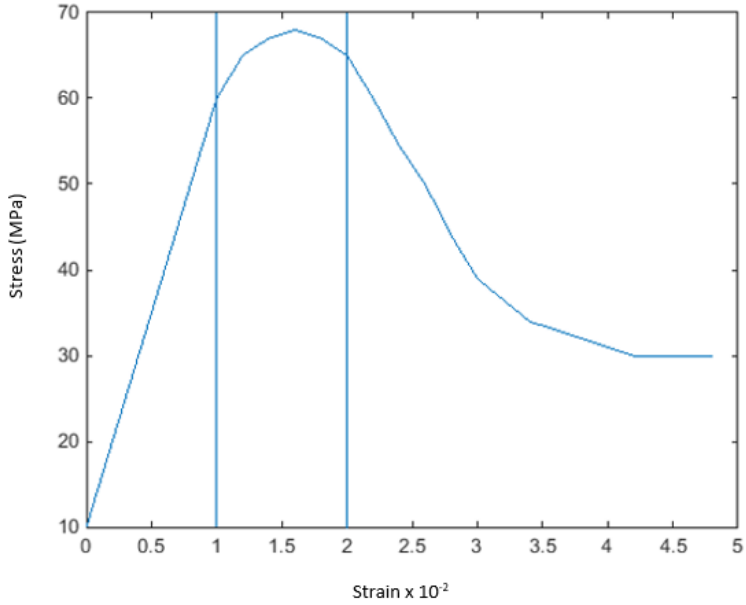

Figure 19: General Stress-Strain graph from Figure 14: classes 1-3 of rock deformation sectioned off from left to right

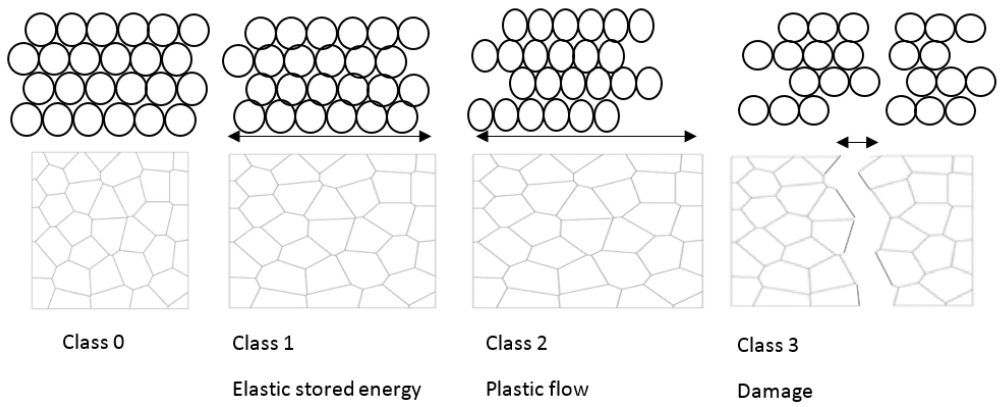

Figure 20: Particle rearrangement associated with the various classes of rock loading

In mechanical models the only source of energy which is input is from loading, this is converted by the continuum to kinetic energy, internal energy, mechanical work and heat generated from mechanical work, according to the first law of thermodynamics.

Which rock class the rock is in changes how energy is stored or dissipated. In class 1 all elastic energy is stored, and all energy can be theoretically reclaimed. Class 1 exists until the yield point is reached when inner particles can no longer keep their arrangement, at this point class 2 begins with plastic flow, dissipating excess energy [10]. Once all possible plastic rearrangements are complete the only way for further energy to be dissipated is through breakage and acceleration of particle bonds [114], represented by class 3. A decrease in material stiffness accommodates class 3, the decrease continues until the material has no other means to resist deformation than by internal friction of broken rock. During the transition from class 2 to 3 some elastic energy is redistributed into fractured fragments through kinematic means; this is later designated KE_D [150]. Ignoring heat created the conservation of energy is shown in equation 9.

$$E_i + KE + KE_D = W \tag{9}$$

where E_i is internal energy, KE is kinetic energy of the continuum, KE_D is kinetic energy of fractured masses and W represents mechanical work done on the continuum through loading. Kinetic energy KE can be calculated from deformation rates and continuum mass, internal energies can be calculated in terms of elastic and plastic energy, calculated from current deformation on a continuum as shown in equation 10.

$$E_i = E_e + E_p \tag{10}$$

where E_e is limited by how much recoverable deformation is possible, hence how much energy is stored elastically, this is represented by class 1 as shown in figure 20. E_p accounts for the energy dissipated through plastic flow through the material, represented by class 2 in Figure 19. These internal energy limits are found experimentally through stress-strain tests [142], [31].

If the material's internally stored energy surpasses the fracture energy threshold for the apparent mode of failure then a failure is declared and energy storage capacity of said material decreases, the decline in rock strength regime in stress-strain plots are usually defined as the class 3 stage of rock

loading as shown in Figures 14 and 20.

In constitutive models, the peak dilation angle of rock represents when the material cannot continue to absorb energy through pure plastic means within the material bonds or flow of particles [122]. The energy need for mode one failure is denoted as R_0, previously discussed in the damage section. Other failure modes are possible, similarly calculated from ultimate tensile and torsion tests.

Energy used during plastic deformation can be calculated by equation 11 [54]:

$$\boldsymbol{W_p} = \int \boldsymbol{\epsilon_p \sigma_e} \tag{11}$$

2.7 Finite strain

The hydrofracture process uses high pressure to break apart the rock strata to access natural gas. During the fracture process, large strains are expected locally along the fluid driven fractures [5]. When modelling these fractures, normal infinitesimal assumptions breakdown, mass is not preserved and material properties are influenced by said volume change. For this reason, constitutive models must be defined in terms of finite strains to model fracture behaviour accurately [60].

The finite strain methodology was proposed originally to model vulcanised rubber [61], rubber when loaded exhibits large deformations and infinitesimal models were found to breakdown in large strains [39].

Infinitesimal strains are incapable of assessing the influence of translations in mechanical calculation. This issue is solved with the consideration of deformation gradients which are based on the relative position of nodes, not their translations [100] and therefore are independent of translations as shown in Figure 21.

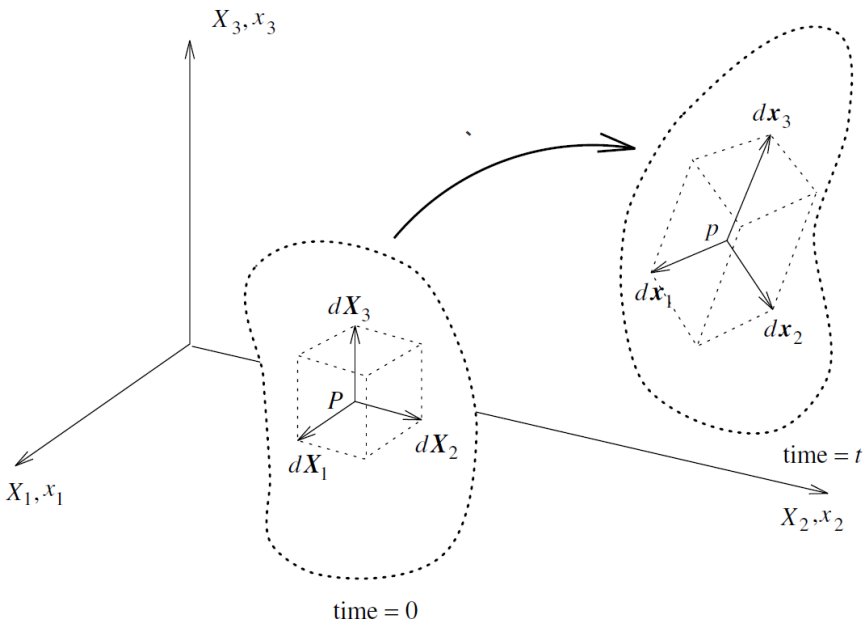

Figure 21: Finite strain principle [15]

where X_1, X_2 and X_3 are the global coordinates and x_1, x_2 and x_3 are local coordinates.

Figure 21 shows that even though the global coordinates of the cube have change significantly, the local coordinates have not. The key distinction is that the large strain methodology focuses on these local deformations to better replicate material behaviour.

2.8 Summary

The need for applicable hydrofractures solutions is clear, however the primary difficulty of utilising hydrofracture methodology is the required computational resources for accounting for both fractures and fluid. Therefore in order to account for large models for fracking, an efficient computational methodology is required.

Hydrofractures involve many phenomena that are important to account for such mechanical models which can realistically predict fracture and flow models for the associated fluid pressure. The problem of hydrofracture consists of a fluid flow and fracture problem, both research fields in their own respect as shown in the literature review.

A broad case of fracture methodologies were explored and compared on terms of accuracy, complexity of implementation and most importantly use of computational resources. A simple damage model utilising a minimisation algorithm was utilised so that the energy transitions within the considered system could be represented accurately, which highlighted by Fracfort and Marigo [52] is an important aspect of fracture mechanics.

Pore network models were reviewed and noted for their high accuracy, however the large number of equations required to solve for each considered fracture is not feasible in practical scenarios. However dual porosity models have been shown capable of modelling multiple fractures to a reasonable degree by modelling sets of fractures as damage fields differentiating where porous fluid or fracture fluid interactions occur.

No models currently exist which fully utilise a damage methodology within a dual porosity model for the flow characteristics within a hydrofracture. Therefore, the dual porosity model developed by Jianjun Ma [95] will be further developed to use a damage model to distinguish porous media from fractured so the different behaviour of the two can be captured with the progression of fluid driven fractures while maintaining fracture/hydrofracture directionality.

Furthermore, the finite deformation framework will be utilised as typical fracture mechanic problems. A model will be created and validated in the remainder of the thesis with appropriate verification examples.

3 Fracture prediction using the energy minimisation Technique

The process of evaluating crack progression can become daunting when more geometric and mechanical variables are introduced. Francfort and Marigo [16] have developed the minimisation technique from the Mumford-Shah functional, originally intended for computer vision scenarios to segment images. Francfort and Marigo applied the idea to segment a field of energy into segments of fractured and intact material whilst maintaining the lowest energy feasible within the model. Francfort and Marigo re-purposed the segmenting nature of the Mumford-Shah functional's capability to analyse branch cracks and overcome the issues of the Griffith crack regarding crack initiation. Accounting for multiple branched cracks simultaneously whilst reducing computational resource demand. The minimisation method considers fields of potential energy paths and solves for the minimal energy path of action in the system. This results in a multi-crack capable model where the number of cracks does not significantly influence compute times [45].

The main driving force of the minimisation method is utilised by inducing the minimal change in energy throughout a sample globally to ensure a stable solution to fracture problems. The minimal energy concept is accepted as an alternative to standard equilibrium solving mechanisms [39] for fracture prediction. The methodology is particularly useful as the same equations are used for crack initiation and propagation, reducing both the number of variables and equations used, simplifying the modelling process and reducing computational resource demand [45].

In this chapter the minimisation methodology utilised in this thesis will be explained followed by a finite deformation constitutive model and how fractures are in turn predicted.

The constitutive model utilised in this thesis is derived for compressible materials; equations 12-14 summarise the free energy function used to calcu-

late the total bulk energy in the considered system.

[15]

$$dE = \frac{1}{2}\mu(I_c - 3) \tag{12}$$

Trace of Cauchy green stain, isolating shear components [15]: described in terms of deformation gradient

$$I_c = trace\left(\begin{bmatrix} \frac{dx^e}{dX} & \frac{dy^e}{dX} & \frac{dz^e}{dX} \\ \frac{dx^e}{dY} & \frac{dy^e}{dY} & \frac{dz^e}{dX} \\ \frac{dx^e}{dZ} & \frac{dy^e}{dZ} & \frac{dz^e}{dZ} \end{bmatrix} \begin{bmatrix} \frac{dx^e}{dX} & \frac{dy^e}{dX} & \frac{dz^e}{dX} \\ \frac{dx^e}{dY} & \frac{dy^e}{dY} & \frac{dz^e}{dX} \\ \frac{dx^e}{dZ} & \frac{dy^e}{dZ} & \frac{dz^e}{dZ} \end{bmatrix}^T \right)$$

$$d\tau = \frac{1}{2}\lambda log(J) - \mu log(J) \tag{13}$$

where λ is the Lame constant, I_c the trace of the left Cauchy-green strain tensor, μ is the shear modulus, $d\tau$ is shear energy and J is volume change.

The total energy in the system is calculated using equation 14. Total energy, consisting of the bulk and shear components described above [35]

$$W = d\tau + dE \tag{14}$$

where W is work done.

The minimisation concept evaluates two possible energy paths, those being defined in equation 15's second and third terms; bulk energy and fracture energy respectively. The minimisation algorithm evaluates the best crack path in order to minimise the total energy contained within the domain. A crack's energy expenditure is modelled by surface energy and mechanical elastically stored energy is described here as bulk energy. The exchange of the two considered energy types are further described in equation 15 [35].

$$E(\boldsymbol{F}(\boldsymbol{x}), D) = min(\int_{\Omega} W(\boldsymbol{F}(\boldsymbol{x}))(D^2 + k_e)d\Omega + R_0 \int_{\Omega} H^{N-1}(D)) \qquad (15)$$

where E is the total energy, k_e is an infinitesimal integration term, $\boldsymbol{F}(\boldsymbol{x})$ is a function describing deformation in the space of x, D is damage variable, Ω is the simulation domain and H^{N-1} is the Hausdorff measure of fractures.

Two forms of energy are primarily considered in this study; bulk energy and surface energy. Bulk energy is stored elastic energy whether due to compressive or tension. The energy stored becomes comparable in magnitude to fracture energy when the energy may be converted into surface energy as previously discussed. Surface energy represents the breakage of bonds within a material. In this study both the surface energy expended and the weakening due to such fractures is represented by a damage model that assumes micro cracks distributed through the material during fracture.

Solving equation 15 for damage and deformation simultaneously is complex, therefore to simplify the process the damage and deformations, solved separately, iterating between the two. The general approach is as follows: initially all material parameters, model geometry and loads are defined. If a crack is in the initial model, then that would be replicated in the model by a set of element's damage variable at 0.1. Forces are prescribed and deformations are calculated from the incurred deformations, the resulting mechanical energy W is then calculated and equation 16 is used to discern where in the continuum fractures occur due to excess energy in elements.

$$E(\boldsymbol{F}(\boldsymbol{x}), D) = min \int_{\Omega} W(\boldsymbol{F}(\boldsymbol{x}))(D_0^2 + k_e)d\Omega + R_0 \int_{\Omega} H^{N-1}(D_0) \qquad (16)$$

where D_0 is the damage variable, which here remains whilst equation 16 is solved. The time steps where elements are damaged do not inherently model the reduction in stiffness due to fracture. For this reason, the time step

must be reset with the damage affected variables remaining, represented by equation 17 to better capture fracture behaviour.

$$E(\boldsymbol{F}(\boldsymbol{x_0}), D) = min \int \Omega W(\boldsymbol{F}(\boldsymbol{x_0}))(D^2 + k_e) d\Omega + R_0 \int \Omega H^{N-1}(D) \quad (17)$$

where $\mathbf{x}_0$ is the initial geometry, which here remains whilst equation 17 is solved. Equations 17 and 16 are iterated between in order to find the minimal energy in terms of fracture and bulk energy.

The solution of this equation is solved by comparing the bulk energy with the surface energy plots. The particular function plotted here can be found in equation 29. The surface energy is calculated using the Poisson equation as a minimiser as shown in the literature [2] [87].

Figure 22 shows a plot of the extension of a hypothetical single element bar in terms of energy versus extension. The amount of stored mechanical potential energy increases with an element's extension as expected. This statement remains true until the extension reaches 0.085m, the intersection point. Here the algorithm would assess that a fracture will reduce the stored bulk energy thus the total of fracture and bulk energy would be reduced.

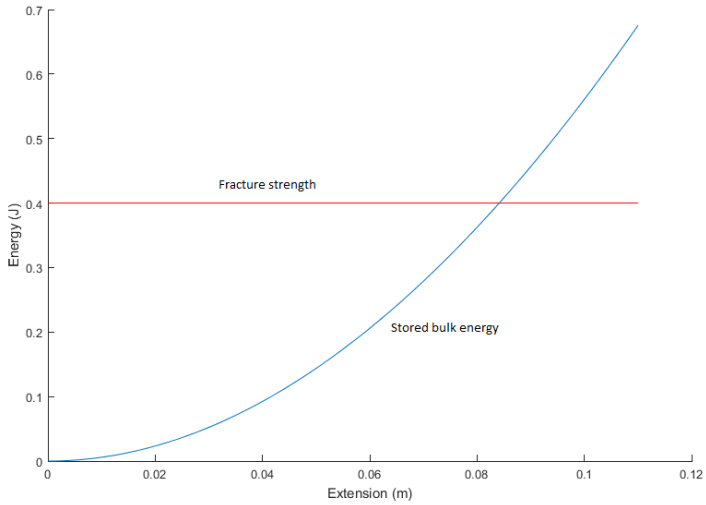

Figure 22: Energy plot of 1D bar under tension over time (Red line- Fracture energy threshold, Blue line- Stored energy

This methodology becomes more complex to solve with multiple element models. With elements depending on each other the total number of energy paths or possible fracture paths increase and the minimisation in the system becomes more complicated.

The two equations are solved individually applying deformation and damage in steps, this process is described in the following paragraphs.

By separating a domain into several sections, the points with the highest deformations and therefore higher stored potential energy; likely crack paths become more pronounced and can be determined to fracture. These determinations can be used to predict fracture behaviour and in this case is alternated between the damaged calculation and deformation calculation in order to find the minimal total energy in consideration of bulk and fracture energy from an energy field that looks similar to that displayed in Figure 23.

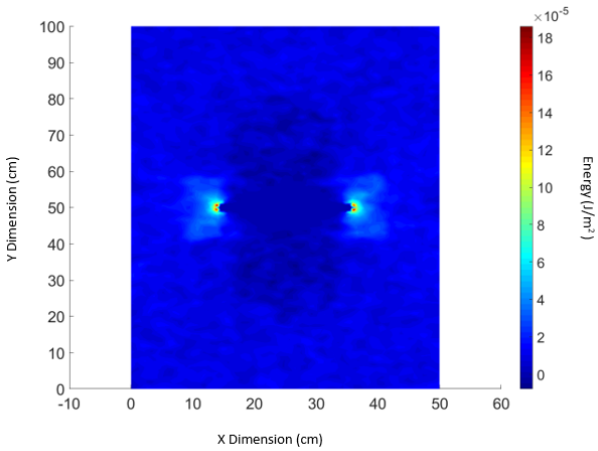

Figure 23: Energy field example showing regions of increasing energy intensity near crack tips

Figure 23 shows the bulk energy calculated by equations 14, there are three identifiable zones in the plot. The areas directly above and below the fracture is the region lowest as the area is under compression, unlikely to fracture in nature due to confinement. The area close to the domain boundaries are above zero but not significant. The fracture tips are where the most interesting behaviour occurs, here energy has accumulated, unsurprisingly where the gradient of deformation is most drastic.

The minimisation algorithm aids the damage methodology predicts where fracture is likely to occur by segmenting the energy plot into two segments at the fracture tips, for example in this case values above $8 \times 10^{-}5$ and below, from this the model can extend the pre-existent fracture and predict the correct fracture path which will be later shown in this chapter. The cut off limit for when segmenting to images can determined via varying the constants within equation 17. All elements are also checked against fracture strengths in order to predict fracture initiation times correctly.

With each iteration of the damage model the distribution of damaged elements grows and the effected weak areas begin to change the load paths within the model. How the minimisation algorithm is applied can dictate how

changes in failure mode can be accounted for, however smaller segmenting of damage are only required when model conditions change readily.

The approach of minimisation requires the use of convex energy functions so that minimal energy solutions can be stable, the free energy function used in this thesis is shown in equation 29 / Figure 24.

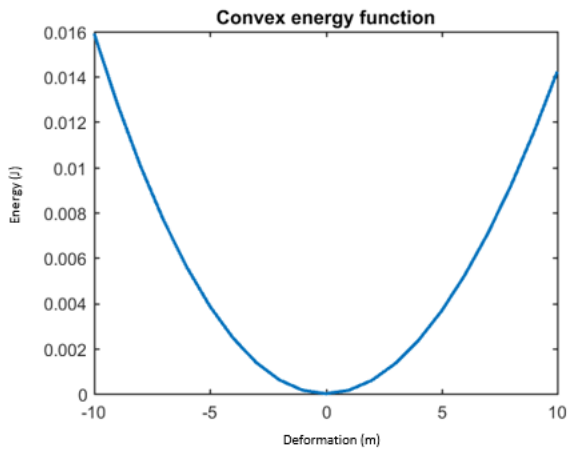

Figure 24: Convex free energy function of Neo-Hookean constitutive model

Figure 24 shows a free energy function plotted for both compression and tension. Figure 24 also shows that as higher and higher deformations occur, jumps in the deformation continuum at the expense of surface energy become preferable to high concentrations of potential energy similar to that shown in equations 18-19.

$$W(f) = W(F), \quad if \quad W(F) < R_0 \tag{18}$$

$$W(f) = R_0 \qquad otherwise \tag{19}$$

3.1 Damage model

When micro cracks occur, the reality is that the stress paths though the continuum are disrupted or in other words the amount of material resisting load is decreasing. This is approximated for by considering the area of internal surfaces as shown in equations: 20-22. Continuum damage mechanics assumes that the area, s is acting to carry the load $\boldsymbol{F_m}$ is reduced by micro cracks thus stress increases when micro cracks occur [85].

$$\frac{\boldsymbol{F_m}}{s} = \frac{\boldsymbol{T}}{1-D} \tag{20}$$

where $\boldsymbol{F_m}$ is external Force, s is the internal surface area, $\boldsymbol{T}$ is the general stress and D is damage. Hence the damage variable can be described by the reduction of resisting material.

$$D = \frac{s - s_1}{s} \tag{21}$$

thus

$$\boldsymbol{\sigma_d} = \frac{\boldsymbol{\sigma_0}}{1-D} \tag{22}$$

where s_1 is the current surface area of flaws, $\boldsymbol{\sigma_d}$ is stress due to damage and $\boldsymbol{\sigma_o}$ is initial stress.

Equations 20-22 showcase the weakening utilised to represent the decline in material stiffness with the propagation of fractures.

3.1.1 Finite deformation

Fracture mechanics can lead to large local deformations, especially if inclusions are created by a set of cracks. For this reason, it is important that implemented constitutive equations and applied framework can still be applied with accuracy following large changes to a model's structure. Here the distinction is made between finite and infinitesimal strains; infinitesimal strains assumed constant volume and a stationary model, when this is not the case, theories that are based on these foundations breakdown and

are no longer applicable [23]. Finite deformation algorithms overcome the shortcomings that translations bring to infinitesimal theories by using the deformation gradient as a primary input. Deformation gradients consider only the relative movements of nodes in relation to each other as shown in equation 23 and hence are unperturbed by translations.

$$[\boldsymbol{R}][\boldsymbol{U}] = [\boldsymbol{F}] \tag{23}$$

where the rotation matrix is described as

$$[\boldsymbol{R}] = \begin{bmatrix} cos(\theta) & -sin(\theta) & -sin(\theta_z) \\ sin(\theta) & cos(\theta) & -sin(\theta_z) \\ sin(\theta_z) & sin(\theta_z) & cos(\theta_z) \end{bmatrix} \tag{24}$$

where θ is the rotation in the x-y plane and θ_z is the rotation in the x-z plane, in this thesis will always be 0.

The stretch matrix, where $\boldsymbol{U}$ is the stretch matrix:

$$[\boldsymbol{U}] = \begin{bmatrix} \frac{dx}{dX} & 0 & 0 \\ 0 & \frac{dy}{dY} & 0 \\ 0 & 0 & \frac{dz}{dZ} \end{bmatrix} \tag{25}$$

$\boldsymbol{R}$ describes the relative rotation of an element and $\boldsymbol{U}$ is the stretch matrix representing the change in distance between nodes.

A translation example is shown in Figure 25, this would be represented in the form of equations 23-25 as shown below. The relative position of every node is unchanged, the corresponding deformation gradient, rotation, stretch matrices are unchanged.

$$\begin{bmatrix} 1 & 0 & 0 \\ 0 & 1 & 0 \\ 0 & 0 & 1 \end{bmatrix} \begin{bmatrix} 1 & 0 & 0 \\ 0 & 1 & 0 \\ 0 & 0 & 1 \end{bmatrix} = \begin{bmatrix} 1 & 0 & 0 \\ 0 & 1 & 0 \\ 0 & 0 & 1 \end{bmatrix}$$

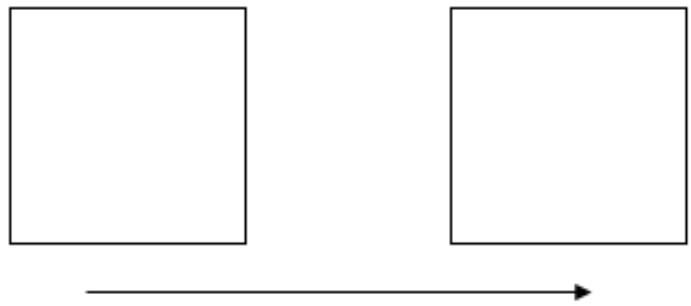

Figure 25: Translation of square element

When the deformation created in Figure 25 is used, the energy calculated by equation 14 also sums to $0J/m^2$ which is representative of reality.

If a rotation is considered on top of the above translation as shown in Figure 26 resolves to $0J/m^2$ as shown below.

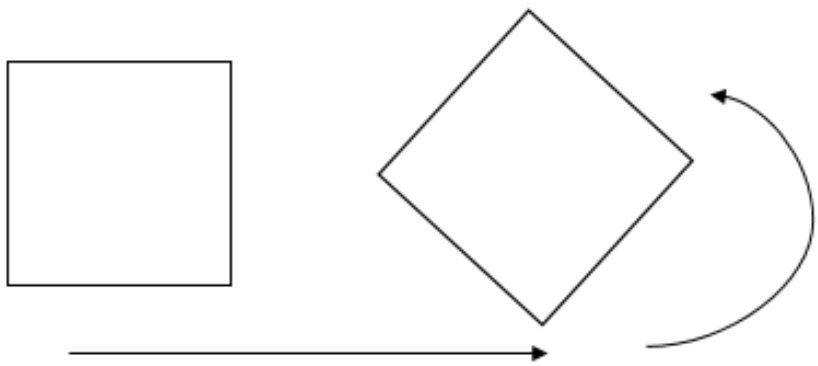

Figure 26: Translation and rotation of square element

$$\begin{bmatrix} cos(45) & -sin(45) & -sin(0) \\ sin(45) & cos(45) & -sin(0) \\ sin(0) & sin(0) & cos(0) \end{bmatrix} \begin{bmatrix} 1 & 0 & 0 \\ 0 & 1 & 0 \\ 0 & 0 & 1 \end{bmatrix} = \begin{bmatrix} 0.707 & -0.707 & 0 \\ 0.707 & 0.707 & 0 \\ 0 & 0 & 1 \end{bmatrix}$$

When the deformation and rotation created in Figure 26 is used in equation the energy calculated in equation 14 sums to $0J/m^2$which is represen-

tative of reality.

If the two above examples were in a framework where the nodes were only compared to their previous location, gross errors would be expected as the translations would be interpreted as strains. Now that strains are represented with the deformation gradient, usual constitutive models are no longer applicable as they are typically based on equation 26, where after the strains become greater than 2 %, the models can become unstable [15].

$$[\boldsymbol{U}] = \begin{bmatrix} \frac{du_x}{dx} & \frac{1}{2}(\frac{du_x}{dx} + \frac{du_y}{dx}) & \frac{1}{2}(\frac{du_x}{dx} + \frac{du_z}{dx}) \\ \frac{1}{2}(\frac{du_y}{dx} + \frac{du_x}{dy}) & \frac{du_y}{dy} & \frac{1}{2}(\frac{du_y}{dz} + \frac{du_z}{dy}) \\ \frac{1}{2}(\frac{du_z}{dx} + \frac{du_x}{dz}) & \frac{1}{2}(\frac{du_z}{dy} + \frac{du_y}{dz}) & \frac{du_z}{dz} \end{bmatrix} \tag{26}$$

Elastic finite strain constitutive models which utilise deformation gradients for modelling non-linear elasticity behaviour such as the Neo-Hookean compressible hyper elastic material, derived from the strain energy function [15].

3.2 Fracture methodology

The method used to calculate strain energy was the Simon and Pister's method, comparing the strain energy to the fracture energy found from a simple notched fracture test, shown in equations 27-29 [15].

$$dE = \frac{1}{2}\mu(I_c - 3) \tag{27}$$

$$d\tau = \frac{1}{2}\lambda log(J)^2 - \mu log(J) \tag{28}$$

$$W = d\tau + dE \tag{29}$$

The change in strain energy is used to decide how much damage an element has undergone. This amount is solved using equations 30 - 31.

$$\frac{2W}{R_o}D = 1 \tag{30}$$

R_0 being the fracture strength defined by the ultimate compressive strength σ_c and stiffness as shown in equation 30.

$$R_0 = \frac{2\sigma_c}{E} \tag{31}$$

Once the new damage has been calculated it is compared to the old damage allocation. The irreversibility condition is evoked so that no elements damage value can increase and undergo healing. A minimum is also used so that an element cannot be damaged to have null strength and deflect unrealistically.

3.2.1 Fracture algorithm

A function calculates the current deformation of the mesh using the *Matlab pdegrad* tool solving the equation through Gaussian reduction.

Gauss reduction method is a simple algorithm used to solve the linear equations throughout this research project.

Note: Run time can be prescribed in either number of time-steps/iterations or with a damage counter to ensure that failure is modelled.

Algorithm 1 Fracture procedure

1: Specify run time t_{full}
2: $j = 0$
3: Create model geometry
4: Interpret geometry to mesh using Delaunay triangulation algorithm [101]
5: Initialise material parameters μ, ν, λ, R_0
6: Initialise damage variable for initial crack
7: **while** $t < t_{full}$ **do** ▷ run time of simulation
8: Calculate stiffness matrix $\boldsymbol{C_{ijkl}} = \frac{\lambda}{J}\delta_{ij}\delta_{kl} + 2\frac{\mu-\lambda ln(J)}{J}\delta_{ik}\delta_{jl}$
9: Calculate internal forces
10: Form Global matrix and Global Force matrix
11: Solve system of Global equations for Δu_i
12: Calculate trial deformation gradients
13: Calculate stored elastic energy
$W = \frac{1}{2}\mu(I_c - 3) + \frac{1}{2}\lambda log(J)^2 - \mu log(J)$
14: Check for fracture $W_e > K_{fratt}$
$\Delta D_j = \min(\frac{W}{R_0}, 1)$
15: Assign damage variable accordingly
16: Calculate total energy
17: **if** $j = 0$ **then**
E_i^{tot}=total energy, $j = j + 1$ goto line 6
18: **else**
19: **if** $E_j^{tot} >= E_{j-1}^{tot}$ **then**
20: $t = t + 1$
21: $j = 1$
22: Update deformations $\boldsymbol{U_t} = \boldsymbol{U_{t-1}} + \Delta \boldsymbol{dU_{t-1}}$
23: Update damage $\boldsymbol{D}_t = \boldsymbol{D}_{t-1} - \Delta \boldsymbol{D}_{i-1}$
24: goto line 6
25: **else** reset deformations E_j^{tot}=total energy j=j+1
26: goto line 6
27: **end**
28: **end**
End while

The deformation gradient is used to formulate the deformation gradient tensor then the Cauchy left strain tensor and change in volume.

These are then used with the trace of the Cauchy strain gradient to calculate the strain energy density of elements.

Damage is assigned accordingly using the displacements to derive energy values.

When the damage approaches < 0.2 (User defined limit, depending on material and user case) then the medium is considered fully fractured [108], having minimal strength of the element being considered as if near void. This approach will be developed further in Chapter 4 with damage influencing parameters relevant to hydrofracture.

3.3 Constitutive Equations

In this approach hyper-elastic constitutive equations derived from a free energy function are used, these are used to the effect that material behaviour is unaffected by rotation or translation, material behaviour that causes inaccuracy in infinitesimally based constitutive models in the prediction of fractures, therefore the constitutive model and free energy function: ψ, must be wholly dependent on strain invariants as shown in equation 32.

$$\boldsymbol{\psi}(I_1, II_2, III_3) \tag{32}$$

where I, II and III denote the strain invariants as described in equations 33-35.

$$I_1 = trace(\mathbf{b}) \tag{33}$$

$$II_2 = trace(\mathbf{bb}) \tag{34}$$

$$III_3 = J = det(\mathbf{b}) \tag{35}$$

where $\mathbf{b}$ is the left Cauchy-green strain and J is volume change.

The Cauchy-green strain gradient is typically used in infinitesimal strain model's however here the stress will be converted to the Piola-Kirchoff stress, used for maintaining true stress in large strain frameworks. In doing this simplifies the plasticity approach, shown later in chapter 6. In order to derive the Cauchy stress tensor and Lagrangian elasticity tensor, first the Piola Kirchoff stress tensor $\mathbf{S}$ must be considered in terms of the deformation gradient as shown in equations 36-37.

$$\mathbf{S} = \boldsymbol{S}(\boldsymbol{F}(\boldsymbol{X}), \boldsymbol{X}) \tag{36}$$

$$\mathbf{S(F(X),X)} = \frac{\boldsymbol{d\psi}}{\boldsymbol{dE}} \tag{37}$$

Furthermore, the work done by **S** can be defined by the free energy function by considering continuum deformation as shown by equation 38, thus the only required input is **F**, the deformation gradient.

$$\boldsymbol{\psi}(\boldsymbol{F}(\boldsymbol{X}),\boldsymbol{X}) = \int E(\boldsymbol{F}(\boldsymbol{X}),\boldsymbol{X}) : \dot{\boldsymbol{F}} dt \tag{38}$$

From equation 38 the derivation for Piola-Kirchoff stress can be as shown in equation 39.

$$\mathbf{S(F(X),X)} = \frac{d\boldsymbol{\psi}(\boldsymbol{F}(\boldsymbol{X}),\boldsymbol{X})}{d\mathbf{F}} = \frac{d\boldsymbol{\psi}(\boldsymbol{F}(\boldsymbol{X}),\boldsymbol{X})}{d\mathbf{E}} \tag{39}$$

With equation 39 considered, the work conjugate $\frac{1}{2}\boldsymbol{C} = \boldsymbol{E}$; equation 40, can be written.

$$\mathbf{S(C(X),X)} = 2\frac{\boldsymbol{d\psi}}{\boldsymbol{dC}} = \frac{\boldsymbol{d\psi}}{\boldsymbol{dE}} \tag{40}$$

As previously mentioned, the free energy function and stress measure must both be invariant of rotation and translation, therefore the stress measure can be written as shown in equations 41 - 44.

$$\mathbf{S} = 2(\frac{\boldsymbol{d\psi}}{\boldsymbol{dI_1}}\frac{\boldsymbol{dI_1}}{\boldsymbol{dC}}+\frac{\boldsymbol{d\psi}}{\boldsymbol{dII_2}}\frac{\boldsymbol{dII}}{\boldsymbol{dC}}+\frac{\boldsymbol{d\psi}}{\boldsymbol{dII_2}}\frac{\boldsymbol{dIII_3}}{\boldsymbol{dC}}) = 2\boldsymbol{\psi_I I_2}+4\boldsymbol{\psi_{II_2}C}+2J^2\boldsymbol{\psi_{III_3}C^{-1}} \tag{41}$$

where

$$\frac{\boldsymbol{dI_1}}{\boldsymbol{dC}} = \mathbf{I}_1 \tag{42}$$

$$\frac{\boldsymbol{dII_2}}{\boldsymbol{dC}} = 2\mathrm{C} \tag{43}$$

$$\frac{\boldsymbol{dIII_3}}{\boldsymbol{dC}} = J^2\boldsymbol{C}^{-1} \tag{44}$$

To transfer the Piola-Kirchoff to true Cauchy stress, equation 45 is considered to produce an equation for Cauchy stress; equation 46. This allows the typically small strain stress Cauchy to be applicable in a large strain

framework.

$$\boldsymbol{\sigma} = J^{-1}\boldsymbol{F}\boldsymbol{S}\boldsymbol{F}^{\boldsymbol{T}} \tag{45}$$

$$\boldsymbol{\sigma} = 2J^{-1}\psi_I\boldsymbol{b} + 4j^{-1}\psi_{II}\boldsymbol{b}^2 + 2J\psi_{III_3}\boldsymbol{I} \tag{46}$$

Equation 46 allows stresses to be derived for any given free energy function. The particular free energy function is used in this research is shown in equation 47 .

$$\psi = \frac{\mu}{2}(I_c - 3) - \mu ln(J) + \frac{\lambda}{2}(ln(J))^2 \tag{47}$$

Therefore the derivatives: $\psi_I, \psi_{II}, \psi_{III}$ in respect to each invariant can be found in equations 48-50:

$$\psi_I = \frac{\mu}{2J} \tag{48}$$

$$\psi_{II} = 0 \tag{49}$$

$$\psi_{III} = \frac{\lambda ln(J^2)}{2} - \frac{\mu ln(J^2)}{2} = -\frac{\mu}{2J^2} + \lambda\frac{ln(J)}{2J^2} \tag{50}$$

Finally, the equation for Cauchy stress can be derived from equations: 46, 48, 49 and 50.

$$\boldsymbol{\sigma} = \frac{\mu}{J}(\mathbf{b} - \mathbf{I}) + \frac{\lambda}{J}ln(J)\mathbf{I} \tag{51}$$

3.4 Simple fracture and the effect of orientation on crack path verification

To show the minimisation process in practice and to demonstrate the previously discussed model's capabilities, a simple crack under a uni-axial load is modelled using the proposed methodology [74]. The results from [74] are both numerical and experimental in nature, the fracture paths predicted by the proposed methodology will be compared against experimental results and the deformation profiles compared against the reference numerical result which achieved reasonable fracture prediction results. Plane stress conditions are utilised during all verification reported in this thesis.

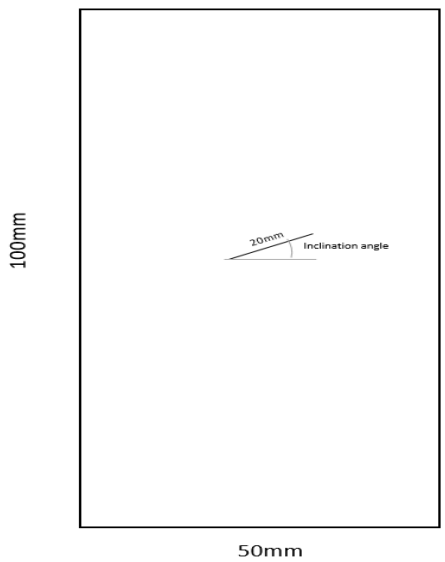

Figure 27: Schematic for fracture methodology verification

The experiment was performed on a rectangular specimen of concrete 100 by 50 mm as seen in Figure 27. Each specimen had a flaw set in during the concrete moulding phase by inserting a 4mm by 20mm aluminium case inside. Once dry, the insert was pulled out to create the slit, causing minimal initial stresses in the specimen. The aluminium case was held in place via a screwed mount and secured with a plastic wedge to ensure accurate placing and consistent slit shape between experiments.

[74] developed a DEM model to predict the fracture behaviour of various slit orientation, numerical results of which achieved reasonable agreement, results that will be used for verification purposes.

All specimens were left to cure 28 days so that the concrete could reach full maturity. The flaw was expected to initiate a fracture across the sample due to loading, allowing the impact of notch orientation on fracture propagation/ initiation to be categorised.

Each sample was compressed uni-axially at a rate of 0.05 mm/s to avoid any rate dependent behaviour effecting results. In the experiment, the top and bottom boundaries were free to move in the x direction to grease placed at both load points in the experimental version of the test. In the numerical simulation the top and bottom were free to move in the x direction. This was calibrated in the intact sample testing comparing against the reference DEM deformation plots.

Table 2: Material properties for single slit experiment

Young's modulus	E	50 GPa
Poisson's ratio	ν	0.25
Fracture strength	K_{Fratt}	$12.5KJ/m^2$

The deformation profiles, crack path and stress- strain profiles were captured during testing and here a comparison will be made using experimental and reference numerical results to verify the proposed fracture methodology.

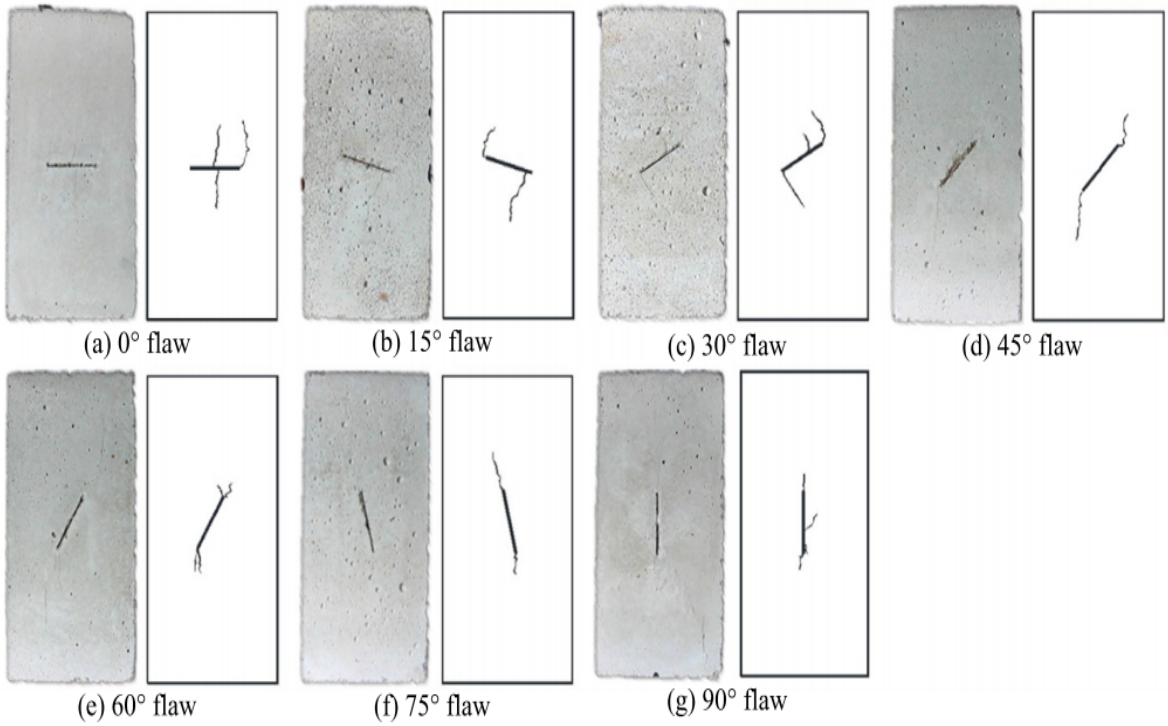

Figure 28: Experimental (gray) and traced experimental (white) fracture initiations for various angled slit results from reference paper [74]

The key points of comparison to experimental data will be on the stress strain plots, a qualitative look at crack initiation and crack propagation through the concrete sample, such as that provided in the reference paper; shown Figure 28. Additional comparisons will be qualitative compared against the deformation plots generated numerically by the DEM reference solution.

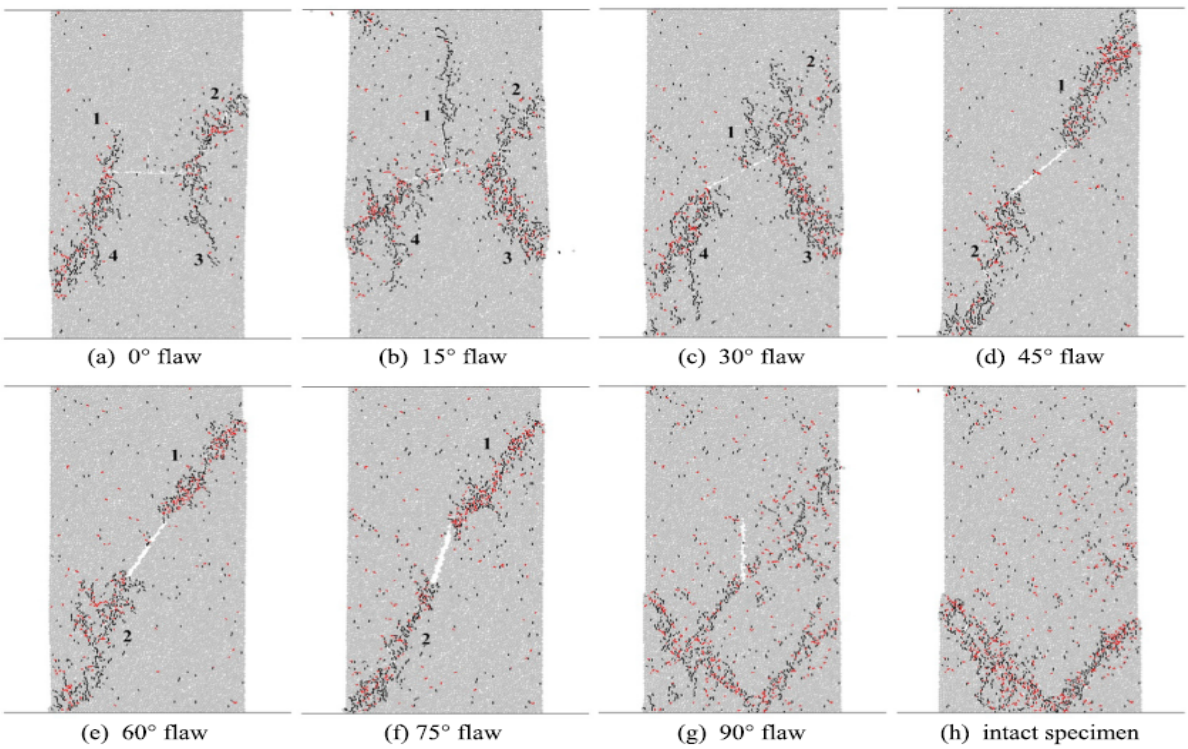

Figure 29: Numerical fracture initiations for various angled slit results from reference paper [74]

As seen in Figure 29 the numerical results from [74] predicted reasonable fracture paths that agreed with the observed experimental results, shown in Figure 32.

The data provided in the reference paper includes stress-strain plots for slit angles from 0 degrees up to 90 degrees in 30 degree increments. The deformation profiles in the principal x direction were recorded in the reference paper for all notch angles up to 90 degrees in 15 degree increments.

The stress and strain plots for all with comparative data are shown in Figure 30.

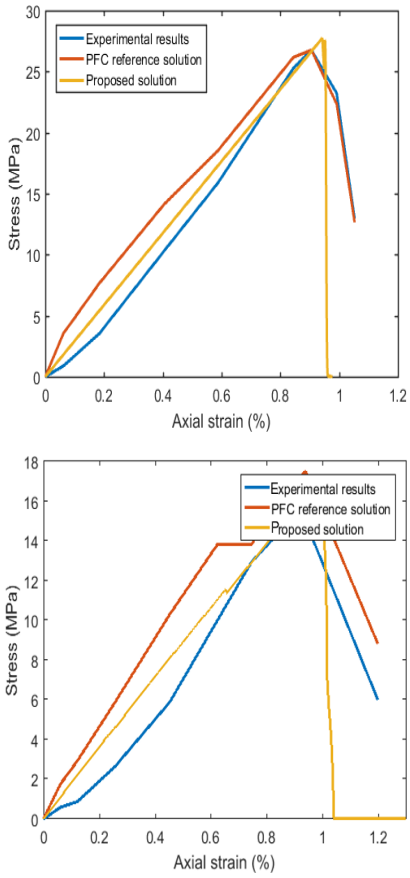

Figure 30: Stress strain plot for intact and 30 degree slit over time

It can be seen in Figure 30 that the methodology account for the slits effect on the stress strain plots are accurate, achieving agreeable results when compared to the reference solutions, either numeric or experimental. Achieving within 8 % of the experimental stiffness achieved (comparing the lowest and highest values shown) and 15 % below that of the reference Particle flow code predicted stiffness. At failure strain however the strain is the same across all three; proposed, experiment and reference solutions at point of failure.

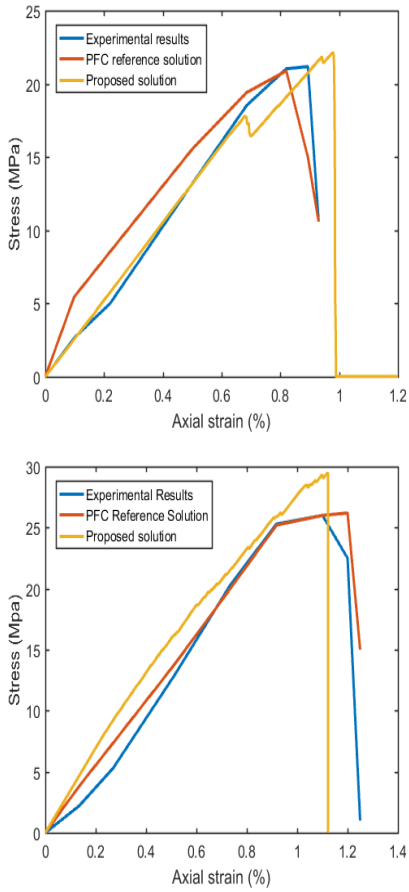

Figure 31: Stress strain plot for 60 and 90 degree slit over time

The proposed fracture methodology matches the failure of an intact sample at 22MPa and 25MPa with similar stiffness in the 60 and 90 degree experiments respectively. The stiffness is more closely predicted here, only disagreements are with 3.2%.

The strength in the 90 degree sample over estimates the failure and post failure behaviour when compared to the reference numerical solution and observed experimental stress stain plot. This is likely due to the predicted failure mode predicting the model splitting in two equally, reducing stress concentrations within the model.

As seen in Figures 30 and 31 the stiffness is more accurately captured in comparison to the reference particle flow code initially, the early error is likely due to the slipping condition imposed as the exact friction profile at contact point and how it carried through the experiment is impossible to measure and replicate.

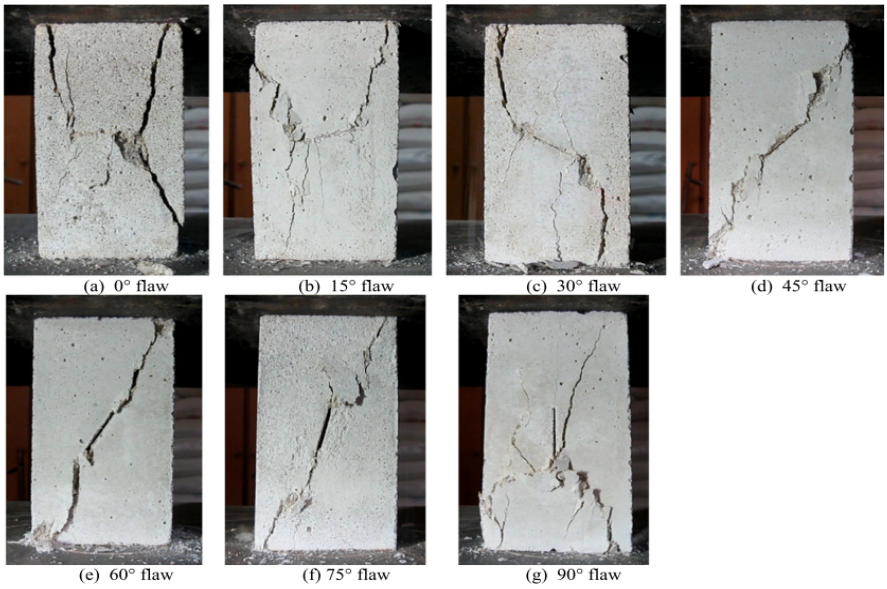

Figure 32: Experimental fully developed fractures for various angled slit results from reference paper [74]

The correct crack paths of angled notched in concrete axial compression tests can be seen in Figure 32, with these the crack path prediction capabilities are verified as shown in Figure 41 and Appendix B. It is seen that after the notch is orientated at 45 degrees or greater the crack path stops bifurcating and becomes singular.

For the stress-strain plots, the strain was known ahead of time due to the displacement driven load however the stress was calculated by taking an average of stress across the whole model. The stress vs strain plots calculated by the proposed model, provides a agreement in terms of the stiffness and points of failure. However, in the case of post failure behaviour, a more

ductile behaviour is incorrectly predicted, this is true for all models except the 90 degree notch model as shown in Figure 31.

Results In this section, several results of the thin slit experiment/verification will be compared and critiqued. Due to the repetitive nature of some of the results only the 0, 45 and 60 degree slits will be examined here with the intact version. The remainder of the results can be found in appendix B.

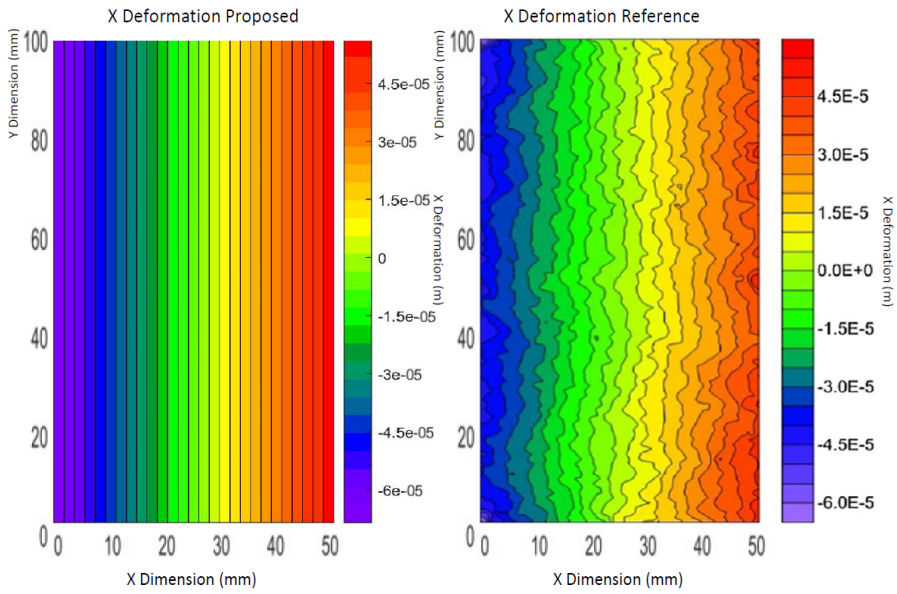

Figure 33: Damage plots; proposed numerical solution (left) and reference numerical solution (right) for intact specimen [74]

Figure 33 shows the deformation profile for an intact sample in comparison to the numeral results from the reference solution. Both samples show a similar amount of x deformation due to Poisson effects from the uniaxial compression, the maximum deformations being within 1.8 %. Figure 33 shows that the heterogeneous nature of Particle Flow Code does not significantly impact the deformation profiles when compared to the similarly spaced deformation bands in the produced homogeneous result.

The lack of friction can be seen in Figure 33's regularity of deformation bands from the proposed solution, showing agreeability in the frictional boundary's modelling.

In the reference paper no value was assigned to a fracture energy term, therefore the fracture strength was acquired through calibration of the model in comparison to the reference model. This was done by calculating the rough area under the provided stress-strain plot by [74], this came to a value of $12.5KJ/m^2$ by calculating the work done during testing.

Using this calculated fracture strength and the proposed method presented reasonable results in the predicted stress-strain graph as seen in Figure 30 producing linear elasticity similar to the reference particle flow code and experimental stress-strain graph from [74].

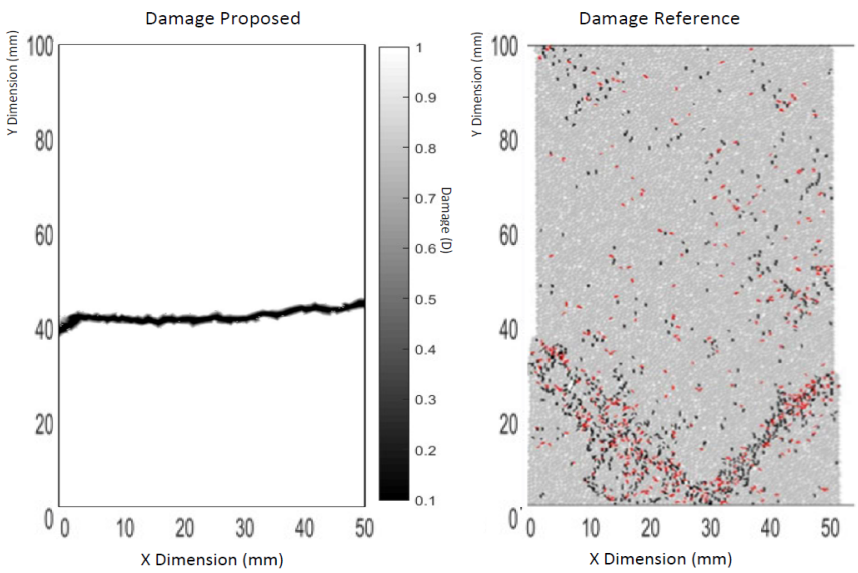

Figure 34: Damage plots; proposed numerical solution (left) and reference numerical solution (right) for intact specimen [74]

Figure 34 shows the crack path predicted for an intact specimen from the proposed and reference numerical model do not align. However the lack of heterogeneity in the proposed model a crack path initiation point is difficult for the model to calculate when compared to the reference computa-

tional result [74]. The heterogeneity stems from the slight friction applied to the boundaries used and the slight heterogeneity from the random particle distribution in the model has not impacted fracture initiation significantly, therefore the material properties do not fluctuate significantly and are not a significant factor in the reference numerical results.

Figure 34 shows two failure paths produced by the reference and proposed solution.

In the reference solution the fracture occurs due the Poisson effects on deformation being slightly more extreme at the corners due to less confinement, indicating issue with the implementation of friction at the boundary layers.

45 degree slit

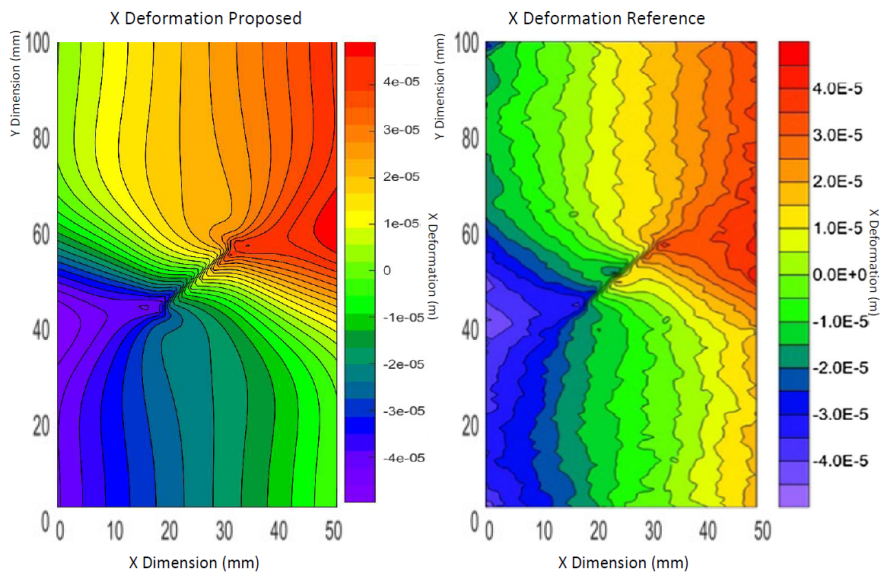

Figure 35: Deformation plots; proposed numerical solution (left) and reference numerical solution (right) for 45 degree slit at initiation [74]

Figures 35 shows that the proposed methodology is suitable predicting the correct crack path and x deformation profile incurred from the uni-axial

load's effect on the 45 degree slit. The crack lips both slide over each other, the contact aiding in the sliding behaviour of the specimen as expected [32].

The slight effect of the light friction can be seen in the deformation boundaries near the top and bottom boundaries, where they trend inwards, held back by the friction. Both deforming similarly in reaction to the applied uni-axial load, showing reasonable agreement in both the deformation trends and magnitude, the maximum deformations being within 2.6 %..

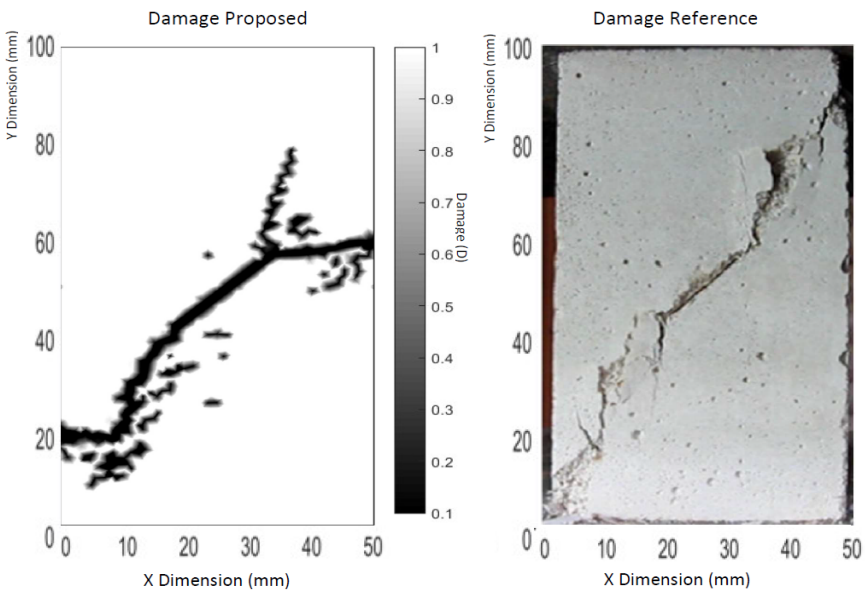

Figure 36: Damage plots; proposed numerical solution (left) and reference traced experimental solution (right) for fracture initiation of 45 degree slit [74]

Figure 36 shows the numerical results from both the proposed and crack initiation of a 45 degree slit under uniaxial load. Both results are similar in nature, both initiating two fractures above at either tip, propagating vertically at a reasonably similar rate.

The branching fracture showcased, is caused by the lateral expansion through shear tension failure, as the sample is compressed the two sides expand marginally. The expansion is greater on the right side. As the top

section as the section moves leftwards, creating a greater stress and energy concentration, creating the large branched fracture, observed in both the experimental and observed fracture paths. The combination of the two effects forms the diagonal fracture shown in Figure 36. The left portion of the sample also exhibits lateral movement and compression however the lateral movement is less than the right side and after the right fracture branch, the stresses on the left side area somewhat relieved hence no branching occurs on the left's side with increased loading.

0 degree notch

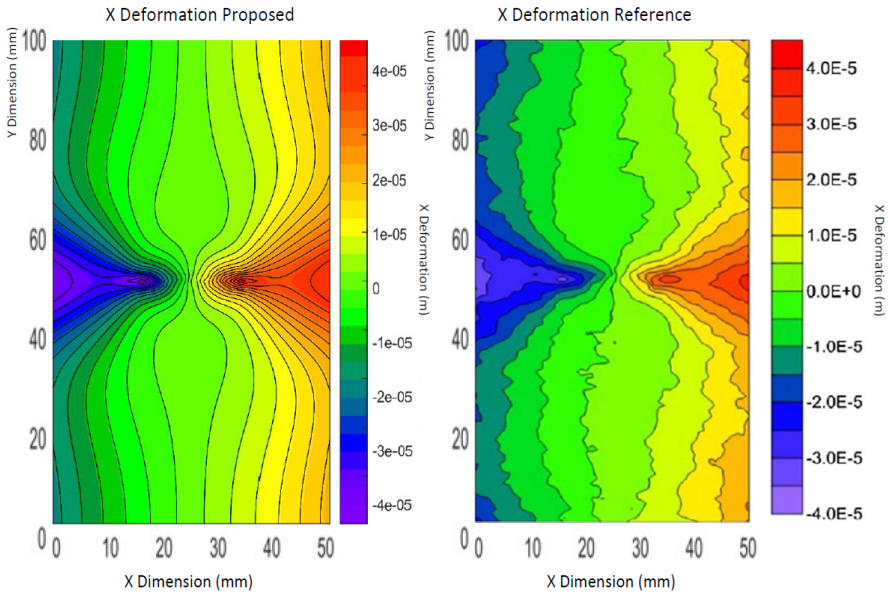

Figure 37: Deformation plots; proposed numerical solution (left) and reference numerical solution (right) for 0 degree slit at initiation [74]

The deformation profiles shown in Figure 37 match up with those calculated by the proposed model, all showing similar x deformation magnitudes and intensity distribution, the maximum deformations being within 1.3 %.. The greatest areas of lateral movement being near the crack tips fanning out towards the edges in both simulations due to Poisson effects being concentrated in the region and the lack of resisting material.

The large deformation gradient across the plotted fans next to the propagating crack contributes to the creation of the crack, the shearing energy building up along the shear plane, creating the cracks as shown in Figure 38.

The deformation result from Figure 37 shows the top half of the sample moving slightly more than the bottom, the lack of symmetry not being an issue in the proposed solution deformation plot.

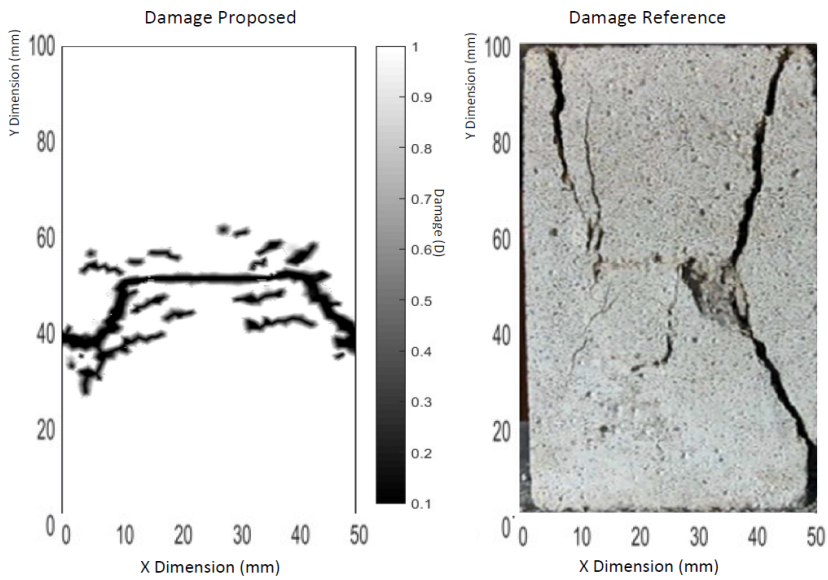

Figure 38: Damage plots; proposed numerical solution (left) and reference traced experimental solution (right) for fracture initiation of 0 degree slit [74]

Figure 38 shows the predicted fracture paths for a 0 degree slit from the proposed model compared to the experimental result.

Two fractures initially propagate from both tips of the slit diagonally towards the closest corners of the sample. The numerically procured angle is observed to be less inclined than the experimental fracture path shown in Figure 38 after a few time steps only the bottom two fractures maintain propagation until complete failure.

The branching fracture from the tip showcased in both the experiment behaviour and proposed solution is caused by shear tension failure. As the sample is compressed uniaxially the two sides also compresses however the

sample also laterally expands marginally, the combination of the two effects forms the diagonal fractures shown in Figure 38.

For both the 0 and 15 degree notch experiments, the methodology fails to predict a crack accurately compared with the rest of the numerical tests carried out in terms of crack path prediction. Both of accompanying x-deformation profiles are both reasonably within the reference plot's deformation trends and magnitude provided by the reference paper [74]. The [74] paper states that during testing of the 0 and 15 degree notches the crack lips contacted/locked, shortly afterwards the crack began propagating perpendicular to the crack due to the change in the load path through the sample.

The implemented damage model works on weakening the internal crack model considerably, allowing void like behaviour, this is reasonable in most cases, however in this case the contact is neglected. The constitutive model uses the volume change and a calculated deformation gradient to dictate internal forces and structural response, in this case the volumes become negative. (For Figure 39 the elements were completely erased for the sake of pointing out the shortfall of the model and its implementation) The result was improved and refined by putting a volume change penalty on the model; the penalty activates if an extreme volume change is detected and the penalty is met with a rapid increase in stiffness, representing an expected contact condition in an ad-hoc manner. The penalty improved the result of the 0 degree predicted crack path as shown in Figure 39, with four fractures initiating simultaneously at similar rates agreeing more favourably with the experimental fracture results.

In the region close to the fracture tips small islands of deformation can be seen in Figure 37, these are the main sources of instability in the model and are the most likely region for inadmissible deformation to occur therefore it is important that the damage model has a residual strength so that elements don't overlap and become unstable.

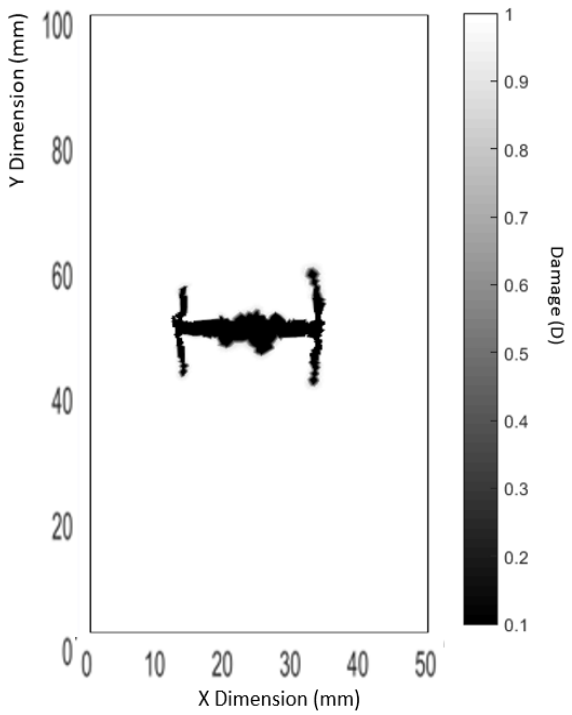

Figure 39: Corrected crack path for 0 degree fracture initiation (Proposed numerical result)

The initial deformation for these results were similar to the uncorrected result, the key difference was in the y deformation, allowing shear planes correctly move position and predict the correct crack path for this slit inclination, thanks to the introduced ad hoc volume penalty.

60 degree notch

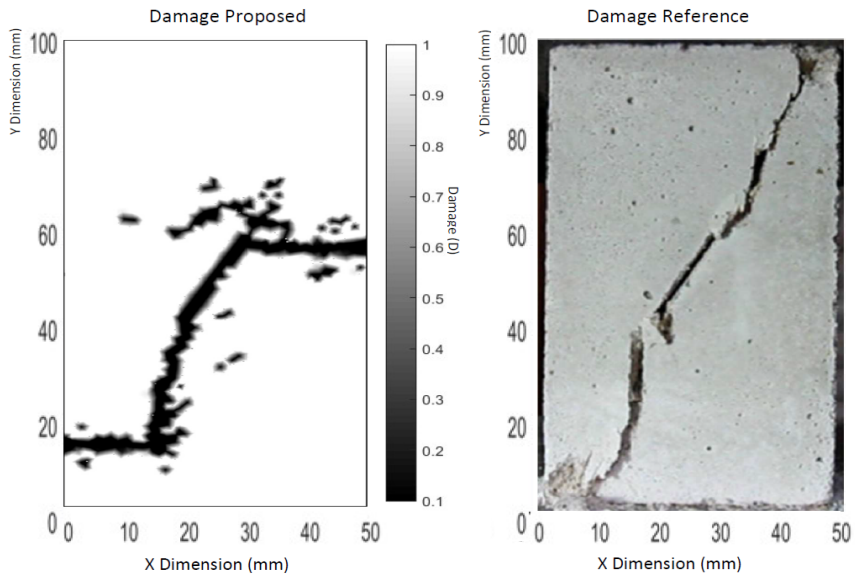

Figure 40: Damage plots; proposed numerical solution (left) and reference experimental solution (right) for full fracture of 60 degree slit [74]

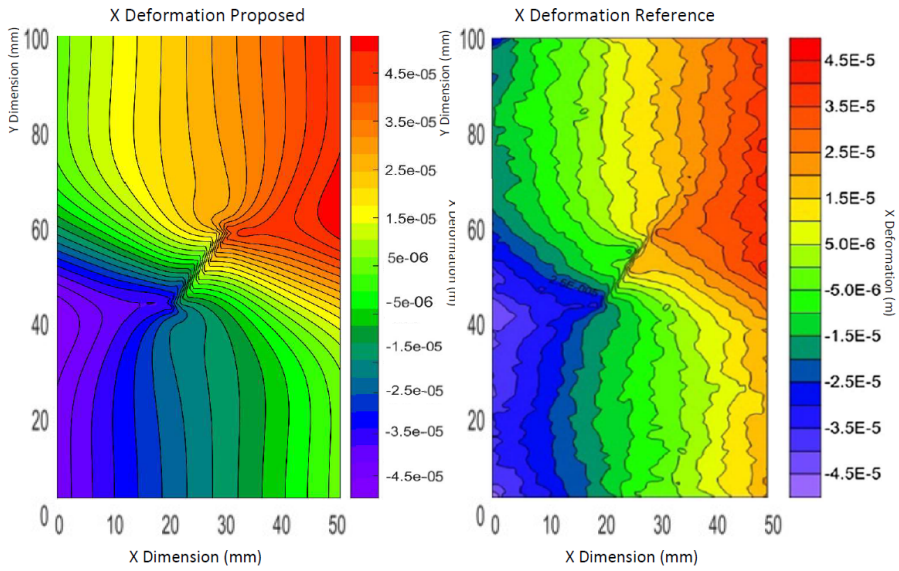

Figure 41: Deformation plots; proposed numerical solution (left) and reference numerical solution (right) for 60 degree slit at initiation [74]

Figure 42 shows that the crack, shown in figure 40 does not begin propagating until the 860s mark, until this point the sample is accumulating mechanical energy, similar to a spring.

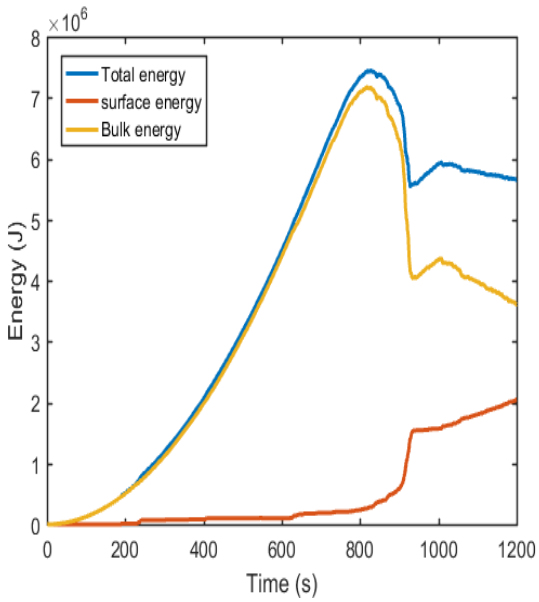

Figure 42: Energy plot over time consisting of fracture (surface energy) and stored energy (bulk) for 60 degree notch

The progressive failure of the sample is shown clearly at the 860s mark shown in Figure 42, where the plot show transitional behaviour from bulk to surface energy. After initial failure a second peak occurs, this is a secondary failure once the newly created structure has redirected load.

At time 860s mark the elements at the tip of the fracture have surpassed the critical energy density and therefore must fail but also that the failure would incur further damage through the model, hence the model algorithm repeats with the damaged elements accounted for. The lengthened crack has new tips which in this case now also surpass the critical energy density, this loop continues until complete failure is achieved. This loop is controlled and dictated by the total energy, here shown as a blue line in Figure 42. Post this point however when the model has completely failed, the reader may notice that the fracture energy rate is constant, and the bulk continues to grow;

this is due to the residual strength taking over the behaviour and should be considered a null result post failure.

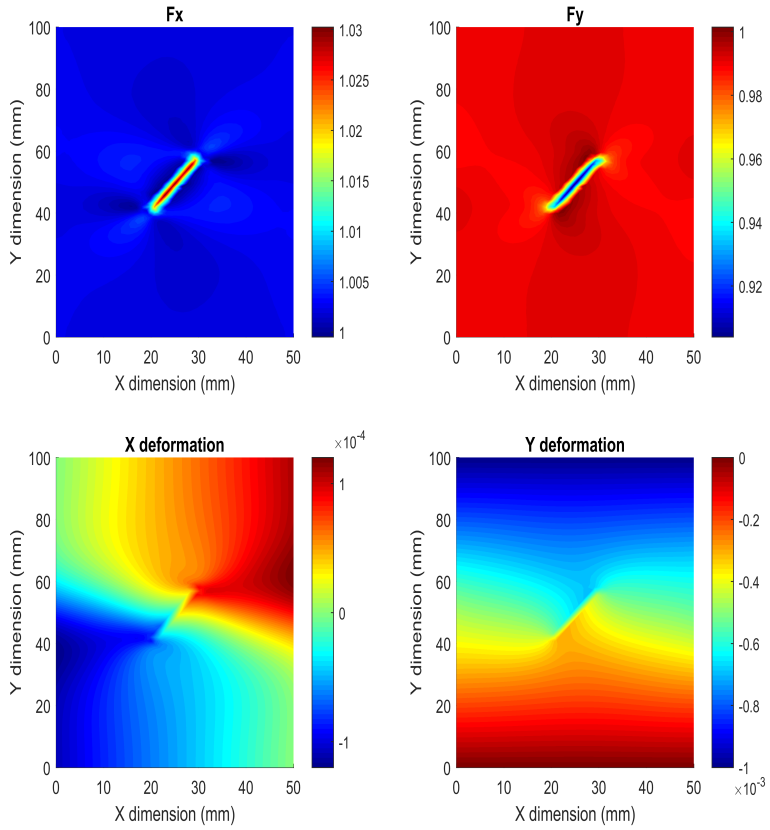

Figure 43: Deformation gradient plot before fracture initiation

Figure 43 shows the deformation gradient and deformation plots for a 60 degree slit for reference. Figure 43 shows prior to fracture. Here is can be seen that the deformation gradient only active in the region of the fracture and a little onward in the process zone as it should be.

3.5 Summary

The minimisation fracture methodology used has been showcased to correctly predict the fracture paths for a complex experimental fracture proce-

dure, remaining stable through the large strains exhibited during the fracturing process, correctly predicting branching behaviour. An issue with the proposed methodology is predicting fracture behaviour in the absence of heterogeneous material models and a clear driving force, this is why the final leg of fracture predictions become less accurate with time. This issue will be shown to be less prevalent when a clearer driving force, fluid pressure, is introduced. Another issue was modelling the contact between two fracture surfaces on the 0 and 15 degree experiments. However, the primary goal of this thesis is to research hydrofracture where complete crack closure and compression is rare. In the next section, a fluid flow model will be introduced and derived then combined with the fracture model shown in this chapter.

4 Fully coupled fracture and pore pressure model

The literature review covered the methods currently used to model hydrofracture phenomena comparing the pros and cons of each. After the comparison is was decided to continue to the work of [95] using a damage model in combination with a dual porosity methodology. This approach was chosen as the computational demand and required variables required are low and inspire a highly practical model for hydrofracture problems.

The methodology is based on two domains: fractured and porous overlapping modelling a fracture porous medium instead of a void like fracture which can realistically model the increase in stress at fracture tips due to crack geometry [153]. The produced methodology by Ma produces reasonable results verified for a pressurised well bore in a confined aquifer however here with the extension of a more sophisticated damage/fracture methodology it will that shown that the dual porosity approach can be extended for penny cracks and more realistic hydrofracture scenarios with minor adjustments to the implementation of Ma's coupled flow equations.

This chapter will explain in detail the derivation of the coupled flow equations used and how the methodology was combined with the fracture methodology previously shown in chapter 3. The primary novelty of this thesis will then be described in terms of how the coupling interacts with introduced fracture methodology.

Verifications of the proposed combined framework can be found later in this chapter where numerical hydrofracture prediction output is compared to several relevant hydrofracture examples found in the literature.

The verification examples include a one dimensional consolidation test to evaluate the suitability of modelling the effects of porous flow using analytical and a reference finite element method solution.

Three penny cracks are simulated under varying conditions, compared qualitatively in terms of analytical and reference numerical solutions. A nu-

merical hydrofracture model is then modelled in comparison to an experiment conducted by [136] where fracture paths produced by non-uniform pressure fields are compared quantitatively.

4.1 Dual porosity coupling framework

A double permeability framework based on Darcy flow by Jiangjun Ma [95] has been developed to model hydromechanical components. Their derivation, spatial and time discretisation are described in the following pages.

The utilised fluid methodology considers two zones, in this case: one fractured and the other porous throughout a considered domain both capable of maintaining fluid flow and interacting with the containing pore/fracture walls.

For the derivation of the coupled global equations the fluid flow velocities within both zones are considered as shown in equation 52.

$$\boldsymbol{v}_{\boldsymbol{\alpha}}^{\boldsymbol{r}} = -\frac{\boldsymbol{k}_{\boldsymbol{\alpha}}}{\mu_f}(\nabla \boldsymbol{p}_{\boldsymbol{\alpha}} + \rho_f \boldsymbol{g}), \quad \alpha = 1 \quad (porous), \quad 2 \quad (fracture) \tag{52}$$

where $\boldsymbol{v}_{\boldsymbol{\alpha}}^{\boldsymbol{r}}$ is the relative velocity of fluid in the respective region, $\boldsymbol{k}_{\boldsymbol{\alpha}}$ is the permeability of the respective region, μ_f is the dynamic viscosity of the fluid considered, $\boldsymbol{p}_{\boldsymbol{\alpha}}$ is the pressure in the respective zones, ρ_f is the fluid density and $\boldsymbol{g}$ is the gravity vector. Gravity here is described as:

$$-\boldsymbol{g} = \begin{bmatrix} 9.81 \\ 0 \end{bmatrix}$$

The subscript notation on permeability, pressure and other variables denotes which zones is referred to, $\alpha = 1$ refers to porous domain and $\alpha = 2$ refers to a fracture's domain, when α is left as is then both are modelled simultaneously in the same space.

Both zone types are considered unique and independent of each other up until coupling behaviour is later introduced in equation 56.

The relative velocity of the fluid to the containing continuum can take the form of equation 53.

$$\boldsymbol{v}_\alpha^r = \phi_\alpha(\boldsymbol{v}_\alpha - \boldsymbol{v}_s) \tag{53}$$

In which $(\boldsymbol{v_\alpha} - \boldsymbol{v_s})$ is the velocity of the soil skeleton considered in the continuum, ϕ_α is porosity of the respective domain and v_α is the absolute velocity of the fluid in the respective domain.

The absolute velocities; $\boldsymbol{v}_\alpha$ and $\boldsymbol{v}_s$ are defined as shown in equations 54 and 55 respectively.

$$\boldsymbol{v}_\alpha = \frac{d\boldsymbol{u}_\alpha}{dt} \tag{54}$$

and

$$\boldsymbol{v}_s = \frac{d\boldsymbol{u}}{dt} \tag{55}$$

where $\boldsymbol{v_\alpha}$ and $\boldsymbol{v_s}$ are the velocities of the fluid and the continuum respectably, $\boldsymbol{u_\alpha}$ is the deformation of the respective zone, $\boldsymbol{u}$ is the general deformation and t is time. Taking the mass balance at a considered boundary between the porous and fractured regions leads to equation 56.

$$\boldsymbol{\nabla}(\phi_\alpha \rho_f \boldsymbol{v}_s) + \frac{\partial(\boldsymbol{\nabla}\phi_\alpha \rho_f)}{\partial t} + (-1)^\alpha \boldsymbol{\Omega} = 0 \tag{56}$$

where $\boldsymbol{\nabla}(\phi_\alpha \rho_f \boldsymbol{v}_s)$ represents changes in porosity and density caused by the fluid flow in the respective region. $(\delta(\boldsymbol{\nabla}\phi_\alpha \rho_f))/\delta t$ represents the changes in fluid density over time through deformation across the spatial domain.

The $(-1)^\alpha \Omega$ term describes effects resulting from fluid leakage from porous to fractured or vice versa, here only active on the boundary between the two considered domains to model fluid exchange along fracture boundaries which develop with fracture propagation.

Substituting equation 53 into equation 56 produces equation 57.

$$-\boldsymbol{\nabla}(\phi_\alpha \rho_f \boldsymbol{v}_s) - \boldsymbol{\nabla}(\rho_f \boldsymbol{v}_\alpha^r) = \frac{\partial(\phi_\alpha \rho_f)}{\partial t} + (-1)^\alpha \boldsymbol{\Omega} \tag{57}$$

Note: the third and fourth term of equation 57 vary in space.

Using the Lagrangian total derivative method concept for both a moving solid; $(d_s(\bullet))/dt = (\partial_s(\bullet))/dt + \boldsymbol{\nabla}(\bullet)v_s$ and fluid; $(d_\alpha(\bullet))/dt = (\partial_\alpha(\bullet))/dt + \boldsymbol{\nabla}(\bullet)v_\alpha$ with an identity vector $\boldsymbol{\nabla}[(\bullet)v_i] = (\bullet)\boldsymbol{\nabla}(v_\alpha) + (\bullet)\boldsymbol{\nabla}v_\alpha$, equation 57 can be re-written as shown in equation 58.

$$-\rho_f \boldsymbol{\nabla}\boldsymbol{v}_\alpha^r = \frac{\phi_\alpha d_\alpha \rho_f}{dt} + \rho_f \frac{d_s \phi_\alpha}{dt} + \phi_\alpha \rho_f \boldsymbol{\nabla}\boldsymbol{v}_s + (-1)^\alpha \boldsymbol{\Omega} = 0 \tag{58}$$

This isolates each term, increasing the simplicity of the formulation, the $\boldsymbol{\nabla}$ terms describe that the variables vary through space. Here the variables that vary in space are simplified to a single function defined by f to clarify the use of the Lagrangian total derivative. The process of reduction is shown below.

The first term $\boldsymbol{\nabla}(\phi_\alpha \rho_f v_s)$ is considered within the solid continuum only as the soil skeleton does not deform with varying fluid density or porosity from the perspective of fluid only as shown in equation 59.

$$\frac{df_s(\phi_s \rho_f \boldsymbol{v}_s)}{dt} = \frac{f_s(\phi_\alpha \rho_f \boldsymbol{v}_s)}{dt} + \frac{d_s \rho_f}{dt}\frac{d_\alpha f_s(\phi_\alpha \rho_f \boldsymbol{v}_\alpha)}{d\rho_f} \tag{59}$$

The second term $\boldsymbol{\nabla}(\rho \boldsymbol{v}_\alpha^r)$, with consideration that the soil skeleton does not deform within the fluid and varying is therefore independent of the two other function parameters as shown in equation 60.

$$\frac{d_\alpha f_\alpha(\rho \boldsymbol{v}_\alpha^r)}{dt} = \frac{f_s(\rho \boldsymbol{v}_\alpha^r)}{dt} + \frac{d_\alpha \rho_f}{dt}\frac{f_\alpha(\rho \boldsymbol{v}_\alpha^r)}{d\rho_f} \tag{60}$$

Then we consider the third term of equation of in both 57 in terms of the fluid: shown in equation 61 and in terms of the soil skeleton: shown in equation 62.

$$\frac{df_\alpha(\phi_\alpha \rho_f)}{dt} = \frac{df_\alpha(\phi_\alpha \rho_f)}{dt} + \frac{df_\alpha(\phi_\alpha)}{dt}\frac{df_\alpha(\phi_\alpha \rho_f)}{d\phi} + \frac{df_\alpha(\rho_f)}{dt}\frac{df_\alpha(\phi_\alpha \rho_f)}{d\rho_f} \tag{61}$$

$$\frac{df_s(\phi_\alpha \rho_f)}{dt} = \frac{df_s(\phi_\alpha \rho_f)}{dt} + \frac{df_s(\phi_\alpha)}{dt}\frac{df_s(\phi_\alpha \rho_f)}{d\phi} + \frac{df_s(\rho_f)}{dt}\frac{df_s(\phi_\alpha \rho_f)}{d\rho_f} \tag{62}$$

Equations (60-62) become equations (63-66):

$$\frac{df(\phi_\alpha \rho_f v_s)}{dt} = \phi_\alpha \rho_f \frac{f(v_s)}{dt} \tag{63}$$

$$\frac{df(\rho_f v_\alpha)}{dt} = \rho_f \frac{f(\boldsymbol{v}_\alpha)}{dt} \tag{64}$$

$$\frac{df_\alpha(\phi_\alpha \rho_f)}{dt} = \phi_\alpha \frac{df_\alpha(\rho_f)}{dt} \tag{65}$$

$$\frac{df_s(\phi_\alpha \rho_f)}{dt} = \rho_f \frac{df_s(\phi_\alpha)}{dt} \tag{66}$$

Equations 64- 66 come together to model the behaviour throughout the model in terms of fluid and soil skeleton velocity. These equations state that soil/rock skeleton velocity i.e. continuum deformation is independent of fluid density and porosity. Porosity is also independent of fluid density as demonstrated in equation 67.

$$-\rho_f \boldsymbol{\nabla} v_\alpha^r = \frac{\phi_\alpha d_\alpha \rho_f}{dt} + \rho_f \frac{d_s \phi_\alpha}{dt} + \phi_\alpha \rho_f \boldsymbol{\nabla} v_s + (-1)^\alpha \boldsymbol{\Omega} = 0 \tag{67}$$

To consider the change in fluid density change with time in a more appropriate manner, fluid density is considered with the change in fluid pressure over time, see equation 68.

$$\frac{d_\alpha \rho_f}{dt} = \rho_f c_f \frac{d_s p_\alpha}{dt} \tag{68}$$

where c_f is the compressibility of the considered fluid. To remove the absolute continuum velocity term v_s, the change in continuum volume over time is considered in terms of continuum velocity, as shown in equation 69.

$$\frac{1}{V_{total}} \frac{d_s(V_{total})}{dt} = \boldsymbol{\nabla} v_s \tag{69}$$

and considering equation 70 the definition of porosity:

$$\frac{d_s\phi_s}{dt} = \frac{1}{V_{total}}(\frac{d_sV_\alpha}{dt} - \phi_\alpha\frac{d_sV_{total}}{dt}) \tag{70}$$

Substituting equation 68, 70 and 69 into equation 67 and expanding α sub scripted terms for extra clarity, describing the contribution of porous and fracture domain to the global equations yields equation 71:

$$\rho_f\boldsymbol{\nabla}\frac{k_\alpha}{\mu_f(\boldsymbol{\nabla}\boldsymbol{p}_\alpha + \rho_f\boldsymbol{g})} = \phi_1\rho_f c_f\frac{(\boldsymbol{\nabla}d_s\boldsymbol{p}_1)}{dt} + \phi_2\rho_f c_f\frac{\boldsymbol{\nabla}d_s(\boldsymbol{p}_2)}{dt} + \frac{1}{V_{total}}\frac{\boldsymbol{\nabla}d_sV_\alpha}{dt} + \boldsymbol{(-1)^\alpha\Omega} \tag{71}$$

The flow framework defined in equation 71 describes flow in both regions; porous and fractured, these equations have been separated to model each flow separately but still coupled as shown in equation 90 and 91 with the structural component shown in equation 89.

Effective stress $\boldsymbol{\alpha}$ terms are used to improve readability of the equations and $(-1)^\alpha\boldsymbol{\Omega}$ has been replaced with the term: $\boldsymbol{\gamma}(\mathbf{p}_1 - \mathbf{p}_2)$ to more clearly demonstrate the leakage concept used where $\boldsymbol{\gamma}$ is a constant leakage term, acting only on the boundary between the porous and the fractured regions. In the applied model it is important to note that the $\boldsymbol{\gamma}$ term develops with fracture/hydrofracture propagation, always acting only on the boundary between the fractured and porous zones, controlling the coupling. Therefore, the leak off coefficient has a scalar value for each element used. Equation 71 can be written as shown in the equation 72, where the volume strain component $\frac{\boldsymbol{\nabla}d_sV_{total}}{dt}$ is described in terms of volumetric strain: $\frac{d\epsilon_v}{dt}$.

$$\rho_f\boldsymbol{\nabla}\frac{\boldsymbol{k}_\alpha}{\mu_f(\boldsymbol{\nabla}\boldsymbol{p}_\alpha + \rho_f\boldsymbol{g})} = \phi_1\rho_f c_f\frac{(\boldsymbol{\nabla}d_sp_1)}{dt} + \phi_2\rho_f c_f\frac{\boldsymbol{\nabla}d_s(\boldsymbol{p}_2)}{dt} + \frac{\boldsymbol{\nabla}d_s\epsilon_v}{dt} + \boldsymbol{\nabla}\gamma(\boldsymbol{p}_1 - \boldsymbol{p}_2) \tag{72}$$

In which the leakage term is defined as $\boldsymbol{\gamma}(\boldsymbol{p}_1 - \boldsymbol{p}_2) = \Omega$.

$$\boldsymbol{\nabla}\frac{\boldsymbol{k}_\alpha}{\mu_f(\boldsymbol{\nabla}\boldsymbol{p}_\alpha + \rho_f\boldsymbol{g})} = \phi_1\rho_f c_f\frac{(\boldsymbol{\nabla}d_s\boldsymbol{p}_1)}{dt} + \phi_2\rho_f c_f\frac{\boldsymbol{\nabla}d_s(\boldsymbol{p}_2)}{dt} + \frac{\boldsymbol{\nabla}d_s\epsilon_v}{dt} + \boldsymbol{\nabla}\gamma(\boldsymbol{p}_1 - \boldsymbol{p}_2) \quad (73)$$

With alpha terms introduced to simplify the coupled equation and $\frac{\boldsymbol{\nabla}d_s\epsilon_v}{dt}$ redefined as $\boldsymbol{\nabla}\boldsymbol{u}$, equation 73 can be re-written as equation 74 using compressibility to relate deformations to increase in fluid pressure.

$$\boldsymbol{\nabla}\Big[\frac{\mathbf{k}_\alpha}{\mu_f}(\mathbf{p}_1+\rho_f\mathbf{g})\Big] = -\alpha_1\boldsymbol{\nabla}\dot{\mathbf{u}}+\alpha_{11}\frac{\boldsymbol{\nabla}d_s(\boldsymbol{p}_1)}{dt}-\alpha_{12}\frac{\boldsymbol{\nabla}d_s(\boldsymbol{p}_2)}{dt}+\boldsymbol{\nabla}\gamma(\mathbf{p}_1-\mathbf{p}_2) \quad (74)$$

Then by transforming the $\frac{d_s(\boldsymbol{p}_1)}{dt}$ terms into time dependent spatial matrix forms, equations 75 - 77 are formed.

$$div[\mathbf{C}_{ijkl}\boldsymbol{\nabla}\dot{\mathbf{u}} + \alpha_1\dot{\mathbf{p}}_1\boldsymbol{\delta} + \alpha_2\dot{\mathbf{p}}_2\delta] + \dot{\boldsymbol{F}_{\boldsymbol{m}}} = 0 \quad (75)$$

$$\boldsymbol{\nabla}\Big[\frac{\mathbf{k}_1}{\mu_f}(\mathbf{p}_1 + \rho_f\mathbf{g})\Big] = -\alpha_1\boldsymbol{\nabla}\dot{\mathbf{u}} + \alpha_{11}\dot{\mathbf{p}}_1 - \alpha_{12}\dot{\mathbf{p}}_2 + \boldsymbol{\gamma}(\mathbf{p}_1 - \mathbf{p}_2) \quad (76)$$

$$\boldsymbol{\nabla}\Big[\frac{\mathbf{k}_2}{\mu_f}(\mathbf{p}_2 + \rho_f\mathbf{g})\Big] = -\alpha_2\boldsymbol{\nabla}\dot{\mathbf{u}} + \alpha_{22}\dot{\mathbf{p}}_2 - \alpha_{21}\dot{\mathbf{p}}_1 + \boldsymbol{\gamma}(\mathbf{p}_2 - \mathbf{p}_1) \quad (77)$$

where $\boldsymbol{\delta} = [1, 1, 1, 0, 0, 0]^\intercal$, $\mathbf{g}$ is the gravity vector, $\mathbf{p}_i$ are the pressure matrices, $\dot{\boldsymbol{F}_{\boldsymbol{m}}}$ is the matrix of forces (including all considered mechanical forces) and ρ_f is the fluid density.

$\boldsymbol{\delta} = [1, 1, 1, 0, 0, 0]^\intercal$ describes that the fluid pressure only has a direct effect on other pressures and that only through the α and γ terms where the fluid is coupled with the deformation aspect of the model.

$$\boldsymbol{\nabla}' = \begin{bmatrix} \frac{\delta}{\delta x} & 0 & 0 \\ 0 & \frac{\delta}{\delta y} & 0 \\ 0 & 0 & \frac{\delta}{\delta z} \\ \frac{\delta}{\delta y} & \frac{\delta}{\delta x} & 0 \\ 0 & \frac{\delta}{\delta z} & \frac{\delta}{\delta y} \\ \frac{\delta}{\delta z} & 0 & \frac{\delta}{\delta x} \end{bmatrix}$$

Equation 75 describes the behaviour for the soil skeleton, equations 76 and 77 describe the changes in pore and fracture pressure respectively. Equation 75 describes the soil skeleton. The first term is a typical continuum mechanics description with the compliance matrix, relating displacements to internal stresses, the derivation of which is showcased in chapter 2. The second and third term describe the effect of pore and fracture pressures on the soil skeleton. Terms α_1 and α_2 are a ratio of effective stress created by fluid pressure. The lower the corresponding alpha the less effect a pressure has on the effective stress within the material and resulting mechanical deformation produced.

When considering the constants of this equation it is important to realise the designation is in a sparse format. The dual porosity model considers two zones which can be stand alone or overlapping. In the hydrofracture algorithm the initial steps designates resources to discretisation of the crack region. The points contained within the crack region would be assigned a non-zero value for α_2 and a zero value for α_1 and the other alpha terms, vice versa for the porous region surrounding the outlying points. The boundary of the two regions is where the leakage parameter is present, as this is where leaking can occur from fracture pressure to porous pressure or vice versa.

The fluid framework was originally used to model soils with pores and micro fractures overlaid, here the model is re-purposed to consider the two zones separate only overlapping at the boundary between fractured and porous media.

In the applied equations porosity is maintained as a constant. Void changing with the application of damage representing fracture propagation; therefore a more thorough description of change in porosity is required to define the porosity development with fracture development, this is shown in equations 78 - 79.

$$\phi_i(D) = \quad \phi_2, \qquad if D = 0.1 \tag{78}$$

$$\phi_i(D) = \quad \phi_1 \qquad otherwise \tag{79}$$

where $\phi_i(D)$ is a general description of porosity and varies with the condition of the continuum determined by: D the damage which in this model can vary from element to element. The coupling coefficients were originally derived in terms of compressibility of the two zones and transition, described here by equations: 80-84.

$$\alpha_1 = c_p/D + \phi_1 c_f \tag{80}$$

$$c = \frac{1}{K_{bulk} D} \tag{81}$$

$$\alpha_2 = c + \phi_2 c_f \tag{82}$$

α_1 describes the compressibility of the porous system, or the material properties before any damage/hydrofracture all with units N/m, relating deformation to change in fluid pressure. As hydfrofracture progress and the damage variable increases so to, does the compressibility of a material. This can be more clearly described in equation 81 while ignoring the effects of fluid compressibility.

$$\alpha_{12} = \alpha_{21} = (\alpha_1 \alpha_2) \tag{83}$$

$$\alpha_{ii} = \phi_i c_f + \alpha_{12} \tag{84}$$

where c_p is the compressibility of the porous media, c is the compressibility of the fractured system, ϕ_i is the porosity in the pore blocks or fracture network.

Equations 80 - 84 are the proposed models primary coupling terms. α_1 and α_2 showcase each materials relative compressibility c_f is included for completeness, only playing a minor role in this thesis.

The equations described here for α terms aid to described the coupling of fluid to the soil skeleton and vice a versa. With the dual porosity model coupling fracture and porous zones separately to the mechanical medium it is important that the two are distinguished and the transition is accounted for. The linear damage model as described in equation 81 allows this.

The compressibility of a material can be calculated from the inverse of the bulk modulus of a material as shown in equation 85.

$$c = \frac{1}{K_{bulk}} \tag{85}$$

As such the typical compressibility magnitude for a given rock is $10^{-6} mm^2/N$.

As prior mentioned the α terms used in the dual porosity model have a different value, depending on zone designation. In this proposed methodology the variable which controls zone designation is the damage variable. When the damage variable is lowest 0.1, then the zone is purely fractured varying only fracture flow, when the damage variable is one then the flow is only porous.

The porosity represents the pores within an element, assumed to be numerous, evenly dispersed and when pressurised, distribute the fluid pressure evenly.

Fractures will be primarily void; this means that the fluid pressure and fluid compressibility will be relied upon for mechanical strength in water filled cracks.

4.1.1 Spatial discretisation

The following steps describes the spatial discretisation of the global equations, later shown in equations 89 - 91.

Equations 86 - 88 can be compartmentalised into a form suitable for finite element

$$\nabla'^T[\mathbf{C}_{ijkl}\nabla\dot{\mathbf{u}}] + \alpha_1\nabla^T\dot{\mathbf{p}}_1\boldsymbol{\delta} + \alpha_2\nabla^T\dot{\mathbf{p}}_2\delta + \dot{\mathbf{F}} = 0 \tag{86}$$

$$\alpha_1\nabla'\dot{\mathbf{u}} - \alpha_{11}\dot{\mathbf{p}}_1 + \alpha_{12}\dot{\mathbf{p}}_2 + \nabla^T\Big[\frac{\mathbf{k}_1}{\mu_f}(\mathbf{p}_1 + \rho_f\mathbf{g})\Big] - \boldsymbol{\gamma}(\mathbf{p}_1 - \mathbf{p}_2) = 0 \tag{87}$$

$$\alpha_2\nabla'\dot{\mathbf{u}} - \alpha_{22}\dot{\mathbf{p}}_2 + \alpha_{21}\dot{\mathbf{p}}_1 + \nabla^T\Big[\frac{\mathbf{k}_2}{\mu_f}(\mathbf{p}_2 + \rho_f\mathbf{g})\Big] - \boldsymbol{\gamma}(\mathbf{p}_2 - \mathbf{p}_1) = 0 \tag{88}$$

Galerkin's weighted residual method is used to estimate the solution of the global equations, applying weighted shape leads to:

$$\int_\Omega(\nabla'^T[\mathbf{C}_{ijkl}\nabla\dot{\mathbf{u}}] + \alpha_1\nabla^T\dot{\mathbf{p}}_1\boldsymbol{\delta} + \alpha_2\nabla^T\dot{\mathbf{p}}_2\delta + \dot{\mathbf{F}})d\Omega = 0 \tag{89}$$

$$\int_\Omega(\alpha_1\nabla'\dot{\mathbf{u}} - \alpha_{11}\dot{\mathbf{p}}_1 + \alpha_{12}\dot{\mathbf{p}}_2 + \nabla^T\Big[\frac{\mathbf{k}_1}{\mu_f}(\mathbf{p}_1 + \rho_f\mathbf{g})\Big] - \gamma(\mathbf{p}_1 - \mathbf{p}_2))d\Omega = 0 \tag{90}$$

$$\int_\Omega(\alpha_2\nabla'\dot{\mathbf{u}} - \alpha_{22}\dot{\mathbf{p}}_2 + \alpha_{21}\dot{\mathbf{p}}_1 + \nabla^T\Big[\frac{\mathbf{k}_2}{\mu_f}(\mathbf{p}_2 + \rho_f\mathbf{g})\Big] - \gamma(\mathbf{p}_2 - \mathbf{p}_1))d\Omega = 0 \tag{91}$$

where Ω represents the continuum that the global equations govern. Where the approximate solutions are estimated by 92-93

$$\tilde{\mathbf{u}} = [\mathbf{N}]\mathbf{u} \tag{92}$$

$$\tilde{\mathbf{p}}_i = [\mathbf{N}]\mathbf{p}_i \tag{93}$$

where $\mathbf{N}$ are shape functions. Then by rearranging and applying Green's theorem the equations 89, 90 and 91 become:

$$\begin{aligned} -\int_\Omega [\nabla\mathbf{N}]^\intercal[\mathbf{C}_{ijkl}]\dot{\mathbf{u}}d\Omega + \int_\Gamma [\mathbf{N}]^\intercal[\mathbf{C}_{ijkl}]\dot{\mathbf{u}}d\Gamma \\ -\int_\Omega \alpha_1[\nabla\mathbf{N}]^\intercal\delta[\mathbf{N}]\dot{\mathbf{p}}_1 d\Omega \int_\Gamma \alpha_1[\mathbf{N}]^\intercal\delta[\mathbf{N}]\dot{\mathbf{p}}_1 d\Gamma \\ \int_\Omega \alpha_2[\nabla\mathbf{N}]^\intercal\delta[\mathbf{N}]\dot{\mathbf{p}}_2 d\Omega \int_\Gamma \alpha_2[\mathbf{N}]^\intercal\delta[\mathbf{N}]\dot{\mathbf{p}}_2 d\Gamma + \int_\Omega [\nabla\mathbf{N}]^\intercal\dot{\mathbf{F}}d\Omega = 0 \end{aligned} \tag{94}$$

$$\begin{aligned} \int_\Omega \alpha_1[\mathbf{N}]^\intercal\delta^\intercal[\nabla\mathbf{N}]\dot{\mathbf{u}}d\Omega - \int_\Omega \alpha_{11}[\mathbf{N}]^\intercal[\mathbf{N}]\dot{\mathbf{p}}_1 d\Omega + \int_\Omega \alpha_{12}[\mathbf{N}]^\intercal[\mathbf{N}]\dot{\mathbf{p}}_2 d\Omega + \\ \int_\Omega [\nabla\mathbf{N}]^\intercal\frac{[\mathbf{k}_1]}{\mu_f}[\nabla\mathbf{N}]^\intercal\mathbf{p}_1 d\Omega + \int_\Gamma [\mathbf{N}]^\intercal[\frac{[\mathbf{k}_1]}{\mu_f}\mathbf{p}_1][\nabla\mathbf{N}]\mathbf{p}_1 d\Gamma - \\ \int_\Omega \gamma[\mathbf{N}]^\intercal[\mathbf{N}]\mathbf{p}_1 d\Omega + \int_\Omega \gamma[\mathbf{N}]^\intercal[\mathbf{N}]\mathbf{p}_2 d\Omega = 0 \end{aligned} \tag{95}$$

$$\begin{aligned} \int_\Omega \alpha_2[\mathbf{N}]^\intercal\delta^\intercal[\nabla\mathbf{N}]\dot{\mathbf{u}}d\Omega - \int_\Omega \alpha_{22}[\mathbf{N}]^\intercal[\mathbf{N}]\dot{\mathbf{p}}_2 d\Omega + \int_\Omega \alpha_{21}[\mathbf{N}]^\intercal[\mathbf{N}]\dot{\mathbf{p}}_1 d\Omega + \\ \int_\Omega [\nabla\mathbf{N}]^\intercal\frac{[\mathbf{k}_2]}{\mu_f}[\nabla\mathbf{N}]^\intercal\mathbf{p}_2 d\Omega + \int_\Gamma [\mathbf{N}]^\intercal\frac{[\mathbf{k}_2]}{\mu_f}[\nabla\mathbf{N}]\mathbf{p}_1 d\Gamma - \\ \int_\Omega \boldsymbol{\gamma}[\mathbf{N}]^\intercal[\mathbf{N}]\mathbf{p}_1 d\Omega + \int_\Omega \boldsymbol{\gamma}[\mathbf{N}]^\intercal[\mathbf{N}]\mathbf{p}_2 d\Omega = 0 \end{aligned} \tag{96}$$

For simplicity, mechanical edger forces are left out and boundary conditions are applied simplifying the equations to:

$$\begin{aligned} -\int_\Omega [\nabla\mathbf{N}]^\intercal[\mathbf{C}_{ijkl}]\dot{\mathbf{u}}d\Omega - \int_\Omega \alpha_1[\nabla\mathbf{N}]^\intercal\delta[\mathbf{N}]\dot{\mathbf{p}}_1 d\Omega \\ \int_\Omega \alpha_2[\nabla\mathbf{N}]^\intercal\delta[\mathbf{N}]\dot{\mathbf{p}}_2 d\Omega = \int_\Omega [\nabla\mathbf{N}]^\intercal\dot{\mathbf{F}}d\Omega \end{aligned} \tag{97}$$

$$\int_\Omega \alpha_1[\mathbf{N}]^\intercal \delta^\intercal [\nabla \mathbf{N}]\dot{\mathbf{u}} d\Omega - \int_\Omega \alpha_{11}[\mathbf{N}]^\intercal[\mathbf{N}]\dot{\mathbf{p}}_1 d\Omega$$
$$+ \int_\Omega \alpha_{12}[\mathbf{N}]^\intercal[\mathbf{N}]\dot{\mathbf{p}}_2 d\Omega - \int_\Omega [\nabla \mathbf{N}]^\intercal \frac{[\mathbf{k}_1]}{\mu_f}[\nabla \mathbf{N}]^\intercal \mathbf{p}_1 d\Omega \tag{98}$$
$$- \int_\Omega \boldsymbol{\gamma}[\mathbf{N}]^\intercal[\mathbf{N}]\mathbf{p}_1 d\Omega + \int_\Omega \boldsymbol{\gamma}[\mathbf{N}]^\intercal[\mathbf{N}]\mathbf{p}_2 d\Omega = \int_\Gamma [\mathbf{N}]^\intercal \mathbf{q}_1 d\Gamma$$

$$\int_\Omega \alpha_1[\mathbf{N}]^\intercal \delta^\intercal [\nabla \mathbf{N}]\dot{\mathbf{u}} d\Omega - \int_\Omega \alpha_{22}[\mathbf{N}]^\intercal[\mathbf{N}]\dot{\mathbf{p}}_2 d\Omega$$
$$+ \int_\Omega \alpha_{21}[\mathbf{N}]^\intercal[\mathbf{N}]\dot{\mathbf{p}}_1 d\Omega - \int_\Omega [\nabla \mathbf{N}]^\intercal \frac{[\mathbf{k}_2]}{\mu_f}[\nabla \mathbf{N}]^\intercal \mathbf{p}_1 d\Omega \tag{99}$$
$$- \int_\Omega \boldsymbol{\gamma}[\mathbf{N}]^\intercal[\mathbf{N}]\mathbf{p}_1 d\Omega + \int_\Omega \boldsymbol{\gamma}[\mathbf{N}]^\intercal[\mathbf{N}]\mathbf{p}_2 d\Omega = \int_\Gamma [\mathbf{N}]^\intercal \ \mathbf{q}_2 d\Gamma$$

After unit substitution for simplification, the equations can be put into matrix format to appear as shown in equations 100 - 105.

In the model used, the two flow models are related via relative compressibility terms and a leakage term. This means that the compressible nature of fractured media has to be known but this can be found from triaxial tests on damaged rock. By referencing the strength of the two flow models, the model is capable of determining how each medium will deform according to internal pore and fracture pressures.

$$\begin{bmatrix} [\mathbf{K}] & \alpha_1[\mathbf{C}_c] & \alpha_2[\mathbf{C}_c] \\ \alpha_1[\mathbf{C}_c]^\intercal & -\alpha_{11} - \beta\Delta t([\mathbf{H}_1] + \gamma[\mathbf{M}]) & \alpha_{12}[\mathbf{M}] + \beta\Delta t[\mathbf{M}] \\ \alpha_2[\mathbf{C}_c]^\intercal & \alpha_{21}[\mathbf{M}] + \beta\Delta t\gamma[\mathbf{M}] & -\alpha_{22}[\mathbf{M}] - \beta\Delta t([\mathbf{H}_1] + \boldsymbol{\gamma}[\mathbf{M}]) \end{bmatrix} \begin{bmatrix} \Delta\mathbf{u} \\ \Delta\mathbf{p}_1 \\ \Delta\mathbf{p}_2 \end{bmatrix} =$$

$$= \begin{bmatrix} \Delta\mathbf{R}_f \\ 0 \\ 0 \end{bmatrix} + \Delta t \begin{bmatrix} 0 \\ (1-\beta)(\mathbf{Q}_1)_t + \beta((\mathbf{Q}_1)_{t+\Delta t} \\ (1-\beta)(\mathbf{Q}_2)_t + \beta((\mathbf{Q}_2)_{t+\Delta t} \end{bmatrix} + \Delta t \begin{bmatrix} 0 \\ (\mathbf{H}_1 + \gamma\mathbf{M})(\mathbf{p}_1)_t + \gamma\mathbf{M})(\mathbf{p}_2)_t \\ (\mathbf{H}_2 + \gamma\mathbf{M})(\mathbf{p}_2)_t + \gamma\mathbf{M})(\mathbf{p}_1)_t \end{bmatrix}$$

where the compliance tensor C_{ijkl}

$$\boldsymbol{C_{ijkl}} = \frac{\lambda}{J}\boldsymbol{\delta}_{ij}\boldsymbol{\delta}_{kl} + 2\frac{\mu - \lambda ln(J)}{J}\boldsymbol{\delta}_{ik}\boldsymbol{\delta}_{jl} \tag{100}$$

Mathematical mass matrix

$$[\boldsymbol{M}] = \int_{\Omega}[\mathbf{N}]^{\intercal}[\mathbf{N}]d\Omega \tag{101}$$

Coupling matrix

$$[\mathbf{C}_c] = \int_{\Omega}[\mathbf{B}_2]^{\intercal}[\mathbf{N}]d\Omega \tag{102}$$

Permeability matrix

$$[\mathbf{H}_i] = \int_{\Omega}[\boldsymbol{B_3}]^{\intercal}\frac{[\mathbf{k}_i]}{\mu_f}[\boldsymbol{B_3}]d\Omega \tag{103}$$

Internal Force matrix

$$[\mathbf{R}_f] = \int_{\Omega}[\boldsymbol{B_3}]^{\intercal}\sigma[\boldsymbol{B_3}]d\Omega \tag{104}$$

Boundary flow matrix

$$[\mathbf{Q}_i] = -\int_{\Gamma}[\mathbf{N}]\frac{\mathbf{k}_i}{\mu_f}[\nabla\mathbf{N}]\mathbf{p}_i d\Gamma \tag{105}$$

Where the matrix terms $\mathbf{B}_1$, $\mathbf{B}_2$, $\mathbf{B}_3$ are the derivatives of respective shape functions, demonstrated below for plane strain problems. $\mathbf{M}$ is the mass matrix, $\mathbf{k}_i$ is the Darcy permeability matrix (i=1 for pore system, i=2 for fracture system), $\mathbf{N}$ shape function matrix, $\Delta\mathbf{R}$ is the loading matrix, $\mathbf{Q}_i$ is the pressure load matrix and $\mathbf{C}_{ijkl}$ is the compliance matrix. μ_f is dynamic viscosity, t is time, β is the time finite difference interpolation factor, α_{ii} are the coupling constants.

$$\boldsymbol{B_1} = \begin{bmatrix} \frac{\delta\mathbf{N}_1}{\delta x_1} & 0 & \dots \\ 0 & \frac{\delta\mathbf{N}_1}{\delta y_1} & \dots \\ \frac{\delta\mathbf{N}_1}{\delta x_1} & \frac{\delta\mathbf{N}_1}{\delta y_1} & \dots \end{bmatrix}$$

$$\boldsymbol{B_2} = \begin{bmatrix} \frac{\delta \mathbf{N}_1}{\delta x_1} & \frac{\delta \mathbf{N}_1}{\delta y_1} & \dots \end{bmatrix}$$

$$\boldsymbol{B_3} = \begin{bmatrix} \frac{\delta \mathbf{N}_1}{\delta x_1} & \dots \\ \frac{\delta \mathbf{N}_1}{\delta y_1} & \dots \end{bmatrix}$$

4.2 Re-visiting minimisation

The procedure for calculating energy is similar to that described in chapter 3, however the main difference is that the fluid pressures are introduced as additional driving forces for fracture, complicating the minimisation procedure.

The Griffith fracture criteria, a global minimum of energy does not apply fluid flow influenced by fracture propagation and resulting internal deformations. Therefore the application of this methodology should aim to minimise only mechanical energy types: elastically stored and fracture as shown by equation 106.

$$\boldsymbol{E}_i(\boldsymbol{F}(\boldsymbol{x}(\boldsymbol{p_1^n}, \boldsymbol{p_2^n}), D) = min \int_\Omega \boldsymbol{W}(\boldsymbol{F}(\boldsymbol{x}(\boldsymbol{p_1^n}, \boldsymbol{p_2^n})))(D_0^2 + k_e) d\Omega + \boldsymbol{R}_0 \int_\Omega \boldsymbol{H}^{N-1}(D_0) \tag{106}$$

where $\boldsymbol{E}_i$ is energy, $\boldsymbol{F}$ is the deformation gradient, $\boldsymbol{x}(\boldsymbol{p_1^n}, \boldsymbol{p_2^n})$ is the deformation caused by the fluid pressure initially calculated for previous iteration and fracture geometry, $\boldsymbol{W}$ is mechanical work, D_0 is initial damage, k_e is a integration term, Ω is the considered continuum, $\boldsymbol{H}^{N-1}$ is the Hausdorff measure of fracture and $\boldsymbol{R}_0$ is the fracture energy term, prescribed on an element by element basis depending on the material modelled.

Then similarly to the old minimisation algorithm the time steps where elements are damaged the time step must be reset with the damage affected variables remaining, represented by equation 107, the pressure is still maintained and not progressing.

$$\begin{aligned} \boldsymbol{E}_i(\boldsymbol{F}(\boldsymbol{x_0}(\boldsymbol{p_1^n}, \boldsymbol{p_2^n}))), \boldsymbol{D}) = min \int \Omega \boldsymbol{W}(\boldsymbol{F}(\boldsymbol{x_0}(\boldsymbol{p_1^n}, \boldsymbol{p_2^n})))(\boldsymbol{D}^2 + k_e) d\Omega \\ + \boldsymbol{R}_0 \int \Omega \boldsymbol{H}^{N-1}(\boldsymbol{D}) \end{aligned} \tag{107}$$

Once the minimal energy profile for the initial pressure is calculated, the pressure can be developed to accommodate the new fracture geometry as

shown in equation 108.

$$\boldsymbol{E}_i(\boldsymbol{F}(\boldsymbol{x}(\boldsymbol{p_1 0}^{\boldsymbol{n+1}}, \boldsymbol{p_2}^{\boldsymbol{n+1}}), \boldsymbol{D}) = min \int_\Omega \boldsymbol{W}(\boldsymbol{F}(\boldsymbol{x}(\boldsymbol{p_1}^{\boldsymbol{n+1}}, \boldsymbol{p_2}^{\boldsymbol{n+1}})))(D_0^2 + k_e)d\Omega \\ + \boldsymbol{R}_0 \int_\Omega \boldsymbol{H}^{N-1}(D_0) \tag{108}$$

where $\boldsymbol{x}(\boldsymbol{p_1}^{\boldsymbol{n+1}}, \boldsymbol{p_2}^{\boldsymbol{n+1}})$ is the deformation caused by the fluid pressure initially calculated for previous iteration and fracture geometry.

$$\boldsymbol{E}_i(\boldsymbol{F}(\boldsymbol{x_0}(\boldsymbol{p_1}^{\boldsymbol{n+1}}, \boldsymbol{p_2}^{\boldsymbol{n+1}}))), \boldsymbol{D}) = \\ min \int \Omega \boldsymbol{W}(\boldsymbol{F}(\boldsymbol{x_0}(\boldsymbol{p_1}^{\boldsymbol{n+1}}, \boldsymbol{p_2}^{\boldsymbol{n+1}})))(\boldsymbol{D}^2 + k_e)d\Omega + \boldsymbol{R}_0 \int \Omega \boldsymbol{H}^{N-1}(\boldsymbol{D}) \tag{109}$$

The fracture geometry changes are not directly coupled to both the fluid pressure and deformation behaviour therefore many iterations through the solution can be required for accurate simulation of hydrofracture behaviour.

It is important to capture how fluid behaves at the tip of the hydrofracture, how the fluid can flow, when a hydrofracture propagates and how the flow conditions change. The resultant fluid lag must be considered to account for the additional forces and pressure accumulating at the hydrofracture tip and their possible effect on behaviour.

How far along a crack can deliver pressure depends on the permeability increase from the tip changing from porous to fracture, during fracture [47].

Consider Figure 44, an internal crack loaded with fluid. As the crack tips extend at the end of a time step the permeability is enhanced, an enhancement that must be considered during time steps. Therefore in order to calculate the hydrofracture procedure accurately, the time step must be repeated to account for the increase in permeability at the tip during calculation

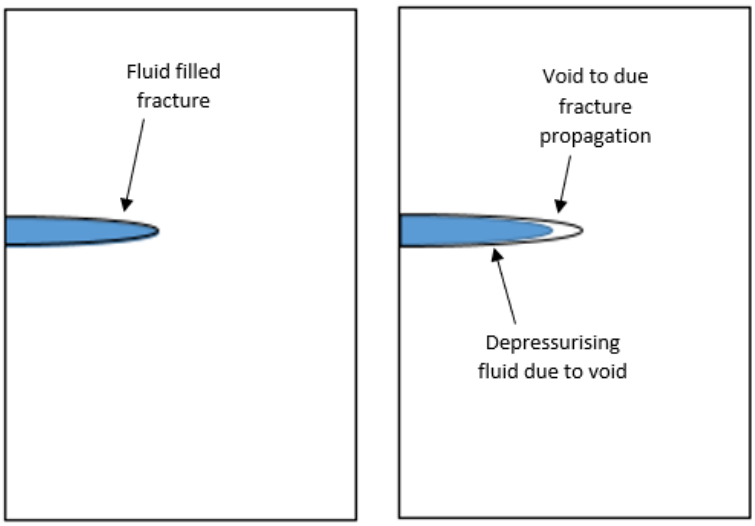

Figure 44: Example of fluid lag

This consideration allows the model to account for fluid lag, when the fracture tip is extended due to the damage process the fluid tip cannot be fully pressurised immediately, this allows for the tip to suffer shrinkage due to confining pressure being momentarily greater than the fluid pressure inside of the fracture, effectively capturing the effect of fluid lag.

4.2.1 Hydrofracture algorithm

A flowchart showing the process the code and implementation follows is shown in Algorithm 2.

Algorithm 2 Hydro-fracture procedure

Specify run time t_{full}
$j = 0$
Create model geometry
Interpret geometry to mesh using Delaunay triangulation algorithm [101]
Initialise damage variable for starting crack
Initialise material parameters on element by element basis; μ, ν, λ, R_0, $\boldsymbol{k_1}$, $\boldsymbol{k_2}$,α_1, α_2, α_{12}, α_{21}, α_{11}, α_{22} and γ
Initialise pore and fracture pressure on continuum
Initialise boundary conditions
while $t < t_{full}$ **do** ▷ run time of simulation
    Calculate mass matrix
    Calculate permeability matrices
    $[\boldsymbol{M}] = \int_\Omega [\mathbf{N}]^\intercal [\mathbf{N}] d\Omega$
    For n=1:3
    Calculate coupling matrices $[\mathbf{C}_c] = \int_\Omega [\mathbf{B}_2]^\intercal [\mathbf{N}] d\Omega$
    For j=1:3
    Calculate internal forces $[\mathbf{R}] = \int_\Omega [\boldsymbol{B_3}]^\intercal \sigma [\boldsymbol{B_3}] d\Omega$
    Calculate stiffness matrix $\boldsymbol{C_{ijkl}} = \frac{\lambda}{J}\boldsymbol{\delta}_{ij}\boldsymbol{\delta}_{kl} + 2\frac{\mu - \lambda ln(J)}{J}\boldsymbol{\delta}_{ik}\boldsymbol{\delta}_{jl}$
    $[\mathbf{H}_i] = \int_\Omega [\boldsymbol{B_3}]^\intercal \frac{[\mathbf{k}_i]}{\mu_f} [\boldsymbol{B_3}] d\Omega$
    Calculate internal forces
    Form global matrix and global force matrix
    Solve system of global equations for ΔU_j
    Calculate trial deformation gradients
    Calculate stored elastic energy
    $W = \frac{1}{2}\mu(I_c - 3) + \frac{1}{2}\lambda log(J)^2 - \mu log(J)$
    Check for fractures $W_e > K_{fratt}$
    $\Delta D_j = \min(\frac{W}{R_0}, 1)$
    Assign damage variable accordingly
    continue for(j)
    continue for(n)
    continue while

27: **continue for(j)**
28: **continue for(n)**
29: **continue while**
30: **if** $j == 0$ **then**
E_j^{tot}=total energy $j = j + 1$ reset deformations and fluid pressures goto line 9
31: **else**
32: **if** $E_j^{tot} >= E_{j-1}^{tot}$ **then**
33: $t = t + 1$
34: $j = 1$
35: Update deformations $\boldsymbol{U_t} = \boldsymbol{U_{t-1}} + \Delta \boldsymbol{U_{j-1}}$
36: Update pressures $\boldsymbol{p_t} = \boldsymbol{p_t} + \boldsymbol{\Delta p}$
37: Update damage $\boldsymbol{D}_t = \boldsymbol{D}_{t-1} - \Delta \boldsymbol{D}_{t-1}$
38: goto line 9
39: **else** reset deformations and fluid pressures $\boldsymbol{p_1^n}$ and $\boldsymbol{p_2^n}$ E_i^{tot}=total energy j=j+1
40: goto line 9
41: **for(j) end**
42: **end**
43: **End for(i)**
44: Redistribute permeabilities and leak off coefficient
45: Calculate total energy
46: **End for(n)**
47: **End while**

4.2.2 Time discretisation

A forward Euler, finite difference temporal approach is used to solve explicitly for pressure changes of time as shown in equations 110-111.

$$\int_{t}^{t+\Delta t} y(t)dt = [(1-\beta)y_t + \beta y_{t+\Delta t}] \tag{110}$$

where y is a temporal function as shown:

$$\Delta y = y_{t+\Delta t} - y \tag{111}$$

When β is used for the type of approximation used. When $\beta = 0$ forward interpolation is used, $\beta = 1$ for backwards and $\beta = 0.5$ for central interpolation, which is the most stable of the methods.

4.2.3 Fracture permeability

The permeability of fractures varies significantly between various scenarios, depending upon the fluid pressure, fracture size and roughness of the fracture walls. In this thesis the cubic law shown in equation 112 is used to model the flow with the aid of an equivalent permeability, shown in equation 113 [74].

$$q = \frac{h^2}{12\mu_f}\frac{dp}{dx} \tag{112}$$

where q is fluid flow, h is fracture width, μ_f is dynamic viscosity, p is pressure and x is a spatial coordinate. Equation 113 assumes two smooth parallel walls containing the fluid separated by a distance of h, fluid contained in a fully saturated environment with constant pressure gradient across the considered fracture walls. The cubic law is widely used in the flow of fluid within hydrofracture methodologies due to its reliance and theoretical basis.

$$k_2 = \frac{h^2}{12} \tag{113}$$

The volume change of damaged elements will be used here in place of the distance between the two plates [151] therefore as fractured element expand/

constrict the permeability, adjusting accordingly. The porous material is assumed to be still present in damaged elements for the purpose of conservation of mass, however a fracture is assumed to have opened in damaged elements. This presents an issue for elements that fracture due to compression, in this case the permeability is considered the same as the porous model up until the damaged element is expanded.

With a theoretical basis for fractured permeability there are less required variables for an applicable hydrofracture model

4.2.4 Matlab implementation

The proposed methodology for hydrofracture and the later introduced plastic methodology was coded using Matlab. The Matlab solvepde solver was used to solve the discretised global equations and fracture equations [101].

4.3 Summary

A Finite strain deformation framework has been derived for hydrofracture problems based on both the energy minimisation for the fracture component from Fracfort and Marigo and a dual porosity methodology adapted from Ma's work, adapting the model to account for both a sophisticated fracture methodology and fractures discrete from the considered porous domain. The methodology solves sets of partial differential equations using the Gauss reduction method in a simpler methodology allowing for performance gains when compared to other hydrofracture methodologies with the added benefit of requiring minimal input variables. The proposed methodology will now be verified using both pre-existent analytical, numerical and experimental results attempting to repeat the experiments with the proposed methodology.

5 Hydrofracture verifications

Whilst setting up a hydrofracture framework it is important to test the created model on each aspect of behaviour the framework is designed to capture. The following four verifications contain a consolidation problem, two numerical hydrofractures and an experimental hydrofracture. These verifications test the hydro-mechanical coupling, the integration of the damage model and the applicability of the model to hydrofracture problems.

5.1 Consolidation verification

For correct prediction of hydraulic fracture, pore pressure must be predicted correctly. To verify this component of the model a one dimensional test has been chosen from literature [130] where a generalised finite element method was compared to an analytical solution,. The solution to Terzaghi's one dimensional consolidation problem as shown in equations. 114-115. This particular verification did not require a second porous zone or the damage model and was hence disabled for this analysis.

For $T_v < T_c$:

$$p = \Sigma \frac{2q_c}{M_v^3 T_c} sin \frac{M_v z}{H_d} [1 - e^{(-M_v^2 T_v)}] \tag{114}$$

For $T_v > T_c$:

$$p = \Sigma \frac{2q_c}{M_v^3 T_c} \frac{sin(M_v z)}{H_d} e^{-M_v^2 T_v} [e^{-M_v^2 T_v} - 1] \tag{115}$$

where p is pore pressure, q_c is surcharge, H_d is drainage height, z is height of interest and M_v is the modulus of volume change. T_c and T_v are dimensionless time factors describing when loading begins. These variables are calculated in equations 116-120:

$$m_v = \frac{(1+v)(1-2v)}{E(1-v)} \tag{116}$$

Where E is the Young's modulus and ν is the Poisson's ratio.

$$M_v = \frac{(2m_v + 1)\pi}{2} \tag{117}$$

$$C_v = \frac{k}{m_v \rho_f} \tag{118}$$

$$T_v = \frac{C_v t}{H^2} \tag{119}$$

$$T_c = \frac{C_v t_c}{H^2} \tag{120}$$

In this test, a 10m by 1m column of soil is considered under a rapidly applied pressure of 1kPa as seen Figure 45. At quarter height intervals, the pore pressure was recorded over time, specifically the increase in pressure due to mechanical loading and mechanical coupling. After loading, consequent pressure dissipation resulting from drainage is also measured. The test was to capture consolidation behaviour and compare to the numerical and analytical results mentioned in [130]. The material properties used during this verification are reported in table 3.

Table 3: Material properties in consolidation test

Young's modulus	E	10000 MPa
Poisson's ratio	ν	0.2
Fracture strength	K_{Fratt}	inf
Porous permeability	k_1	$5 \times 10^{-8} m/s$
Fracture permeability	k_2	0
Coupling coefficient	α_1	1
Coupling coefficient	α_2	1
Coupling coefficient	α_{12}	0
Coupling coefficient	α_{21}	0
Leakage parameter	γ	0
Water density	ρ_f	$0 kg/m^3$

Note 1. Fluid density was considered as $0kg/m^3$ similar to reference to not incur any additional fluid pressure or deviate from compared data set.

Note 2. This particular verification did not require a second porous zone or the damage model active but were left in for clarity.

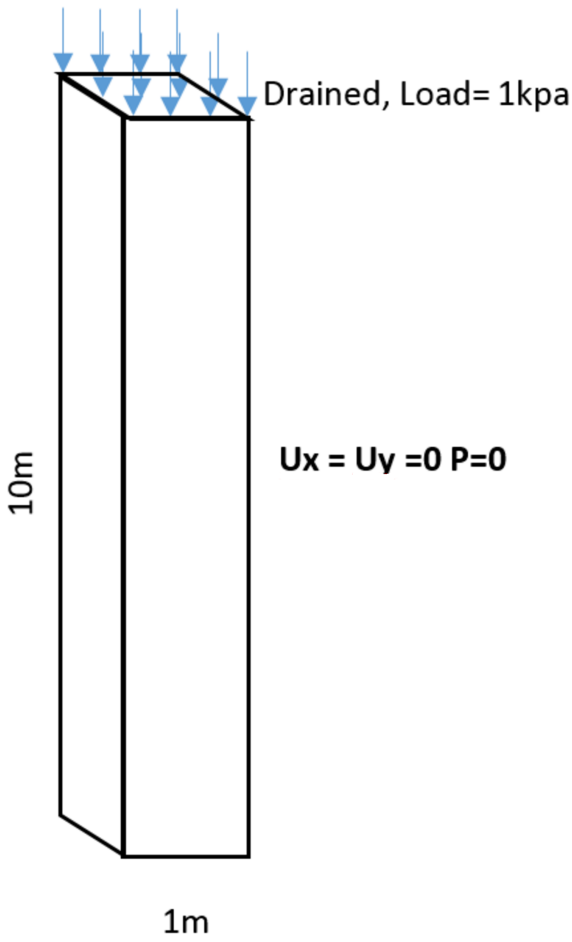

Figure 45: Schematic for one dimensional consolidation test

The load was applied then kept constant as shown in Figure 46.

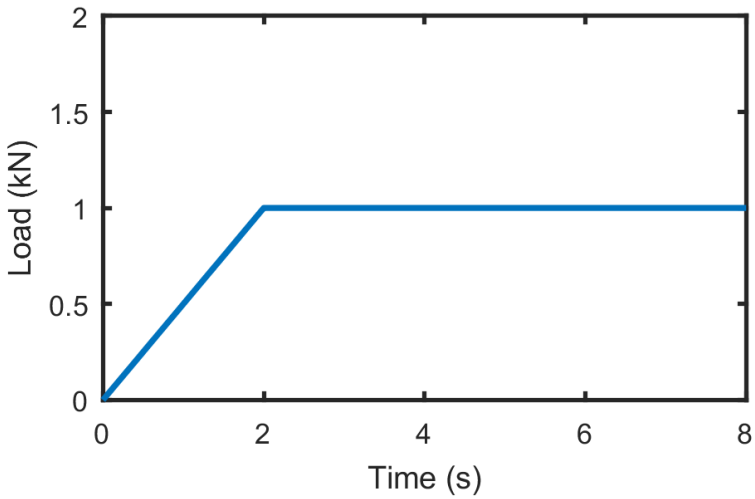

Figure 46: Graph showing the applied load during one dimensional consolidation test

The one-dimensional consolidation test starts off initially with zero pore pressure with fluid density set to $0kg/m^3$. A 1kPa load is then applied with the pore pressure response being monitored and shown in Figure 47. In Figure 47 each line represents the average pore pressure in the 10m tall sample at 25%, 50%, 75% and 100% height intervals. The pressure change corresponds to the 1kPa load and dissipates to become consolidated once more.

Algorithm 3 Hydro flow procedure

1: Specify run time t_{full}
2: Create model geometry
3: Interpret geometry to mesh using Delaunay triangulation algorithm [101]
4: Initialise material parameters; $\mu, \nu, \lambda, k_1, \alpha_1, \alpha_2, \alpha_{12}, \alpha_{21}, \alpha_{11}, \alpha_{22}, \gamma$
5: Initialise pore pressure on continuum
6: **while** $t < t_{full}$ **do** ▷ run time of simulation
7: Calculate stiffness matrix
$\boldsymbol{C_{ijkl}} = \frac{\lambda}{J}\delta_{ij}\delta_{kl} + 2\frac{\mu - \lambda ln(J)}{J}\delta_{ik}\delta_{jl}$
8: Calculate mass matrix
$[\boldsymbol{M}] = \int_\Omega [\mathbf{N}]^\intercal [\mathbf{N}] d\Omega$
9: Calculate internal forces
$[\mathbf{R}] = \int_\Omega [\boldsymbol{B_3}]^\intercal \sigma [\boldsymbol{B_3}] d\Omega$
10: Calculate Pore and fracture pressure matrix
11: $[\mathbf{H}_i] = \int_\Omega [\boldsymbol{B_3}]^\intercal \frac{[\mathbf{k}_i]}{\mu_f} [\boldsymbol{B_3}] d\Omega$
12: Calculate Coupling matrices
$[\mathbf{C}_c] = \int_\Omega [\mathbf{B}_2]^\intercal [\mathbf{N}] d\Omega$
13: Calculate Permeability matrices
$[\mathbf{H}_i] = \int_\Omega [\mathbf{B}_3]^\intercal \frac{[\mathbf{k}_i]}{\mu_f} [\mathbf{B}_3] d\Omega$
14: Form Global matrix and Global Force matrix
15: Solve system of Global equations for $\Delta \boldsymbol{u}$, $\Delta \boldsymbol{p_1}$ and $\Delta \boldsymbol{p_2}$
16: Update deformations, pore pressure and fracture pressure
17: Goto line 6
18: **end**

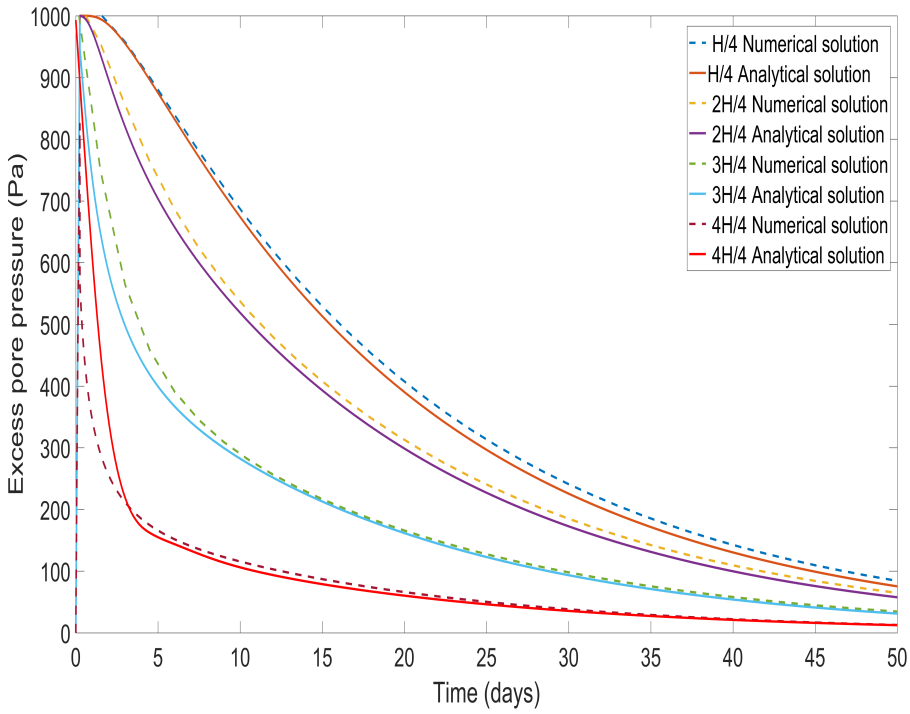

Figure 47: One dimensional graph showing pore pressure at various height intervals through the sample over time during the consolidation process

Figure 47 shows the model generated solution versus the analytical solution. The numerical results were obtained by averaging the pore pressures at the desired interval with all points 1% above and below, this explains the 100% pressure plots marginally underestimating the pressure due to the drained boundary condition represented by zero pressure at the top boundary. Figure 47 also shows the initial pressurisation stage on day 0.

The result compares to the analytical solution with favourable agreement despite typical finite deformation implementation [103], the pressure-mechanical aspect is less hindered due to the coupling on this aspect being simplistic in nature not accounting for changes in porosity. The coupled hydromechanics aspects behave as expected, the highest pressure drops occurring soon after the peak pressure. Pressure's rate of change reducing over time in the expected asymptotic manner, slowly approaching full equilibrium/ consolidation.

As well as checking the consolidation results over time according to equation 115 the theoretically predicted pressure distributions were also tested over several time stamps by varying the z variable. The results were close and show that proposed models' pressure components are working stable and accurate.

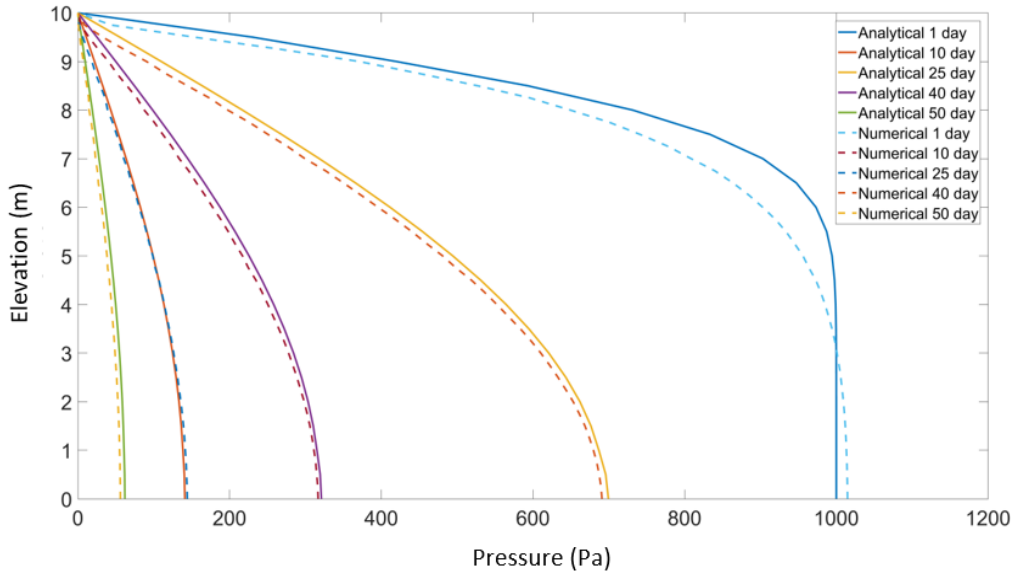

Figure 48: Pore pressure distributions through the one dimensional sample at various times

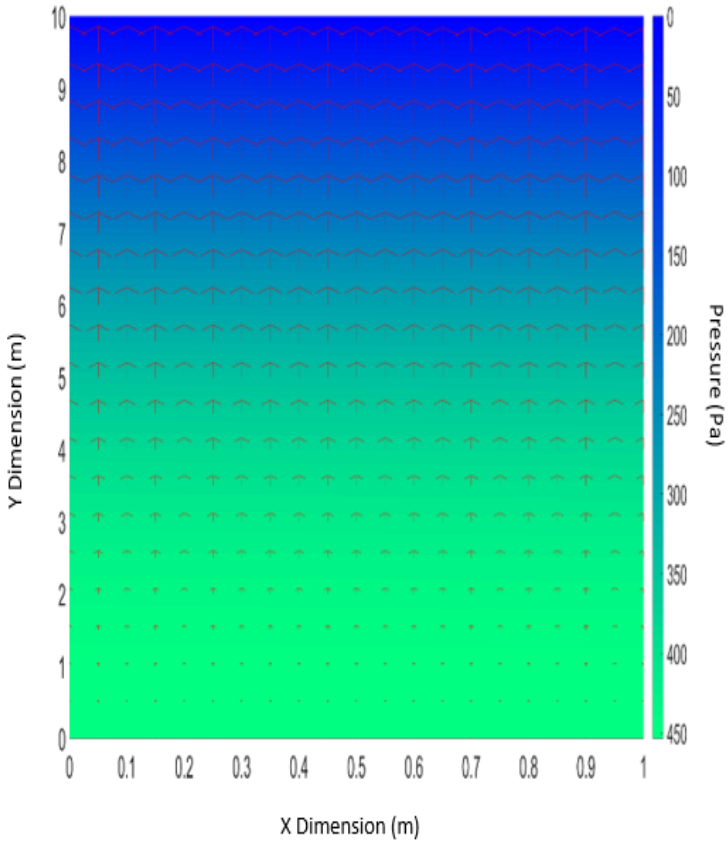

Figure 49: Consolidation snapshot with pressure and flow distributions

The equal flow distribution is further shown in Figure 49 at the 40 day mark. The pressure profiles back this up as shown in Figure 48, equal flow out of the sample as expected over time, here depicted by vertical arrows. The pressure disparity of 450Pa between the top and bottom show the flow of "water" out of the sample.

5.2 Hydrofracture verification

Data used in this penny hydrofracture verification of the model's fracture capabilities were sourced from [106]. The paper utilises a general finite element model (GFEM), similar to XFEM using local enrichment functions to capture fracture behaviour. The flow methodology utilised by [106] is similar to the proposed model; Darcy's model for porous flow.

The problem is a rectangular 3875 mm by 975 mm domain with crack dimensions 0.5mm thick, 180mm long in the centre of the sample modelled by fractured media, the damage value D set to 0.1 as shown in Figure 50.

Three segments A-A, B-B, C-C and D-D shown in Figure 50 are used in this verification to measure pressure plots. Plots to later compared to reference results to aid in validation.

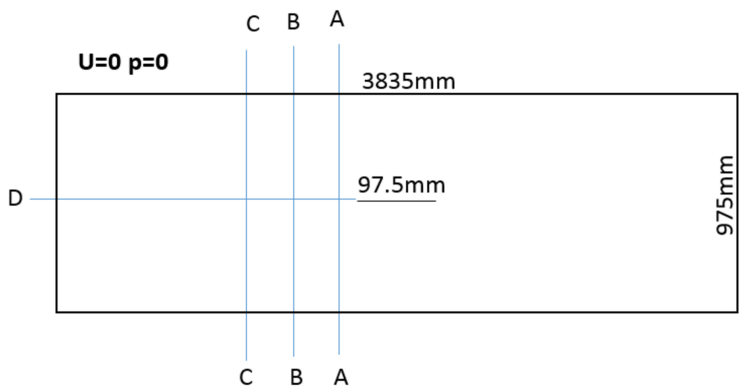

Figure 50: Schematic for pressured penny crack test

A corresponding pressure of 20 MPa, was applied and maintained in the crack via the fracture pressure matrix. The material properties used in the verification are shown in table 4. The permeability post fracture was not mentioned in the reference paper, therefore was calculated by the cubic flow rule as shown in the literature [107].

Table 4: Material properties in single slit hydrofracture

Young's modulus	E	2000 MPa
Poisson's ratio	ν	0.3
Fracture strength	K_{Fratt}	$1kJ/m^2$
Porous permeability	k_1	$5 \times 10^{-15} m/s$
Fracture permeability	k_2	$Calculated$
Porosity	ϕ_1	0.25
Coupling coefficient	α_1	$Calculated$
Coupling coefficient	α_2	$Calculated$
Coupling coefficient	α_{12}	$Calculated$
Coupling coefficient	α_{21}	$Calculated$
Leakage parameter	γ	$Calculated$
Water density	ρ_f	$1000kg/m^3$
Dynamic viscosity	μ_f	$10^{-15} Pas$
Residual strength coefficient	min(D)	0.1

The boundaries were considered fixed mechanically with zero pressure flux considered to be across the boundaries for either partial differential equations representing the fracture and porous domains.

The primary comparisons for verification was the crack opening size over time, the results from the reference paper [106] are displayed in blue with the proposed model's results shown in orange, and the crack opening was obtained via comparing the max displacement of the nodes above and below the crack.

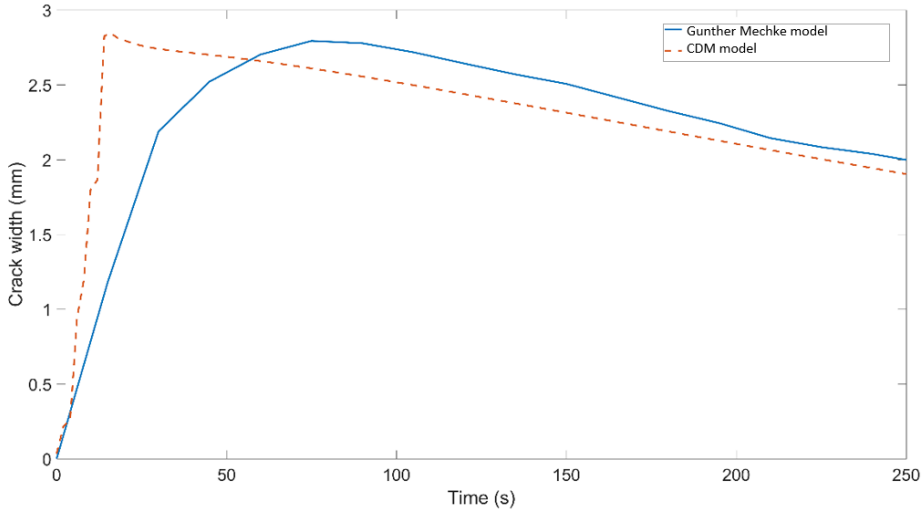

Figure 51: Crack opening over time [106]

The proposed model expands similar to the reference solution as seen in Figure 51, demonstrating agreeably in stiffness prediction of the fracture before the initial fracture at 5 seconds. The premature fracture clearly shows that the proposed model was premature in the initial fracture prediction. However, the developed method using a finite deformation framework remained stable whilst opening up to 3mm wide steadily as expected [106], peaking before decreasing again. The proposed model critically fractures at 20s as shown clearly in the peak. After this point fluid leakage into the surrounding area increases. The fracture continues to propagate until 75s into the experiment, each fracture ever becomes less evident in figure 51 as there is less built up pressure inside of the crack relative the to the surrounding pressure. Post initial fracture behaviour modelled begins to diverge, in [106]'s work, the crack slowly closes in a slow manor, whereas the proposed model has a more sudden response. The stiffness of 2 GPa can hold a lot of stored elastic energy due to fluid pressure as seen in Figure 51. This contributes to the proposed model's greater snap back in crack opening size. The slight increase the rate of opening can be attributed to the fact that the fluid compressibility is accounted for in the solution approach when compared to the reference solution by Gunther [106].

Crack closure is due to pore pressure redistribution or in other words through fluid leakage. From the onset of the numerical test, fluid is leaking out of the crack into the surrounding continuum via the leakage parameter, increasing the surrounding pore pressure. With the pressure surrounding the crack increasing, the crack's internal pressure is overcome by the surrounding pressure starting closure. The crack propagation increases at the rate of transferred pressure. The problem becomes akin to a two dimensional consolidation problem, where crack propagation acts as a catalyst for the process, increasing the rate of leakage.

Evidence for the crack behaving as a two dimensional problem due to increased fluid pressure leakage, due to fracture propagation, can be seen in Figure 52, with time-steps: 10s, 40s and 80s respectively. After the 80s mark the pressure has increased to 20MPa, matching the pressure inside of the penny crack. The leaked pressure now surrounding the crack begins to close the crack, decreasing the energy stored in the elements at the crack tips; preventing further crack propagation.

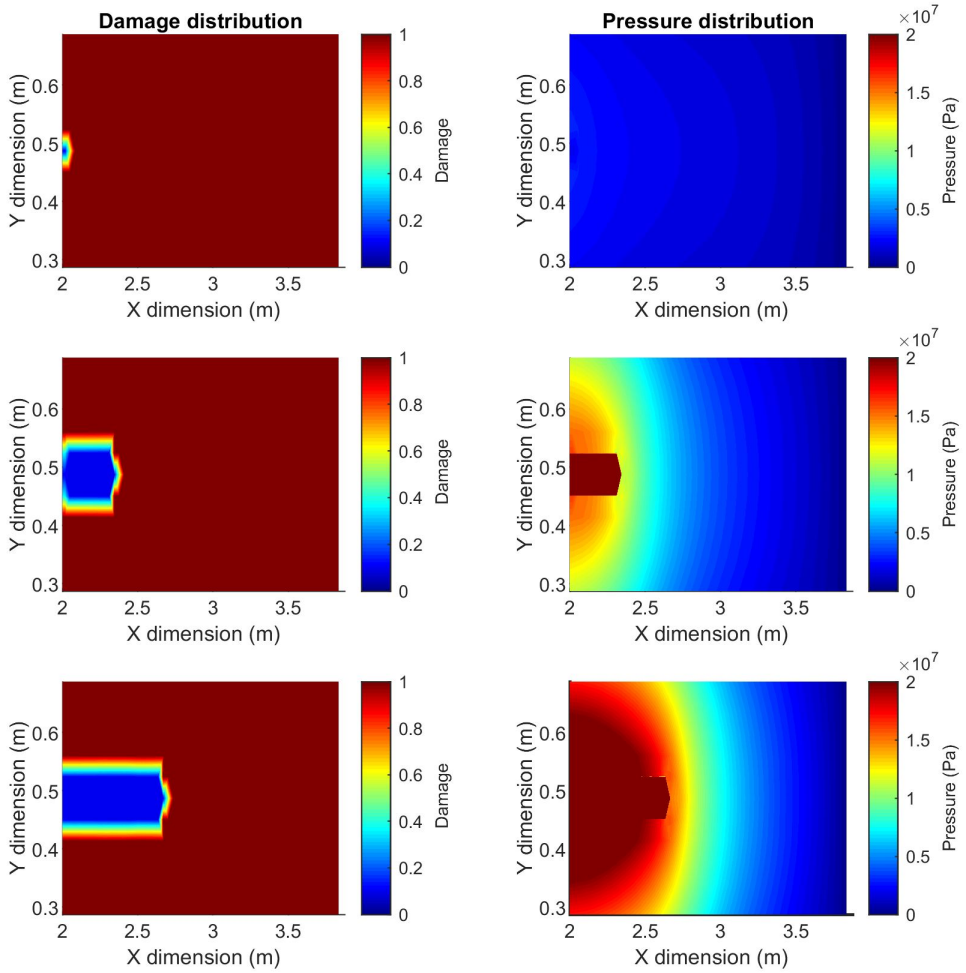

Figure 52: Pressure development with time at crack tip

To verify the developed computational framework in predicting the flow behaviour, similar to [106], fluid pressure along four lines A-A, B-B, C-C and D-D have been studied at intervals $1.75m$, $1.544m$ and $1.2725m$, respectively. Figure 53 shows the distribution of pressure along these cross sections. A non-linear behaviour for pressure distribution is predicted with our model for each cross section, and it is seen that pressure along the section C-C significantly increases after $80s$ when crack reaches this section. These findings agree with discussions on pressure behaviour in compressible porous media presented by [17].

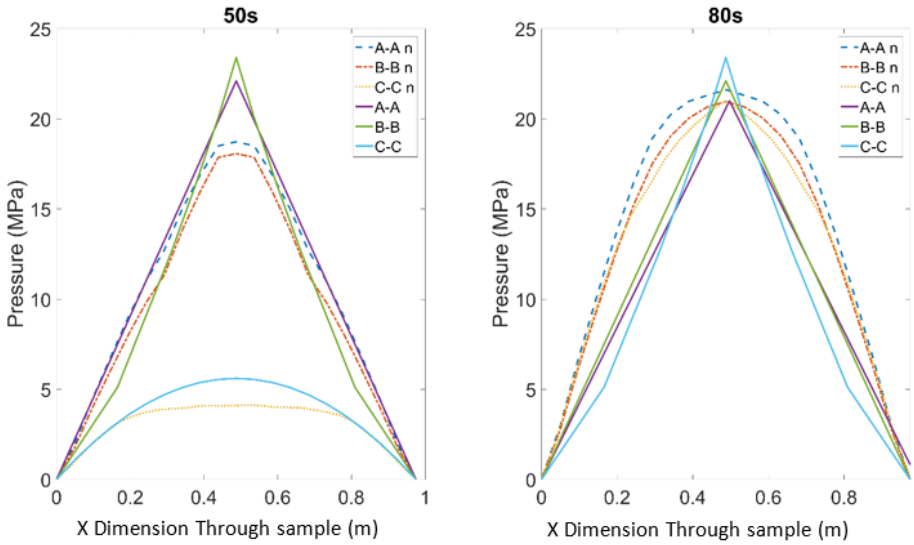

Figure 53: Fluid pressure distribution across A-A at 50s and 80s with fluid compressibility enabled

The reason of the difference between the results of our model and those presented by [106] is the consideration of compressibility of both fluid and porous media [104]. This is proved by results of our simulations repeated with the assumption of the incompressible fluid and porous domain (i.e. ignoring third and fourth terms of equation 89) which are presented in Figure 53b in greater agreement with results of [106]. The pressure profiles along $A - A$, $B - B$, $C - C$ at time $50s$ as presented in Figure 54.

As pores compress during crack expansion, pore pressure increases due to the consequences of the third $\alpha_{11}\ \boldsymbol{p_1}$ and fourth term, $\alpha_{12}\ \dot{\boldsymbol{p}}_2$ of equation 102.

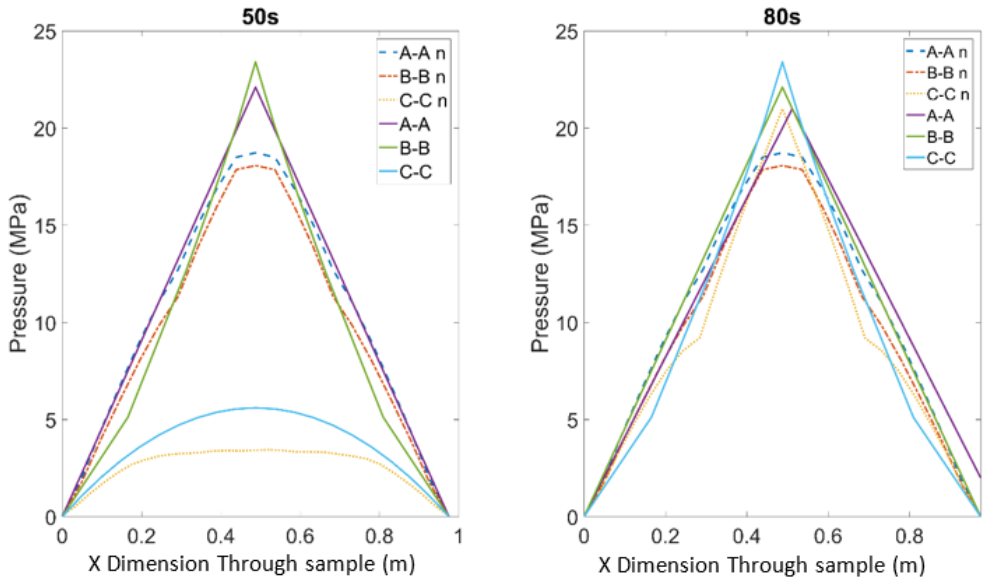

Figure 54: Fluid pressure distribution across A-A, B-B and C-C at 50s and 80s with fluid compressibility disabled

5.2.1 Stress contour verification

The reference paper for this verification is [147], the paper simulates a penny crack with an internal growing pressure. The reference paper provides analytical points of comparison, the analytical equations are derived in the simplified environment of a boundless domain and therefore the solution is also simplified.

The crack opening, length and well pressure data is also available to compare, which the reference paper used against analytical results from [74].

The theoretical equations used for verification will be derived initially in this chapter for completeness and for ease of understanding their limitations of the analytical equations used for verification. The finite element approach used by [147] achieves good agreement with the smooth behaviour exhibited by the theoretical equations and numerical results from the reference solutions, the results will be shown after the relevant analytical equations are shown in equation 121.

$$u(a, p, x) = \frac{2}{E'}(p - \sigma_h)(a^2 - x^2)^{\frac{1}{2}} \tag{121}$$

where u is the crack opening depth, E' is the Young's Modulus, p is pressure, σ_h is horizontal stress, a is the crack half-length and x is the distance from the crack centre considered.

Equation 121 describes the crack opening behaviour of a single penny crack with constant internal pressure across the whole crack enclosed in a porous medium. This equation can be used to find the maximum crack opening displacement by substituting $x = 0$, this leads to equation 122.

$$u_{max}(a, p) = \frac{2}{E'}(p - \sigma_h)a \tag{122}$$

A smooth elliptical crack shape is assumed in the reference paper for the shape of the two dimensional crack. Knowing only the maximum opening,

the total volume of the crack can be assumed and extrapolated, as shown in equation 123.

$$V(a,p) = \pi a u_{max}(a,p) = \frac{2\pi(p-\sigma_h)a^2 h}{E'} \tag{123}$$

by setting $V = qt$ in that the volume equal to the injected fluid volume, assuming no fluid compression or fluid lag, an equation describing crack length can be formed as seen in equation 124:

$$a(t) = \left(\frac{Eqt}{2\pi(p_c - \sigma_h)}\right)^{\frac{1}{2}} \tag{124}$$

where q is the pump flow rate (m^3/s), p_c is the critical fracture pressure and t is time, plotted for comparison in Figure 57 against the proposed methodology.

Equation 124 can be substituted into equation 123 for an equation describing the deformation along the crack whilst accounting for crack lengthening; see equation 125.

Considering volume conservation with the known volume of fluid injected, the crack length can also be calculated, see 124. For these equations to work the crack is assumed fully saturated so that no voids are present, and that crack propagation must be singular in direction.

It is important to note that the theoretical basis of the equation does not consider damage directly, the increase in fracture length is formed under the assumption of an elliptical crack progressing at the crack tips only, assuming the crack opening can be predictable in terms of the mechanics given in equations; 121 - 122.

The theoretical result assumes an elliptical shape crack opening depending upon the crack length, hence can be calculated from equation 125. This result can be seen plotted in Figure 56 compared against the solution produced by the proposed methodology.

The initial verification compares the effect of constant pressure on crack depth and length, whilst the second test, disables the damage component, in effect fixing crack length so that pressure's direct influence on crack opening can be measured, using equation 125.

$$u(a,p,x) = \left(\frac{2}{E'}(p-\sigma_h)\frac{Eqt}{2\pi(q-\sigma_h)}\right)^{\frac{1}{2}} \tag{125}$$

[147] uses a Darcy flow equation for the flow component of the model and a Biot term to describe the resultant expansion. The fracture methodology utilises a maximum horizontal stress of 15 MPa, this poses an issue to the verification simulation as the proposed fracture methodology uses energy terms to determine the point of fracture, therefore conversion between the methods required. The method of conversion starts with the displacement field normal to an impermeable fracture wall, where pressure acts to open the penny crack, shown in equation 126.

$$\frac{\delta p}{\delta t} - \nabla\Big(\frac{k}{\mu}\nabla p\Big) = -\alpha\frac{\delta\epsilon_v}{\delta t} \tag{126}$$

where α is a biot term and K_s is the solid grain modulus.

This version is more akin to the proposed methodology (see equations 80-83) accounting for internal grain compressibility in the porous medium considered, giving more control over the variables input.

The reference solution for this verification uses a similar methodology showcased in section 5.3, in that they both uses Biot flow and porous deformation equations, the key similarity being in the use of the pressure equations. [147] uses equation 138 whereas this paper uses equation 127:

$$W(a,p) = \frac{\pi h a}{E'}(p^2 - \sigma_h^2) \tag{127}$$

where W is energy released in a fracture event, h is height of fracture, a is the half length of the fracture, p is the internal mechanical pressure, σ_h is horizontal pressure and E' is the Young's Modulus. If a fracture is

considered to release R_0 energy when fractured, then the energy release rate for a fracture of length a will correspond to equation 128

$$\frac{dW}{dA} = 2R_0 \tag{128}$$

where R_0 is the fracture energy and A is area.

Equating equations 127 and 128 for an infinitesimal fracture gives equation 129, allowing for the calculation of the fracture energy required for an element.

$$2R_0 = \frac{\pi a^2}{E}(p^2 - \sigma_h^2) \tag{129}$$

Therefore, a fracture energy requirement of 66.7 kJ/m^2 can be calculated using the values given in table 5 to give us a suitable value for fracture energy term.

Table 5: Material properties in second hydrofracture verification

Young's modulus	E	10 GPa
Horizontal confining stress	σ_h	-1×10^7 Pa
Fluid pressure	p_2	1.1×10^7 Pa
Poisson's ratio	ν	0.25
Fracture strength	K_{Fratt}	$66.7KJ/m^2$
Porous permeability	k_1	$5 \times 10^{-15} m/s$
Fracture permeability	k_2	*Calculated*
Coupling coefficient	α_1	*Calculated*
Coupling coefficient	α_2	*Calculated*
Coupling coefficient	α_{12}	*Calculated*
Coupling coefficient	α_{21}	*Calculated*
Leakage parameter	γ	*Calculated*
Water density	ρ_f	$1000kg/m^3$
Initial crack length	a_0	40.4m
Porosity	ϕ_1	0.25

Coupling coefficients and leakage parameter are prescribed as appropriate

on the fracture boundary to ensure correct coupling characteristics.

The hydrofracture problem considers a 1000m square domain with a centralized predefined penny crack 40.4m long which is 1m thick as shown in Figure 55. These boundaries were utilised to define the hydrofracture problem in a manner more akin to a infinite domain, reducing the influence of boundary conditions unlike the two other hydrofracture examples shown in this thesis. All boundaries are fixed mechanically in the x direction as stated in the derivation of the analytical equations, the y direction is free on all boundaries. The pressure flux was fixed on all boundaries.

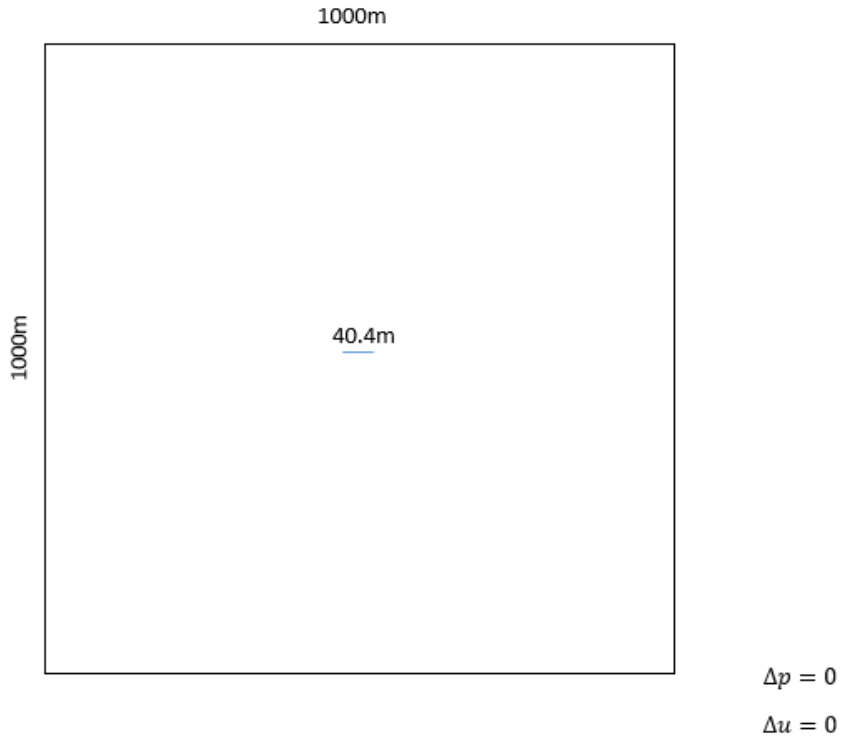

Figure 55: Validation case: Hydrofracture fluid schematic

Both equations 125 and 124 are plotted in Figures 56 and 57 to show that the proposed methodology predicts reasonable crack lengthening/widening.

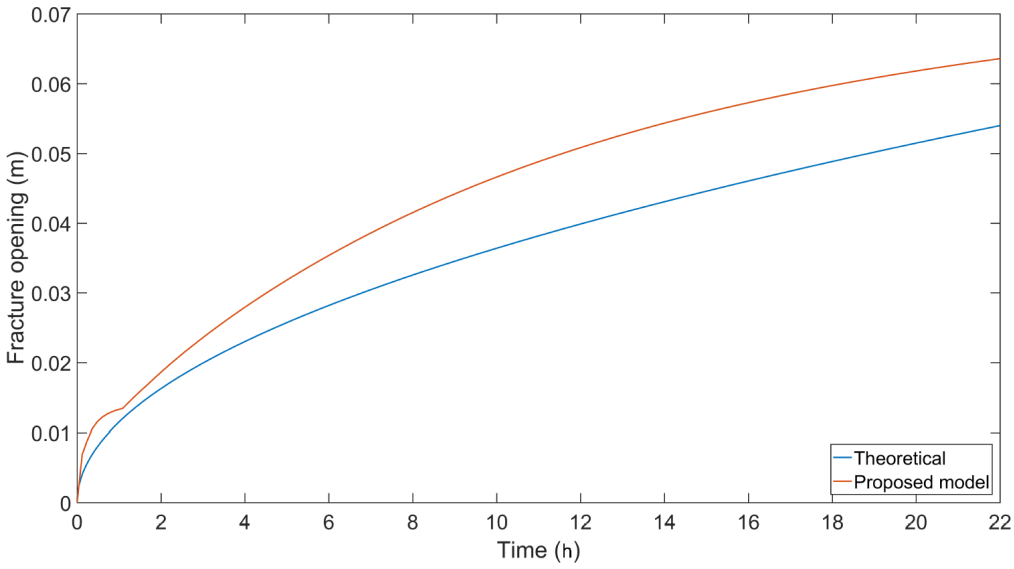

Figure 56: Crack opening over time with constant pressure; analytical solution (blue) vs proposed solution (Orange)

Constant pressure causes the crack to expand at a constant rate initially, tapering towards a constant value of 0.015m. The smooth trend seen up until this point, is similar to the theoretical result's behaviour. When the fracture lengthens at time 2.5 hours the trend rate of opening increases due to increased pressure and decrease in stifness. At time 22 hours the opening has a 16% difference the rate of change however is similar. The change in length during this period is constant, as seen in Figure 57, later it will also be shown in Figure 62 that when damage is disabled and the length fixed, the crack opening growth remains smooth.

Roughly at the time period of 2.5h the crack begins to propagate. The rate of propagation being steady until there is not enough pressure in the crack to warrant further propagation, as seen in Figure 57. Afterward the crack does carry on opening indefinitely not displaying the same two dimensional consolidation phenomena exhibited in the previous hydrofracture verification see section: 5.2. The opening does not equilibrate, instead the rate of opening does, which is to be expected when the fracture length remains stable for a

prolonged amount of time. This type of equilibrium occurs due to the large domain. The leaked fluid takes a long time to reach the boundary and have something to push against to close the fracture. With the fluid unable to reach the boundary, the problem behaved similarly within an infinite domain.

The change in length is less steady, as the pressure distribution of the fluid is changing and the surrounding crack structure is also changing due to crack lengthening, weakening the structure and increasing the area which pressure can act upon.

The crack length was measured by finding the left most and right most point elements contained within the crack (elements with a damage value 0.1), comparing their relative positions.

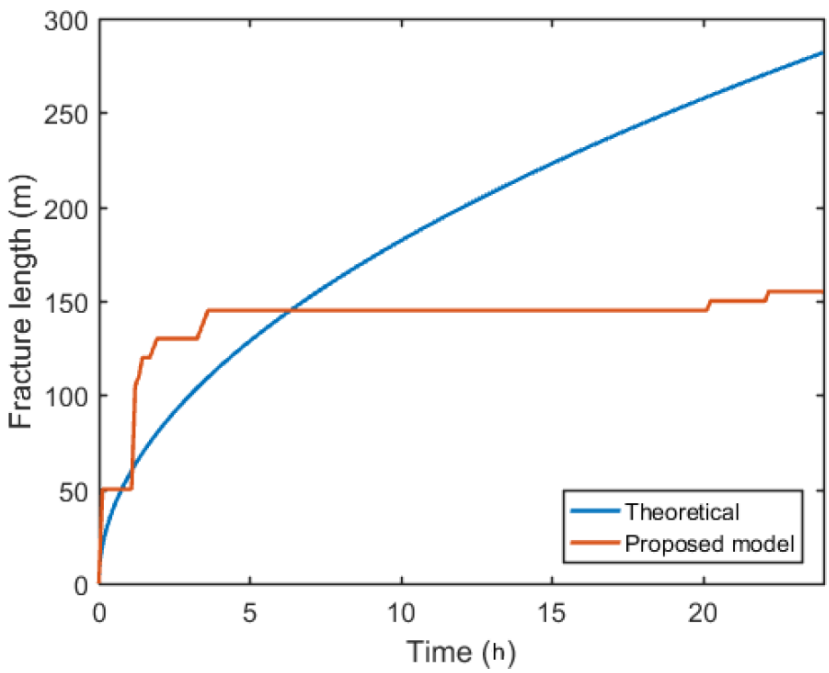

Figure 57: Crack length over time with constant pressure-theoretical solution (blue) vs proposed solution (Orange)

The crack length after the 4.5 hour time period becomes constant and no further propagation is no observed, this is due to the pressure lost in the

fracture along with it the hydrofracture's driving force.

The considered hydrofracture's rate of progress slows halfway.

Thus is because the pressure leak-off variable, contributing to a similar two dimensional consolidation problem catalysed with the crack growth and the area which pressure can leak-off, grows [93]. This observed result is similar to that observed in Gunther's work [106], expected with a similar leak-off variable. However not to the same extent due to the greater distance from the boundary.

The inflow on this verification is higher than the Gunther Meshke model verification example. This explains several successive cracks are required for a reduction in crack propagation momentum to occur. Furthermore, due to the boundaries being further from the pressurised crack itself, the pressure buildup surrounding the crack took longer as there was more space for the fluid to leak into and the boundaries hence took affect on the penny crack.

Effective stress and fluid pressure comparisons

The effective stress has been calculated in the principal direction y-y as that is the only comparison point provided by the reference paper shown in Figure 59.

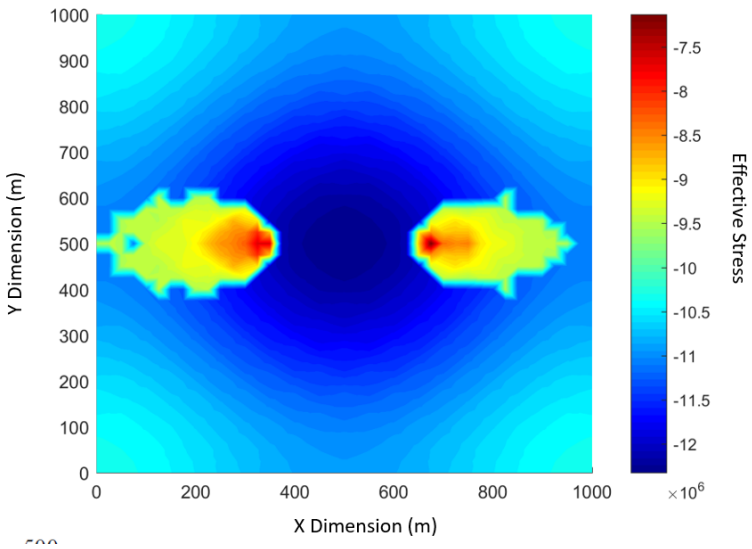

Figure 58: Effective Stress y-y homogeneous numerical hydrofracture result

Figure 58 shows two defining features in the stress contour plot; the stress due to compression above and below the crack where the peak effective stresses are most prominent, primarily due to pore pressure compounding with the compressive stresses built up due to the crack opening up. The max stress in the middle of Figure 58 produced by the proposed solution is -12×10^6 Pa compared to the -11.15×10^6 Pa from the reference solution showing a 7.6 % increase, as seen in Figure 59.

The other defining feature is at either crack tip, which is where the greatest tension stresses occur within the structures, here counteracted somewhat by the fluid pressure. The two results compare similarly in stress magnitude at the fracture tips; the proposed solution's maximum stress being -7.5×10^6 Pa compared to the reference solutions -8×10^6 Pa, showing reasonable agreement of 6.7% in terms of stress magnitude as well as effective stress behaviour due to hydrofracture.

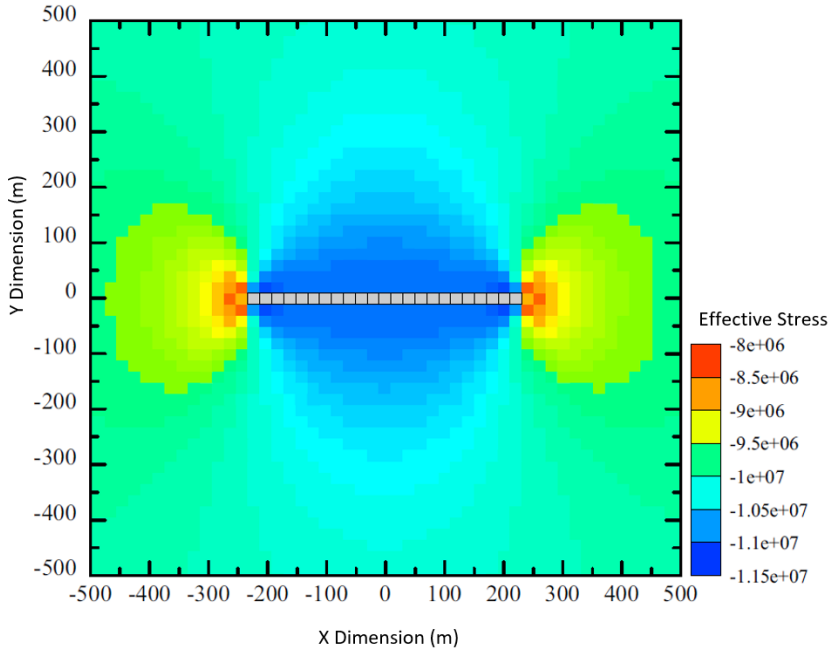

Figure 59: Effective pressure y-y homogeneous numerical hydrofracture result

Figure 59 has effective stress features typical of a confined hydrofracture shown in the results from similar numerical experiments. [90] shows that seepage of fluid pressure primarily from the crack's boundaries is common, in the case of [90] the boundaries are fixed for zero fluid flux across the boundaries where, as in this case, the flow is free to pass through the boundaries.

The minimum stress here is due to the pore pressure over-balancing the effect of the mechanical stress at the tips, however the effect of the tips on stress profile is clear also, the stress peaking at the tip and fanning of in the direction away from the crack, similar again to the results of confined hydrofractures from [160] and [159]

Fluid pressure comparison

The max pore pressure is similar in both results and both tend towards a steady rate from the crack edges to the containing boundaries as expected to a stable pressure of -1.2×10^7 Pa shown in Figure 60 proposed solution compared to the reference solution, shown in: Figure 61.

The highest fluid pressure being on the inside of the fracture where the pressure is injected over time during, therefore it makes sense that the diffusion solution to this problem has fluid pressure decreasing with distance from the crack.

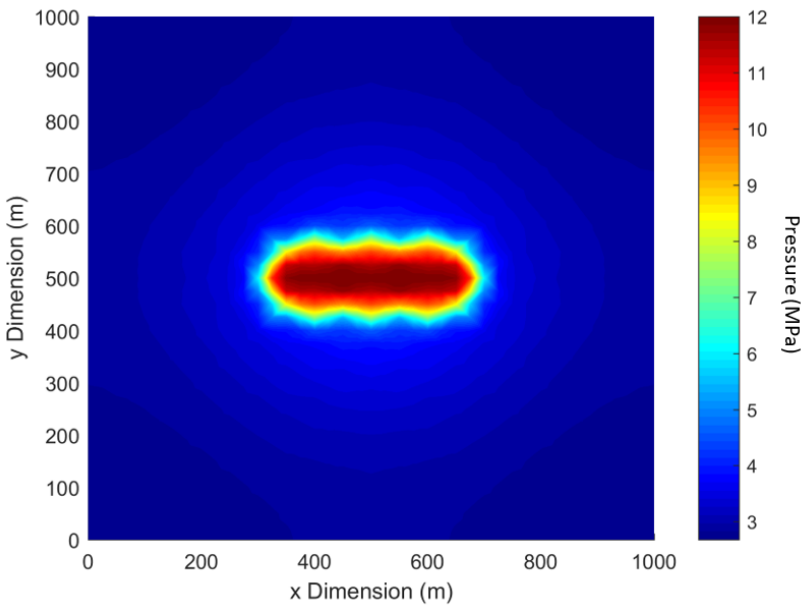

Figure 60: Fluid pressure distribution result from proposed solution

The reference solution assumes both aspects of mechanical-fluid coupling could be neglected and therefore a decoupled solution approach could be used solving for pressure and mechanical deformation iteratively. The proposed solution from this thesis can solve for pressure-mechanical coupling and can provide a simplified approach to the problem in comparison to the reference

solution through the solution of Biot's equations. The addition of the coupling terms allows the methodology to model more complex hydrofracture scenarios which are later showcased in this work.

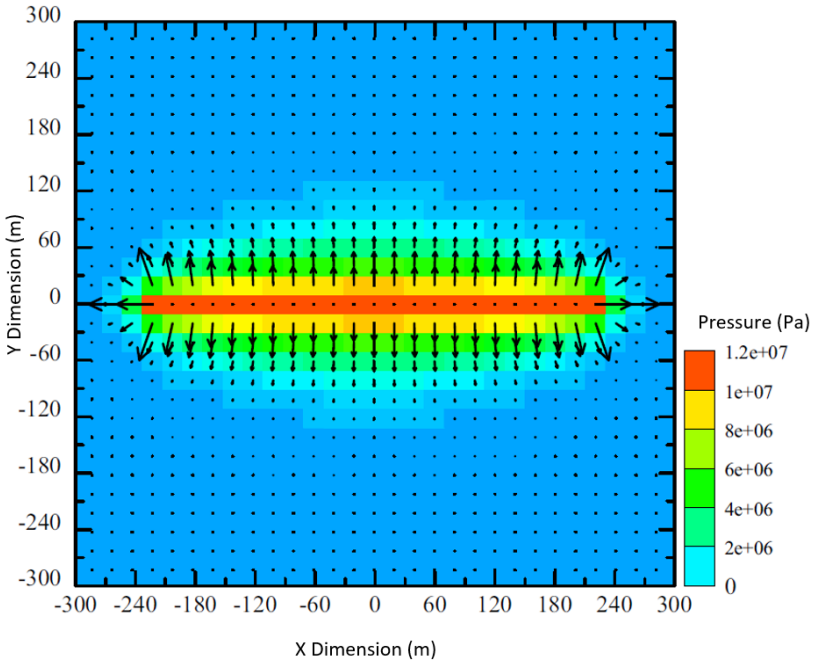

Figure 61: Fluid pressure distribution result from reference solution

5.2.2 Undamaged fracture opening vs theoretical result

Here the experiment is repeated with the damage model disabled to test the proposed model's coupling terms between pressure and the physical body via swelling only. To test the fluid pressure to mechanical coupling, the pressure was gradually increased to 11 MPa with the resulting crack opening deformation recorded.

The generated pressure values over time were used in equation 122 where the length of the crack is considered constant. This version was replicated in the numerical model with the damage variable disabled and the crack length remaining constant, to generate an ideal elliptical crack opening scenario; the results are shown in Figure 62. The maximum y deformation in the

penny crack was recorded; used to compare against the simplified theoretical equation 125.

An agreeable 5 % between the theoretical and proposed model's results was found as shown in Figure 62. Both the reference and proposed solution predicting a penny crack at 11MPa opening by 0.05m. The stiffness of the crack at the start of the test were identical and asymptotic trend of deformation was also similar. This small comparison against the theoretical solution shows the model's capabilities to capture the effect of increasing pressure's effect on the crack's walls.

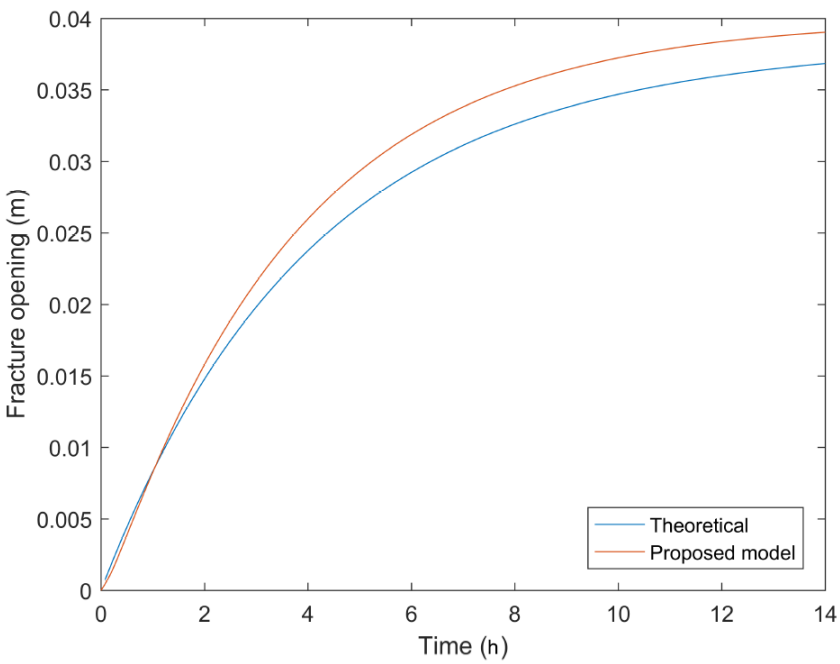

Figure 62: Crack opening over time with rising pressure Theoretical solution (blue) vs proposed solution (Orange)

Unlike in the simulation version with the damage model crack opening is far smoother as expected as the structure of the continuum was constant. The opening of the crack agreeing more with the analytical prediction by equation 122, both solutions opening steadily to 0.05-0.06m, not surprising considering the derivation of the crack opening assumes an elliptical crack shape, which

the undamaged version maintains. The crack opening equilibrates in this scenario much quicker; the crack still opening up at the 20s mark, however due to the smaller crack the rate of opening is smaller while the fluid pressure travels towards the boundary, causing 2D consolidation as discussed.

5.3 Continuous fracture flow example

The key strengths of the proposed methodology are the evolving permeability matrices with the development of cracks, capturing the accompanying change in strength and permeability. The next verification will demonstrate how the pressure distribution changes over time with constant pumping and how the model correctly predicts the repeat pressure losses due to crack propagation, which occur due to fracture volume increasing with associated fluid lag.

The reference paper [146] uses a set of analytical equations derived from Biot's equations for pore-elastic media and Láme's continuum mechanics equations for estimating hydrofracture behaviour. Analytical equations used for comparison from the reference paper are first derived and explained with their underlying assumptions and limitations.

The paper from [146] has qualitative results for pressure drops associated with fracture propagation, this allows a comparison on how the fluid pressure varies with many fracture events over time. Other comparisons are in relation to the deformation profiles using both the output results from the reference paper and the theoretical solution to the hydrofracture problem, derived from Láme's equations and Biot's porous flow equations.

5.3.1 Continuous flow undamaged

In [146] a large square model 100 by 100 m^2 is considered with a central penny crack with total length of 5.2m as shown in Figure 63. This value coincided with the mesh density utilised in the reference paper [146]. The penny crack is pressurised until the time step of 400 is reached, as this is the range of comparison results available from [146]'s solution.

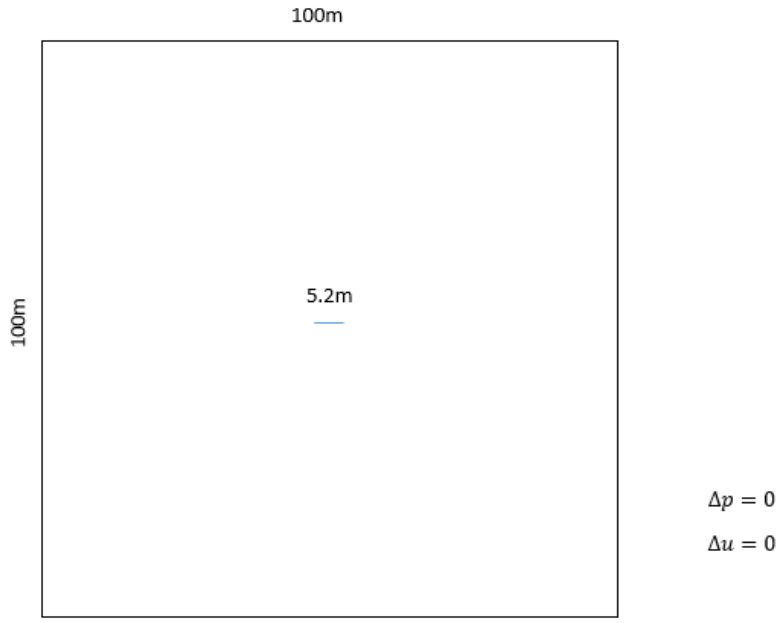

Figure 63: Hydrofracture fluid schematic

The reference damage methodology with a fracture threshold defined by a critical strain converted to an energy threshold. No value for fracture energy term was assigned in the paper [146], therefore a typical fracture energy term for rock has been calculated using an equation derived from particle packing using the material properties shown in table 6, see equation 140.

The reference solution consists of two models: one without fracture propagation, the other with. In the initial sample the damage model was disabled and the mechanical and pressure respond to a pressurised penny crack were measured over time along the domain, here we replicate both scenarios respectively.

Table 6: Material properties for large scale penny crack hydrofracture

Young's modulus	E	50 GPa
Poisson's ratio	ν	0.25
Fracture strength	K_{Fratt}	$39.5KJ/m^2$
Porous permeability	k_1	$5 \times 10^{-15} m/s$
Fracture permeability	k_2	$Calculated \quad from \quad cubic \quad law$
Coupling coefficient	α_1	$Calculated$
Coupling coefficient	α_2	$Calculated$
Coupling coefficient	α_{12}	$Calculated$
Coupling coefficient	α_{21}	$Calculated$
Leakage parameter	γ	$Calculated$
Water density	ρ_f	$1000kg/m^3$
Initial crack length	a_0	5.2m
Porosity	ϕ_1	0.25
Well pressure	q	2.5 MPa

Coupling coefficients and leakage parameter are prescribed as appropriate on the fracture boundary to ensure correct coupling.

The fracture strength used in this verification assumes mode one fracture.

Analytical equation basis: Biot's equation for coupled flow and deformations in porous media are used in the reference solution, shown in equation 130.

$$\frac{\delta \boldsymbol{\sigma_{ij}}}{\delta \boldsymbol{x_j}} = -\rho_f \boldsymbol{\delta_{i3}} \tag{130}$$

where $\boldsymbol{\sigma_{ij}}$ is stress, $\boldsymbol{x_j}$ are the spatial coordinates and the term $\rho_f \boldsymbol{\delta_{i3}}$ describes the effect of fluid mass on the porous system in the z direction. In the considered solution to this hydrofracture problem the approach is a 2D system where the z direction is ignored and hence $\rho \boldsymbol{\delta_{i3}} = 0$ is assumed.

When considered in terms of effective stress and in a 2D plane framework the effective stress term can be calculated as shown in equation 131:

Effective stress Lamé equation:

$$\boldsymbol{\sigma'_{ij}} = \boldsymbol{\sigma_{ij}} - \alpha p \boldsymbol{\delta_{ij}} = -(\lambda \boldsymbol{\epsilon_{kk}} \boldsymbol{\delta_{ij}} + 2G \boldsymbol{\epsilon_{ij}}) \tag{131}$$

where p represents fluid pressure and ϵ strain is represented by equation 132:

$$\boldsymbol{\epsilon_{ij}} = \frac{1}{2}(\frac{\delta \boldsymbol{u_i}}{\delta \boldsymbol{x_j}} + \frac{\delta \boldsymbol{u_i}}{\delta \boldsymbol{x_i}}) \tag{132}$$

where u represents deformation and the mechanical Lame's constant and shear modulus; λ and G; can be described by equation 133.

$$\lambda = \frac{\nu E}{(1+\nu)(1-2\nu)} \quad and \quad G = \frac{E}{2(1+nu)} \tag{133}$$

Equation 131 can be expanded to equation 134.

$$(\lambda + G)\frac{\delta^2 u_k}{\delta x_i \delta x_k} + G\frac{\delta^2 u_k}{\delta x_i \delta x_k} - \alpha \frac{\delta p}{\delta x_i} = 0 \tag{134}$$

where α is a measure of the compressibility of the porous domain, described by equation 135:

$$\alpha = \frac{K_{bulk}}{H} \tag{135}$$

where K_{bulk} is the bulk modulus and H is the pore-elastic expansion coefficient. In this case the boundaries are fixed both in terms of deformation and pressure flux.

Lamé's equation here is simplified to a one dimensional format as equation 136.

$$\frac{\delta^2 u}{\delta x_c^2} = \frac{1}{2G + \lambda}\frac{\delta p}{\delta x_c} \tag{136}$$

where x_c is the distance along the considered fracture.

Equation 136 can then be solved simply to provide a deformation quantity to compare produced results against, shown in equation 137.

$$u(t, x_c) = \frac{1}{2G + \lambda} \int_0^x (p(t, x_c')dx_c' - p_0 x_c) \tag{137}$$

where u is deformation along the centre of the sample equation 137 and is plotted in this case horizontally through the sample; G is the shear modulus, λ is Lamé's constant and x is the point along the sample considered.

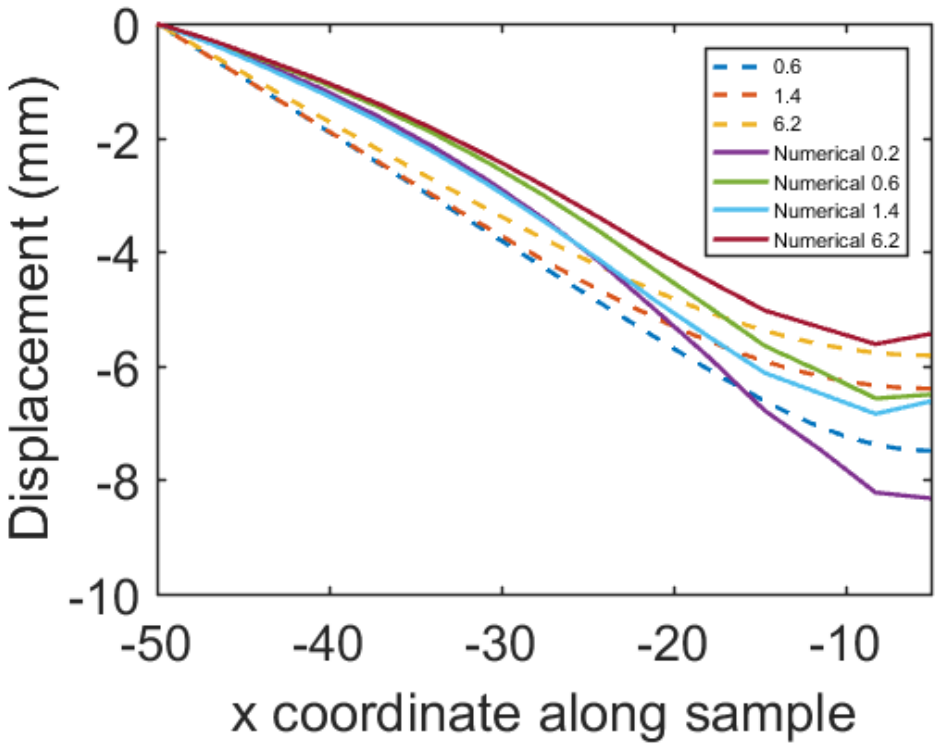

Figure 64: Deformation profile through section A-A at various time steps reference solution (Dashed lines) vs proposed solution (solid lines)

Figure 64 shows the deformation profile generated using the proposed solution for deformation through the sample at different time intervals compared against the analytical result from equation 137.

The proposed solution predicts the increasing deformation over time, especially local to the fracture tip.

The proposed solution predicts a decrease in deformation with increased distance from the penny crack where pressure increased, however the overall trend is different.

The reference solution is linear from the crack opening to the boundary, whereas the proposed solution predicts a sloping deformation trend.

This result makes sense due to the increased coupling in the solution, because the fluid is compressible, therefore where the pressure increases towards the boundary (seen in Figure 65), the fluid's compressibility gains strength and resists deformation more as pressure increases.

The α term: Biot coefficient is assumed to be one in the reference analytical formulation for simplicity, this reduces the coupling between pressure and continuum deformation, reducing required computational resources, however also reducing the predicted accuracy. The reference solution only considers the compressibility of the fluid in the calculation of pressure and not in the deformation on top of the lack of direct coupling.

The Biot pressure equation used is stated as equation 138:

$$S\frac{\delta p}{\delta t} - \nabla(\frac{k}{\mu_f}\nabla p) = -\alpha\frac{\delta \epsilon}{\delta t} \tag{138}$$

where S represents the specific storage coefficient and the alpha value is the Biot modulus relating fluid pressure to deformation, similar to the proposed framework's α_i variable as previously discussed.

It can be seen in equation 138's first term, the change in pressure is dependent on volumetric change [105]; in this verification the main source of pressure from the fluid pumped directly into the penny crack considered. Therefore, the specific storage coefficient (shown in equation 139) is neglected and co-dependence of mechanical behaviour and fluid pressure is reduced. For this reason [146] solved their system of finite element equations in a decoupled framework, utilising equations 138 and 131 separately, calculating the pressure initially then the resulting deformation. The difference in solution

is different from the proposed solution's coupled capability.

$$S = \frac{dV}{dp}\frac{1}{A} \tag{139}$$

where V is an element volume

The pressure flux at the boundaries were maintained at zero.

[146] calculated the increase of permeability according to the cubic flow rule and averaging with the rock's intrinsic permeability, an evolving equation dependent on the width of the crack, according to equations 140 - 141.

$$k_{av} = (1 - \frac{w}{h})k_1 + (\frac{w}{h})k_2 \tag{140}$$

where w is the opening of the crack, h is the intrinsic element size (representing fracture height), k_1 is the permeability of the rock and k_2 is the permeability of the fractured zone, determined by equation 141.

where the permeability exclusive to the fractured zone is calculated according to the crack opening.

$$k_2 = \frac{1}{12}w^2 \tag{141}$$

In the case of compression, the fractured zone's permeability does have the capability to be lower than the rock's intrinsic permeability hence that in the implementation the permeability is limited by equation 142. The fracture aperture, w must me greater than $(\frac{1}{12}k_f h^{\frac{1}{3}})$ in order to fracture permeability to occur as posed in equation 142.

$$w >> w_{min} = (\frac{1}{12}k_f h^{\frac{1}{3}}) \tag{142}$$

The proposed model uses equations 141 - 142 to model the rock permeability of porous and damaged/fractured zones, the implementation of these equations are eased by the use of structured mesh similar to the reference solution with elements of $1m \times 1m$ in size, a total of 5000 tetrahedral elements. The deformation varies from element to element, changing the w term in equation 141 marginally and easing implementation of the prior mentioned width restriction.

The equation used for an analytical comparison of fluid pressure along the sample is derived and begins with Biot's equation for pressure, shown in equation 143.

$$\frac{d}{dt}\int \rho_f dV = \frac{d}{dt}\int \phi_c \rho_f dV \tag{143}$$

where ϕ_c is the fracture zone's volume fraction, later described in equation 146 in terms of area of voids.

This is extended to include the mass pumped into a crack contained within the continuum as equation 144 shows.

$$\frac{d}{dt}\int \phi_c \rho_f dV + \int \rho_f v_D \mathbf{n} dA = \dot{\mathbf{M}}_{in} \tag{144}$$

where v_d is fluid flow rate into the crack and $\mathbf{n}$ is the normal to the incoming surface.

Pressure equation:

$$\phi_c c_f \frac{\delta p}{\delta t} - \nabla(\frac{k_1}{\mu}\nabla p) = -\frac{\delta \phi_c}{\delta t} \quad (outside \quad injection)$$
$$or \quad \frac{Q_{in}}{h^2}\nabla \quad (inside \quad injection) \tag{145}$$

where ϕ_c is represented by a volume fraction, showcased in equation 146.

$$\phi_c = \frac{A - A_0}{A_0} \tag{146}$$

where A_0 is the area of void space. Equation 145 is re-written in a non-dimensional format to ease to solution method, here shown in equations 147-151.

$$p' = \frac{p}{p_o} \tag{147}$$

$$x_c' = \frac{x_c}{l} \tag{148}$$

With an introduced scaled time variable for the equations to reach steady

state as shown in equation 152 allowing for simpler solution.

$$t' = \frac{t}{t_0} \tag{149}$$

where

$$t_0 = \frac{S\mu l^2}{k} \tag{150}$$

$$\frac{\delta p}{\delta t} - \frac{\delta^2 p}{\delta x_c'^2} = 0 \tag{151}$$

The solution of this non dimensional pressure equation is shown in equations 152- 154.

Calculating the pressure across the fracture, the pressure variable, this study will be used to verify the behaviour of the proposed framework.

$$p(t', x_c') = (x_c' + \Sigma \quad a_n sin(\lambda_n x_c') exp(-\lambda_n^2 t') p_0 \tag{152}$$

where the constants a_n and λ_n are described by equations 153 and 154.

$$a_n = \frac{2(-1)^n}{\lambda_n} \tag{153}$$

$$\lambda_n = n\pi \tag{154}$$

where n is an integer tending to infinity. In this numerical implementation, this value is calculated to 10000 numerically in reference comparisons.

The pressure profile provided by both the reference solution and the supplied analytical solution assumes a stationary crack and the fluid pressure's motion is purely dictated by diffusion through a fixed permeability field developing the pressure field as shown in Figure 65.

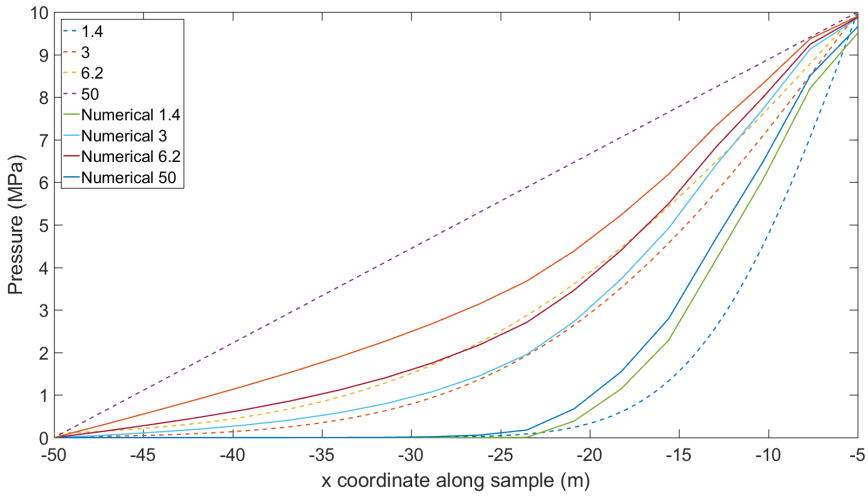

Figure 65: Pressure profiles along segment D-D reference (Dashed lines) vs proposed solution (Solid lines)

Figure 65 shows the predicted pressure profile compared against the analytical result for a stationary fracture subjected to steady fluid pressure of 10MPa. Again, similar to the deformation result, the magnitude of the pressure profiles are similar and the trend of a decrease with distance from the fracture is also present and there are discrepancies. The trend is again a result of the more complex coupling in the proposed model. The consideration of fluid compressibility resulting in a pressure increase further along the sample. Figure 65 reinforces this explanation with that if this were true the trend would be similar at the beginning of the experiment but as time progressed the effects of coupling would become more evident and the trend's differences would also increase with time.

The pressure along the lateral direction is also compared using analytical comparison, however in this case the pressure distribution accounts for fluid compressibility. For calculating the normalized pressure along the sample in the lateral direction with time, equation 155 was utilised.

$$p(r,t) = \frac{Q}{4\pi k_1 dz} E_1 \frac{\phi c_f \mu_f r^2}{4k_1 t} + p_0 \tag{155}$$

where p is the pressure, r is the distance from the crack, t is time, μ_f is dynamic viscosity, k is permeability, dz is the height through the section, Q is flow into the crack, ϕ is porosity, c_f is fluid compressibility, p_0 is initial pressure and E is an exponential integral as shown in equation 156.

$$E_1 = \int \frac{e^{-t}}{t} \tag{156}$$

With the fluid compressibility considered the agreement between analytical and the proposed numerical result is better than the previous comparison.

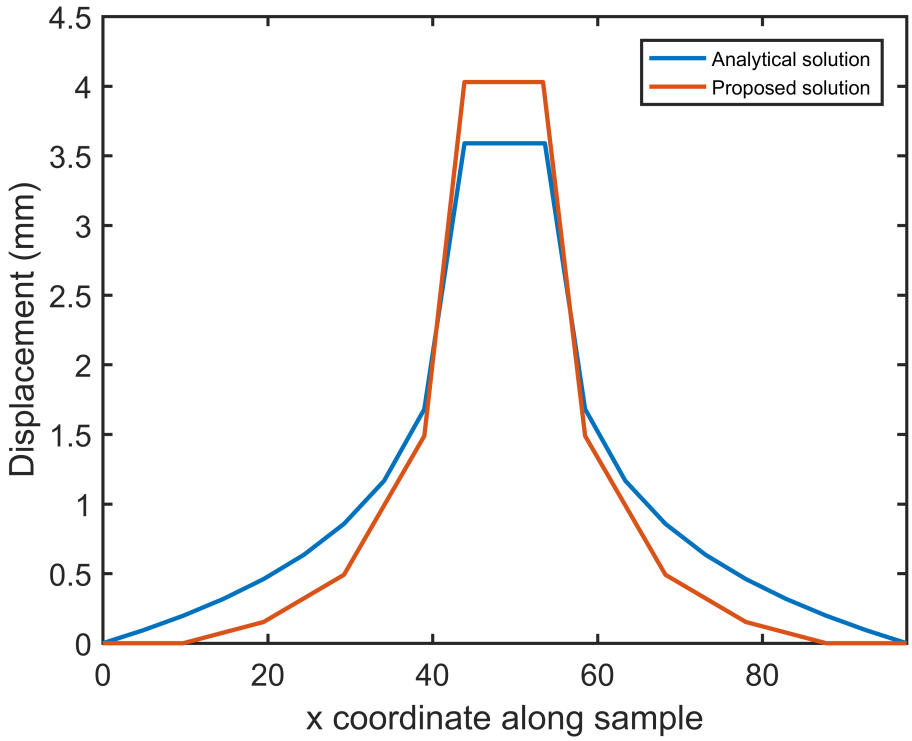

Figure 66: D-D pressure profile across fracture, analytical (Blue) vs proposed (orange)

Figure 66 shows the pressure profile generated by the proposed framework and the analytical pressure distribution described by equation 155.

The pressure trend is in good agreement in the sloping trend being maintained as time progresses, it is not surprising that there is not a perfect

correlation as the analytical equations are not coupled and the mechanical component in the analytical solution is not affected by fluid compressibility, simplifying the analytical equations.

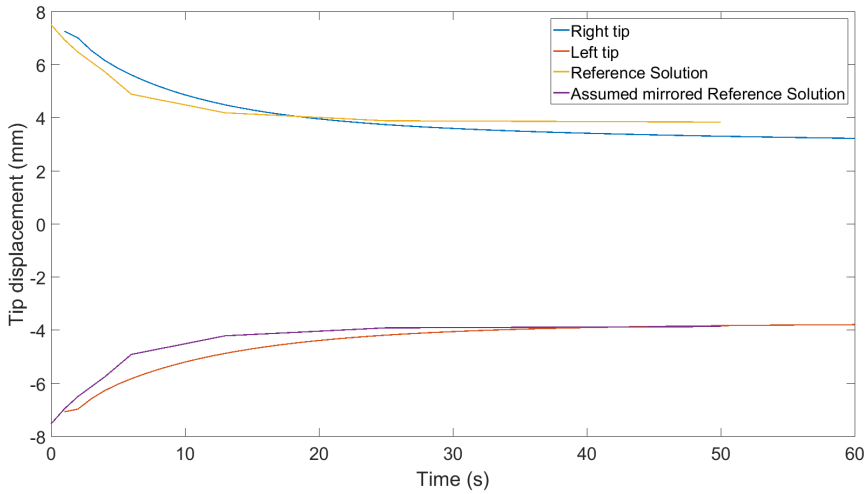

Figure 67: Tip deformation over time reference solution vs proposed solution

The reference solution provided a tip deformation plot from their numerical result for an undamaged version of the problem, if the problem of symmetry is solved then both tips should deform correctly. Figure 67 shows that the crack is deforming in a symmetric manner and deforming similarly to the solution provided by the reference paper.

5.3.2 Continuous flow damaged

Pressure was injected into the penny crack so that the crack would expand, the pressure reaches the fracture threshold early into the simulation and causes a pressure drop as represented in the reference pressure plot: Figures 68 and reproduced pressure plot: Figures 69.

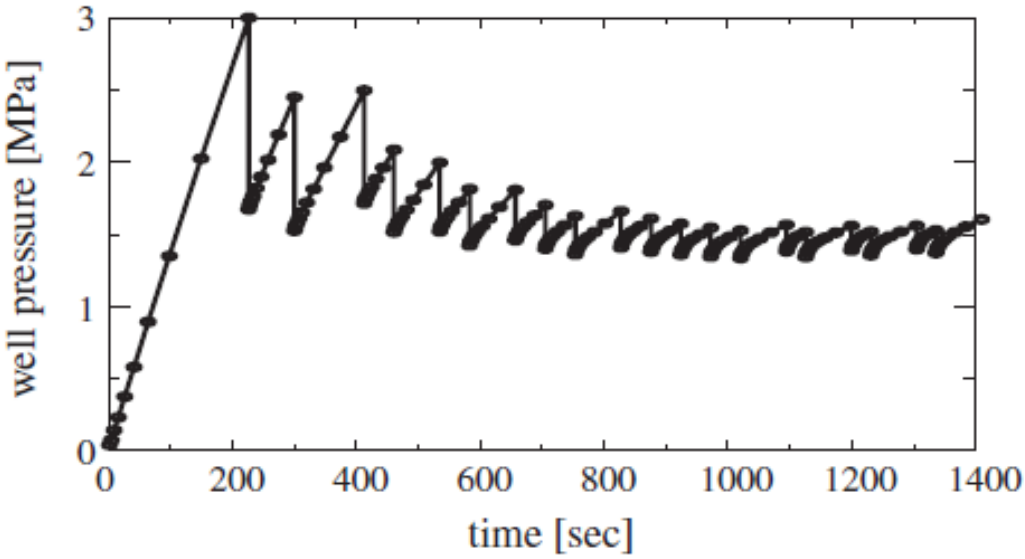

Figure 68: Pressure variation over time inside of fracture (Reference solution [146])

Figure 68 shows that the crack continues to propagate, growing in length. Each fracture event decreases the pressure inside of the fracture as the newly created void space needs filling and the crack walls that used to hold the pressure have moved further from the crack. Similar to the Gunther Mechke verification, the drop in pressure corresponds to a further reduction in crack opening.

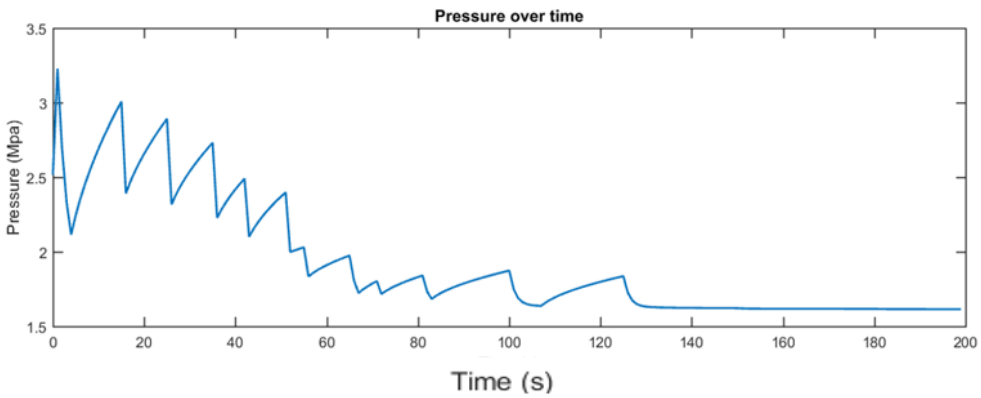

Figure 69: Pressure variation over time inside of fracture (Proposed solution)

It can be seen in Figure 69, the proposed pressure plot next to the reference pressure plot that the rate of pressure drops is similar in terms of regularity and magnitude as seen in Figure 70. However this is short lived after 120 seconds of running pressure drops due to fracture no longer occur. However, the general magnitude of the pressure does not decrease significantly over time unlike the reference solution. This implies that some coupling components may be inadequate to capture swelling and may not be appropriate for hydro-fracture mechanics.

[146] suggests that the pressure required to open the crack decreases over time as the area that internal crack pressure can act upon increases. Therefore, to produce the same net force on the crack wall less pressure is required.

The damage shown in Figure 70 rises at a similar, constant rate, when compared to bond breakage shown in Figure 71. The pressure drops over time are also similar in nature, the pressure drops corresponding to an increase in total damage; in this case representing crack propagation.

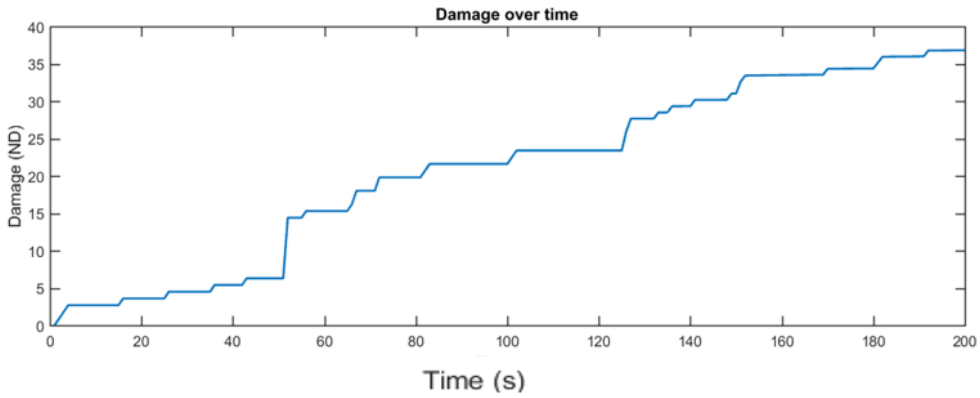

Figure 70: Accumulative damaged over time during hydrofracture progress (Proposed solution)

The damage methodologies used in the proposed model and reference models are fundamentally different, one based on element energy, the other on bond. However a quantitative comparison can be made on the rate of damage by plotting the total damaged elements and bonds vs time, as seen in Figures 70 and 71, both having similar rates of degradation.

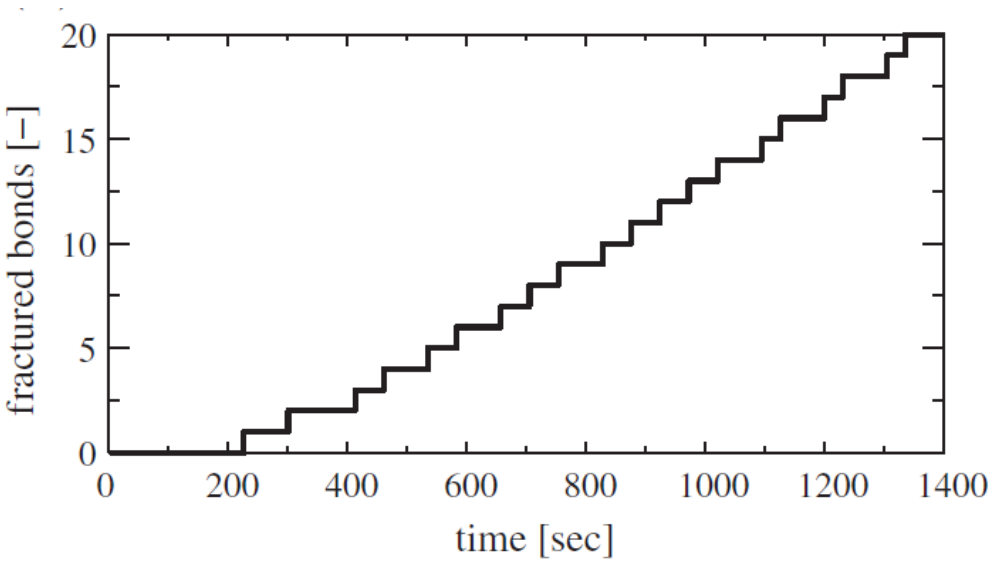

Figure 71: Cumulative damage (Bonds broken) over time during hydrofracture progress (Reference solution [146])

Figure 72 shows that the hydrofracture propagated at a near equal rate

on both sides of the hydrofracture as expected with the homogeneous nature of the model.

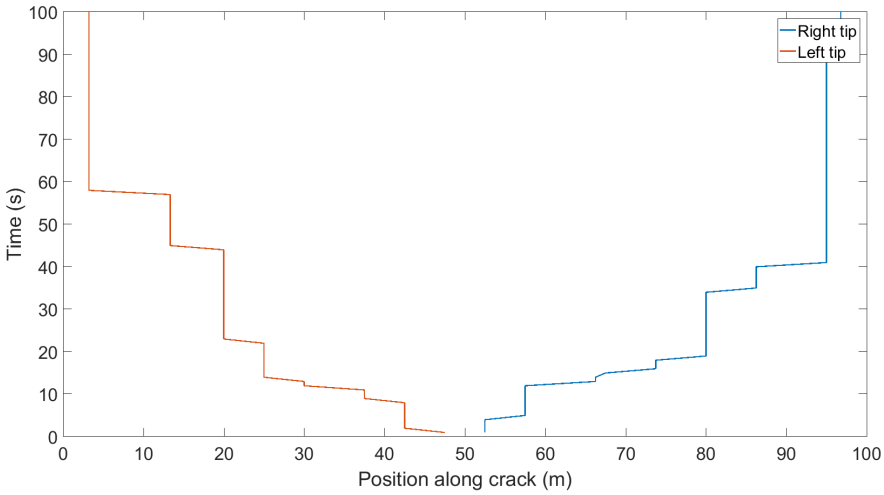

Figure 72: Fracture propagation over time during hydrofracture propagation showing symmetry

5.3.3 Fluid lag behaviour

As a hydrofracture propagates, the ratio of fluid to void space varies significantly with time, the variation behaviour depending heavily on fracture progression, media permeability, surrounding media permeability and the dynamic viscosity of the fluid. The phenomenon of fluid lag can be seen in Figure 73 [22].

In [22]'s experiment, injected fluid causes an infill of pressure until crack propagation. Just before this point, the fluid was noted to have undergone compression with a noticeable void at the crack front.

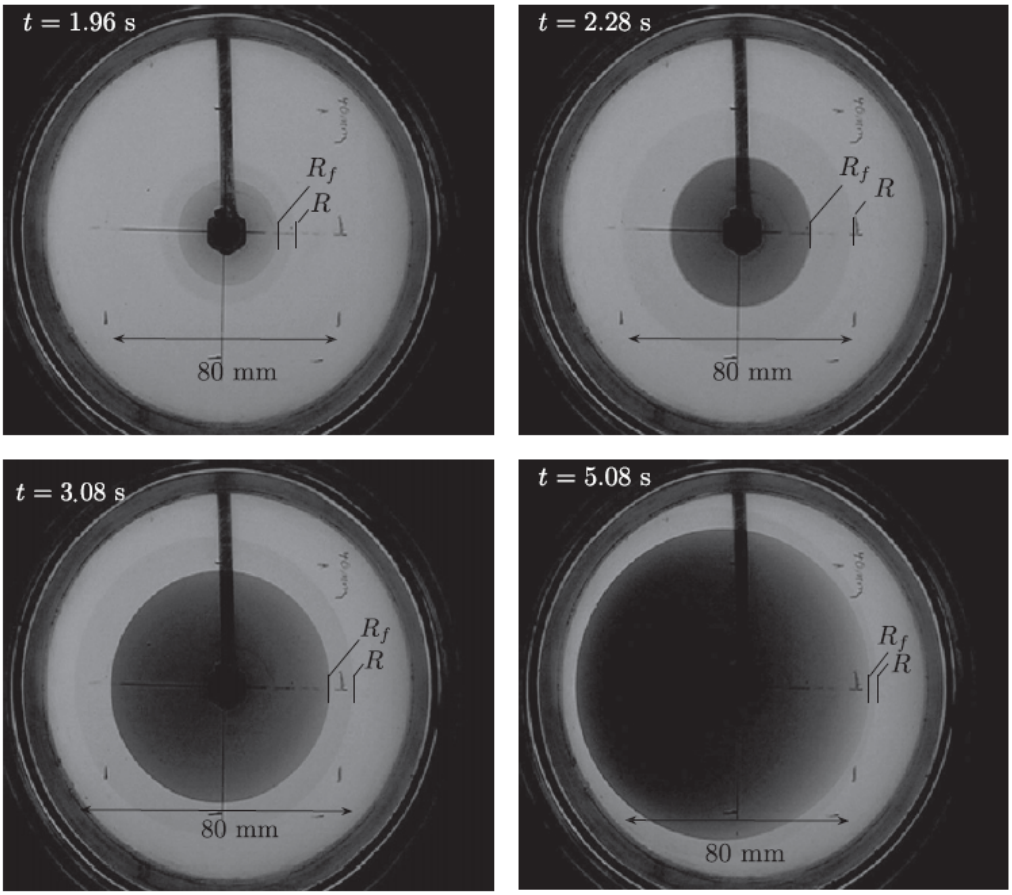

Figure 73: Fluid lag behaviour captured in hydrofracture experiment [22].

Figure 73 shows a perspex box which initially had a thin slit connected to a pump.

The pump was turned on and pressure filled the slit, building pressure. Once the fluid pressure had built to a sufficient level the slit fractured. After propagation a void was created ahead of the fracture front denoted R_f, the void denoted in Figure 73 as R. Figure 73 shows four different time steps at: 1.96, 2.38, 3.08 and 5.08 seconds, a fracture event between each step. It can be seen that during fracture progression, fluid lag becomes less significant as fluid to newly create void ratio diminishes.

The evidence of fluid lag can be noted to be present at each fracture event, at the same time a pressure drop is observed in the system, similar to the hydrofracture verification presented in this thesis.

Section 5.3.2 showcases the proposed methodology's ability to capture fluid lag, [21]. Fluid lag becomes more relevant in situations where confining pressure is low and the surrounding media is impermeable [7], primarily because the fluid lag depends highly upon fracture saturation and volume space created during a fracture event. In single phase model approaches to capturing hydrofracture behaviour, it isn't uncommon to find the author assuming the Stefan condition where the crack velocity matches fluid velocity; no fluid lag due to the difficulty of solving the pressure equations with the inclusion of leak-off [133].

Further evidence of fluid lag being captured by the proposed methodology is showcased in Figure 69, after the initial drop in pressure an oscillating pressure nature can be spotted. A.A. Andreev [4] spots a similar trend in their hydrofracture simulations. The oscillating nature is noted to cause instability within the model, the same can be said for the proposed model, when time steps are too short, the oscillations in pressure become too volatile and begins to create numerical errors. The cause of the oscillation nature comes from the pressure disparity between the crack tip and the main body the fracture, if the disparity becomes too large and the pressure flow equations cannot normalise the pressure before further crack propagation then the disparities begin to build up to unrealistic pressures causing errors in future calculation. [82] Kumar succeeds in modelling the fluid lag behaviour by stimulating the fracture tip with temporary suction zones, if the suction zones are too great, numerical instability still occurs however.

Once a crack has progressed sufficiently, the ratio of fluid stored to newly created void space due to a fracture event decreases; Peirce [119] show that the effect of fluid lag decreases after some time due to decreased fluid supply. [133] Bao also showed that the effect of fluid lag must be considered, otherwise the crack half-length may be predicted incorrectly. The model used by [133] is similar to [22] showcasing the need for fluid lag consideration. The relevance of leak-of is neglected in both papers, therefore it is difficult to conclude the effect of fluid lag with varying crack length when leak-off is involved. It can

be conjectured that the length assumption may not apply for leak-off models, this would follow logically as the volume stored in a leaking fracture would vary, attributing to a higher probability of fluid lag occurring.

It is of note to mention also the agreement of experimental results to analytical achieved in [22] for saucepan shaped crack was also for very small cracks with no leak off. Without further experimental data it is difficult to confirm the possible relation of fluid leakage to fracture propagation and the extend of said effect. It makes sense logically but cannot yet be proven through experimental means. There is currently little numerical/analytical evidence to back up this claim as [37] and [1] mentions solving for both volume fraction and crack propagation in the presence of fracture propagation is a difficult task and no full solution in the literature yet yields a satisfactory solution. The verifications conducted in this thesis demonstrate that the correct use of the leak-off coefficient is necessary in the simulation of realistic hydrofracture behaviour.

5.4 Non-uniform pressure field crack prediction

All hydrofracture verifications so far conducted have been single hydrofractures, fluid traveling through singular newly propagated section of the fracture, building pressure and repeating until equilibrium in a linear direction with a somewhat expected fracture path and singular in nature.

The following hydrofracture example has two points of pressurisation and will show that the proposed methodology can account for multiple pressure instances, uni-axial load conditions and non-uniform pressure fields. The verification will also capture how the aforementioned variables will change with fracture propagation and how crack path deviation will impact hydrofracture behaviour.

Song [136] casts a cuboid of sandstone with two distinct holes bored, as shown in Figure 74. pressuring the two holes within the cuboid of dimensions are 100mm (wide) x 100mm (Deep) x 200mm (long) with two holes placed as shown in Figure 74.

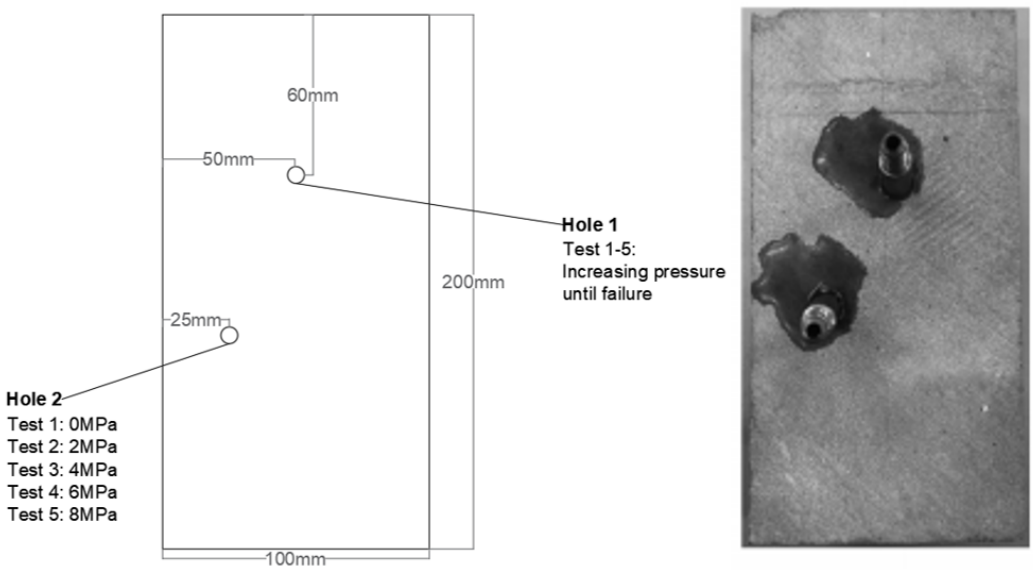

Figure 74: Non-uniform pressure schematic (left) and experimental set up (right)

The schematic for this experiment shown in Figure 74 shows there are two designated holes; one and two. Hole one's pressure is constantly increased until complete failure is achieved.

Whereas hole two's pressure is maintained constant throughout individual experiments.

Several experiments by Song [136] were conducted with different pressure values between experiments, shown in table 7. Table 7 showcases the experiments undertaken, showing the uni-axial pressure and constant hole two fluid pressure for each test preformed.

Table 7: Experimental setups

Experiment Number	Axial Pressure (MPa)	hole two Pressure (MPa)
1	10	0
2	10	2
3	10	4
4	10	6
5	10	8

The two holes are both 55mm deep; hole one having an additional notch 2mm deep at the bottom to ensure clean crack initiation during the experiment. Once both holes were drilled, two pump nozzles (260D Syringe pump) were placed in the holes, the nozzle radius at 3.175mm (approx) and a pressure sensitivity of 0.1 %, both sealed with epoxy to ensure low pressure loss.

In the five experiments carried out the data presented include the pressure over time in hole one and the distribution of pressure, damage and deformation in the x direction through numerical means. The three variables are dependent on each other in nature and in the following presentation of results the links between three variables will be showcased and explored, additionally the effect of newly created crack paths and their effect on the model will also be observed and analysed. Test 1 and 5 are shown here in chapter 5, tests 2-4 can be found in Appendix C. Material properties used are shown in table 8.

Table 8: Material properties

Young's modulus	E	35 MPa
Poisson's ratio	ν	0.25
Fracture strength	K_{Fratt}	$12.5KJ/m^2$
Porous permeability	k_1	$5 \times 10^{-15} m/s$
Fracture permeability	k_2	$Calculated$
Coupling coefficient	α_1	0.1
Coupling coefficient	α_2	0.1
Coupling coefficient	α_{12}	0.2
Coupling coefficient	α_{21}	0.2
Leakage parameter	γ	$Calculated$
Water density	ρ	$1000kg/m^3$
Initial crack length	a_0	5.2m
Porosity	ϕ_1	0.25
Well pressure	q	$2.5MPa$
Residual strength coefficient	min (D)	0.1

Coupling coefficients and leakage parameter are prescribed as appropriate on the fracture boundary to ensure correct coupling characteristics.

The boundary conditions set for movement in the y direction are fixed for both the top and bottom, with a set deformation of 0.5 mm to recreate the uni-axial stress of 10 MPa.

The top and bottom mechanical boundary conditions in the x direction, accounts for a coefficient of friction of 0.25, this is the cause for the asymmetric deformation profiles presented as the model showed a tendency to slide to one side or the other; further exaggerated by the asymmetric fracture paths and accompanying pressure fields. The accuracy of this value is difficult to calculate accurately as the variable is difficult to measure in nature. The pressure boundary conditions fixed pressure flux as the experiment was open to the environment.

Test 1: 10MPa Axial pressure, 0MPa hole two pressure

The reference experimental result of pressurising only hole one in test one is shown in Figure 75, hole two only impacting the preceding crack path with a void of material and associated weakness.

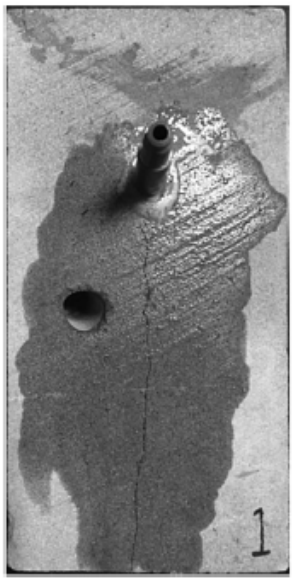

Figure 75: Test 1, Experimental fracture path [136]

Figure 75 shows that only hole one has the 260D Syringe pump inserted, the singular pressure building up to a single vertical crack straight down the centre, where the tensile forces are at their maximum.

The primary mode of failure shown in Figure 75 was a tensile crack down the centre of the sample, caused by the pressure in hole one pushing the sample apart laterally. The fracture is defined below hole one as the middle of the sample is prone to Poisson effects from the uniaxial load.

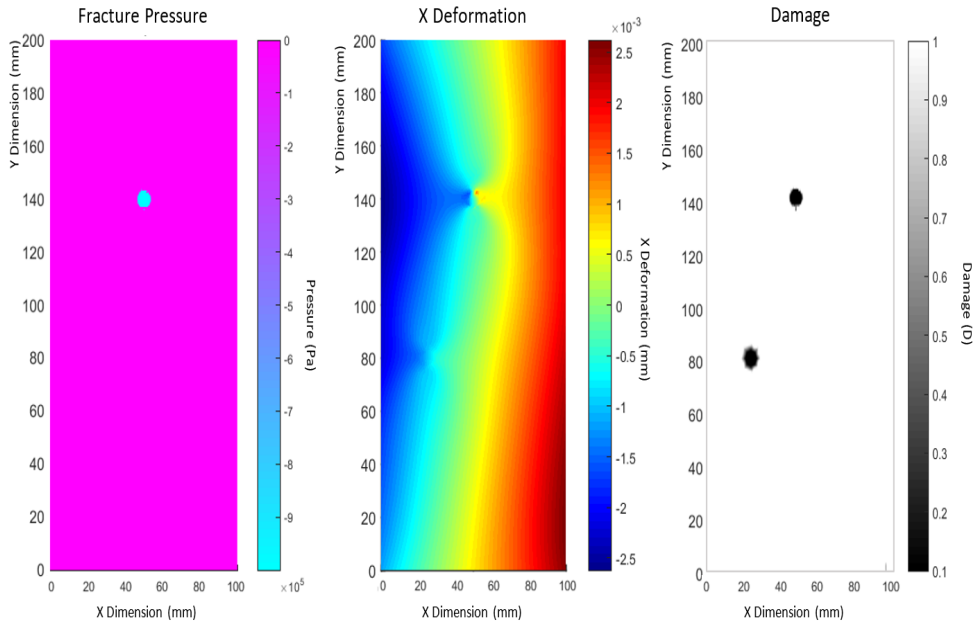

Figure 76: Test 1, Numerical Hydrofracture at time=0s showing from left to right; fluid pressure distribution, X deformation and damage distribution

Figure 76 shows the initial deformation profile in the numerical result produced by the proposed methodology. The initial fracture pressure at 0.8 MPa and the uni-axial pressure applied. The amount of stored mechanical energy in any part of the model has not surpassed the required fracture energy to initiate a fracture local to hole one.

The deformation plot shows the structural impact of both holes, hole two is experiencing x deformation due to the applied uni-axial compression and lack of resisting material; exhibiting a similar deformation trend to the slit experiments prior. However, hole one where fluid pressure is present shows an exaggerated deformation profile as expected of the pressurised location and will become the primary driving force of the fractures propagation in all experiments carried out acting through the coupling terms in the numerical models.

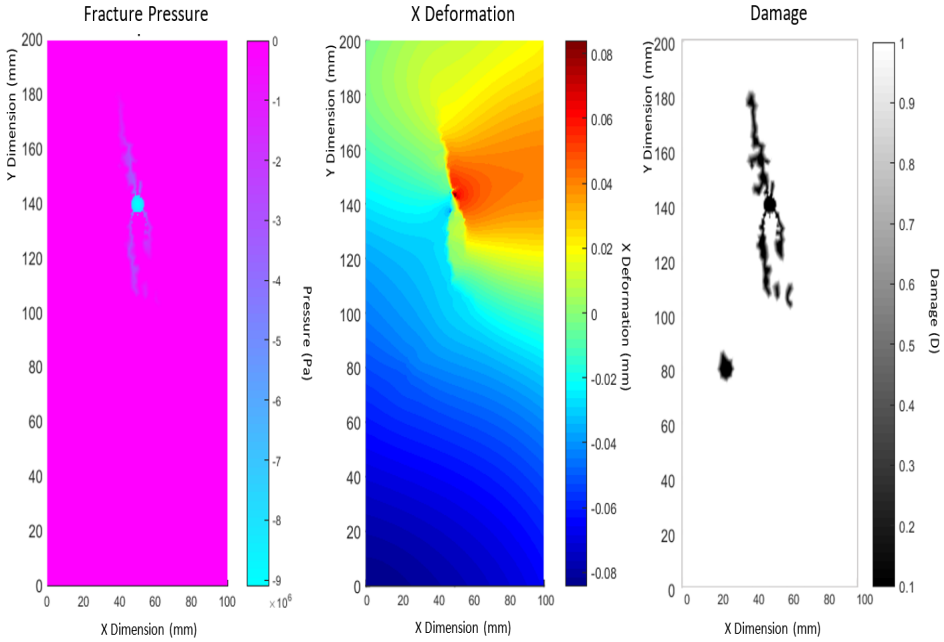

Figure 77: Test 1, Numerical Hydrofracture at time=25s showing from left to right; fluid pressure distribution, X deformation and damage distribution

Figure 77 shows crack initiation from hole one in a vertical manner agreeing with the provided crack path in the provided photo by [136], not impacted by hole two, shown in Figure 75.

This "snapshot" was taken shortly after the stored mechanical energy surpassed the fracture strength threshold typical for sandstone.

The deformation profile is more dramatic in comparison to the deformation profile shown in Figure 76. This is due to the generally increased fluid pressure and the fracture pressure development. It can be seen in Figure 77 that the deformation profile is more consistent across the faces of hole one; left and right when compared to Figure 76's deformation profile, this is due to the main driving force of deformation/stress has built up pressure along the crack face.

Figure 77 shows that the fluid has flowed along the newly created fracture, the transport of the pressure through the fracture aids in the momentum of fracture growth and exchange of mechanical to fracture energy, leading to the future damage distribution and complete failure of test one's sample, see Figure 78.

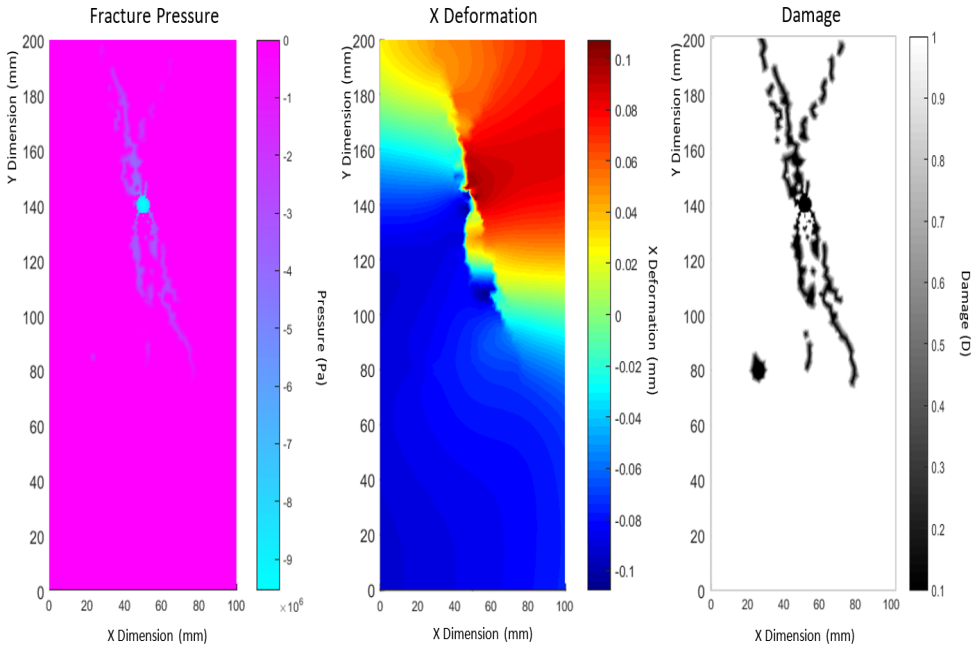

Figure 78: Test 1, Numerical hydrofracture at time=35s showing from left to right; fluid pressure distribution, X deformation and damage distribution

Figure 78 shows that a failure mode has been predicted within the sample, leading to the crack changing direction towards both supports and right branching; similar to the fracture path shown in the experimental result.

As the top boundary is pushed down due to applied uni-axial load, the more the dominant stress path changes direction, the closer the fracture edges towards the top boundary. The fracture path becomes similar to the fracture path previously observed in the 15 degree slit experiment.

It is important to note that as the branched fractures propagate, the fluid pressure in them accumulate. With time the failure mode of the hydrofracture becomes dominated by tensile failure due to the mounting fluid pressure pushing the fracture's walls apart. The fluid in the fractures influences the fractures direction by maintaining the stress field surrounding the fracture maintaining the direction unless other significant loads occur. Therefore, once a hydrofracture has initiated in the following set of experiments it is rare that a change of direction is observed. The point of branching is always local to the two pressurised holes as this is where fluid pressure is applied, acting in all directions and the accompanying equilibrium require branching to be maintained. This behaviour can be seen in the range of results showcased in appendix C.

The experimentally observed fractures from the reference paper [136] favour downwards fracture propagation, fractures towards the top boundary remain faint and less distinguished when compared to the fracture propagating down the sample. The favour of downwards propagation is likely to be due to the notch placed in each sample during preparation.

The damaged elements in the model utilised have low stiffness and are subject to the high pressure and therefore if left unchecked can undergo inadmissible deformation.

The deformation in the x direction now is been heavily influenced by the fracture and contained fluid pressure on the profile has been overwhelmed by the now eccentrically applied uni-axial load. This has driven a crack path prediction error. This large deformation across the fractured elements influences the fluid pressure by changing the permeability of the damaged elements via the implementation of the cubic flow rule. This explains the pressure plot in Figure 78 is more drastic than that shown in Figure 77. With the increase in permeability the driving force and mobility of the fluid increases over time as the fracture's aperture grows throughout the sample, increasing each hydrofracture's rate of growth over time. This trend acts in

all tests carried out, the rate of hydrofracture increasing due to the introduced cubic flow rule.

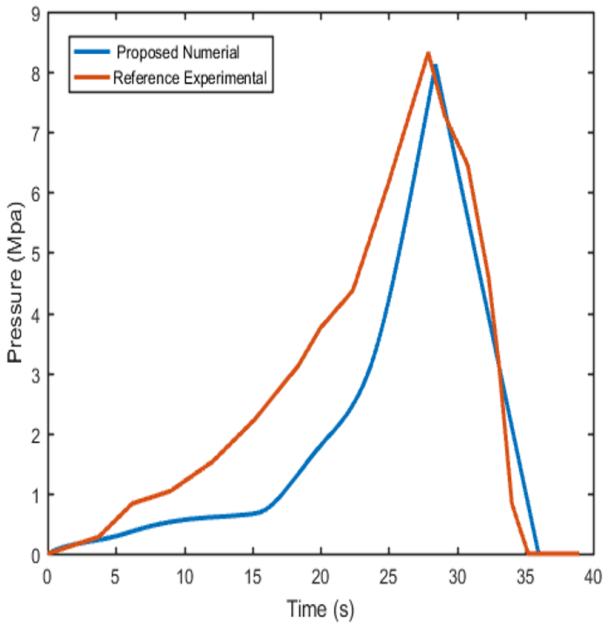

Figure 79: Test 1, Fluid pressure in hole one over time

Figure 79 shows the pressure averaged from the elements contained within hole one over time compared to the experimentally observed pressure.

Figure 79 shows reasonable agreement in both the trend and magnitude for the proposed solution vs experimental reference data [22].

Although present in all experiments it is important to mention the influence of gravity on the fluid flow through the sample in the experiment performed by [136]. In the photos provided by [136] the crack path is mostly seen to be traveling in a downwards fashion. This is likely due to the porous sandstone used and downward positioned notch. The only pressure profile data supplied by [136] is in the form of an accompanying computational model attempting to simulate the same crack path with changes in the non- uniform pressure fields and the wetted photo is showing where fluid has travelled roughly. In these photos the fluid is never seen fully wetting the top boundary of the sample unlike the bottom boundary. This is likely due to gravity increasing

fluid flow more than the pump in terms of porous flow. The fluid is leaking from the top at a greater rate as the fluid that is leaked flows down the porous rock, increasing the pressure gradient between the fracture pressure and the surrounding porous pressure. This pressure gradient increases the rate of leakage from the top fracture and further impedes fracture progress towards the top boundary. This effect leads to fluid tending down the sample. This is likely increasing the pressure confining the lower fractures below hole one.

When the fluid leaks into the surrounding porous domain the fluid has no boundaries to push upon due to the drained boundaries. Therefore, in this case, the porous flow does not influence the mechanical behaviour of the sample other than in the decrease of the fluid pressure within the fracture. This discrepancy is captured by the dual porosity methodology and demonstrates how the two sets of boundaries are needed to predict hydrofracture behaviour.

Test 5: 10MPa Axial pressure, 8MPa hole two pressure

Figure 80: Test 5, Experimental fracture path [136]

Figure 110 shows that with an increase in hole two's pressure, the crack path was led through both holes, in the case of experiment five the pressure in hole two overwhelmed the pressure in hole one and was sufficient enough to create a fracture itself.

The deformation profile in Figure 83 shows that the green/yellow deformation contour line (representing neutral deformation) is more central than previous numerical hydrofracture experiments where the hole two has been pressurised initiating a more unified crack throughout the specimen. The beginning of a more consistent fracture can also be spotted the deformation profile of Figure 82.

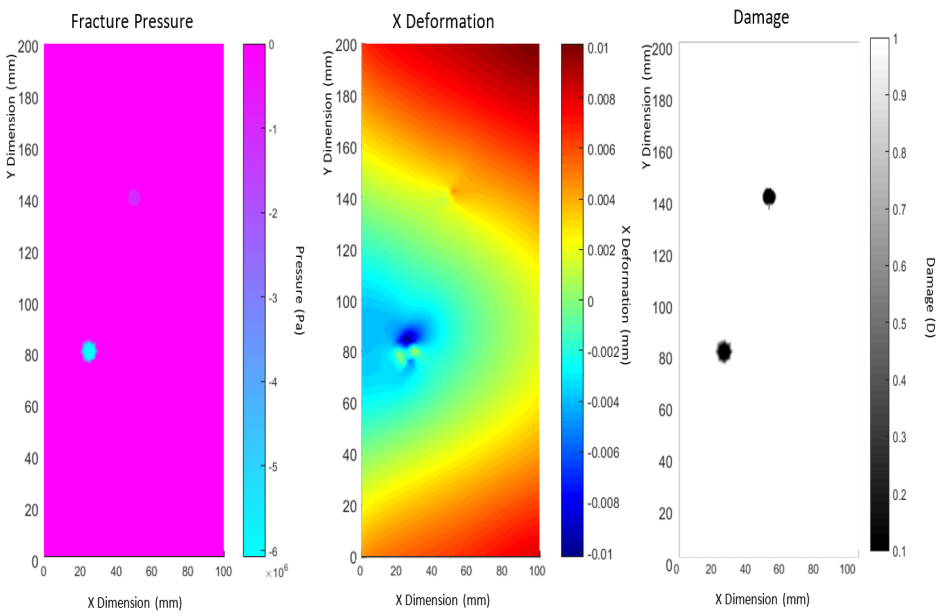

Figure 81: Test 5, Numerical Hydrofracture at time=0s showing from left to right; fluid pressure distribution, X deformation and damage distribution

At this stage it is clear that the pressure in hole two is far greater than the pressure in hole one and the effect on the X deformation is clear, as shown in Figure 81. At this point not too different from the initial plots from experiments 2-4 although is again exaggerated in terms of magnitude as expected.

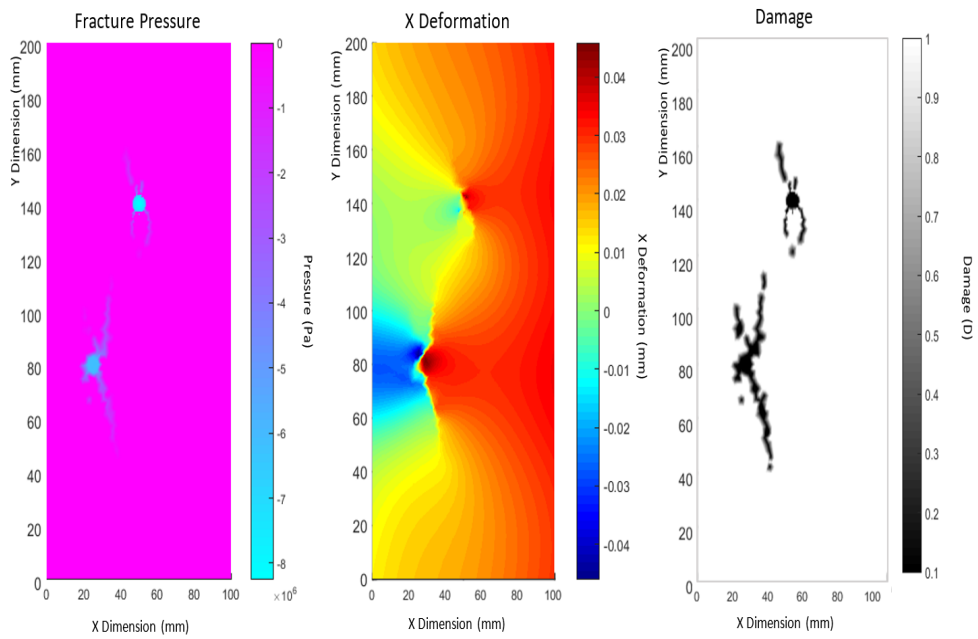

Figure 82: Test 5, Numerical Hydrofracture at time=25s showing from left to right; fluid pressure distribution, X deformation and damage distribution

Throughout all five experiments as pressure has increase a wedge like pattern has emerged in the deformation profile. This is caused by the fluid pressure exerting force on the newly developed fracture, this is shown in Figure 82.

The wedge shape shown in all numerical plot's first time snapshot deformation plots is caused by the pressure attempting to split the model in two.

In all experiments conducted the wedge is always shown to tend to the left, this is due to the placement of hole two, whereas hole one is unbiased in direction as seen in test one's results, see Figure 78. Hole two's placement leads to resilient material on the right of the hole which the pressure from hole two can act against, pushing the material surrounding hole two, leftwards.

The crack sourced from hole one seems vertical, the lower half heading towards the central section of the section where in 113 is where the two

fractures met. The crack from hole two is slanted, similar to the experimental results shown in Figure 80.

Figure 83 showcases the proposed methodology's ability to model multiple fluid driven cracks at once in an efficient manner, as with the addition of another hydrofracture computation time is similar at about 20 minutes on a standard desktop machine (I7 2018).

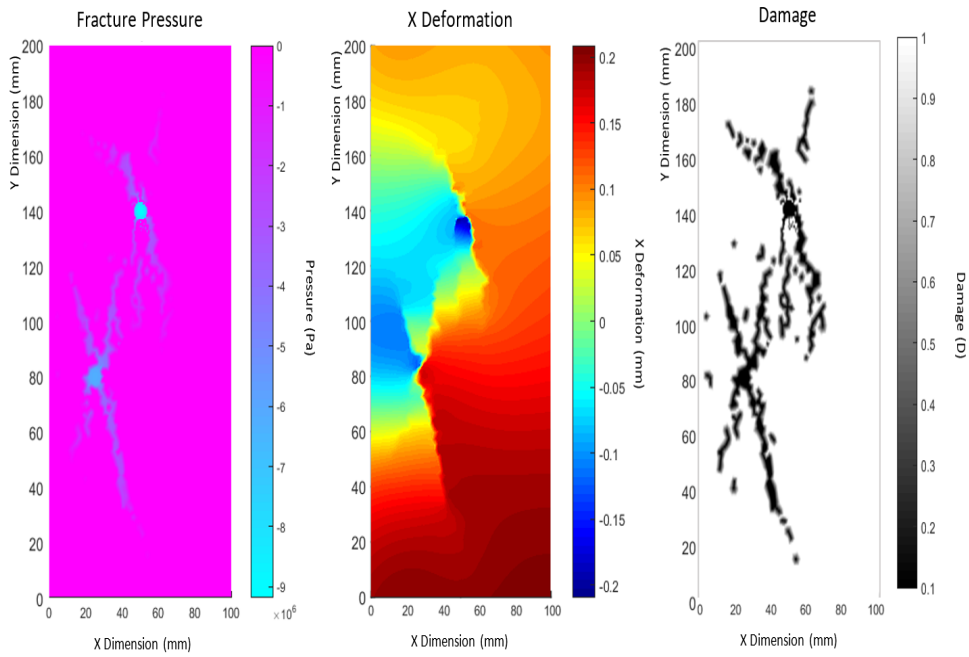

Figure 83: Test 5 Numerical Hydrofracture at time=35s showing from left to right; Fluid pressure distribution, X deformation and damage distribution

Figure 83 shows that the crack has bifurcated/branched one heading towards the left boundary, the other branch being vertical in nature, showing agreement with the experimental results shown in Figure 80.

The crack from hole one has met up with the upwards crack from hole two again agreeing with the experimental results from [136]. The two hydrofractures shown in Figure 102, both aid the opening of the other, widening the path that they both take, increasing the fracture width and flow. The fluid is

seen to be traveling from both holes into the newly created fractures aiding the fracture propagation with the built up pressure. In test one where there were only singular fractures, the apertures at the sources were far wider than the front of the fractures, creating a permeability gradient and stable fracture behaviour.

When comparing the final fracture path predicted in Figure 83 the wing crack shown in Figure 80 below hole two is predicted with reasonable accuracy. The cause for this crack's sudden change in direction can be attributed to the geometry and stress paths changing within the model/experiment with the significant cracks observed. At this point in both experiments the uniaxial load is equally split between two sections divided by the top fracture, the right section is shown in Figure 83 to be moving significantly to the right. The resulting tension creates the crack to bifurcate into a typical fracture and wing crack, this theory is further confirmed in the observed x deformation plot, where the contour of the cyan section follows closely the same pattern of a smooth curve, similar to the wing crack shown in Figure 80.

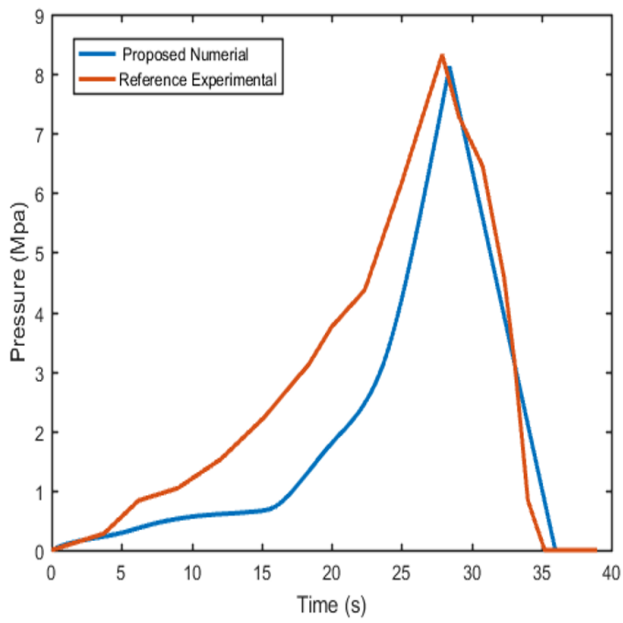

Figure 84: Test 5 fluid pressure in hole one over time (Test 5)

Figure 84 shows the pressure averaged from the elements contained within hole one over time compared to the pressure results observed in the reference experimental test. Figure 84 shows that the pressure in hole one pressurises in the numerical result at a greater rate when compared to the reference experimental results, this is due to the delayed fracture in the numerical result, with no leakage the numerical test the pressure built at a higher rate.

Figure 84 shows the experimental result builds pressure at a comparatively more stable rate when compared to the numerical pressure increases. The point of failure is clearly identifiable near the 28s mark at 8Mpa, this is the point where the fracture from hole one meets the bottom boundary in both the numerical and experiential test. The numerical result shows good agreement with the experimental pressure plot.

Two pumps are inserted into both holes as shown in Figure 80. The strength of the two pumps and influence on the structure are unknown. However, the material model, the reference paper provided are shown in table 8 and from that, some reasonable estimation can be made. However, the estimation of the pump's structural influence upon the structure is likely to introduce some error in both the proposed and reference solutions both experimentally and numerically.

Over all trends

It is clear that with the introduction of asymmetric pressure fields the crack path is influenced significantly and that the proposed methodology is fully capable of modelling the effects of non-uniform pressure fields and the resulting crack propagation. The fluid has flown into the newly propagated fractures, the pressure from which has begun to split apart the model. This creates further tension cracks as seen in the deformation plot.

The pressure plots: Figure 78 shows that generally as more pressure is introduced into the system through hole two, the lower the pressure must be in hole one for complete failure to occur in the sample. Test 3 is the only version which does not agree with this trend. The pressure increases in hole one as more fluid is pumped into the system as expected, the rate of pressure increase also increases as the fluid leaking from hole one begins to reduce the pressure gradient across hole one's boundaries and hence the rate of flow and pressure leakage decreases. This allows the pressure to build more efficiently with time due to less leakage. Once a fracture connects hole one to a boundary the fluid pressure rapidly drops as the fluid can now traverse to a drained boundary quickly and can no longer store fluid to build pressure.

5.5 Summary

The proposed methodology has been compared to several verification examples showing various aspects of the proposed methodology. The fluid-mechanical coupling aspect was tested in the one dimensional test, correctly predicted the fluid pressure response to the initial mechanical loading and fluid boundary drainage. Three hydrofracture examples from the literature were replicated with the proposed hydrofracture methodology comparing favourably with analytical and numerical results on fronts of coupling and hydrofracture behaviour prediction. Finally, the proposed model was used to re-create experimental hydrofractures in porous sandstone with non-uniform fluid pressure fields, replicating the experimental fracture paths due to the concentrated fluid pressure.

6 An Introduction to Plasticity

In reality, rocks don't exhibit linear elastic behaviour, the model previously defined, neglects plasticity and the effects of strain hardening/softening.

The following chapter demonstrates the application of a simple set of Mohr Coulomb constitutive equations in a finite strain scenario thanks to the application of the Hencky strain.

6.1 Finite deformation procedure

Fracture mechanics can lead to large local deformations at the tip.

For this reason, it is important that implemented constitutive equations and applied framework can still be applied with accuracy following large changes to a model's structure. Here the distinction is made between finite and infinitesimal strains. Infinitesimal strains assume constant volume and stationary elements, when this is not the case, theories that are based on these foundations breakdown and become unstable [23].

Finite deformation algorithms overcome the shortcomings that translations bring to infinitesimal theories by using the deformation gradient as a primary input. Deformation gradients consider only the relative movements of nodes in relation to each other as previously shown in equation 25.

However, if plasticity is required in a model, the addition of plastic strain becomes problematic, to overcome this, the Hencky strain can be considered [65].

The conversion of the strains, using Hencky's log strain, assumes that the material properties are constant during volume change, if not then the new dependency must be included within the model accordingly [20], this explains isochoric assumptions that are typically seen in finite formulations to simplify formulation procedure.

If we consider a strain on a one dimensional bar, as an integral of the change in strain as shown in equation 157.

The change in length can be denoted by a stretch vector $\boldsymbol{U}$.

$$\epsilon = \int \delta\epsilon = \int \frac{\delta l}{l} = ln(\frac{\delta l}{l}) = ln(\boldsymbol{U}) \tag{157}$$

where ϵ is strain, l is length, δl is change in length and $\boldsymbol{U}$ is the stretch vector.

In this form the infinitesimal strains can be extracted from finite deformation calculations whilst independent of translations, maintaining the constitutive framework and strength of the finite deformation methodology.

With finite deformation another issue arises when plastic strains are considered, usually plastic strains are simply added to elastic strains however the deformation gradient setup, this is not possible mathematically due to the use of deformation gradients and stretch matrices [15]. The following occurs with the addition of a plastic flow rule, in infinitesimal formulation the typical isolation of plastic strains is as described in equation 158.

$$\epsilon = \epsilon_e + \epsilon_p \tag{158}$$

where ϵ_e and ϵ_p are elastic and plastic infinitesimal strains respectively, assumed in an incremental setting [9].

Equivalent log plastic and elastic strains allow for infinitesimal plastic constitutive models to remain applicable with the use of equation 159, this is called the lee decomposition. The Lee decomposition allows for plastic constitutive models to remain applicable [23] as shown in equations 160. The log strain allows for infinitesimal constitutive models use within principal stretches [112].

$$ln(\boldsymbol{U}) = ln(\boldsymbol{U_e}) + ln(\boldsymbol{U_p}) = ln(\boldsymbol{U_e}\boldsymbol{U_p}) \tag{159}$$

where $\boldsymbol{U_e}$ and $\boldsymbol{U_p}$ are the elastic and plastic constituents of the stretch variable respectively [15]. Instead of trial plastic infinitesimal strains, trial plastic stretch matrices are used as shown in equation 160 [130].

$$[\boldsymbol{F}] = [\boldsymbol{F^e}][\boldsymbol{F^p}] \tag{160}$$

where $[\boldsymbol{F}]$ is the deformation gradient defined by equations 161 and 162 and the elastic and plastic components are $[\boldsymbol{F^e}]$ and $[\boldsymbol{F^p}]$ respectively [23].

$$[\boldsymbol{F}] = \mathbf{R}\boldsymbol{U} \tag{161}$$

where $\mathbf{R}$ is the rotational component of the deformation gradient, dictating the angle of which the stretch gradient $\boldsymbol{U}$ acts through, describing an element's deformation magnitude.

$$[\boldsymbol{F}] = 1 + \frac{\boldsymbol{du}}{\boldsymbol{dX}} \tag{162}$$

where $\boldsymbol{u}$ is deformation and $\boldsymbol{X}$ is a set of spatial coordinates or the original coordinates or in matrix form:

$$[\boldsymbol{F}] = \begin{bmatrix} \frac{dx}{dX} & \frac{dx}{dY} & \frac{dx}{dZ} \\ \frac{dy}{dX} & \frac{dy}{dY} & \frac{dy}{dZ} \\ \frac{dz}{dX} & \frac{dz}{dY} & \frac{dz}{dZ} \end{bmatrix}$$

where x, y and z are the deformed coordinates and X, Y and Z are the original spatial coordinates.

6.2 Algorithm applicability

Finite deformation relies on a Lagrangian coordinate system whereas infinitesimal relies on a Euclidean system, hence it is important to be able to convert in algebraic terms between the two systems. The following will show that infinitesimal algorithms can be applicable to finite deformation scenarios by using various assumptions. To show that this approach is possible the associated increment of deformation within a finite deformation framework is considered as shown in equation 163.

$$[\Delta \boldsymbol{F_{n+1}}] = \left[[1] - [\frac{\delta(\Delta \boldsymbol{u})_{n+1}}{\delta \boldsymbol{X}_{n+1}}]\right]^{-1} = [1] + \left[\frac{\delta(\Delta \boldsymbol{u})_{n+1}}{\delta \boldsymbol{X}_n}\right] \tag{163}$$

where $[\Delta \boldsymbol{F_{n+1}}]$ is the change in the deformation gradient of an element between each iteration. $\boldsymbol{u}$ is the deformation across the spatial coordinates $\boldsymbol{X}_n$ and n is the iterator. $[\Delta \boldsymbol{F_{n+1}}]$ is calculated by utilising the non-linear structure matrix and the accompanying fluid pressures: $\boldsymbol{p_1}$ and $\boldsymbol{p_2}$ for hydrofracture problems. The updated deformation gradient is obtained through the relationship as shown in equation 164:

$$[\boldsymbol{F_{n+1}}] = [\Delta \boldsymbol{F}_{n+1}][\boldsymbol{F}_n] \tag{164}$$

The deformation gradient can also be calculated from spatial data generated by a material formulation, using nodal deformation with the original coordinate's positions using equation 165.

$$[\boldsymbol{F}_{n+1}] = [1] + \left[\frac{\delta \boldsymbol{u}_{n+1}}{\delta \boldsymbol{X}}\right] \tag{165}$$

for completion, the deformation gradient increment can also be obtained from the two iterated deformation gradients as shown in equation 166.

$$[\Delta \boldsymbol{F}_{n+1}] = [\boldsymbol{F}_{n+1}][\boldsymbol{F}_m]^{-1} \tag{166}$$

The trial Cauchy-Green strain matrix can be described by equation 167

$$[\boldsymbol{b}_t^e] = [\Delta \boldsymbol{F}_{n+1}][\boldsymbol{b}_n^e][\Delta \boldsymbol{F}_{n+1}]^T \tag{167}$$

6.2.1 Plastic flow update

Important care must be taken numerically when calculating the plastic deformation gradient $\boldsymbol{F}_p$, ensuring appropriate elastic spring back in the finite deformation model.

Initially the Plastic velocity gradient is in a stress free given configuration is given as equation 168.

$$[\boldsymbol{L}^p] = [\boldsymbol{F}^p][\boldsymbol{F}^p]^{-1} \tag{168}$$

where $[\boldsymbol{F}^p]$ is the plastic deformation gradient and $[\boldsymbol{F}^p]$ is the instantaneous plastic gradient. The plastic gradient is calculated by assuming the same rotational component $[\boldsymbol{R}_e]$ as the elastic, as shown in equation 169.

$$[\boldsymbol{L}_p] = [\boldsymbol{R}_e]\left[[\dot{\boldsymbol{F}}^p][\boldsymbol{F}^p]^{-1}\right][\boldsymbol{R}_e]^T \tag{169}$$

The rate of plastic stretching in the current configuration is given by equation 170. Equation 170 assumes that the deformation is homogeneous with zero plastic spin.

$$[\boldsymbol{L}_p] = \dot{\gamma}_p[\boldsymbol{g}_p] \tag{170}$$

where γ_p is the consistency parameter and $\boldsymbol{g}_p$ is the plastic potential function. Combining equations 169 and 170 gives equation 171.

$$[\boldsymbol{L}_p] = \dot{\gamma}_p[\boldsymbol{R}_e]^T\frac{dg}{d\sigma}][\boldsymbol{R}_e] \tag{171}$$

Eterovic and Bathe [40] showed that, through the use of an implicit exponential integration map, the updated plastic deformation gradient can be given by equation 172:

$$[\boldsymbol{F}^{\boldsymbol{p}}_{\boldsymbol{n+1}}] = [\boldsymbol{R}^{\boldsymbol{e}}_{\boldsymbol{n+1}}]^T exp[\Delta\gamma_p\frac{dg}{d\sigma}|_{n+1}][\boldsymbol{R}^{\boldsymbol{e}}_{\boldsymbol{n+1}}][\boldsymbol{F}^{\boldsymbol{p}}_{\boldsymbol{n}}] \tag{172}$$

An updated deformation gradient is given by equation 173.

$$[\boldsymbol{F}^{\boldsymbol{e}}_{\boldsymbol{n+1}}] = [\boldsymbol{F}_{\boldsymbol{n+1}}][\boldsymbol{F}^{\boldsymbol{p}}_{\boldsymbol{n+1}}]^{-1} = [\Delta\boldsymbol{F}][\boldsymbol{F}_{\boldsymbol{n}}][\boldsymbol{F}^{\boldsymbol{p}}_{\boldsymbol{n+1}}]^{-1} = [\Delta\boldsymbol{F}][\boldsymbol{F}^{\boldsymbol{e}}_{\boldsymbol{n}}][\boldsymbol{F}^{\boldsymbol{p}}_{\boldsymbol{n}}][\boldsymbol{F}^{\boldsymbol{p}}_{\boldsymbol{n+1}}]^{-1} \tag{173}$$

where $[\Delta\boldsymbol{F}]$ is the increment of the deformation gradient, by substituting equation 173 into 171 we obtain equation 174.

$$[\boldsymbol{F}^{\boldsymbol{e}}_{\boldsymbol{n+1}}] = [\Delta\boldsymbol{F}][\boldsymbol{F}^{\boldsymbol{e}}_{\boldsymbol{n}}][\boldsymbol{R}^{\boldsymbol{e}}_{\boldsymbol{n+1}}]^T exp[-\Delta\gamma_p\frac{d\boldsymbol{g}}{d\boldsymbol{\sigma}}|_{n+1}][\boldsymbol{R}^{\boldsymbol{e}}_{\boldsymbol{n+1}}] \tag{174}$$

Then by multiplying both sides by $[\boldsymbol{R}^e_{n+1}]^T$ we obtain the stretch trial elastic stepped solution, shown in equation 175.

$$[\boldsymbol{U^e_{n+1}}] = [\boldsymbol{F^e_t}][\boldsymbol{R^e_{n+1}}]^T exp[-\Delta\gamma_p \frac{d\boldsymbol{g}}{d\boldsymbol{\sigma}}|_{n+1}] \tag{175}$$

where $[\boldsymbol{F}_t]$ is the trial deformation gradient.

The natural log of equation 175 provides equation 176, a similar method to a infinitesimal strain based constitutive model.

$$[\boldsymbol{\epsilon^e_{n+1}}] = [\boldsymbol{\epsilon^e_t}] - \Delta\gamma_p[\frac{d\boldsymbol{g}}{d\boldsymbol{\sigma}}|_{n+1}] \tag{176}$$

Equations 175 and 176 have been implemented to capture plastic deformation while maintaining a finite deformation framework. The model maintains independence from translation and rotation.

The updated Cauchy stress is obtained through the conversion shown in equation 177

$$\boldsymbol{\sigma}_{n+1} = \frac{1}{J_{n+1}}\boldsymbol{S}_{n+1} \tag{177}$$

where $\boldsymbol{\sigma}_{N+1}$ is the Cauchy stress in the new configuration, J_{n+1} is volume change in the new configuration and $\boldsymbol{S}_{N+1}$ is the Piola Kirchoff stress in the new configuration.

6.3 Constitutive Equations

The model considered is an elasto-plastic damage model; the elastic component being a Neo-Hookean model, the plastic: a Mohr coulomb criterion, the damage determined on thermodynamic energy principles. Equations 178 will be solved in a coupled format.

$$\nabla[\mathbf{C}^e_{ijkl}\nabla\dot{\mathbf{u}}_e] + \dot{\mathbf{F}}^e = 0 \tag{178}$$

where $\mathbf{C}^e_{ijkl}$ is the elastic compliance matrix $\dot{\mathbf{F}}^e$ are the internal forces due to internal stresses, these are calculated according to equations 178 and

100 [15]:

$$\mathbf{C}^{\dot{e}}_{ijkl} = \int \frac{\mu}{J}(\mathbf{b} - \mathbf{I}) + \frac{\lambda}{J}(ln(J))\mathbf{I} \tag{179}$$

where **b** is the Cauchy strain tensor and **I** is an identity matrix. **b** can be calculated as shown in equation 180.

$$\mathbf{b} = [\boldsymbol{F}]^T[\boldsymbol{F}] \tag{180}$$

and J can be calculated by finding the determinant of the deformation gradient, shown in equation 181:

$$J = det[\boldsymbol{F}] \tag{181}$$

The elastic and plastic force matrices are calculated, using the respective elastic/plastic deformation gradient and material properties.

6.3.1 Elastic component

The Elastic compliance matrix here is described by equation 182.

$$\boldsymbol{C^e_{ijkl}} = \frac{\lambda}{J}\boldsymbol{\delta_{ij}\delta_{kl}} + 2\frac{\mu - \lambda ln(J)}{J}\boldsymbol{\delta_{ik}\delta_{jl}} \tag{182}$$

with the introduction of damage, the stiffness values are expected to lower, reducing the considered continuum's mechanical resistance.

6.3.2 Plasticity component

The constitutive equation used for plasticity in this model were used from [143] due to their simplicity and relevance to the planned rock model application [28].

The general Yield function considered is shown in equation 183.

$$f_y = \tau - \sigma_m sin(\phi) - C_u \tag{183}$$

where f_y is the yield value, τ is shear stress shown in equation 184, σ_m is mean stress shown in equation 185, ϕ is friction angle and C_u is cohesion.

$$\tau = \frac{\sigma_1 - \sigma_3}{2} \tag{184}$$

$$\sigma_m = \frac{\sigma_1 + \sigma_3}{2} \tag{185}$$

The finite deformation framework considered the flow rule is written as shown in equation 186.

$$\Delta ln(\boldsymbol{U^p}) = \gamma_p \frac{\partial \boldsymbol{g}_p}{\partial \sigma} \tag{186}$$

The plastic potential function as shown in equation 187

$$g_p = \tau - \sigma_m \sin(\psi) - c \tag{187}$$

where ψ is the angle of dilation.

Equations 185 and 184 substituted into equation 186, yields the flow function in terms of σ_1 and σ_3 allowing equations 188 - 190.

$$g_p = \frac{\sigma_1 - \sigma_3}{2} - \frac{\sigma_1 + \sigma_3}{2} \sin(\psi) - c \tag{188}$$

Differentiation of equation 188 yields the equations:

$$\frac{dg_p}{d\sigma_1} = \frac{1}{2}(1 - sin(\psi)) \tag{189}$$

$$\frac{dg_p}{d\sigma_2} = 0; \tag{190}$$

$$\frac{dg_p}{d\sigma_3} = -\frac{1}{2}(1 + sin(\psi)) \tag{191}$$

Equations 189 -191 are substituted into equation 188 showing the change in principal strains can be described as shown in equations 192-194.

$$\Delta ln(U_1^p) = \Delta \epsilon_1^p = \gamma_p \frac{\delta g_p}{\delta \sigma_1} = \frac{1}{2}\gamma_p(1 - sin(\psi)) \tag{192}$$

$$\Delta ln(U_2^p) = \Delta\epsilon_1^p = \gamma_p \frac{\delta g_p}{\delta \sigma_1} = 0 \tag{193}$$

$$\Delta ln(U_3^p) = \Delta\epsilon_1^p = -\gamma_p \frac{\delta g_p}{\delta \sigma_1} = -\frac{1}{2}\gamma_p(1 + sin(\psi)) \tag{194}$$

where the sub script i=1-3 represents the designated principal axis and γ_p is the unsolved consistency variable. The consistency variable can be described as shown in equation 195 [127].

$$\gamma_p = \frac{f_y(\sigma_1, \sigma_3)}{(\alpha_p - \lambda N_\psi) - (\alpha_p - \lambda N_\psi)N_\phi} \tag{195}$$

where

$$N_\phi = \frac{1+\phi}{1-\phi} \tag{196}$$

$$N_\psi = \frac{1+\psi}{1-\psi} \tag{197}$$

With the plastic corrections procedure complete, the adjustments to a deformation gradient can be highlighted.

From the new reduced elastic stress matrix and equation 198, the elastic stretches calculated are then combined with plastic stretches to create the final deformation gradient as shown in equation 198 [28].

$$[\boldsymbol{F}] = [\boldsymbol{F_e}][\boldsymbol{F_p}] = [\boldsymbol{R_e}][\boldsymbol{U_e}][\boldsymbol{R_e}][\boldsymbol{U_p}] = \tag{198}$$

$$[\boldsymbol{R_e}] \begin{bmatrix} exp(\Delta ln(U_1^p)) & 0 & 0 \\ 0 & exp(\Delta ln(U_3^p)) & 0 \\ 0 & 0 & 1 \end{bmatrix} [\boldsymbol{R_e}] \begin{bmatrix} exp(\Delta ln(U_1^e)) & 0 & 0 \\ 0 & exp(\Delta ln(U_3^e)) & 0 \\ 0 & 0 & 1 \end{bmatrix}$$

Note: when the internal elastic forces are recalculated for the next iteration, the initial spatial coordinates must be accounted for to ensure realistic behaviour. This is to ensure that if and when driving forces return to zero the resting position accounts for plastic deformation but is still stable as shown in Figure 85. If this was not considered, then in stage 3 of Figure 85 the x deformation would be incorrectly represented by 0.91, leading to an internal elastic force resisting nothing, causing model instability. Note: A 1 % plastic

strain was allowed before all resistance was assumed to ceases. this was done to replicate softening behaviour.

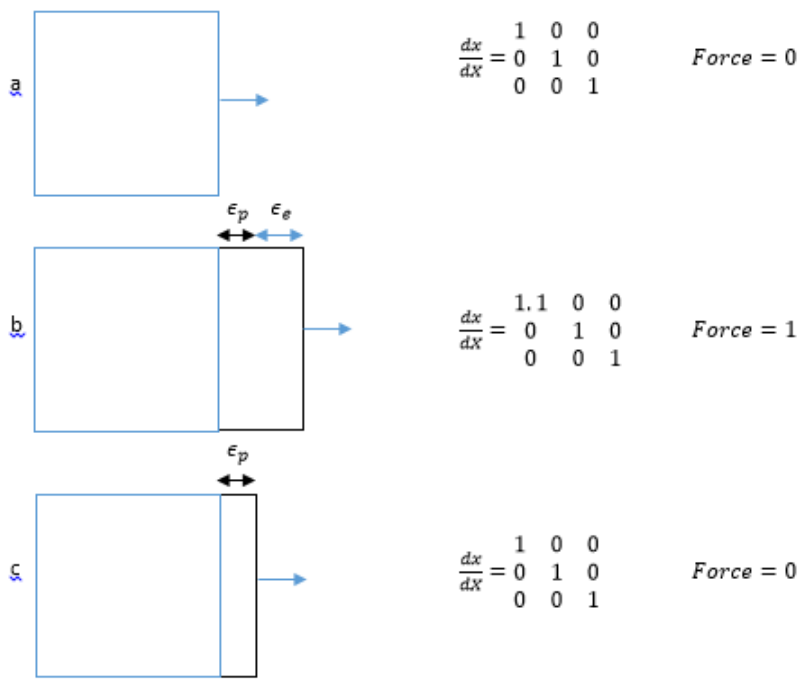

Figure 85: Example of updating spatial coordinates with plastic considerations

6.3.3 Plastic energy dissipation

The damage law used in this constitutive model is energy based, for this reason it is important with the introduction of plasticity and hardening, that the energy of these be considered. The hardening function allows for additional energy to be stored in a recoverable method; this concept is explained in Figure 86.

When plasticity behaviour is active the particles are rearranged due to plastic flow, initially into a softer configuration, this is represented by the hardening/softening regime. During the hardening/softening regime, the stiffness of the material can increase/decrease allowing for greater overall

internal energy storage.

It can be seen on the left of the Figure 86 that after yielding the material can store more energy due to softening compared to purely elastic stored energy. However due to yielding and reduction in stiffness, if the material was unloaded and reloaded the energy capacity is reduced. What remains is the energy dissipated through plastic flow, this function must be dependent on the flow function. Figure 86 shows on that after unloading that the amount of energy that can be absorbed is reduced due to plastic softening, hence the lower stiffness.

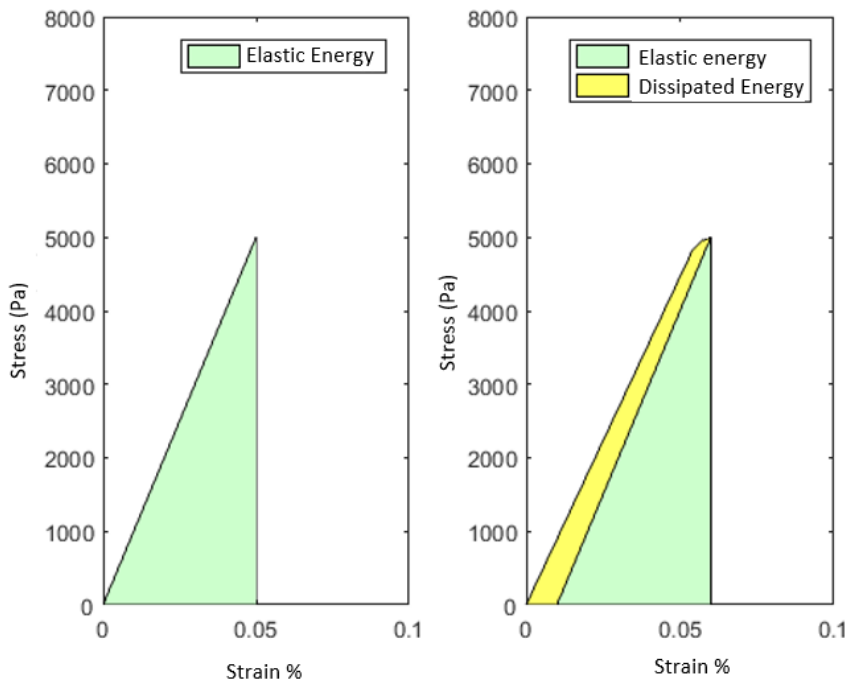

Figure 86: Energy usage in a constitutive model

The free energy functions used in this model describe how much energy is stored internally as loading progresses. These are derived from consideration of averaging the strengths of long chain molecules. The constitutive model used for determining both the compliance matrix and free energy functions in this paper is named the Neo-Hookean model [28]. Here we adjust in order to

account for the effect of plasticity on energy accumulation in the continuum in consideration of plastic deformations offsetting spatial coordinates using a modified version for shear calculation, shown in equations 199 - 201.

$$dE = \frac{1}{2}\mu(I_c^* - 3) \tag{199}$$

where dE is bulk energy, μ is the shear modulus and I_c^* is the trace of the Cauchy strain vector, a vector of the principal strains.

$$I_c^* = trace\left(\begin{bmatrix} \frac{dx^e+dx^p}{dX_p} & \frac{dy^e+dy^p}{dX_p} & \frac{dz^e+dz^p}{dX_p} \\ \frac{dx^e+dx^p}{dX_p} & \frac{dy^e+dy^p}{dY_p} & \frac{dz^e+dz^p}{dX_p} \\ \frac{dx^e+dx^p}{dZ_p} & \frac{dy^e+dy^p}{dZ_p} & \frac{dz^e+dz^p}{dZ_p} \end{bmatrix} \begin{bmatrix} \frac{dx^e+dx^p}{dX_p} & \frac{dy^e+dy^p}{dX_p} & \frac{dz^e+dz^p}{dX_p} \\ \frac{dx^e+dx^p}{dX_p} & \frac{dy^e+dy^p}{dY_p} & \frac{dz^e+dz^p}{dX_p} \\ \frac{dx^e+dx^p}{dZ_p} & \frac{dy^e+dy^p}{dZ_p} & \frac{dz^e+dz^p}{dZ_p} \end{bmatrix}\right)$$

where dX_p, dY_p and dZ_p are the spatial coordinates, accounting for plastic deformation.

$$d\tau = \frac{1}{2}\lambda log(J) - \mu log(J) \tag{200}$$

where $d\tau$ is the surface energy, λ is the Lamé's material constant and J is volume change calculated according to equation 201.

$$J = det\left(\begin{bmatrix} \frac{dx^e+dx^p}{dX_p} & \frac{dy^e+dy^p}{dX_p} & \frac{dz^e+dz^p}{dX_p} \\ \frac{dx^e+dx^p}{dX_p} & \frac{dy^e+dy^p}{dY_p} & \frac{dz^e+dz^p}{dX_p} \\ \frac{dx^e+dx^p}{dZ_p} & \frac{dy^e+dy^p}{dZ_p} & \frac{dz^e+dz^p}{dZ_p} \end{bmatrix} \begin{bmatrix} \frac{dx^e+dx^p}{dX_p} & \frac{dy^e+dy^p}{dX_p} & \frac{dz^e+dz^p}{dX_p} \\ \frac{dx^e+dx^p}{dX_p} & \frac{dy^e+dy^p}{dY_p} & \frac{dz^e+dz^p}{dX_p} \\ \frac{dx^e+dx^p}{dZ_p} & \frac{dy^e+dy^p}{dZ_p} & \frac{dz^e+dz^p}{dZ_p} \end{bmatrix}\right)$$

$$W = d\tau + dE \tag{201}$$

where W is total work.

The plasticity methodology implementation is shown in algorithm 4.

Algorithm 4 Fracture procedure with plasticity

1: Set initial parameters; C_u, μ, ν, mass and boundary conditions
2: **while** $t < t_{full}$ **do** ▷ run time of simulation
3: **while** $\delta\Delta log(\boldsymbol{U_p}) > 0.05$ **do** check1
4: Assume elastic case on first increment of each time step
5: Derive deformation gradients from deformation and spatial coordinates by $\boldsymbol{F} = \frac{du}{dX}$
6: Calculate internal pressures and self-weight and put in matrix forms; $\dot{\mathbf{F}} = \int \frac{\mu}{J}(\mathbf{b} - \mathbf{I}) + \frac{\lambda}{J}(ln(J))\mathbf{I}dxdy$
7: Solve for step deformations: $\nabla[\mathbf{C}^e_{ijkl}\nabla\dot{\mathbf{u}}_e] + \dot{\mathbf{F}}^e = 0$
8: Find new deformation gradient $[\boldsymbol{F_{n+1}}]$
9: Decompose into elastic rotation and stretch component; $[\boldsymbol{R_{n+1}}]$ and $[\boldsymbol{U_{n+1}}]$
10: Find equivalent Hencky strain $\epsilon = log([\boldsymbol{U_n} + \mathbf{1}])$
11: Assume $[\boldsymbol{R^p_n}] = [\boldsymbol{R^e_{n+1}}]$
12: Check yield criteria for each element: $f = \tau - \sigma_m sin(\phi) - c$
13: Calculate trial plastic strains
$\Delta ln(\boldsymbol{U^p}) = \gamma_p \frac{\partial \boldsymbol{g_p}}{\partial \sigma}$ $g_p = \sigma_1 - \sigma_3 \sin(\psi)$ $\gamma_p = \frac{1}{h}\frac{\delta f}{\delta \sigma}$ $h = -(\frac{1}{3}(1 + sin(\phi)sin(\psi)))^{\frac{1}{2}}$
14: convert plastic and elastic strain to trial stretch vectors
$[\boldsymbol{U_p}] = [1 + \epsilon_p, 0; 0, 1 + \epsilon_p]$ $[\boldsymbol{U_e}] = [1 + \epsilon_e, 0; 0, 1 + \epsilon_e]$
15: Find new deformation gradients and volume change, assuming previous rotation gradient $[\boldsymbol{F_p}] = [\boldsymbol{U_p}][\boldsymbol{R_e}]$ $[\boldsymbol{F_e}] = [\boldsymbol{U_e}][\boldsymbol{R_e}]$, $J_e = det(\boldsymbol{F_e})$ and $J_p = det(\boldsymbol{F_p})$
16: Calculate energy in each element and compare energy capacity an assign damage
$\Delta D = \min(\frac{W}{R_0}, 1)$
$D = max(D - \Delta D, 0.1)$
17: **End While** $\delta\epsilon > 0.05$
18: Finish current time step, $t = t + 1$
19: Goto line 2
20: **End while** $t < t_{full}$

6.4 Finite deformation plasticity verification

In this section the plasticity equations and procedure within a large strain framework will be verified on a simple/ classic foundation bearing problem.

The Prandtl solution to bearing capacity failure has been used to verify the plastic constitutive equations implementation. First background on the problem will be presented, followed by results produced by the proposed plasticity code and Abaqus.

The plasticity failure mechanism of a pad foundation according to Prandtl is shown in Figure 87.

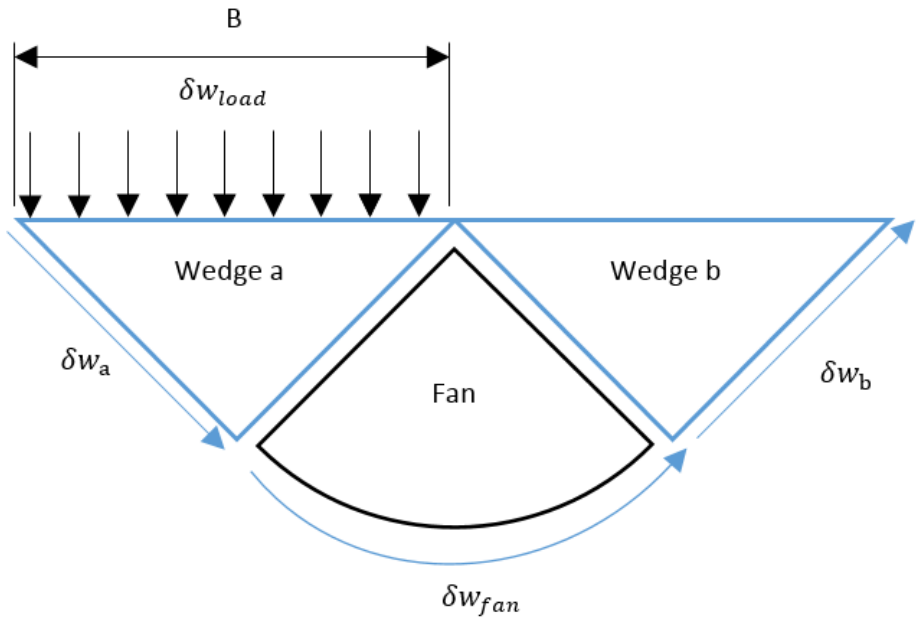

Figure 87: Upper bound solution by Prandtl for bearing capacity

where δw_{load} is the displacement of the load F and hence the work done by the load δW, is as shown in equation 202.

$$\delta W = B w_{load} \tag{202}$$

where, δw_a and δw_b are the slip plane displacements of the two failure wedges and δw_{fan} is for the fan. B is the width of the foundation

The internal energy accumulated can be calculated by considering the cohesion along the boundary of the failure envelope; two wedges and a fan.

Table 9: Internal energies

Section	Length	Displacement	Work done
Wedge a	$\frac{1}{\sqrt{2}}B$	$\sqrt{2}\delta w_f$	$C_u B \delta w_f$
Wedge b	$\frac{1}{\sqrt{2}}B$	$\sqrt{2}\delta w_f$	$C_u B \delta w_f$
Fan	πB	δw_f	$\pi C_u B \delta w_f$
Total			$(2+\pi)C_u \delta w_f$

A slip plane failure is assumed for the failure of the foundation. The values calculated in the second column of table 9 show the length of the failure surface that appears on the given wedge, the length that is supported by soil cohesion. The displacement describes the distance that forces generated by cohesion act through.

With equilibrium assumed the failure load can be calculated thus equation 203 shows:

$$\delta W = B w_{load} \delta w_f = (2+\pi) C_u \delta w_f \tag{203}$$

therefore:

$$B w_{load} = (2+\pi) C_u \tag{204}$$

To ensure that the plasticity component of the model is working, a simple foundation pad failure process has been selected from the literature. In the paper by Nazem [111] [110], the considered model verification is 4m by 8m, the pad 0.5m long as shown in Figure 88.

To accommodate this the pad force for simplicity was modelled as a small square placed on the pad to re-create the load, the load is incrementally increased, the resultant deformation of all points within the pad are recorded

and compared to a reproduced Abacus model with Mohr Coulomb plasticity model.

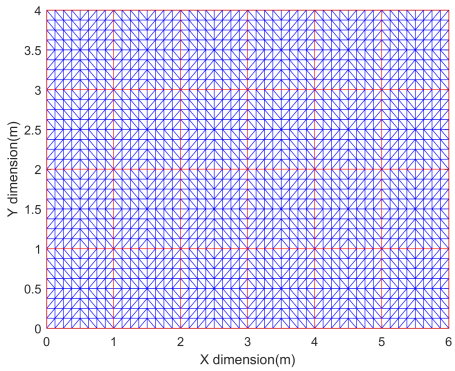

Figure 88: Pad verification model layout

The material properties used in this verification can be found in table 10. For this simulation both the fluid coupling and damage model were disabled to allow a clearer comparison of the plastic methodologies.

Table 10: Material properties for numerical pad experiment

Young's modulus	E	2 MPa
Poisson's ratio	ν	0.3
Angle of friction	ϕ	15
Dilation angle	ψ	15
Cohesion	C_u	2 kPa

In this model the pad is loaded incrementally, here at a constant rate.

The analytical approach assumes the two wedge's self-weights counteract each other but for simplicity model symmetry is used and self-weight is ignored in both the proposed and Abaqus model.

The applied load required for failure is related to the cohesion as previously discussed, hence the results shown in Figure 89 have their vertical load normalised by the cohesion, in this case: $2 \times 10^3 Pa$.

The bottom boundary was considered fixed in all directions, the two edge boundaries only fixed in the x deformation and the rest of the boundaries were considered free. The model was calculated assuming plane stress conditions. Pad deformation was calculated by averaging the displacement of the nodes contained in the pad region, this calculated average is shown in figure 89.

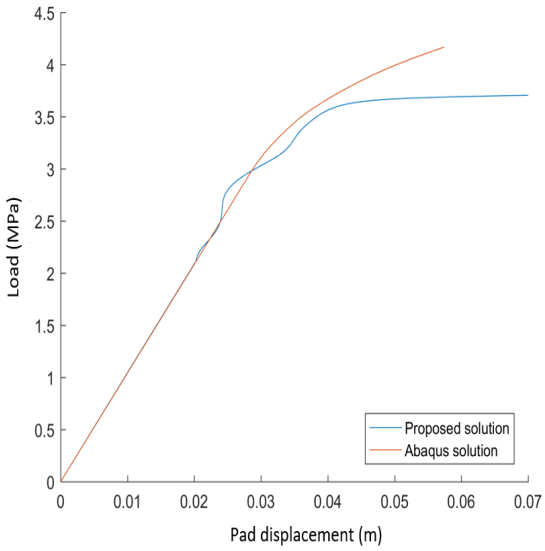

Figure 89: Load displacement graph for a loaded foundation comparing; Abaqus output (yellow) and proposed solution (blue)

As seen in Figure 89 the elastic response is similarly predicted when compared to the Abaqus solution showing good agreement of the Neo-hookean finite model with the linear elastic model utilised by Abaqus, showing similar stiffness.

Figure 89 also shows similarities in prediction of the yield occurring when the load is at 2MPa having deformed 0.03m, after this point the prescribed 1% strain softening behaviour and wedge failure take place.

The transition to perfectly plastic behaviour is uneven, starting at a pad displacement of roughly 0.025m where a sudden increase in stiffness is evident. The proposed model compensates at a pad displacement of 0.035m

becoming more stable once fully plastic in the failing region. This deformation pattern indicates that more consistency is required particularly in the yielding component with more care taken on internal stress calculations during yield. The model becomes unstable at 0.07m of pad displacement, after this point no results could be produced.

The point of failure/ultimate failure load is similar to that of the solution from Abaqus; roughly at the load of 3.95MPa and pad deformation of 0.03m. The proposed model shows a slight premature failure when compared to the 4.1MPa failure prediction from Abaqus. The proposed solution is more stable than the Abaqus solution, shown by the prolonged strains that are allowed to occur becoming unstable at 0.07m of deformation as shown in Figure 93.

The steady strain softening behaviour can be spotted in the proposed solution, to the point where the modelled soil material can no longer provide any resistance to the applied load, hence the large strains that occur post yield.

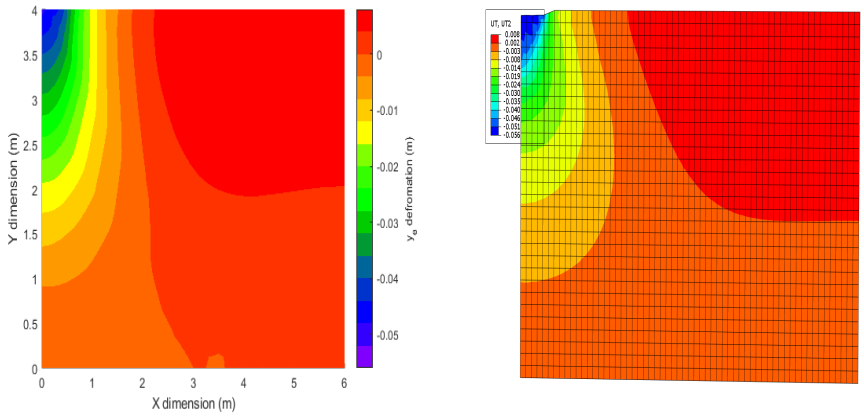

Figure 90: Elastic deformation from proposed solution (left) and Abaqus solution (right)

Both models shown in Figures 90 and 91 demonstrate the expected wedge failure mode exhibited in Figure 87. The wedge clearly identifiable in both Figures 92 and 93. The model deforms downwards local to the pad and the

adjacent material heaves to accommodate the motion of material. The x deformation direction is conforming to the flow of material to accommodate the predicted heaving in the observed failure mode.

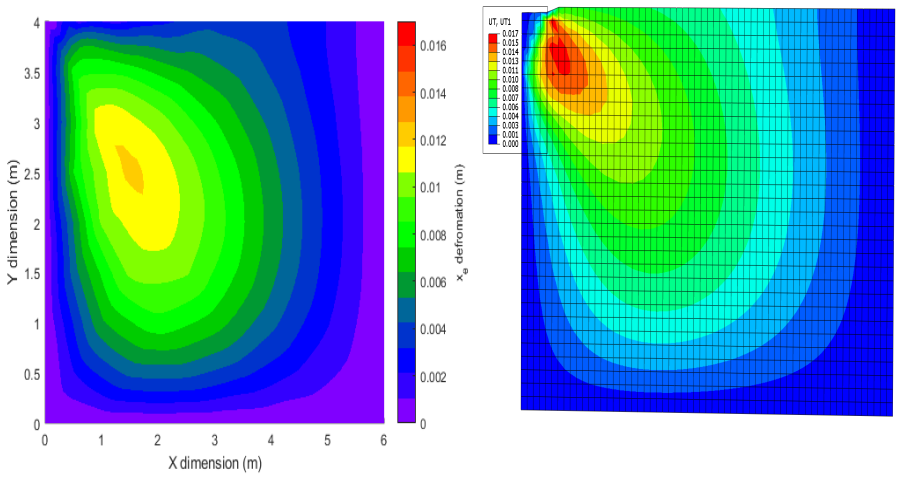

Figure 91: Elastic deformation from proposed solution (left) and Abaqus solution (right)

The magnitudes of the calculated deformations are similar, the maximum elastic y deformation from the proposed solution is -0.04m and a maximum heave deformation of 0.006m. When compared to the Abaqus solution of -0.05 pad deformation and 0.005m heave.

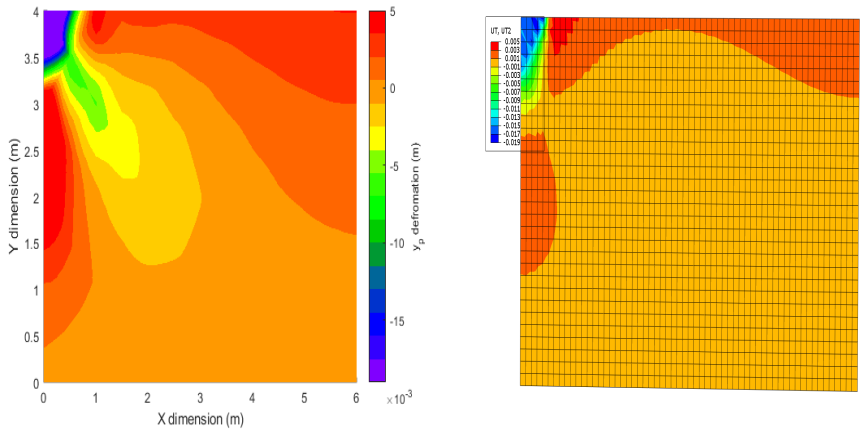

Figure 92: Plastic deformation from proposed solution (left) and Abaqus solution (right)

Both models demonstrate the expected failure mode shown in Figure 87, the wedge is identifiable again in both Figures 93 and 92.

Figure 92 and 91 show the Abaqus plastic deformation plot in both the x-x and y-y direction at point of yield whereas Figure 93 shows the deformation profiles produced by the proposed solution using the Hencky strain transformation.

There is a slight plastic heave predicted in both models, showing good agreement. The proposed solution over predicts the plastic deformation at a magnitude of 0.3m. The calculated plastic deformation from the Abaqus solution predicts a maximum y deformation of 0.17m.

The model deforms local to the pad and the adjacent material heaving to accommodate the motion similar to that shown in the plastic x deformation plot shown Figure 90 comparing the proposed solution vs the output Abaqus solution.

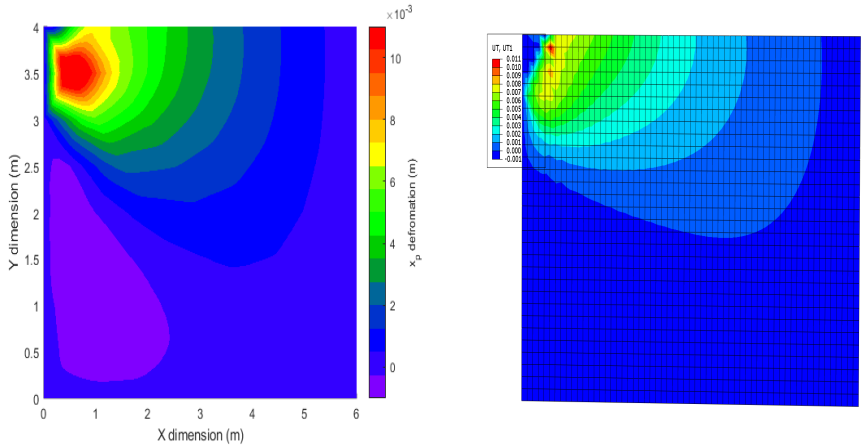

Figure 93: Plastic deformation from proposed solution (left) and Abaqus solution (right)

The deformation in the x direction is conforming the flow of material to accommodate the expected heaving. Most deformation is local to the applied load, decreasing with distance from the load.

Figure 91 and 93 shows that using an equivalent Hencky strain allows plastic theorems, in this work: Mohr coulomb is applied within the finite deformation framework to capture realistic soil behaviour.

As expected after observing the relevant deformation plots and failure modes in Figures 93 and 92 the yield occurs along the failure plane of the wedge mechanism in the top left of the model. This is confirmed in figure 94

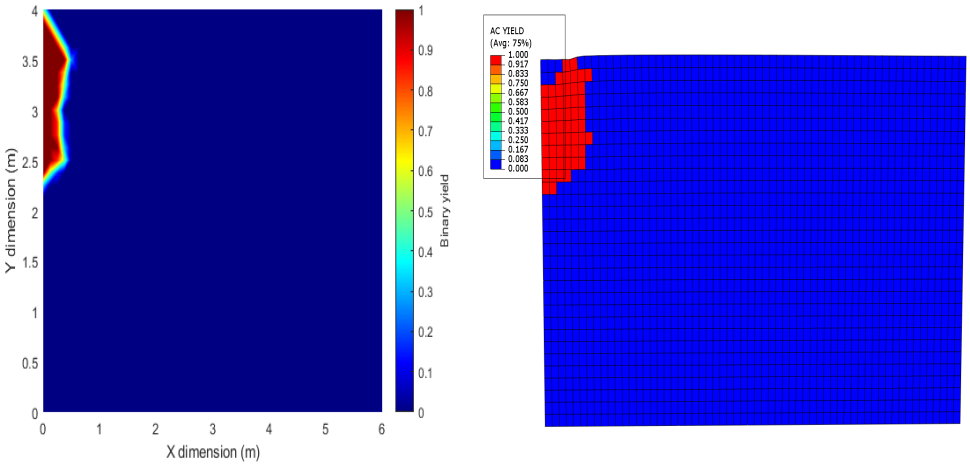

Figure 94: Plastic yield plots from proposed solution (left) and Abaqus solution (right)

For completion the specific points of yielding are shown in Figure 94.

6.5 Summary

The Hencky strain conversion has been applied to an infinitesimally based constitutively based model Mohr-Colomb to a large strain framework. The resultant methodology is compared with the classical solutions for the failure surface of a pad foundation along with a numerical Abaqus solution. The results for this numerical experiment showed reasonable agreement.

The produced plasticity framework is stable and applicable to the hydrofracture problem but requires more rigorous validation within the context of fractures/hydrofractures, especially within the context of hydrostatic stress confinement. The developed plasticity framework has issues with maintaining sign, magnitude and boundary conditions, further development is required to couple the elastic and plastic behaviours especially in regard to behaviour at considered boundaries.

7 Analysis

The initial goal of this thesis was to model complex hydrofractures with relatively low computational demand and minimal input variables. Through the verification a suitable hydrofracture model has been produced and validated against experimental works. The methodology offers a numerical model capable of solving many hydrofracture problems. However, the developed framework needs to be built upon for practical application as the following analysis will highlight.

7.1 Minimisation algorithm analysis for fracture

The fracture framework in this thesis is based on the pre-existing work by Fracfort and Marigo on minimisation work with a pre-existing finite deformation constitutive model; the Neo-Hookean model [39], introduced in section 3. This model is derived from strain invariants of a free energy function [15] which gives the model its unique properties. Using this approach; internal stresses and stored energy, the methodology is simplified.

In this thesis the methodology is applied to more complex fracture scenarios, see section: 3.4 and 5.4 for examples.

It has been shown that the fracture methodology is capable of predicting experimental fracture path results with reasonable accuracy as shown in with a range of verification examples discussed in section 3.4.

The proposed model is computationally simple to solve, many variables are reused in the calculation of both the internal stresses, deformation, energy and damage.

The framework's shortfall is that it assumes an isotropic material and a specific constitutive model originally developed for homogeneous isotropic vulcanised rubber [61]. The proposed model can be adapted for heterogeneous behaviour, however the relation between the Láme constant and shear modulus must be accounted for in order to maintain the model's benefits.

Isotropic behaviour is inherently baked into the derivation of the free energy function utilised and therefore a new free energy function and con-

stitutive model would be required in order to account for more complex anisotropic materials, limiting the proposed methodologies capabilities.

The minimisation process can be applied to any constitutive model if there is a method for calculating accumulated damage through energy and stored mechanical energy. By considering two types of energy during the fracturing process, this specific application of the minimisation process of the stored energy and fracture energy neglects the effect of kinetic energy and is therefore limited to quasi-static load cases.

The minimisation algorithm could be applied by alternating between additional fields of energy however as the process would be decoupled the amount of iterations between the considered energies would escalate the computational demand of the algorithm, compromising the main strength of this approach.

In this work the methodology cannot account for the work done by boundary forces they are neglected and replaced by displacement boundary conditions.

The simple slit verification example produced reasonable results in the prediction of fracture initiation and propagation as shown in section 3.4. Created inclusions at the top and bottom of the sample were incorrectly accounted for in post failure behaviour when the fractures were compression or shear-tension based, offering incorrect residual strength. This is most evident in the 90 degree slit experiment.

The minimisation algorithm calculates the gradient of energy terms throughout the domain as described in section 3. When a branch fracture occurs and both branch fractures are equal in magnitude the algorithm is reasonably accurate in predicting branching behaviour. The issue arises when the two branches are not equal in magnitude, the algorithm can tend to favour the dominating branch and as a result overestimate the larger crack and under estimate the smaller branch, similar to the fracture shown in section 3.4 Fig-

ure 38. The prediction algorithm by the minimisation approach becomes more accurate by varying the amount of allowed newly damaged material, increasing the capability of picking up on branching behaviour.

It is mentioned that as this methodology was developed for hydrofractures where the main driving force is the pressurised fluid. However, with all hydrofracture methodologies considered the final goal is to model large fracking scenarios where both hydrofractures and typical fractures are required to be modelled simultaneously [136]. Therefore, if the model is taken forward this problem needs to be overcome for large scale applications.

The issue with incorrectly predicting branches was overcome in sections: 3.4 and 5.4. This was overcome by shortening the time step used in the numerical simulation and reducing the minimisation parameters k_e and $v(k)$, shown in equation 15. These values improved the ability to predict unusual branching fractures with less user input, consequentially however, the simulation time increased.

In most results obtained, the values of k_e and $v(k)$ were modified to ensure that any expected branching behaviour was captured by the proposed methodology, which again, was only possible with pre-existing data sets and is not feasible in practical application.

The damage model utilised in this model is simplistic, but is based on theory which offers up wide range of uses, hence why it is applied in many other works [85] [86] [81] [102] due to its simplicity and inherent flexibility of the damage approach.

The damage values in this thesis are based on an element by element basis, making all produced results to an extent, mesh dependent. In most of the numerical experiments undertaken in this thesis without complex branching behaviour fine meshes were not required. Some coarse meshes of 100 elements can be used for modelling test one in the non-uniform hydrofracture experiment, shown in section 5.4. this was only possible because the load case was the fluid pressure splitting the model in two.

In the single slit numerical slit experiments carried out, the newly damaged elements were considered to maintain their mass and some of their original strength. For added accuracy additional data would be required to determine post fracture mass and strength accurately.

Mass reduction was not an issue in the presented methodology as self-weight was never the driving force for fracture initiation in the undertaken numerical tests. However, reduced strength played a key part in post fracture behaviour. The self-weight of voids i.e. in the slit numerical experiment and the non-uniform experiment the mass densities were set as $0kg/m^3$.

Furthermore, the friction between fracture walls was not captured and would require significant changes in order to implement within the existing framework.

This issue was solved for the 0 degree slit example in an ad-hoc manner, see Figure 34 for further details. However, this was a specific case where the expected result was already observed experimentally. The fix was trial and error until the correct volume penalisation was found. In reality this is not possible unless a range of experimental data is already available that is applicable to the scenario.

The proposed model proved reasonably stable during numerical experiments. In the numerical experiments from section 3.4, stability was never truly tested due to the slow rate of loading of 0.05 mm/s. The model could take on deformation driven loads of 20 mm/s and be stable until the 200mm tall sample was compressed 100mm, which was sufficiently stable for the needs of the numerical verification.

In the single slit experiment, there were no signs of damage until $0.8mm$ of deformation, this value could have been jumped to with a single large time step then resuming at 0.05 mm/s and would have maintained the same degree of accuracy. In order to achieve this however a large degree of experience about the modelled test would be required.

The single slit examples in section 3.4 acted with the slit's position known ahead of time and does not reflect a realistic, practical fracture initiation scenario.

The variable fracture energy term used to determine the capacity of materials was calculated from pre-existing stress-strain graphs provided and would not always be available in practical scenarios, especially in regard to hydrofractures.

Plane stress issues: fracking scenarios are vast in size and need to account for three dimensional space. The current implementation is plane stress and cannot account for realistically fractures/ hydrofractures in its current state.

A key strength of the minimisation methodology is the model's capability to capture multiple fractures propagating. The minimisation framework evaluates the whole continuum's energy field and therefore every element is considered whether damaged or not, therefore the computational demand of the utilised methodology does not increase with additional fractures. However, in order to model several fractures accurately the mesh must be adequate for fractures, which can rack up the computational cost. This drawback would be solved with dynamic mesh refinement.

An issue with the considered framework is the initiation of newer fractures after some fractures have already gathered momentum. This occurs when there is more energy included within pre-existing fractures, the energy included within fracture initiations far smaller and therefore the existing fractures take priority.

The large deformation framework allows the inclusions created during fracture to remain stable. The main cause of the proposed methodology becoming unstable was through in admissible deformation. This allows some post failure behaviour to be observed in the single slit experiments after a small chunk fractures off. By reducing the energy contributions of fully damaged elements they will no longer dominate fracture behaviour.

7.2 Hydrofracture algorithm analysis

In the literature review pore network models were mentioned as the most accurate solution for modelling multiple flow paths through rocks. Pore network models are cumbersome computationally and are difficult to implement with fracture models due to their complex structure when compared to continuum fracture prediction approaches.

The presented work uses a damage model with a dual porosity flow framework in order to capture realistic flow networks created from hydrofractures. All simulations were carried out on a single machine on an I7 processor (2016; solutions calculated in under an hour).

The fluid methodology derived in section 4.1 assumes fully saturated soil/rock. Therefore, the methodology is unsuitable to account for dry or partially dry scenarios. During fracking it is not uncommon for fracking fluid to come a across dry voids, losing fluid pressure. This loss in pressure is important in determining the length and direction of created fractures.

Fractures occur in three dimensions, these fractures carry flow also in three dimensions. Three dimensions are required for the realistic analysis of hydrofracture problems. The main challenge with extending to the third dimension is a problem of available computational resources.

The Mumford Shah functional is easily posed in three dimensions, however the solving of the three dimensional equations is far more difficult to solve in an accurate timely manner [87]. A three dimensional version of the free energy function would be capable of modelling the energy with a three dimensional domain, the challenge would rise from the consideration of additional fracture modes. With additional energy paths, further development would be required in order to implement the equations similarly. Further computational demand could be reduced by compartmentalising the minimisation algorithm more intelligently at fracture tips instead of constant monitoring the full domain at each time step/iteration. This would compromise accuracy somewhat as some energy would be disregarded however

resources saved via compartmentalising could be better spent elsewhere such as finer mesh.

The minimisation concept applied in this thesis considers the entirety of the domain when evaluating possible fracture propagation. With the advent of fluid driven fractures, satisfying the minimisation algorithm and finding the energy minimal whilst maintaining pressure equilibrium has increased computational demand. However, it need only be applied in regions that are already damaged, potentially reducing computational demand. It is reasonable to assume that fractures will only initiate from pre-existing fractures as there is an abundance of fractures in shale rock and the driving force from fluid is easy. This is also why the failure of predicting the fracture path in the intact sample does is less significant in the context of fracking problems.

In the formulation of the coupled dual porosity framework the traction force component was neglected for simplicity, this does reduce the capacity of the framework. However, in the context of fracking, shale rock typically is under constant confinement with no active external forces applied [122].

Confinement can be modelled artificially by displacement forced boundaries when knowing the Young's modulus of the rock modelled and even calibrated to ensure the correct stress conditions throughout the work are maintained. Confining stress has not been tested with this methodology due to the difficulty of testing such conditions experimentally, hence no data to validate the results could be sourced in the literature.

In section 7.1 the applied minimisation would sometimes favour one fracture over another when running through the minimisation loop which compares different damage compositions and how much either energy either store.

This problem changes with the introduced fluid methodology. Instead of sometimes having only one fracture instead of a branch, branching fractures are almost encouraged with the fluid aspect introduced into the minimisation algorithm. The encouragement results from the minimisation algorithm realising that branched fractures spread pressure and can dissipate energy at a greater rate, hence the large degree of branching shown in Figure 103.

To ensure fluid can flow into newly created fractures, the minimisation loop is rerun with the new fracture permeability in place, letting fluid pressure in the system to exchange further energy in the system. This can be simply remedied by reducing the number of reset loops during the minimisation algorithm, however as a trade of the fluid flow is stagnated, no longer capturing fluid lag behaviour.

In the pressurised Penny Crack verification example from sections 5.2.1 and 5.3: the approach was stable primarily due to the fracture driving forces being minimal and not highly localised when compared to the locality of fluid pressure applied to the walls of the penny shaped fractures.

In the application of high fluid pressure in section 5.4: there were occasionally cases where damaged elements would be subject to a high local fluid pressure and undergo large inadmissible displacement. This was solved in many cases by reducing the time step and pressure changes. This allows for smoother pressure changes and stable behaviour in the implemented framework. This was a particular issue in the non-uniform verification examples where fully saturated voids were modelled as massless damaged elements. To fix this an intervention was made in the algorithm to improve stability, this is not reasonable in practical application, as it requires knowledge ahead of the test.

The Darcy equations used in the derivation of the fluid methodology shown in section 4 assumes steady saturated flow, which cannot account for fluid momentum. Which in the case of realistic fracking scenarios can be important [14].

Another assumption made during the derivation of the fluid methodology was isotropic, homogeneous permeability and porosity in all directions. In the case of rock fabric there is usually a tendency for fluid pressures to favour flow in the direction of the rock fabric or pre-existing fractures or both. The

proposed methodology would require additional work in order to account for the natural heterogeneity of rock.

In chapter 3, the fluid methodology is combined with a damage methodology in order to capture when porous material becomes fractured, capturing an associated change in permeability and porosity. The change in these material properties are numerically harsh and the transition is not reflective of what occurs in hydrofracture scenarios, albeit effective modelling at computationally low demand.

Ignoring the changes in material properties due to hydrofracture propagation leads to the question of what occurs to the fluid pressure in a considered element while transitioning. It is assumed in this approach that the fluid pressure is conserved and carried over from the porous pressure p_1 to fracture pressure p_2 initially. This pressure is recalculated in the following algorithm iteration to account for the new displacements and the resulting pressure changes, capturing fluid lag to an extent. This is reasonable for the verification examples considered as the porous pressure has not been significant when compared to the fracture pressures and have not led to fracture within considered context [124].

Fluid lag is captured within the framework, as shown in the non-uniform hydrofracture experiments however, the fluid was still calculated in a quasi-static manner not transferring the fluids momentum over in to the methodology, further specialised testing would be required to verify this aspect of the model.

Throughout this thesis the proposed methodology is compared against several pre-existing analytical solutions, such as the; one dimensional consolidation problem in section 5.1, pressure filled penny crack dimension and the pressure distributions around a fluid filled fracture in section 5.

The consolidation problem used a fluid density of $0kg/m^3$ in order to reduce complexity, this should not affect the result but rather the rate of con-

solidation. However this discrepancy has been shown in other works to not affect the consolidation curve significantly when compared to analytical solutions [87].

For the continuous flow penny crack example in section: 5.3, the analytical fracture equation 155 assumes constant permeability in the crack, however with the cubic flow equation used in the framework implementation, the permeability of the fracture is not constant. Although, the fracture opening in this particular verification does not vary significantly enough to affect the result in this case readers should be mindful of the discrepancy.

In the two penny crack fractures shown in sections 5.2.1 and 5.3 the domains are considered are 20+ times larger than the initial crack length compared to the initial penny fracture. This gives the penny fracture independence from imposed boundary conditions, hence the differing pressure profiles and the varying appearance of two dimensional consolidation behaviour.

The implemented damage model cannot model micro fractures or their flow. These are estimated with Darcy's equations. The implemented damage model works on an element basis and is inherently mesh dependent with the addition of fluid pressure assumed to fill the entirety of the element it is modelling. Modelled pressures generate force in all directions equally, this introduces some error into the methodology. The errors can be reduced by finer mesh however the issue will always be present regardless of how fine the mesh becomes. Micro fractures naturally occur in rock through their formation, the damage model also limits how micro fractures can be accounted for.

7.3 Plastic algorithm analysis

The plastic component in this thesis is the least rigorous compared qualitatively as shown in section 6.

During the derivation of the plastic large strain conversion the plastic rotation matrix constituent of the plastic deformation gradient was considered to act in the same manner as the elastic rotation matrix.

This combined with the exponential terms used in the Hencky strain conversion increases the instability of the approach, shown in equation 6.3.2, section 2.5. This assumption hinders the approach so the original strength of the elastic version being based on a finite deformation framework, almost irrelevant. However, the large strain methodology utilised allows infinitesimal constitute methodologies to be used in large strain context increasing their stability when compared against purely infinitesimal approaches.

As prior mentioned in both prior analysis sections 7.1 and 7.2; with additional components the number of comparisons of energy paths increases when additional behaviour is introduced, the computational demand increases. This is especially true in the plastic hydrofracture as the plastic correction would also require the fluid pressures be re calculated during significant plastic deformations.

To accommodate the minimisation compartment additional reset loops were created to ensure the lowest energy value was found whilst maintaining integrity on the fluid/plastic side. These additional loops cause some of the equilibrium equations to be modified with slight variations in damage fields, requiring more computational resources.

This drawback sacrifices computational demand for accuracy however by assuming the flow/ plastic deformations occur independently of fracture development these loops may be reduced. In the case of the repeated single slit experiment with plasticity, there was little difference in results when the number of minimisation loops were reduced. The key difference was observed in the fluid extension of the framework. When the loops were reduced, complex branching behaviour was reduced, instead only equal branches were observed. In most cases this did not impact the results from the numerous hydrofracture verifications undertaken including consolidation, penny crack, continuous flow penny crack, stress contour penny crack and the tests 1:3.

Tests 4:5 were the only hydrofracture verifications that required multiple minimisation loops in order to yield reasonable results.

Mohr Coulomb was used in the proposed plasticity framework due to constitutive model's shown favour of modelling highly compressible materials such as rock/ concrete [122], discussed in section 2.5.

The Mohr Coulomb constitutive methodology's key strength relies on the growing yield criteria with confining stress and prediction of shear failure. The model's lack of accounting for tension failure in this framework does pose an issue with disregard to plastic tension mode failures. Furthermore, the Mohr coulomb model assumes steady loading conditions, which is not the most suitable for fracture/hydrofracture problems [162]. A more suitable constitutive model would be required for accurate ductile modelling.

8 Conclusion

The goal of this research was to produce and numerically implement a hydrofracture framework that can correctly capture the complex phenomena that occur when matter is subject to highly pressurised such as porous flow, fracture propagation, flow within fractures, fluid compressibility, fluid-mechanical coupling and finite deformation.

The framework proposed in this thesis uses two pre-existing frameworks for modelling fracture and geomechancial systems, combining the two, using the damage variable to distinguish fractured and porous domains. This simplifies the modelling process, reducing the required computational resources and initial laboratory testing for variables required.

The result was a highly efficient model which requires minimal input variables and is computationally inexpensive, all solutions provided have been ran on a single (i7 Processor) desktop computer. The ability of the proposed model to capture fracture/ hydrofracture behaviour has been demonstrated through various verifications against numerical, analytical and experiential data sets as shown in sections: 3.4, 5.1, 5.2.1, 5.3 and 5.4.

The key findings and developments of this research are as follows:

1. The Methodology has been proven to demonstrate accurate prediction of many hydrofracture scenarios.
2. The minimisation methodology is suitable for modelling complex fracture behaviour, proven by comparing numerical outputs against experimental and numerical fracture paths.
3. The minimisation approach is computationally inexpensive, flexible and simple to implement within existing framework. The main drawback being that the computational overhead increases as more phenomena are introduced into the considered framework.

4. Several methodologies from geomechanics and fracture mechanics have been considered to create a model post fracture behaviour in terms of strength and fluid flow.

5. The prediction algorithm by the minimisation approach becomes more accurate by varying the amount of allowed newly damaged material unless the change in distribution becomes one element of damage with each iteration.

6. The dual porosity coupling can be used to capture the flow properties of hydro fractures. The use of which has the potential to reduce the number of required variables.

7. In section 5.2 and 5.2.1 the issue of two dimensional consolidation in closely confined penny cracks inhibit the progress of hydrofractures was classified. The Penny crack within a large domain shown in section: 5.3 further verified this behaviour trend.

8. Section 5.2 and 5.2.1 also showed how leakage from fractures to the surrounding porous system dictate pressure changes within the continuum and the resultant mechanical changes further proving that leakage is an important consideration mechanically as well as environmentally.

9. Section: 5.1 and showed that the developed methodology can capture geotechnical behaviour. All whilst maintaining fracture/ hydrofracture capability and suitability.

10. The laminar flow assumption of the utilised Darcey equations discussed in section 7.2, is reasonable in the aspect of small scale hydrofractures as shown in section 5.4 where flow rate did not effect hydrofracture path direction, hence the accurate prediction of hydrofracture path by the developed model.

11. That the Hencky log strain conversion for infinitesimal constitutive models is applicable to large strain fractures for quick applications of pre-existing plasticity methodologies.

12. The brittle-to-ductile transition is simulated accurately in the pad slip plane simulation, showing that the softening behaviour from the Mohr Coulomb was transferable to the large strain model.

8.1 Further work

In summary the model developed in this study shows promise in both its simplicity and capability. However, the hydrofracture theory requires development in three dimensions and to be compared against practical fracking results, particularly fracking scenarios under high confining pressures. The plasticity framework requires further development so the hydrofracture model may regain the flexibility the elastic approach maintains to improve stability. Further validation against laboratory experiments which contain plasticity fracture behaviour.

Specific aspects for suggested further work include:

1. Coupling the hydro aspect of the methodology with damage. This could effectively reduce number of required equations, improving computational efficiency and accuracy.

2. Extending the methodology into the third dimension. This would allow for more realistic hydrofracture scenarios. Furthermore, the implementation should perhaps move to an efficient coding language, to improve computational efficiency. Matlab was used in this approach for simplifying the numerical implementation of fluid coupling. However Matlab did impede on the progress of calculation time, not allowing the approach's efficiency to be compared to other methods in terms of resource usage.

3. Adopting a hypo-elastically derived plastic function in order to improve stability and rigorous testing of ductile fractures with closely observed comparisons.

4. Account for additional phenomena such as temperature, dual liquid flows, etc. Further improving the model's capability to model fracking scenarios practically.

9 References

[1] Adachi, J. I., and Detournay, E. Plane strain propagation of a hydraulic fracture in a permeable rock. *Engineering Fracture Mechanics 75*, 16 (2008), 4666–4694.

[2] Alberti, G., Bouchitté, G., and Dal Maso, G. The calibration method for the mumford-shah functional and free-discontinuity problems. *Calculus of Variations and Partial Differential Equations 16*, 3 (2003), 299–333.

[3] An, S., Yao, J., Yang, Y., Zhang, L., Zhao, J., and Gao, Y. Influence of pore structure parameters on flow characteristics based on a digital rock and the pore network model. *Journal of Natural Gas Science and Engineering 31* (2016), 156–163.

[4] Andreev, A., Galybin, A., and Izvekov, O. Application of complex sie method for the prediction of hydrofracture path. *Engineering Analysis with Boundary Elements 50* (2015), 133–140.

[5] Areias, P., Rabczuk, T., and Camanho, P. Finite strain fracture of 2d problems with injected anisotropic softening elements. *Theoretical and Applied Fracture Mechanics 72* (2014), 50–63.

[6] Bao, J., Fathi, E., and Ameri, S. A coupled finite element method for the numerical simulation of hydraulic fracturing with a condensation technique. *Engineering Fracture Mechanics 131* (2014), 269–281.

[7] Bao, J., Fathi, E., and Ameri, S. A unified finite element method for the simulation of hydraulic fracturing with and without fluid lag. *Engineering Fracture Mechanics 162* (2016), 164–178.

[8] Barton, N., Bandis, S., and Bakhtar, K. Strength, deformation and conductivity coupling of rock joints. *International journal of rock mechanics and mining sciences & geomechanics abstracts 22*, 3 (1985), 121–140.

[9] Bathe, K.-J. *Finite element procedures.* Klaus-Jurgen Bathe, 2006.

[10] Bažant, Z. P. Size effect in blunt fracture: concrete, rock, metal. *Journal of engineering mechanics 110*, 4 (1984), 518–535.

[11] Bell, F. G. *Engineering properties of soils and rocks.* Elsevier, 2013.

[12] Bidgoli, M. N., Zhao, Z., and Jing, L. Numerical evaluation of strength and deformability of fractured rocks. *Journal of Rock Mechanics and Geotechnical Engineering 5*, 6 (2013), 419–430.

[13] Biot, M. A. General theory of three-dimensional consolidation. *Journal of applied physics 12*, 2 (1941), 155–164.

[14] Blick, E., Civan, F., et al. Porous-media momentum equation for highly accelerated flow. *SPE reservoir engineering 3*, 03 (1988), 1–048.

[15] Bonet, J., and Wood, R. D. *Nonlinear continuum mechanics for finite element analysis.* Cambridge university press, 1997.

[16] Bourdin, B., Francfort, G. A., and Marigo, J.-J. Numerical experiments in revisited brittle fracture. *Journal of the Mechanics and Physics of Solids 48*, 4 (2000), 797–826.

[17] Boutin, C., and Venegas, R. Assessment of the effective parameters of dual porosity deformable media. *Mechanics of Materials 102* (2016), 26–46.

[18] Broumand, P., and Khoei, A. The extended finite element method for large deformation ductile fracture problems with a non-local damage-plasticity model. *Engineering Fracture Mechanics 112* (2013), 97–125.

[19] Brown, S. R. Fluid flow through rock joints: the effect of surface roughness. *Journal of Geophysical Research: Solid Earth 92*, B2 (1987), 1337–1347.

[20] Bruhns, O., Xiao, H., and Meyers, A. Constitutive inequalities for an isotropic elastic strain-energy function based on hencky's logarithmic strain tensor. *Proceedings of the Royal Society of London. Series A: Mathematical, Physical and Engineering Sciences 457*, 2013 (2001), 2207–2226.

[21] Bunger, A. P., and Detournay, E. Experimental validation of the tip asymptotics for a fluid-driven crack. *Journal of the Mechanics and Physics of Solids 56*, 11 (2008), 3101–3115.

[22] Bunger, A. P., Gordeliy, E., and Detournay, E. Comparison between laboratory experiments and coupled simulations of saucer-shaped hydraulic fractures in homogeneous brittle-elastic solids. *Journal of the Mechanics and Physics of Solids 61*, 7 (2013), 1636–1654.

[23] Caminero, M. Á., Montáns, F. J., and Bathe, K.-J. Modeling large strain anisotropic elasto-plasticity with logarithmic strain and stress measures. *Computers & Structures 89*, 11-12 (2011), 826–843.

[24] Chaves, F. J., Da Silva, L., De Moura, M., Dillard, D., and Esteves, V. Fracture mechanics tests in adhesively bonded joints: a literature review. *The Journal of Adhesion 90*, 12 (2014), 955–992.

[25] Chen, Y., and Wang, Z. Solution of multiple crack problem in a finite plate using coupled integral equations. *International Journal of Solids and Structures 49*, 1 (2012), 87–94.

[26] CHEN, Y.-f., CAI, D.-m., FAN, Z.-f., LI, K.-c., and Jun, N. 3d geological modeling of dual porosity carbonate reservoirs: A case from the kenkiyak pre-salt oilfield, kazakhstan. *Petroleum Exploration and Development 35*, 4 (2008), 492–497.

[27] Contrafatto, L., and Cuomo, M. A framework of elastic–plastic damaging model for concrete under multiaxial stress states. *International Journal of Plasticity 22*, 12 (2006), 2272–2300.

[28] COOMBS, W., ET AL. *Finite deformation of particulate geomaterials: frictional and anisotropic Critical State elasto-plasticity.* PhD thesis, Durham University, 2011.

[29] CURNIER, A. *Computational methods in solid mechanics*, vol. 29. Springer Science & Business Media, 2012.

[30] CˇERVENKA, J., AND SAOUMA, V. E. Numerical evaluation of 3-d sif for arbitrary finite element meshes. *Engineering Fracture Mechanics 57*, 5 (1997), 541–563.

[31] DAI, Y., GRUBER, D., AND HARMUTH, H. Observation and quantification of the fracture process zone for two magnesia refractories with different brittleness. *Journal of the European Ceramic Society 37*, 6 (2017), 2521–2529.

[32] DAVID, E., BRANTUT, N., SCHUBNEL, A., AND ZIMMERMAN, R. W. Sliding crack model for nonlinearity and hysteresis in the uniaxial stress–strain curve of rock. *International Journal of Rock Mechanics and Mining Sciences 52* (2012), 9–17.

[33] DAVIS, C. The politics of "fracking": Regulating natural gas drilling practices in colorado and texas. *Review of Policy Research 29*, 2 (2012), 177–191.

[34] DE VRIES, E. T., RAOOF, A., AND VAN GENUCHTEN, M. T. Multiscale modelling of dual-porosity porous media; a computational pore-scale study for flow and solute transport. *Advances in water resources 105* (2017), 82–95.

[35] DEL PIERO, G., LANCIONI, G., AND MARCH, R. A variational model for fracture mechanics: numerical experiments. *Journal of the Mechanics and Physics of Solids 55*, 12 (2007), 2513–2537.

[36] DENG, J., LIN, C., YANG, Q., LIU, Y., TAO, Z., AND DUAN, H. Investigation of directional hydraulic fracturing based on true tri-axial

experiment and finite element modeling. *Computers and Geotechnics 75* (2016), 28–47.

[37] Detournay, E., and Peirce, A. On the moving boundary conditions for a hydraulic fracture. *International Journal of Engineering Science 84* (2014), 147–155.

[38] Dhar, S., Dixit, P., and Sethuraman, R. A continuum damage mechanics model for ductile fracture. *International Journal of Pressure Vessels and Piping 77*, 6 (2000), 335–344.

[39] Ehlers, W., and Eipper, G. The simple tension problem at large volumetric strains computed from finite hyperelastic material laws. *Acta Mechanica 130*, 1-2 (1998), 17–27.

[40] Eterovic, A. L., and Bathe, K.-J. A hyperelastic-based large strain elasto-plastic constitutive formulation with combined isotropic-kinematic hardening using the logarithmic stress and strain measures. *International Journal for Numerical Methods in Engineering 30*, 6 (1990), 1099–1114.

[41] Fakhimi, A., and Tarokh, A. Process zone and size effect in fracture testing of rock. *International Journal of Rock Mechanics and Mining Sciences 60* (2013), 95–102.

[42] Fan, J., Bailey, T. P., Sun, Z., Zhao, P., Uher, C., Yuan, F., and Zhao, M. Preparation and properties of ultra-low density proppants for use in hydraulic fracturing. *Journal of Petroleum Science and Engineering 163* (2018), 100–109.

[43] Feng, G.-q., Liu, Q.-g., Zhang, L.-h., and Zeng, Y. Pressure transient behavior analysis in a dual-porosity reservoir with partially communicating faults. *Journal of Natural Gas Science and Engineering 32* (2016), 373–379.

[44] Flekkøy, E. G., Malthe-Sørenssen, A., and Jamtveit, B. Modeling hydrofracture. *Journal of Geophysical Research: Solid Earth 107*, B8 (2002), ECV–1.

[45] Francfort, G. A., and Marigo, J.-J. Revisiting brittle fracture as an energy minimization problem. *Journal of the Mechanics and Physics of Solids 46*, 8 (1998), 1319–1342.

[46] Galouei, M., and Fakhimi, A. Size effect, material ductility and shape of fracture process zone in quasi-brittle materials. *Computers and Geotechnics 65* (2015), 126–135.

[47] Gangi, A. F. Variation of whole and fractured porous rock permeability with confining pressure. *International Journal of Rock Mechanics and Mining Sciences & Geomechanics Abstracts 15*, 5 (1978), 249–257.

[48] Gerke, H. H., Badorreck, A., and Einecke, M. Single-and dual-porosity modelling of flow in reclaimed mine soil cores with embedded lignitic fragments. *Journal of contaminant hydrology 104*, 1-4 (2009), 90–106.

[49] Gerke, H. H., and Van Genuchten, M. T. A dual-porosity model for simulating the preferential movement of water and solutes in structured porous media. *Water resources research 29*, 2 (1993), 305–319.

[50] Goodman, R. E. *Introduction to rock mechanics*, vol. 2. Wiley New York, 1989.

[51] Grassl, P., Grégoire, D., Solano, L. R., and Pijaudier-Cabot, G. Meso-scale modelling of the size effect on the fracture process zone of concrete. *International Journal of Solids and Structures 49*, 13 (2012), 1818–1827.

[52] Griffith, A. A. Vi. the phenomena of rupture and flow in solids. *Philosophical transactions of the royal society of london. Series A, containing papers of a mathematical or physical character 221*, 582-593 (1921), 163–198.

[53] Gudmundsson, A., Kusumoto, S., Simmenes, T. H., Philipp, S. L., Larsen, B., and Lotveit, I. F. Effects of overpressure variations on fracture apertures and fluid transport. *Tectonophysics 581* (2012), 220–230.

[54] Gui, Y.-L., Bui, H. H., Kodikara, J., Zhang, Q.-B., Zhao, J., and Rabczuk, T. Modelling the dynamic failure of brittle rocks using a hybrid continuum-discrete element method with a mixed-mode cohesive fracture model. *International Journal of Impact Engineering 87* (2016), 146–155.

[55] Guo, J.-C., Nie, R.-S., and Jia, Y.-L. Dual permeability flow behavior for modeling horizontal well production in fractured-vuggy carbonate reservoirs. *Journal of hydrology 464* (2012), 281–293.

[56] Guo, M., Alam, S. Y., Bendimerad, A. Z., Grondin, F., Rozière, E., and Loukili, A. Fracture process zone characteristics and identification of the micro-fracture phases in recycled concrete. *Engineering Fracture Mechanics 181* (2017), 101–115.

[57] Ha, K., Baek, H., and Park, K. Convergence of fracture process zone size in cohesive zone modeling. *Applied Mathematical Modelling 39*, 19 (2015), 5828–5836.

[58] Haeri, F., Izadi, M., and Zeidouni, M. Unconventional multi-fractured analytical solution using dual porosity model. *Journal of Natural Gas Science and Engineering 45* (2017), 230–242.

[59] Han, W., and Reddy, B. D. *Plasticity: mathematical theory and numerical analysis*, vol. 9. Springer Science & Business Media, 2012.

[60] Hencky, H. The law of elasticity for isotropic and quasi-isotropic substances by finite deformations. *Journal of Rheology (1929-1932) 2*, 2 (1931), 169–176.

[61] Hencky, H. The elastic behavior of vulcanized rubber. *Rubber Chemistry and Technology 6*, 2 (1933), 217–224.

[62] Heuze, F., Shaffer, R., Ingraffea, A., and Nilson, R. Propagation of fluid-driven fractures in jointed rock. part 1—development and validation of methods of analysis. *International Journal of Rock Mechanics and Mining Sciences & Geomechanics Abstracts 27*, 4 (1990), 243–254.

[63] Hokka, M., Black, J., Tkalich, D., Fourmeau, M., Kane, A., Hoang, N.-H., Li, C., Chen, W., and Kuokkala, V.-T. Effects of strain rate and confining pressure on the compressive behavior of kuru granite. *International Journal of Impact Engineering 91* (2016), 183–193.

[64] Homand-Etienne, F., Hoxha, D., and Shao, J.-F. A continuum damage constitutive law for brittle rocks. *Computers and Geotechnics 22*, 2 (1998), 135–151.

[65] Houlsby, G. T. *Study of plasticity theories and their applicability to soils.* PhD thesis, University of Cambridge, 1981.

[66] Houlsby, G. T., and Puzrin, A. M. *Principles of hyperplasticity: an approach to plasticity theory based on thermodynamic principles.* Springer Science & Business Media, 2007.

[67] Huang, K., Shimada, T., Ozaki, N., Hagiwara, Y., Sumigawa, T., Guo, L., and Kitamura, T. A unified and universal griffith-based criterion for brittle fracture. *International Journal of Solids and Structures 128* (2017), 67–72.

[68] Hwang, K., Jiang, H., Huang, Y., Gao, H., and Hu, N. A finite deformation theory of strain gradient plasticity. *Journal of the Mechanics and Physics of Solids 50*, 1 (2002), 81–99.

[69] Jafari, A., and Babadagli, T. Estimation of equivalent fracture network permeability using fractal and statistical network properties. *Journal of Petroleum Science and Engineering 92* (2012), 110–123.

[70] Jaspal, R., Nerlich, B., and Lemańczyk, S. Fracking in the polish press: Geopolitics and national identity. *Energy Policy 74* (2014), 253–261.

[71] Jenni, A., Gimmi, T., Alt-Epping, P., Mäder, U., and Cloet, V. Interaction of ordinary portland cement and opalinus clay: Dual porosity modelling compared to experimental data. *Physics and Chemistry of the Earth, Parts A/B/C 99* (2017), 22–37.

[72] Jerbi, C., Fourno, A., Noetinger, B., and Delay, F. A new estimation of equivalent matrix block sizes in fractured media with two-phase flow applications in dual porosity models. *Journal of hydrology 548* (2017), 508–523.

[73] Jiang, T., Shao, J., Xu, W., and Zhou, C. Experimental investigation and micromechanical analysis of damage and permeability variation in brittle rocks. *International Journal of Rock Mechanics and Mining Sciences 47*, 5 (2010), 703–713.

[74] Jin, J., Cao, P., Chen, Y., Pu, C., Mao, D., and Fan, X. Influence of single flaw on the failure process and energy mechanics of rock-like material. *Computers and Geotechnics 86* (2017), 150–162.

[75] Jing, Y., Armstrong, R. T., and Mostaghimi, P. Rough-walled discrete fracture network modelling for coal characterisation. *Fuel 191* (2017), 442–453.

[76] Kazumasa Shimamoto, Yu Sekiguchi, C. S. Mixed mode fracture toughness of adhesively bonded joints with residual stress. *International Journal of Solids and Structures 102-103* (2016), 120–126.

[77] Khoei, A. R. *Extended finite element method: theory and applications*. John Wiley & Sons, 2014.

[78] Kim, D.-J., Pereira, J., and Duarte, C. A. Analysis of three-dimensional fracture mechanics problems: A two-scale approach using

coarse-generalized fem meshes. *International Journal for Numerical Methods in Engineering 81*, 3 (2010), 335–365.

[79] Kovalyshen, Y., and Detournay, E. Fluid-driven fracture in a poroelastic rock. In *Effective and Sustainable Hydraulic Fracturing*. IntechOpen, 2013.

[80] Koyama, T., Neretnieks, I., and Jing, L. A numerical study on differences in using navier–stokes and reynolds equations for modeling the fluid flow and particle transport in single rock fractures with shear. *International Journal of Rock Mechanics and Mining Sciences 45*, 7 (2008), 1082–1101.

[81] Krajcinovic, D. Damage mechanics. *Mechanics of materials 8*, 2-3 (1989), 117–197.

[82] Kumar, S., Zielonka, M., Searles, K., and Dasari, G. Modeling of hydraulic fracturing in ultra-low permeability formations: The role of pore fluid cavitation. *Engineering Fracture Mechanics 184* (2017), 227–240.

[83] Lama, R., and Vutukuri, V. *Handbook on mechanical properties of rocks-testing techniques and results-volume iii*, vol. 3. Trans Tech Publications, 1978.

[84] Lee, S., Wheeler, M. F., and Wick, T. Pressure and fluid-driven fracture propagation in porous media using an adaptive finite element phase field model. *Computer Methods in Applied Mechanics and Engineering 305* (2016), 111–132.

[85] Lemaitre, J. How to use damage mechanics. *Nuclear engineering and design 80*, 2 (1984), 233–245.

[86] Lemaitre, J. Coupled elasto-plasticity and damage constitutive equations. *Computer Methods in Applied Mechanics and Engineering 51* (1985), 31–49.

[87] Lemenant, A. A selective review on mumford–shah minimizers. *Bollettino dell'Unione Matematica Italiana 9*, 1 (2016), 69–113.

[88] Li, Q., Pang, X., Tang, L., Chen, G., Shao, X., and Jia, N. Occurrence features and gas content analysis of marine and continental shales: A comparative study of longmaxi formation and yanchang formation. *Journal of Natural Gas Science and Engineering 56* (2018), 504–522.

[89] Li, T., and Yang, X. Stability of plane strain tunnel headings in soils with tensile strength cut-off. *Tunnelling and Underground Space Technology 95* (2020), 103138.

[90] Li, Z., Li, L., Li, M., Zhang, L., Zhang, Z., Huang, B., and Tang, C. A numerical investigation on the effects of rock brittleness on the hydraulic fractures in the shale reservoir. *Journal of Natural Gas Science and Engineering 50* (2018), 22–32.

[91] Lieb, M., Neckel, T., Bungartz, H.-J., and Sun, S. Towards a navier stokes-darcy upscaling based on permeability tensor computation. *Procedia Computer Science 9* (2012), 717–726.

[92] Liu, K., and Chen, S. Finite element implementation of strain-hardening drucker–prager plasticity model with application to tunnel excavation. *Underground Space 2*, 3 (2017), 168–174.

[93] Liu, Y., Guo, J., and Chen, Z. Leakoff characteristics and an equivalent leakoff coefficient in fractured tight gas reservoirs. *Journal of Natural Gas Science and Engineering 31* (2016), 603–611.

[94] Long, J., Remer, J., Wilson, C., and Witherspoon, P. Porous media equivalents for networks of discontinuous fractures. *Water Resources Research 18*, 3 (1982), 645–658.

[95] Ma, J. Coupled flow deformation analysis of fractured porous media subject to elasto-plastic damage. *Thesis* (2014).

[96] Ma, L., Xu, H., Tong, Q., Dong, L., Zhang, N., and Li, J. Post-yield plastic frictional parameters of a rock salt using the concept of mobilized strength. *Engineering geology 177* (2014), 25–31.

[97] Maleki, K., and Pouya, A. Numerical simulation of damage–permeability relationship in brittle geomaterials. *Computers and Geotechnics 37*, 5 (2010), 619–628.

[98] Marji, M. F. Numerical analysis of quasi-static crack branching in brittle solids by a modified displacement discontinuity method. *International Journal of Solids and Structures 51*, 9 (2014), 1716–1736.

[99] Martínez-Pañeda, E., and Betegón, C. Modeling damage and fracture within strain-gradient plasticity. *International Journal of Solids and Structures 59* (2015), 208–215.

[100] Martínez-Pañeda, E., and Niordson, C. F. On fracture in finite strain gradient plasticity. *International Journal of Plasticity 80* (2016), 154–167.

[101] MathWorks. delaunay triangulation. https://uk.mathworks.com/help/matlab/ref/delaunaytriangulation.html.

[102] Matzenmiller, A., Lubliner, J., and Taylor, R. A constitutive model for anisotropic damage in fiber-composites. *Mechanics of materials 20*, 2 (1995), 125–152.

[103] Meijer, K. L. Comparison of finite and infinitesimal strain consolidation by numerical experiments. *International journal for numerical and analytical methods in geomechanics 8*, 6 (1984), 531–548.

[104] Menéndez, C., Nieto, P. G., Ortega, F. A., and Bello, A. Non-linear analysis of the consolidation of an elastic saturated soil with incompressible fluid and variable permeability by fem. *Applied Mathematics and Computation 216*, 2 (2010), 458–476.

[105] Merxhani, A. An introduction to linear poroelasticity. *arXiv preprint arXiv:1607.04274* (2016).

[106] Meschke, G., and Leonhart, D. A generalized finite element method for hydro-mechanically coupled analysis of hydraulic fracturing problems using space-time variant enrichment functions. *Computer Methods in Applied Mechanics and Engineering 290* (2015), 438–465.

[107] Mohammadnejad, T., and Khoei, A. An extended finite element method for hydraulic fracture propagation in deformable porous media with the cohesive crack model. *Finite Elements in Analysis and Design 73* (2013), 77–95.

[108] Molladavoodi, H., and Mortazavi, A. A damage-based numerical analysis of brittle rocks failure mechanism. *Finite Elements in Analysis and Design 47*, 9 (2011), 991–1003.

[109] Mousavi, S., Grinspun, E., and Sukumar, N. Higher-order extended finite elements with harmonic enrichment functions for complex crack problems. *International Journal for Numerical Methods in Engineering 86*, 4-5 (2011), 560–574.

[110] Nazem, M., Kardani, M., Bienen, B., and Cassidy, M. A stable maximum-entropy meshless method for analysis of porous media. *Computers and Geotechnics 80* (2016), 248–260.

[111] Nazem, M., Sheng, D., and Carter, J. P. Stress integration and mesh refinement for large deformation in geomechanics. *International Journal for Numerical Methods in Engineering 65*, 7 (2006), 1002–1027.

[112] Ogden, R. W. *Non-linear elastic deformations.* Courier Corporation, 1997.

[113] Okada, H., and Ohata, S. Three-dimensional j-integral evaluation for cracks with arbitrary curvatures and kinks based on domain integral method for quadratic tetrahedral finite element. *Engineering Fracture Mechanics 109* (2013), 58–77.

[114] Ostrovsky, L., and Johnson, P. Dynamic nonlinear elasticity in geo materials. *Rivista del Nuovo Cimento della Societa Italiana di Fisica 24*, 7 (2001), 1–46.

[115] Papanastasiou, P. The influence of plasticity in hydraulic fracturing. *International Journal of Fracture 84*, 1 (1997), 61–79.

[116] Papanastasiou, P. The influence of plasticity in hydraulic fracturing. *International Journal of Fracture 84*, 1 (1997), 61–79.

[117] Park, D., and Michalowski, R. L. Three-dimensional stability analysis of slopes in hard soil/soft rock with tensile strength cut-off. *Engineering Geology 229* (2017), 73–84.

[118] Park, K., Paulino, G. H., and Roesler, J. R. A unified potential-based cohesive model of mixed-mode fracture. *Journal of the Mechanics and Physics of Solids 57*, 6 (2009), 891–908.

[119] Peirce, A., and Detournay, E. An implicit level set method for modeling hydraulically driven fractures. *Computer Methods in Applied Mechanics and Engineering 197*, 33-40 (2008), 2858–2885.

[120] Petch, T. Proof that chemical fracking harms fish. https://www.anglersmail.co.uk/news/proof-chemical-fracking-harms-fish-72535.

[121] Pommier, S., Gravouil, A., Moes, N., and Combescure, A. *Extended finite element method for crack propagation.* John Wiley & Sons, 2013.

[122] Pourhosseini, O., and Shabanimashcool, M. Development of an elasto-plastic constitutive model for intact rocks. *International Journal of Rock Mechanics and Mining Sciences 66* (2014), 1–12.

[123] Presho, M., Wo, S., and Ginting, V. Calibrated dual porosity, dual permeability modeling of fractured reservoirs. *Journal of Petroleum Science and Engineering 77*, 3-4 (2011), 326–337.

[124] Prud'homme, A. *Hydrofracking: What Everyone Needs to Know®*. Oxford University Press, 2013.

[125] Ranjith, P., and Viete, D. Applicability of the 'cubic law'for non-darcian fracture flow. *Journal of Petroleum Science and Engineering 78*, 2 (2011), 321–327.

[126] Robbins, K. Awakening the slumbering giant: how horizontal drilling technology brought the endangered species act to bear on hydraulic fracturing. *Case W. Res. L. Rev. 63* (2012), 1143.

[127] Rosales, L. A. O. Flac, online manual table of contents, 2005.

[128] Salimzadeh, S. *Numerical modelling of two phase fluid flow through deformable fractured porous media.* PhD thesis, School of Civil and Environmental Engineering The University of New South Wales, 2014.

[129] Salvadori, A. A plasticity framework for (linear elastic) fracture mechanics. *Journal of the Mechanics and Physics of Solids 56*, 5 (2008), 2092–2116.

[130] Samimi, S., and Pak, A. Three-dimensional simulation of fully coupled hydro-mechanical behavior of saturated porous media using element free galerkin (efg) method. *Computers and Geotechnics 46* (2012), 75–83.

[131] Sharqawy, M. H. Construction of pore network models for berea and fontainebleau sandstones using non-linear programing and optimization techniques. *Advances in water resources 98* (2016), 198–210.

[132] Sheibani, F., Olson, J., et al. Stress intensity factor determination for three-dimensional crack using the displacement discontinuity method with applications to hydraulic fracture height growth and non-planar propagation paths. *International Society for Rock Mechanics and Rock Engineering* (2013).

[133] Shen, Y. A variational inequality formulation to incorporate the fluid lag in fluid-driven fracture propagation. *Computer Methods in Applied Mechanics and Engineering 272* (2014), 17–33.

[134] Sidiq, H., Silalahi, E., Skinner, G., and Pamurty, P. N. The role of reservoir modelling in unlocking unconventional (resource) plays. *The APPEA Journal 53*, 2 (2013), 440–440.

[135] Słowik, M. Numerical analysis of the width of fracture process zone in concrete beams. *Computational Materials Science 50*, 4 (2011), 1347–1352.

[136] Song, C., Lu, Y., Tang, H., and Jia, Y. A method for hydrofracture propagation control based on non-uniform pore pressure field. *Journal of Natural Gas Science and Engineering 33* (2016), 287–295.

[137] Sutera, S. P., and Skalak, R. The history of poiseuille's law. *Annual review of fluid mechanics 25*, 1 (1993), 1–20.

[138] Talabi, O. A. Pore-scale simulation of nmr response in porous media.

[139] Talabi, O. A. Pore-scale simulation of nmr response in porous media. *Department of Earth Science and Engineering, Imperial College London* (2008).

[140] Tarokh, A., and Fakhimi, A. Discrete element simulation of the effect of particle size on the size of fracture process zone in quasi-brittle materials. *Computers and Geotechnics 62* (2014), 51–60.

[141] Vavro, L., Souček, K., Kytỳř, D., Fíla, T., Keršner, Z., and Vavro, M. Visualization of the evolution of the fracture process zone in sandstone by transmission computed radiography. *Procedia engineering 191* (2017), 689–696.

[142] Vaz Jr, M., and Owen, D. Aspects of ductile fracture and adaptive mesh refinement in damaged elasto-plastic materials. *International Journal for Numerical Methods in Engineering 50*, 1 (2001), 29–54.

[143] Vermeer, P. A., and De Borst, R. Non-associated plasticity for soils, concrete and rock. *HERON, 29 (3), 1984* (1984).

[144] Wang, P., Cai, M., and Ren, F. Anisotropy and directionality of tensile behaviours of a jointed rock mass subjected to numerical brazilian tests. *Tunnelling and Underground Space Technology 73* (2018), 139–153.

[145] Wang, Y., Pu, J., Wang, L., Wang, J., Jiang, Z., Song, Y.-F., Wang, C.-C., Wang, Y., and Jin, C. Characterization of typical 3d pore networks of jiulaodong formation shale using nano-transmission x-ray microscopy. *Fuel 170* (2016), 84–91.

[146] Wangen, M. Finite element modeling of hydraulic fracturing on a reservoir scale in 2d. *Journal of Petroleum Science and Engineering 77*, 3-4 (2011), 274–285.

[147] Wangen, M. A 2d volume conservative numerical model of hydraulic fracturing. *Computers & Structures 182* (2017), 448–458.

[148] Wei, M., Dai, F., Xu, N., Zhao, T., and Xia, K. Experimental and numerical study on the fracture process zone and fracture toughness determination for isrm-suggested semi-circular bend rock specimen. *Engineering Fracture Mechanics 154* (2016), 43–56.

[149] Wei, M.-D., Dai, F., Xu, N.-W., and Zhao, T. Stress intensity factors and fracture process zones of isrm-suggested chevron notched specimens for mode i fracture toughness testing of rocks. *Engineering Fracture Mechanics 168* (2016), 174–189.

[150] Winner, R. A., Lu, G., Prioul, R., Aidagulov, G., and Bunger, A. P. Acoustic emission and kinetic fracture theory for time-dependent breakage of granite. *Engineering Fracture Mechanics 199* (2018), 101–113.

[151] Witherspoon, P. A., Wang, J. S., Iwai, K., and Gale, J. E. Validity of cubic law for fluid flow in a deformable rock fracture. *Water resources research 16*, 6 (1980), 1016–1024.

[152] Wu, J., Feng, M., Yu, B., Zhang, W., Ni, X., and Han, G. Experimental investigation on dilatancy behavior of water-saturated sandstone. *International Journal of Mining Science and Technology 28*, 2 (2018), 323–329.

[153] Wu, Y.-S., Liu, H., and Bodvarsson, G. A triple-continuum approach for modeling flow and transport processes in fractured rock. *Journal of Contaminant Hydrology 73*, 1-4 (2004), 145–179.

[154] Xiao, S., Wang, H.-L., Liu, B., and Hwang, K.-C. The surface-forming energy release rate based fracture criterion for elastic–plastic crack propagation. *Journal of the Mechanics and Physics of Solids 84* (2015), 336–357.

[155] Xue, L., and Wierzbicki, T. Ductile fracture initiation and propagation modeling using damage plasticity theory. *Engineering Fracture Mechanics 75*, 11 (2008), 3276–3293.

[156] Yoon, J. S., Zang, A., and Stephansson, O. Numerical investigation on optimized stimulation of intact and naturally fractured deep geothermal reservoirs using hydro-mechanical coupled discrete particles joints model. *Geothermics 52* (2014), 165–184.

[157] Yu, H., Wu, L., Guo, L., Wu, H., and Du, S. An interaction integral method for 3d curved cracks in nonhomogeneous materials with complex interfaces. *International Journal of Solids and Structures 47*, 16 (2010), 2178–2189.

[158] Yudhowijoyo, A., Rafati, R., Haddad, A. S., Raja, M. S., and Hamidi, H. Subsurface methane leakage in unconventional shale gas reservoirs: A review of leakage pathways and current sealing techniques. *Journal of Natural Gas Science and Engineering 54* (2018), 309–319.

[159] Zeng, Q., Liu, W., and Yao, J. Numerical modeling of multiple fractures propagation in anisotropic formation. *Journal of Natural Gas Science and Engineering 53* (2018), 337–346.

[160] Zeng, Q.-D., Yao, J., and Shao, J. Numerical study of hydraulic fracture propagation accounting for rock anisotropy. *Journal of Petroleum Science and Engineering 160* (2018), 422–432.

[161] Zhao, G.-F., Russell, A. R., Zhao, X., and Khalili, N. Strain rate dependency of uniaxial tensile strength in gosford sandstone by the distinct lattice spring model with x-ray micro ct. *International Journal of Solids and Structures 51*, 7-8 (2014), 1587–1600.

[162] Zhao, J. Applicability of mohr–coulomb and hoek–brown strength criteria to the dynamic strength of brittle rock. *International Journal of Rock Mechanics and Mining Sciences 37*, 7 (2000), 1115–1121.

[163] Zhao, L., Zhu, Q., Xu, W., Dai, F., and Shao, J.-F. A unified micromechanics-based damage model for instantaneous and time-dependent behaviors of brittle rocks. *International Journal of Rock Mechanics and Mining Sciences 84* (2016), 187–196.

[164] Zheng, H., Liu, F., and Du, X. Complementarity problem arising from static growth of multiple cracks and mls-based numerical manifold method. *Computer Methods in Applied Mechanics and Engineering 295* (2015), 150–171.

[165] Zhu, X., Liu, G., and Chao, Y. Three-dimensional stress and displacement fields near an elliptical crack front. *International Journal of fracture 109*, 4 (2001), 383–401.

Appendix A: Newton-Raphson Solver

Newton-Raphson Solver Here the Newton-Raphson (NR) is used to solve the global equations iteratively. The problem reduces to solving equation 205.

$$\boldsymbol{K}\delta\boldsymbol{u}_{[n+1]} = \boldsymbol{F}_{res} \tag{205}$$

where $\boldsymbol{K}$ is the global stiffness matrix, $\delta\boldsymbol{u}_{n+1}$ is the deformation and $\boldsymbol{F}_{res}$ are the residual load left from the previous iteration. The residual force is calculated by taking the difference of external and internal loads within the model as shown in equation 206. These loads are those accumulated over the model's captured deformation over $\delta\boldsymbol{u}_{n+1}$

$$\boldsymbol{F}_{res} = \boldsymbol{F}_{ext} - \boldsymbol{F}_{int} \tag{206}$$

The deformation $\delta\boldsymbol{u}_{n+1}$ is the sum of all iterated solutions calculated during the NR approach, as shown in equation 207

$$\boldsymbol{u}_{n+1} = \boldsymbol{u}_n + \Sigma\delta\boldsymbol{u}_n + 1 \tag{207}$$

The global stiffness matrix is given generally by equation 208, the pressure terms becoming zero in cases of typical fractures.

$$\boldsymbol{K}(\boldsymbol{D}) = \frac{\delta f_{res}(\boldsymbol{p_1}, \boldsymbol{p_2}, \boldsymbol{F_m}, \boldsymbol{D})}{\delta\boldsymbol{u}_{n+1}} \tag{208}$$

where $\boldsymbol{D}$ is damage, $\boldsymbol{p_1}$ is the pressure within the porous system, $\boldsymbol{p_2}$ is the pressure within the fractured system and $\boldsymbol{F_m}$ is the deformation gradient of the previous iteration's configuration. The Global stiffness matrix is calibrated for the use in a large strain environment. The changes in volumes are used to calculate changes in permeability and porosity in the model when significant volume changes occur.

$\delta\boldsymbol{F}_{res}(\boldsymbol{p_1}, \boldsymbol{p_2}, \boldsymbol{F}, \boldsymbol{D})$, is used to evaluate the progress of the iterative solution's progress according to equation 209.

$$\frac{\boldsymbol{F}_{res}}{\boldsymbol{F}_{ext}} < tolerance \tag{209}$$

The initiation of further iterations assumes no residual forces from the previous iterative solution.

The integrals used in evaluating both the global stiffness matrix and force matrix are calculated via Gauss quadrature, in this case the integrals were across tetrahedral elements.

Force integration When implementing a complex set of coupled equations via the finite element method, an equilibrium of externally applied loads are considered in equilibrium with the internal stresses and when required internal fluid pressures. Here we go through how the general solution process undergoes little change with the addition of internal fluid/fracture pressure [29]. This can be represented in the non purely mechanical sense as shown in equation 210.

$$\int (\boldsymbol{\sigma})\nu - [\boldsymbol{F}^b - \rho_g \boldsymbol{g}] d\Omega = 0 \tag{210}$$

where $\boldsymbol{\sigma}$ are the internal stresses, $\boldsymbol{F}^b$ are the body forces, ρ_g is self weight, $\boldsymbol{g}$ is acceleration due to gravity and ν is any given deformation field.

It is assumed that equation 210 is satisfied for any given displacement field. Discretisation of equation 210 gives equation 211 which must be maintained.

$$\boldsymbol{F}_{internal}(\boldsymbol{F}) - \boldsymbol{F}_{exterior} = 0 \tag{211}$$

Or in the presence if fluid pressures:

$$\boldsymbol{F}_{internal}(\boldsymbol{F}, \boldsymbol{p}_1, \boldsymbol{p}_2) - \boldsymbol{F}_{exterior} = 0 \tag{212}$$

where the internal forces are obtained from equations 213 and 214.

$$\boldsymbol{F}_{internal} = \int [\mathbf{N}]^T \boldsymbol{\sigma} d\Omega \tag{213}$$

$$\boldsymbol{F}_{exterior} = \int [\mathbf{N}]^T \boldsymbol{F}^b d\Omega + \int \mathbf{N}^T t d\Gamma \tag{214}$$

Where $\boldsymbol{N}$ is a set of updated nodal shape functions and $\boldsymbol{B}$ are strain displacement matrices, shown in Chapter 4.

Appendix B: Chapter 3 results

15 degree notch

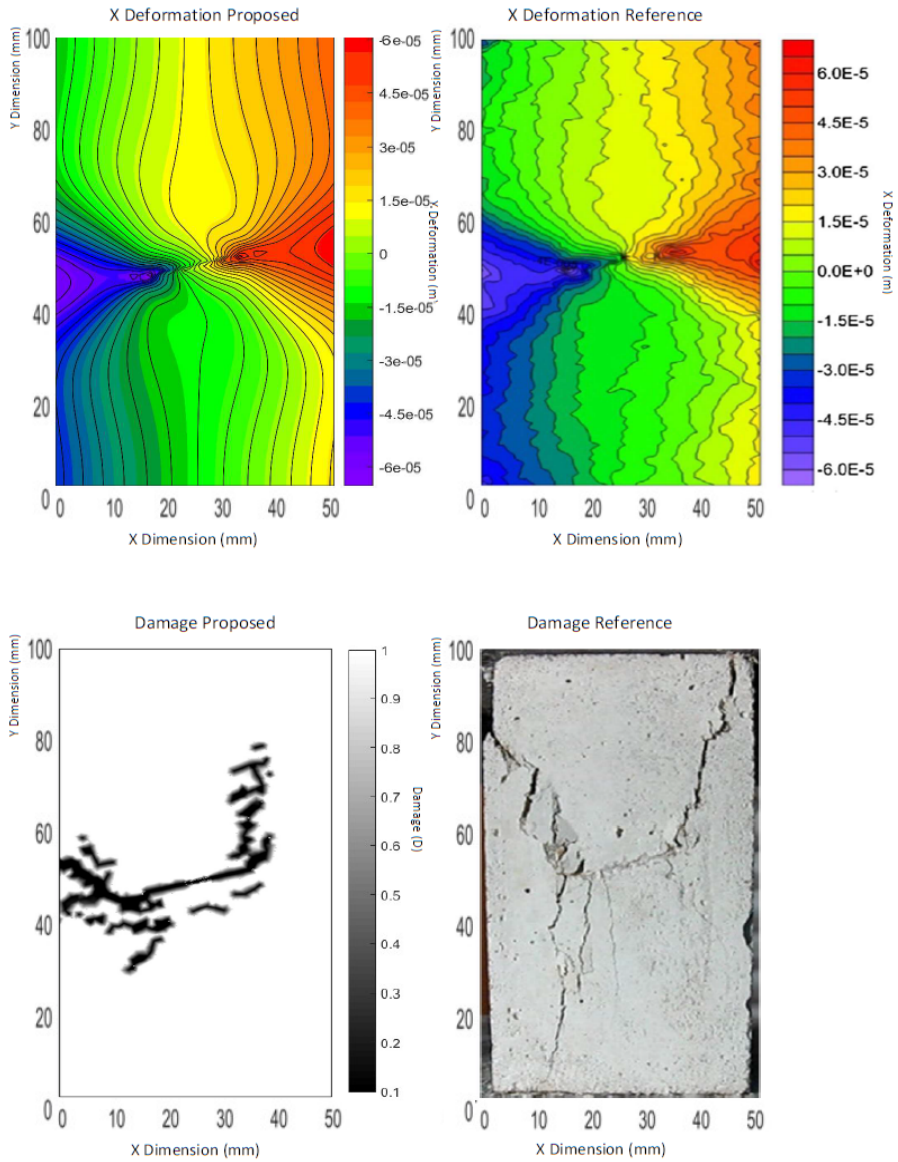

Figure 95: Deformation and Damage plots; proposed numerical solution (left) and reference numerical solution (right) for 15 degree slit at initiation [74]

30 degree notch

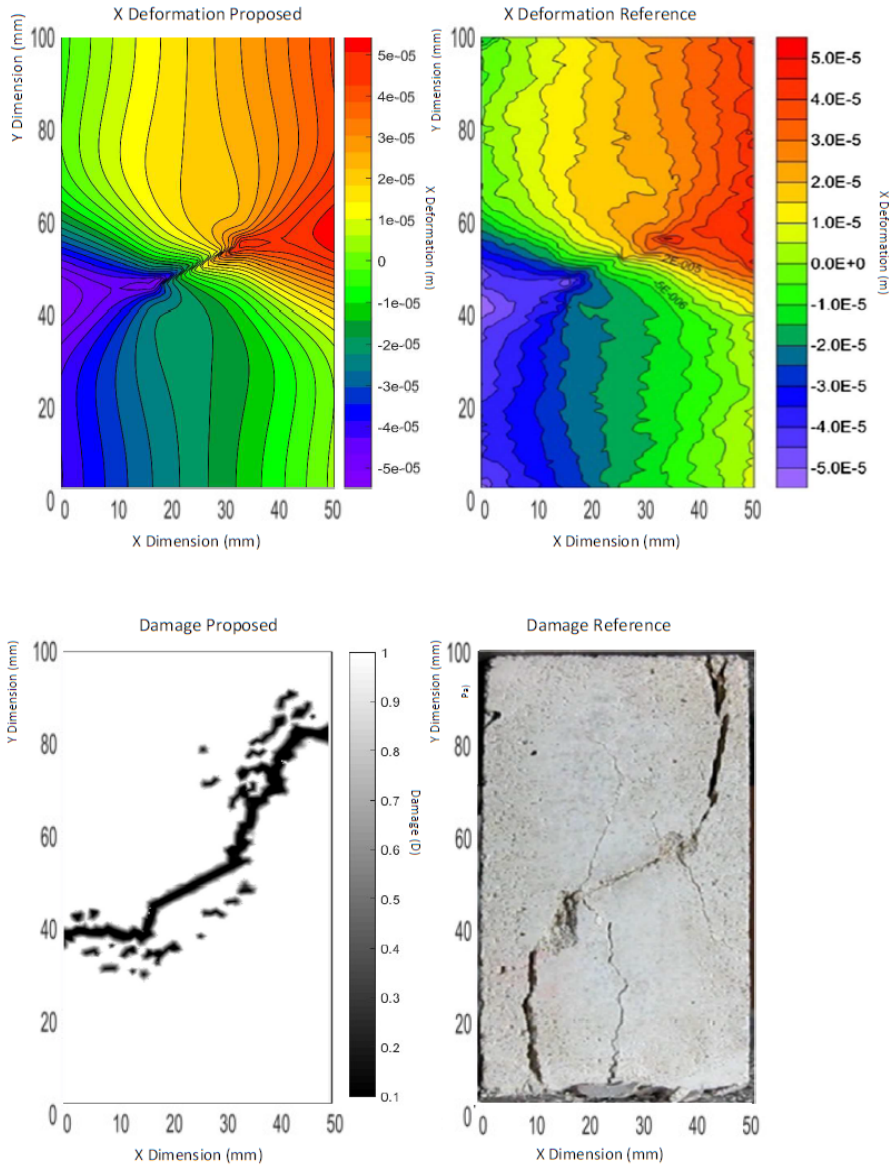

Figure 96: Deformation and Damage plots; proposed numerical solution (left) and reference numerical solution (right) for 30 degree slit at initiation [74]

Note: Experimental reference photo has been flipped on the x axis to match reference deformation result

75 degree notch

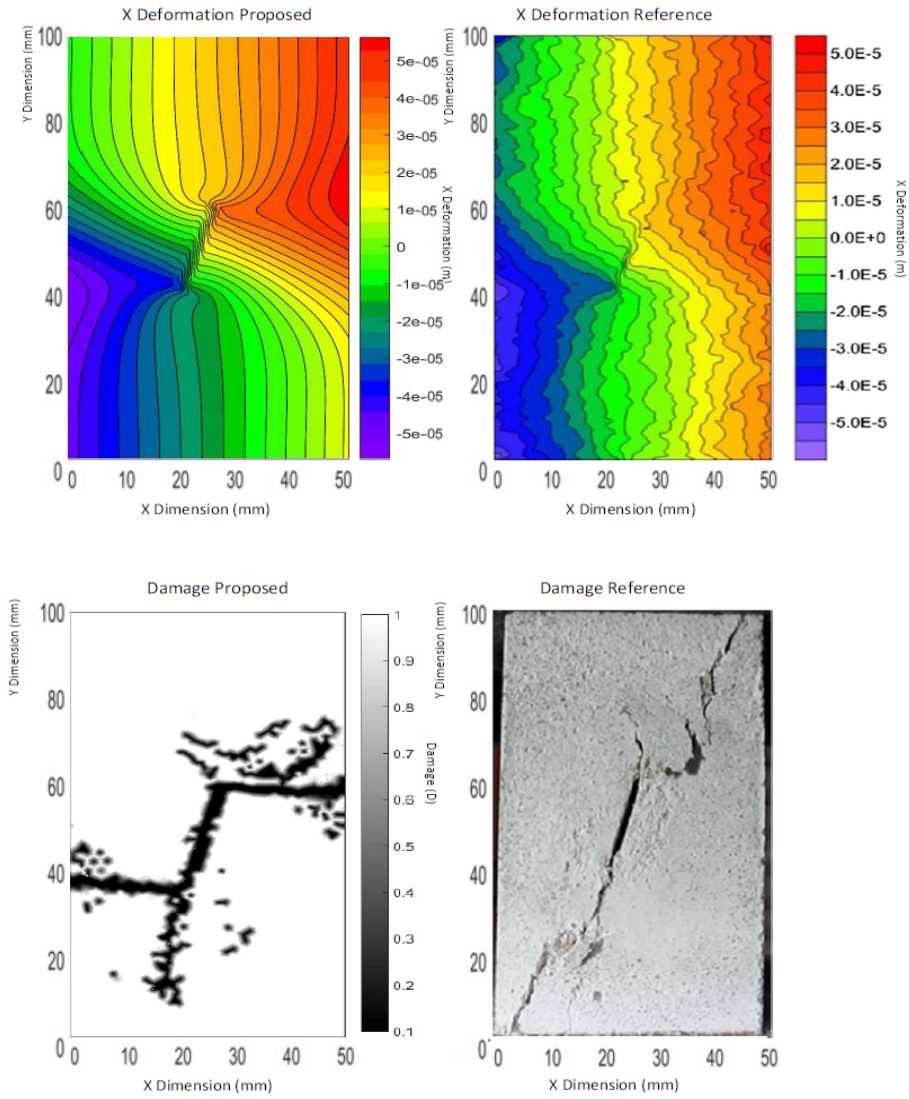

Figure 97: Deformation and Damage plots; proposed numerical solution (left) and reference numerical solution (right) for 75 degree slit at initiation [74]

Figure 98 shows that the fracture is far more violent in comparison to the 60 degree fracture shown in figure 42 as the energy transfer occur in a far shorter time span.

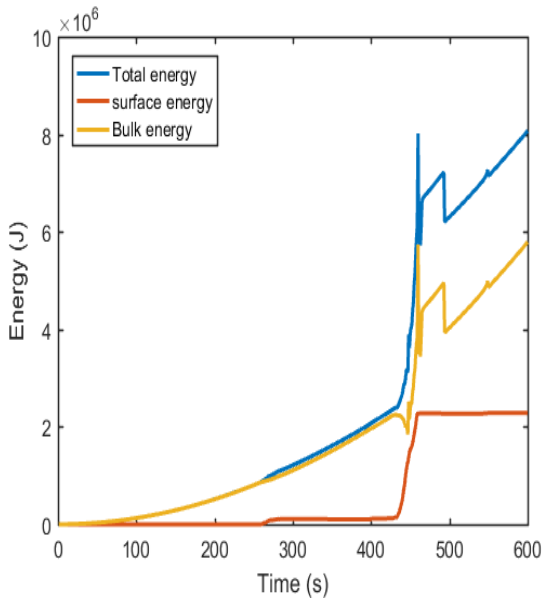

Figure 98: Energy plot over time consisting of fracture (surface energy) and stored energy (bulk) over time (s) for 75 degree notch

90 degree notch

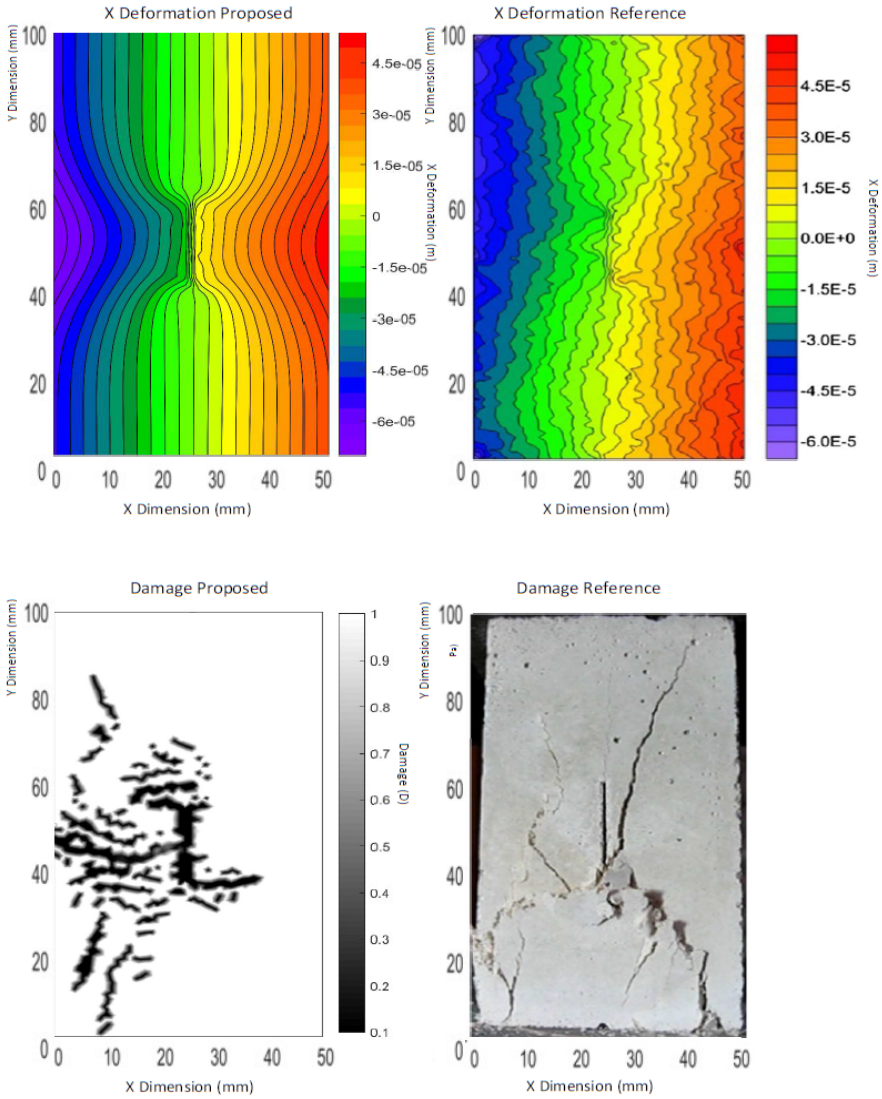

Figure 99: Deformation and Damage plots; proposed numerical solution (left) and reference numerical solution (right) for 90 degree slit at initiation [74]

As shown in Figure 99 there wasn't any major stress concentrations therefore crack initiation was more difficult for the model to predict. This leads to a more sporadic crack path in both the numerical and experimental results.

Appendix C: Chapter 5 results

Test 2: 10MPa Axial pressure, 2MPa hole two pressure

Figure 100: Test 2, Experimental fracture path [136]

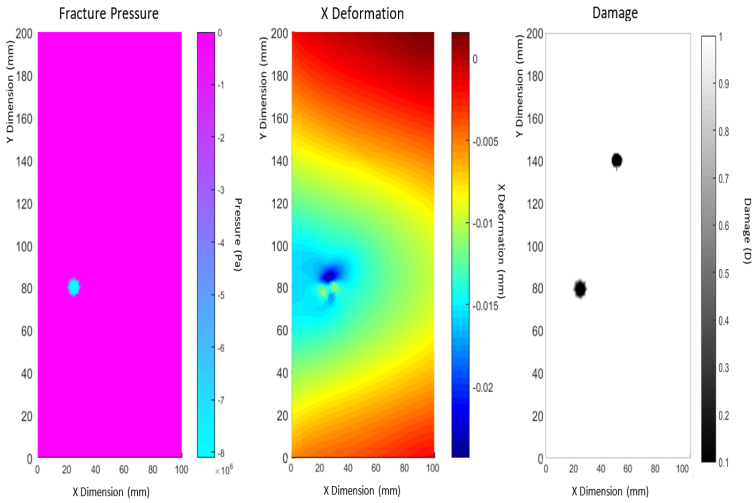

Figure 101: Test 2, Numerical Hydrofracture at time=0s showing from left to right; fluid pressure distribution, X deformation and damage distribution

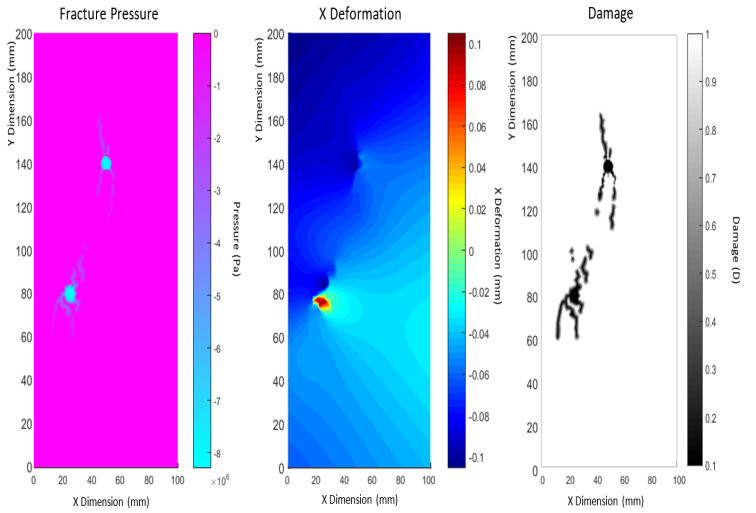

Figure 102: Test 2, Numerical Hydrofracture at time=25s showing from left to right; fluid pressure distribution, X deformation and damage distribution

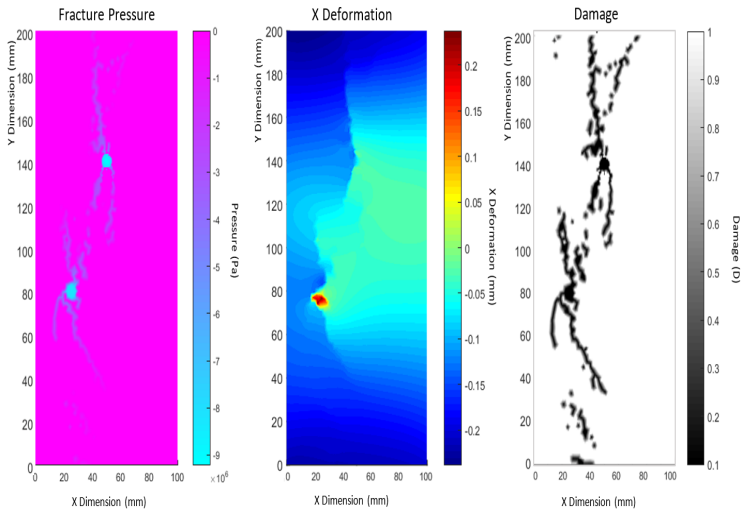

Figure 103: Test 2, Numerical Hydrofracture at time=35s showing from left to right; fluid pressure distribution, X deformation and damage distribution

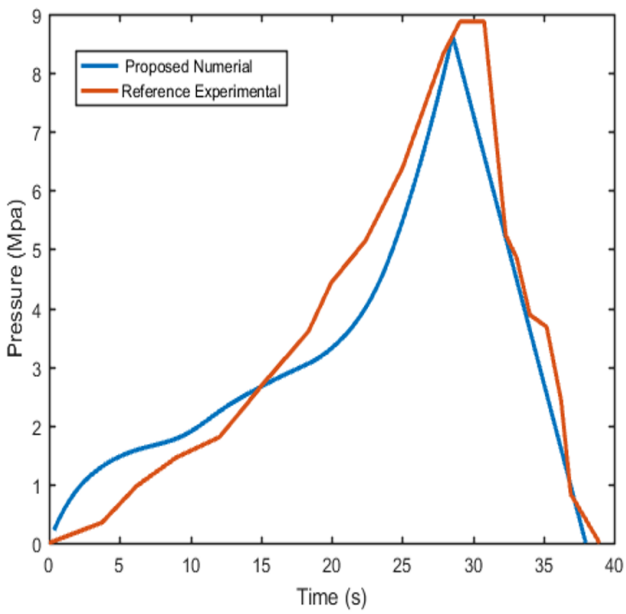

Figure 104: Test 2, fluid pressure in hole one over time

Test 3: 10MPa Axial pressure, 3MPa hole two pressure

Figure 105: Test 3, Experimental fracture path [136]

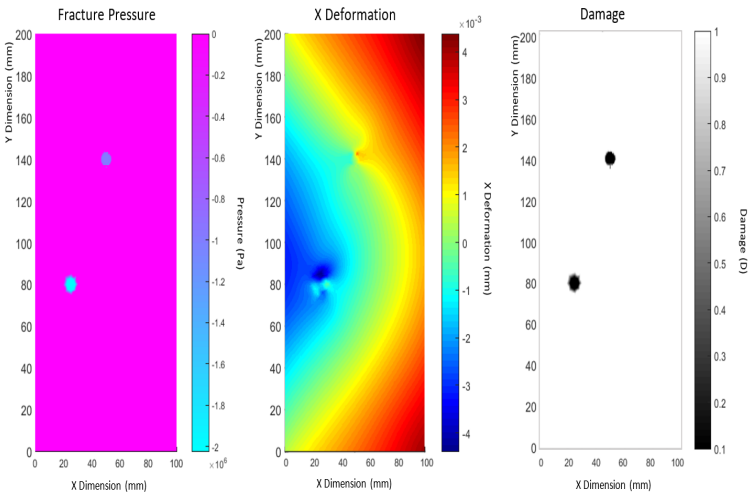

Figure 106: Test 3, Numerical Hydrofracture at time=35s showing from left to right; fluid pressure distribution, X deformation and damage distribution

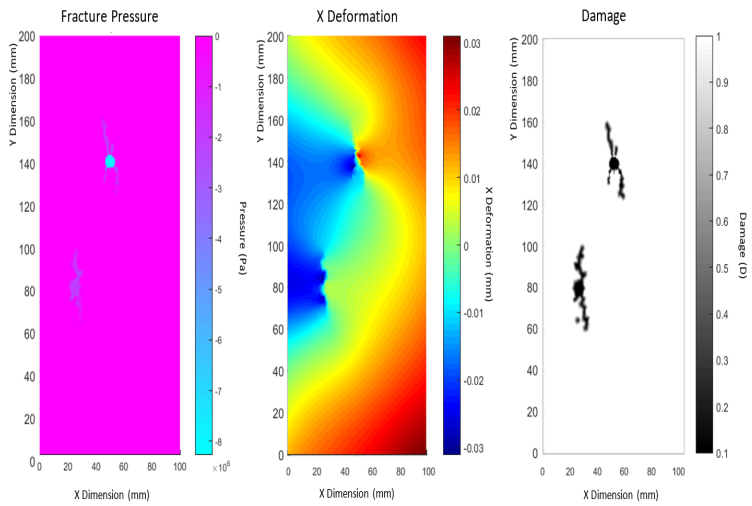

Figure 107: Test 3, Numerical Hydrofracture at time=25s showing from left to right; fluid pressure distribution, X deformation and damage distribution

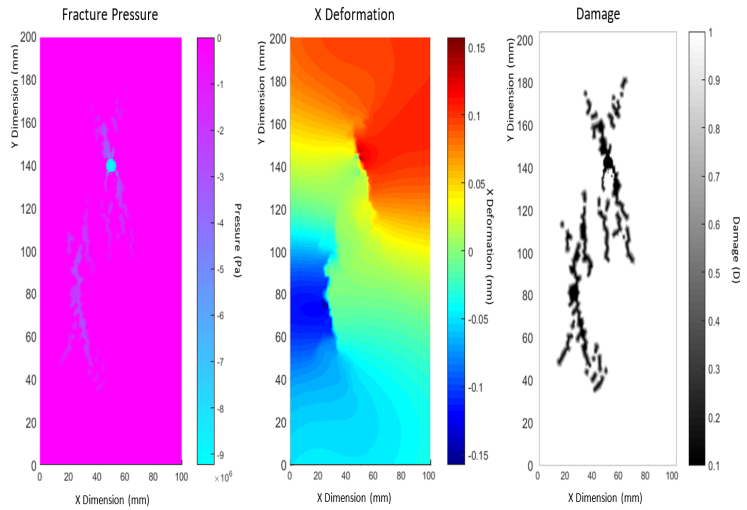

Figure 108: Test 3, Numerical Hydrofracture at time=35s showing from left to right; fluid pressure distribution, X deformation and damage distribution

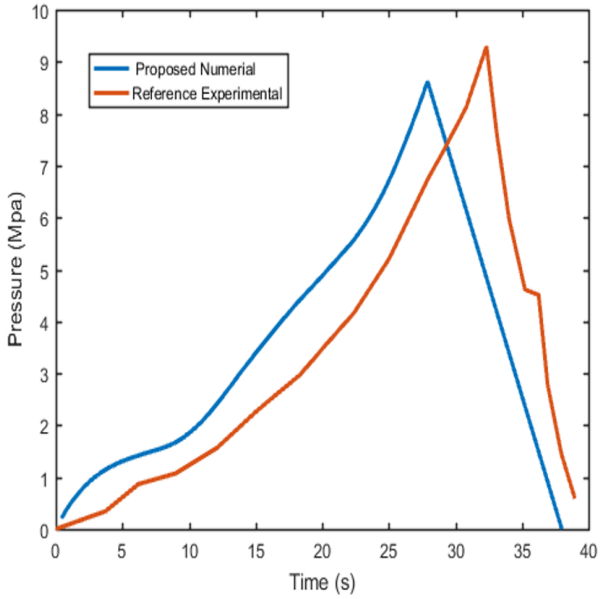

Figure 109: Test 3, fluid pressure in hole one over time

Test 4: 10MPa Axial pressure, 6MPa hole two pressure

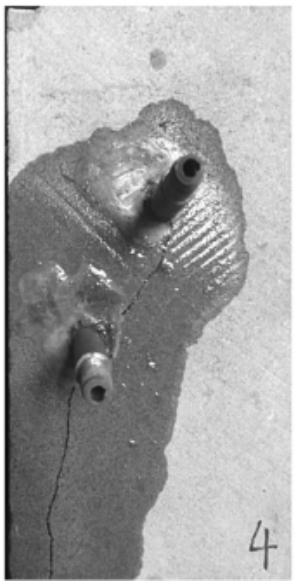

Figure 110: Test 4, Experimental fracture path [136]

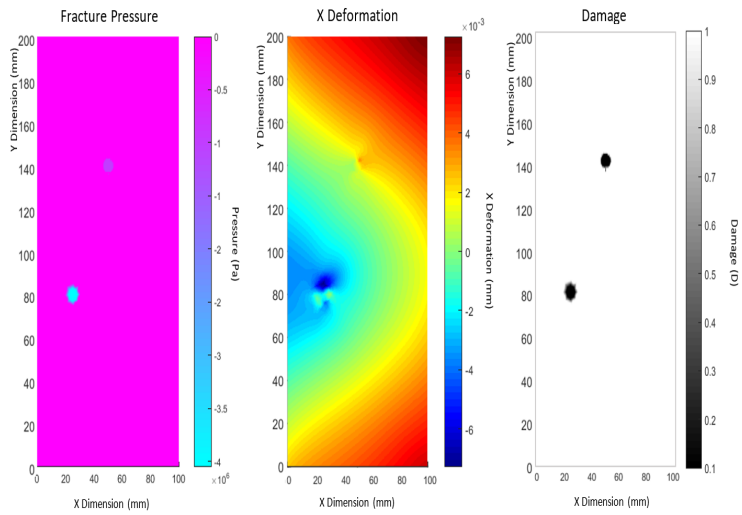

Figure 111: Test 4, Numerical Hydrofracture at time=0s showing from left to right; fluid pressure distribution, X deformation and damage distribution

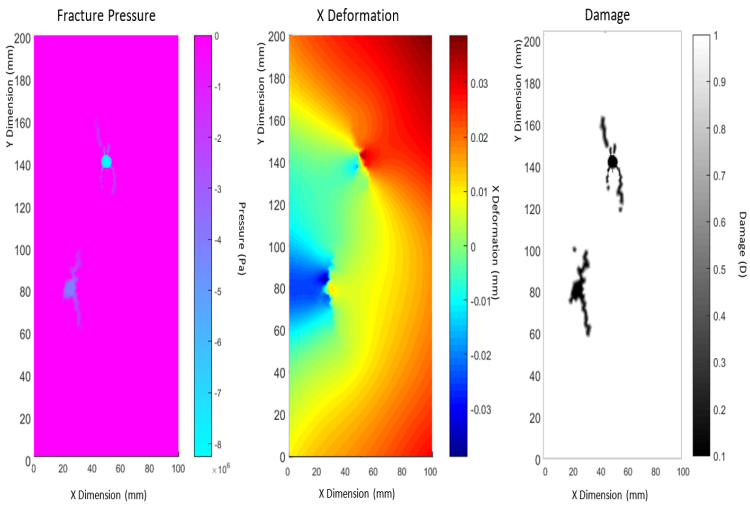

Figure 112: Test 4, Numerical Hydrofracture at time=25s showing from left to right; fluid pressure distribution, X deformation and damage distribution

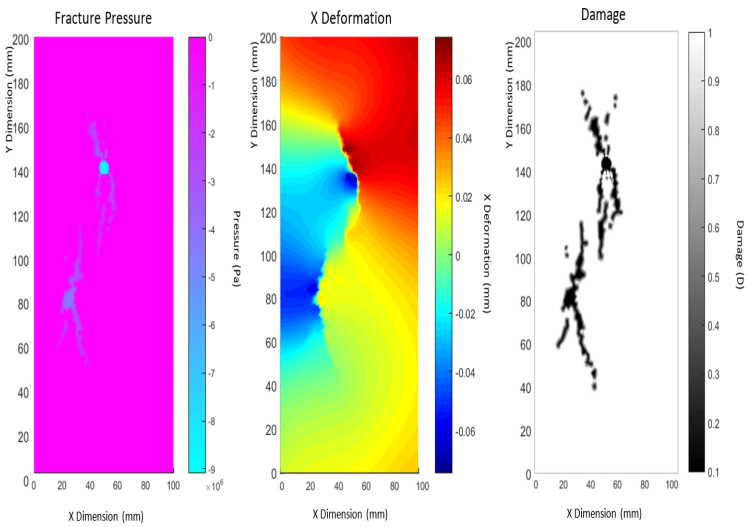

Figure 113: Test 4, Numerical Hydrofracture at time=35s showing from left to right; fluid pressure distribution, X deformation and damage distribution

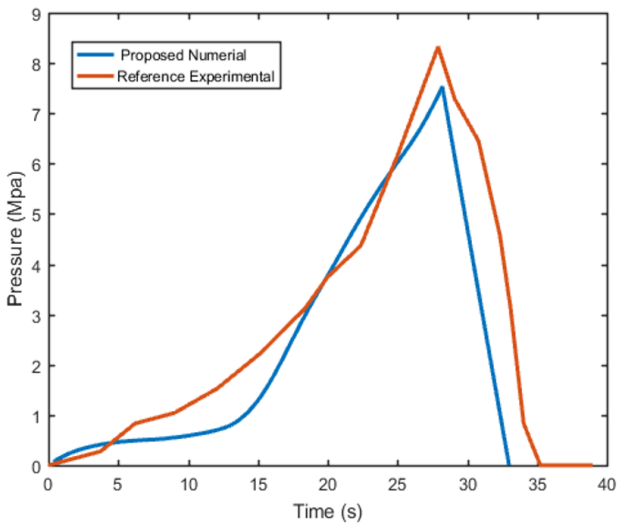

Figure 114: Test 4, fluid pressure in hole one over time (Test 4)